Conjugate Analysis of Two-Dimensional Ablation and Pyrolysis in Rocket Nozzles

by

Peter G. Cross

A dissertation submitted in partial fulfillment
of the requirements for the degree of
Doctor of Philosophy
(Aerospace Engineering)
in The University of Michigan
2017

Doctoral Committee:

Professor Iain D. Boyd, Chair
Professor Arvind Atreya
Associate Professor Karthik Duraisamy
Professor Venkat Raman

"Almighty God, Who hast created man in Thine own image, and made him a living soul that he might seek after Thee and have dominion over Thy creatures, teach us to study the works of Thy hands that we may subdue the earth to our use, and strengthen the reason for Thy service; and so to receive Thy blessed Word, that we may believe on Him Whom Thou hast sent to give us the knowledge of salvation and the remission of our sins. All which we ask in the name of the same Jesus Christ our Lord."

——James Clerk Maxwell [1]

Peter G. Cross

crosspg@umich.edu

ORCHID iD: 0000-0003-4612-6963

For Tara, Quinn, and Ophelia

ACKNOWLEDGEMENTS

A number of individuals and organizations are deserving of recognition for providing various forms of support that made this dissertation possible.

First, I would like to thank my advisor, Professor Iain Boyd, for his guidance and encouragement during the course of this research project. Your flexibility in working with the challenges posed by the unique nature of my gradate studies are appreciated. I also thank the members of my committee, Professors Arvind Atreya, Karthik Duraisamy, and Venkat Raman, for their time spent reviewing this dissertation.

I would also like to express my gratitude to my management at the Naval Air Warfare Center Weapons Division for permitting and enabling me to pursue my Ph.D. I assure you it will make me a more productive employee in the long run. To my colleague Rick Burnes, who introduced me to the topic of ablation modeling, I wish to say that most days I am really thankful that you did. Thanks are extended to Dr. Matthew Gross for discussions regarding the reduced Jeppson reaction mechanism.

Thanks also go to Dr. Mark Ewing for numerous fruitful conversations and for suggestions on running the ITRAC code. There are a number of members of the Nonequilibrium Gas and Plasma Dynamics Laboratory who helped me learn how to use the LeMANS and MOPAR-MD codes. In particular, I would like to thank Drs. Hicham Alkandry, Abhilasha Anna, Erin Farbar, and Jon Wiebenga.

Finally, and most importantly, I thank my wife, Tara, and children, Quinn and Ophelia, for enduring my absence, in both body and mind, as I worked on this dissertation. I love you dearly.

Funding for this work was provided by the Naval Air Warfare Center Weapons Division Fellowship Program; the Science, Mathematics, and Research Transformation Scholarship; and the Naval Air Warfare Center Weapons Division Independent Applied Research Program. Computational resources were provided in part by the Department of Defense High Performance Computing Modernization Office.

TABLE OF CONTENTS

CHAPTER

LIST OF FIGURES

Figure

LIST OF TABLES

Table

LIST OF APPENDICES

Appendix

LIST OF ABBREVIATIONS

ABRES Advanced Ballistic Reentry System

ACE Aerotherm Chemical Equilibrium

ASCC ABRES Shape Change Code

AWEC Ablating Wall – Enthalpy Conductance

AWHF Ablating Wall – Heat Flux

BSL Baseline

CEA Chemical Equilibrium with Applications

CFD Computational Fluid Dynamics

CFL Courant Friedrichs Lewy

CFL3D Computational Fluids Laboratory 3-Dimensional Flow Solver

CHAR Charring Ablator Response

CMA Charring Material Thermal Response and Ablation

FIAT Fully Implicit Ablation and Thermal Analysis Program

FUN3D Fully Unstructured Navier-Stokes

GMRES Generalized Minimum Residual

HIPPO High Internal Pressure-Producing Orifice

HTPB Hydroxyl-Terminated Polybutadiene

IESC Integrated Equilibrium Surface Chemistry

ILU Incomplete Lower Upper

ITRAC Insulation Thermal Response and Ablation Code

JANAF Joint Army Navy Air Force

KATS Kentucky Aerothermodynamics and Thermal Response Solver

LeMANS “Le” Michigan Aerothermodynamic Navier-Stokes Solver

MOPAR-1D Modeling of Pyrolysis and Ablation Response – One-Dimensional

MOPAR-MD Modeling of Pyrolysis and Ablation Response – Multidimensional

MPI Message Passing Interface

NASA National Aeronautics and Space Administration

NAT Nozzle Aerothermochemistry

NCEC Noncatalytic Wall – Enthalpy Conductance

NCHF Noncatalytic Wall – Heat Flux

NIST National Institute of Standards and Technology

ODE Ordinary Differential Equation

PATO Porous-material Analysis Toolbox based on OpenFOAM

PBAN Polybutadiene Acrylonitrile

PICA Phenolic Impregnated Carbon Ablator

RANS Reynolds-Averaged Navier-Stokes

RMS Root Mean Square

SEB Surface Energy Balance

SST Shear Stress Transport

TACOT Theoretical Ablative Composite for Open Testing

TITAN Two-Dimensional Implicit Thermal Response and Ablation

TPS Thermal Protection System

LIST OF SYMBOLS

a	Speed of sound, $\mathrm{m/s}$
A	Area, m^2
A	Arrhenius pre-exponential factor
a_1	Turbulence model coefficient
arg_1	Blending function argument
arg_2	Blending function argument
b	Temperature exponent
B'	Nondimensional mass flux
c_f	Skin friction coefficient
c_p	Pressure coefficient
C_p	Specific heat at constant pressure, $\mathrm{J/kg{\cdot}K}$
C_v	Specific heat at constant volume, $\mathrm{J/kg{\cdot}K}$
C_ω	Cross-diffusion of specific dissipation
$CD_{k\omega}$	Blending function argument
d	Depth from initial surface, m
d	Distance from wall to centroid of cell adjacent to the wall, m
D	Binary diffusion coefficient, $\mathrm{m^2/s}$
D	Diameter, m
D_k	Destruction of turbulent kinetic energy
D_ω	Destruction of specific dissipation
e	Specific energy, $\mathrm{J/kg}$

E	Volumetric total energy, $\mathrm{J/m^3}$
F	Blowing fraction
$\mathbf{F}$	Flux vector
F_1	Turbulence model blending function
F_2	Turbulence model blending function
g_H	Enthalpy conductance, $\mathrm{kg/m^2{\cdot}s}$
g_M	Mass transfer conductance, $\mathrm{kg/m^2{\cdot}s}$
h	Specific enthalpy, $\mathrm{J/kg}$
J	Mass diffusion, $\mathrm{kg/m^2{\cdot}s}$
$\mathbf{J}$	Jacobian (sensitivity) matrix
$\tilde{J}$	Element diffusion mass flux, $\mathrm{kg/m^2{\cdot}s}$
$\tilde{J}_{error}$	Diffusion correction term, $\mathrm{kg/m^2{\cdot}s}$
k	Reaction rate coefficient, $\mathrm{mol} - \mathrm{cm} - \mathrm{s}$
k	Turbulent kinetic energy, $\mathrm{J/kg}$
K	Permeability, m^2
L	Characteristic length, m
Le	Lewis number
M	Mach number
M	Gas mass content, kg
$\mathbf{M}$	Gas mass content vector, kg
$\dot{M}$	Rate of change of gas mass content, $\mathrm{kg/s}$
$\dot{\mathbf{M}}$	Rate of change of gas mass content vector, $\mathrm{kg/s}$
$\dot{m}''$	Mass flux, $\mathrm{kg/m^2{\cdot}s}$
$\dot{m}'''$	Volumetric mass source term, $\mathrm{kg/m^3{\cdot}s}$
$\mathscr{M}$	Molecular weight, $\mathrm{kg/kmol}$
n	Aluminum content in propellant, %
n	Flow solver iteration number

N	Number of faces on the ablating wall
N	Number of nodes in mesh
N	Shape function
N_A	Avogadro's constant, $6.022 \times 10^{26}\ ^{1}/_{\mathrm{kmol}}$
$\hat{n}$	Unit normal vector
P	Pressure, Pa
P_k	Production of turbulent kinetic energy
$\tilde{P}_k$	Unlimited production of turbulent kinetic energy
P_ω	Production of specific dissipation
Pr	Prandtl number
$\dot{q}''$	Heat flux, $^{\mathrm{W}}/_{\mathrm{m}^2}$
$\mathbf{Q}$	Conserved variable vector
$\mathbf{Q}$	Energy content vector, J
$\dot{Q}$	Rate of change of energy content, W
$\dot{\mathbf{Q}}$	Rate of change of energy content vector, W
R	Gas constant, $^{\mathrm{J}}/_{\mathrm{kg \cdot K}}$
R^-	Outward-running Riemann invariant
R_u	Universal gas constant, $8.314\ ^{\mathrm{kJ}}/_{\mathrm{kmol \cdot K}}$
Re_θ	Momentum thickness Reynolds number
Re_x	Stream length Reynolds number
S	Normalized sensitivity coefficient
$\dot{s}$	Surface recession rate, $^{\mathrm{m}}/_{\mathrm{s}}$
$\mathbf{S}$	Source term vector
S_B	Blowing wall empirical correction
Sc	Schmidt number
St	Stanton number
t	Time, s

T	Temperature, K
$\mathbf{T}$	Temperature vector, K
u	Velocity, $^{\mathrm{m}}/_{\mathrm{s}}$
U	Velocity magnitude, $^{\mathrm{m}}/_{\mathrm{s}}$
u^+	Dimensionless, sublayer-scaled, velocity
u_τ	Friction characteristic velocity, $^{\mathrm{m}}/_{\mathrm{s}}$
V	Volume, m^3
w	Dimensionless relative density
$\dot{w}$	Volumetric energy source term, $^{\mathrm{W}}/_{\mathrm{m}^3}$
x	Spatial coordinate, m
y	Distance from cell centroid to the closest wall, m
y	Spatial coordinate, m
Y	Mass fraction
$\tilde{Y}$	Element mass fraction
y^+	Dimensionless, sublayer-scaled, wall distance
β	Degree of char
β	Turbulence model coefficient
$\beta^\star$	Turbulence model coefficient
γ	Ratio of specific heats
γ	Turbulence model coefficient
Γ	Pyrolyzing component volume fraction
ε	Convergence threshold value, %
ε	Emissivity
ε	Perturbation parameter
ζ	Modified nondimensional blowing rate
ζ	Particle volume fraction
κ	Thermal conductivity, $^{\mathrm{W}}/_{\mathrm{m\cdot K}}$

λ	Blowing correction parameter
μ	Dynamic viscosity, ${}^{\mathrm{kg}}/_{\mathrm{m\cdot s}}$
μ_t	Eddy viscosity, ${}^{\mathrm{kg}}/_{\mathrm{m\cdot s}}$
$\tilde{\mu}_t$	Unlimited eddy viscosity, ${}^{\mathrm{kg}}/_{\mathrm{m\cdot s}}$
ν	Stoichiometric coefficient
ξ	Variable to collectively refer to multiple other variables
ρ	Density, ${}^{\mathrm{kg}}/_{\mathrm{m^3}}$
$\boldsymbol{\rho}_{\mathbf{g}}$	Pyrolysis gas density vector, ${}^{\mathrm{kg}}/_{\mathrm{m^3}}$
σ	Stefan-Boltzmann constant, $5.67 \times 10^{-8}\,{}^{\mathrm{W}}/_{\mathrm{m^2\cdot K^4}}$
σ_k	Turbulence model coefficient
σ_ω	Turbulence model coefficient
τ	Viscous stress, Pa
ϕ	Porosity
ψ	Reaction order
ψ	Under-relaxation factor
ω	Specific dissipation, ${}^{1}/_{\mathrm{s}}$
Ω	Vorticity magnitude, ${}^{1}/_{\mathrm{s}}$
Ω_{blw}	Blowing correction factor

Subscripts

0	Absence of blowing
0	Initial
0	Total (stagnation)
1	Inside viscous sublayer
2	Outside viscous sublayer
∞	Freestream
$\perp$	Perpendicular to the plies

$\|$	Along the plies
a	Activation
abl	Ablation
B	Blowing
bnd	Boundary
c	Char
cl	The cl^{th} cell; cell to the left of a face
$cond$	Conduction
$conv$	Convection
cr	The cr^{th} cell; cell to the right of a face
cs	Control surface
cv	Control volume
e	Boundary layer edge
f	Face
$flow$	Gas flow
FS	Flow solver
g	Gas
$grid$	Grid convection
i	The i^{th} pyrolyzing component
i	The i^{th} vector component
I	Inviscid
j	The j^{th} vector component
k	The k^{th} element, face, or node, depending on context
l	Laminar
m	Mesh
M	Mixture
min	Minimum

MR	Material response solver
n	Normal
p	Nodal position of interest
p	Particle
r	Recovery
r	The r^{th} reaction
rad	Radiation
res	Reservoir
RMS	Root mean square
s	Solid
s	The s^{th} species
S	Source term
src	Source
$stor$	Storage
t	Turbulent
tr	Translational-rotational mode
v	Virgin
V	Viscous
ve	Vibrational-electron-electronic mode
w	Wall

Superscripts

$-$	Associated with fluxes from the right cell to the left cell
$+$	Associated with fluxes from the left cell to the right cell
n	The n^{th} time step
ν	The ν^{th} Newton-Raphson iteration

ABSTRACT

The development of a methodology and computational framework for performing conjugate analyses of transient, two-dimensional ablation of pyrolyzing materials in rocket nozzle applications is presented. This new engineering methodology comprehensively incorporates fluid-thermal-chemical processes relevant to nozzles and other high temperature components, making it possible, for the first time, to rigorously capture the strong interactions and interdependencies that exist between the reacting flowfield and the ablating material. By basing thermal protection system engineering more firmly on first principles, improved analysis accuracy can be achieved.

The computational framework developed in this work couples a multi-species, reacting flow solver to a two-dimensional material response solver. New capabilities are added to the flow solver in order to be able to model unique aspects of the flow through solid rocket nozzles. The material response solver is also enhanced with new features that enable full modeling of pyrolyzing, anisotropic materials with a true, two-dimensional treatment of the porous flow of the pyrolysis gases. Verification and validation studies demonstrating correct implementation of these new models in the flow and material response solvers are also presented.

Five different treatments of the surface energy balance at the ablating wall, with increasing levels of fidelity, are investigated. The Integrated Equilibrium Surface Chemistry (IESC) treatment computes the surface energy balance and recession rate directly from the diffusive fluxes at the ablating wall, without making transport coefficient or unity Lewis number assumptions, or requiring pre-computed surface thermochemistry tables. This method provides the highest level of fidelity, and can inherently account for the effects that recession, wall temperature, blowing, and the presence of ablation product species in the boundary layer have on the flowfield and ablation response.

Multiple decoupled and conjugate ablation analysis studies for the HIPPO nozzle test case are presented. Results from decoupled simulations show sensitivity to the wall temperature profile used within the flow solver, indicating the need for conjugate analyses. Conjugate simulations show that the thermal response of the nozzle is relatively insensitive to the choice of the surface energy balance treatment. However, the surface energy balance treatment is found to strongly affect the surface recession predictions. Out of all the methods considered, the IESC treatment produces surface recession predictions with the best agreement to experimental data. These results show that the increased fidelity provided by the proposed conjugate ablation modeling methodology produces improved analysis accuracy, as desired.

CHAPTER I

Introduction

1.1 Motivation

Solid propellant rocket motors are employed in a wide range of applications, including tactical missiles, strategic missiles, sounding rockets, attitude control systems, and space access systems [2]. Perhaps the most well-known solid rocket motor design (and one of the largest) is that for the boosters used to launch the space shuttle.

There are two main types of solid propellants used in rockets: double-based and composite. Double-based propellants are a homogeneous blend of nitroglycerin and nitrocellulose explosives. The more common, and higher performance, composite propellants consist of a powdered oxidize, usually ammonium perchlorate (though other oxidizers can also be used), suspended in a polymer binder, such as hydroxyl-terminated polybutadiene (HTPB) or polybutadiene acrylonitrile (PBAN), that also serves as the fuel. Powdered aluminum metal is also often included as a high-energy fuel in many composite propellants.

Critical solid rocket components are often manufactured from ablating thermal protection system (TPS) materials. These are materials such as graphite, carbon-carbon, carbon-phenolic, silica-phenolic, or filled rubbers that ablate (lose mass) when subjected to high heating conditions. The main purpose of these materials is to protect the structure and other system components (e.g. control actuators) from the high temperature combustion gases, but they are also used to produce the contour of the nozzle that accelerates the flow to produce thrust.

Producing an optimized rocket motor system requires accurately predicting ablator performance. For example, the enlargement of the nozzle throat due to ablation has a direct, negative impact on system performance that must be anticipated [2]. Erosion of the throat has been identified as the second largest source of losses in the nozzle for the space shuttle booster (which had an initial throat diameter of 1.39 m), reducing the specific impulse of the motor by 0.9 s [2]. Powers et al. [3] report that reducing the erosion of the shuttle booster throat by 40 % would increase the specific impulse by 0.6 s, which corresponds to a gain in payload capability of 227 kg. The impact of throat erosion is even more significant for smaller motors (those used in tactical missiles have throats with initial diameters ranging from 6 mm to 0.13 m [2]), as the percent enlargement of throat area for a given recession value increases as initial throat area decreases. For most applications, throat area enlargement must remain below 5 % [2].

In addition to recession, it is important to accurately predict the in-depth thermal response of the nozzle material, as thermal stresses in the ablating material can lead to nozzle structural failure. Also, minimizing TPS material permits an increase in payload or performance, but having insufficient TPS material will lead to system failure. For a hypothetical air-to-air missile (with an outer diameter of 125 mm, a case thickness of 5 mm, an insulation thickness of 5 mm, and a port diameter of 40 mm), reducing the internal insulation thickness by half allows the propellant load to be increased by more than 10 %, without making any changes to the airframe outer mold line. An analysis of three large solid rocket motors characterized in the text by Sutton and Biblarz [2] indicates that the internal insulation protecting the motor case contributes on the order of 20 % of the inert mass of the motor. The nozzle, which is largely constructed from ablating materials, contributes an additional 20 % to 40 %

of the motor inert mass. A study investigating lower-cost, lighter-weight carbon-phenolic materials for the shuttle booster nozzle showed that reducing nozzle mass by 532 kg would result in an increase in payload capability of 97 kg [3]. While these large motors have a low inert mass fraction (under 10 %), the relative importance of the mass associated with ablating materials is amplified for rocket motors used for tactical missiles, which can have inert mass fractions ranging from 25 % to 70 % [2].

Because of deficiencies associated with current ablation analysis methodologies, development of rocket motor components and other thermal management systems relies extensively on costly physical testing. Also, the necessity of avoiding system failure, combined with large analysis uncertainly, usually means that thermal protection systems are over-designed to provide margin, consuming portions of the volume and mass budget for the system that could otherwise be dedicated to additional propellant or increased payload [4]. A common factor of safety used in TPS design is to require the initial material thickness to be no less than the sum of twice the expected surface recession and 1.25 times the expected final char thickness [3, 5]. The resultant TPS therefore has more than twice the amount of material than is strictly necessary to protect the underlying structure. With improved analysis methodologies, it should be possible to reduce this factor of safety and achieve reliable TPS designs that have lower mass, take less volume, and provide increased performance.

This work in primarily concerned with the ablation of carbon-phenolic nozzles in missiles and space access boosters that utilize aluminized composite propellants, though the methodologies developed could be applied to other ablating materials and applications. Smaller solid rocket motors (such as used in tactical missiles), where the effects of surface recession and the mass fraction consumed by ablating materials are greater, would benefit the most from improvements to the accuracy of ablation analysis methodologies.

Ablation is a very complex problem with numerous important physical processes and strong mutual interactions between the nozzle flowfield and the ablation response of the material. Ablating materials can be categorized into two broad groups. The first is non-pyrolyzing (or non-charring) materials, which only experience mass loss from the exposed surface. Examples include graphite and carbon-carbon composites. Pyrolyzing (or charring) materials, on the other hand, experience mass loss due to in-depth thermal decomposition, in addition to ablation at the exposed surface. Carbon-phenolic, silica-phenolic, and filled rubbers are all examples of pyrolyzing materials. This work is focused on pyrolyzing materials; non-charring materials involve only a subset of the physical processes associated with the ablation of pyrolyzing materials.

The physical processes involved in the ablation of pyrolyzing materials are illustrated in Figure 1.1. A pyrolyzing ablator can be divided into three zones: the virgin TPS material (which remains unaffected by heat), a pyrolysis zone where the heat transfer from the surface causes the TPS to pyrolyze (thermally decompose), and a char zone formed by the solid residue of the pyrolysis process. A substructure supports and is thermally protected by the ablating material. High temperature, high pressure, reacting, turbulent, particle-laden flow passes through the nozzle of a solid rocket, which provides strong convective heating to the TPS material. The gases released from the material by the pyrolysis process flow through the porous char, then induce a blowing interaction with the boundary layer, which generally reduces the heat transfer. A radiative heat transfer mechanism between the combustion products and the surface of the ablator can also exist, especially for solid rocket propellents with a large aluminum fuel content. Char material is removed from the surface due to chemical processes (such as reactions with the boundary layer edge gases or by sublimation) and by mechanical processes (e.g. particle impingement, aerodynamic shear, spallation, ply lifting, melting). Depending on the material, additional physical processes can take place at depth within the material. Some materials exhibit intumescence (swelling) as part of the pyrolysis process. Coking (densification of

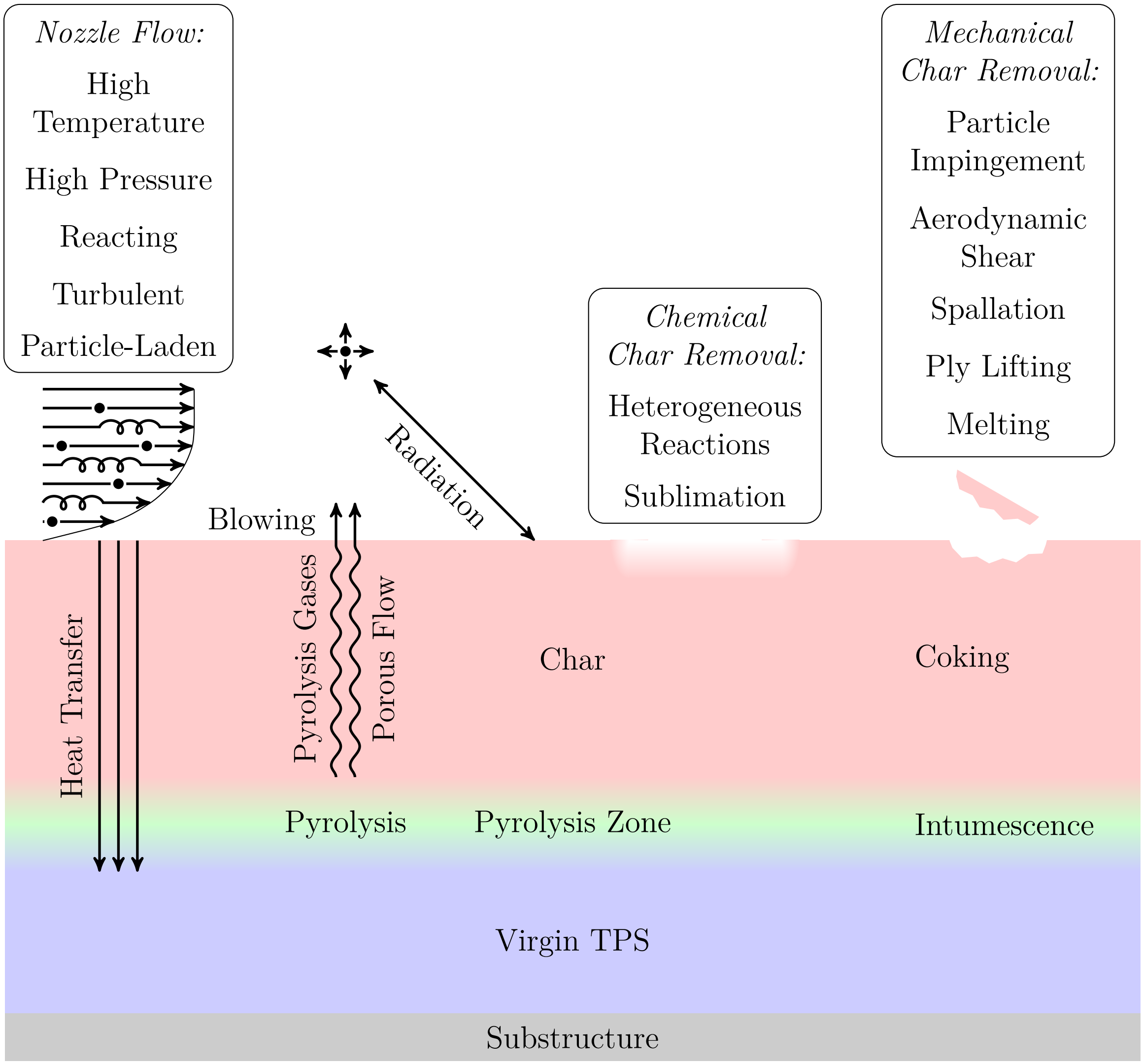

Figure 1.1: Schematic illustrating important physical processes at work during ablation of pyrolyzing materials.

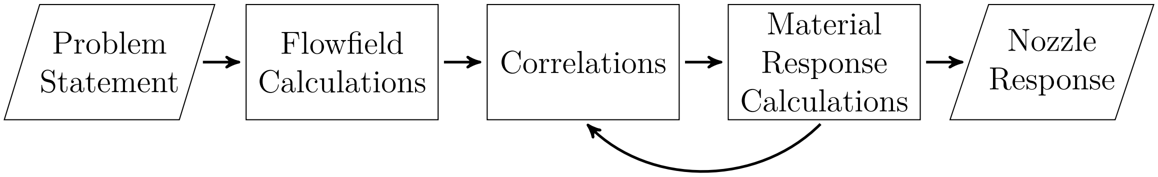

(a) Historical decoupled analysis methodology.

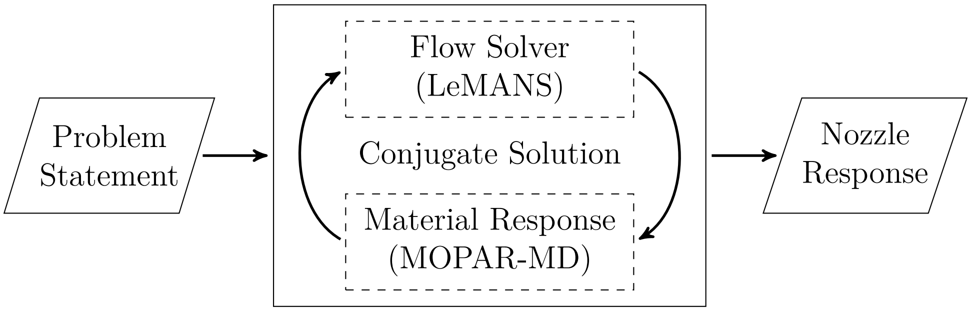

(b) Objective conjugate analysis methodology.

Figure 1.2: Flowcharts comparing the historical decoupled analysis methodology and the conjugate analysis methodology of this work.

the char due to the precipitation of carbon from the pyrolysis gases) also occurs for some materials. Mechanical char removal processes, intumescence, and coking are not considered in this work.

Some of the earliest work on ablation modeling [6] recognized the need to perform conjugate simulations in order to capture the coupling between the boundary layer, the thermal response of the material, and heat and mass transfer at the ablating surface. In spite of this acknowledged need, historically, ablation in rocket nozzles has been modeled using an approach in which the computation of the convective boundary conditions is decoupled from the thermal response of the ablator (see top diagram in Figure 1.2). In this traditional approach, calculations to determine the convective heating environment in the nozzle are performed first. Often an empirical correlation called the Bartz equation [7] is used to obtain the convective heating conditions. A common alternative is to use a 1D isentropic expansion calculation combined with integral boundary layer techniques [8], but computational fluid dynamics (CFD) techniques can also be used to determine the convective heating conditions. Usually these

CFD analyses are performed assuming a nonablating wall. The thermal response and ablation of the thermal protection system (TPS) is then calculated with CMA [9] or a similar one-dimensional ablation code. To account for the effects of surface recession and blowing on the boundary layer, empirical corrections are applied by the material response solver to the pre-computed convective boundary conditions. The surface energy balance at the ablating surface is determined based upon transport coefficient assumptions and pre-computed surface thermochemistry (B') tables.

With this decoupled approach it is not possible to rigorously account for geometric effects or thermo-chemical buffering of the boundary layer. Coupling between the flow solver and the material response solver is required in order to capture the effects of shape change due to recession [10]. Also, char mass flux (recession rate) is sensitive to composition at the ablating surface [11], which is affected by the transport coefficient diffusion model assumption. Additionally, in this work it has been found that the material response of the nozzle depends upon the wall temperature profile assumed when computing the cold wall heat flux (see Section 7.3.2). Decoupled analyses are therefore unable to rigorously capture the mutual interactions that occur at the ablating boundary between the flowfield and the material response. A detailed review of ablation modeling methodologies is provided by Milos and Rasky [4], which emphasizes the need for conjugate analysis methodologies.

For conjugate analyses, the flowfield and material response are computed in a tightly-coupled manner (see lower diagram in Figure 1.2), in order to capture the strong interactions and dependencies that exist between the reacting flowfield and the ablating material. As a result, improved analysis accuracy is anticipated.

1.2 Review of Related Work

The key effort that established the landscape of ablation modeling for decades to come was the development of the CMA code in the 1960s [6, 9, 12]. CMA can solve the one-dimensional, transient ablation problem for charring materials. A finite-difference scheme is used in conjunction with a translating mesh fixed to the ablating surface. Nodes are removed from the back surface of the mesh to account for recession, and sub-nodes are used to resolve the sharp solid density gradients produced by pyrolysis. The pyrolysis equations (using a three-component model) are solved explicitly using the previous temperature solution, while the energy equation is solved implicitly. The explicit pyrolysis solution approach causes CMA to encounter stability issues when solving problems with high heat fluxes. Pyrolysis gases are assumed to be immediately ejected from the ablator (quasi-steady assumption); a transport equation for the porous flow is therefore not required. The surface energy balance at the surface is computed using transport coefficient assumptions and pre-computed B' tables. Temperature-dependent properties are lagged one time step. While CMA could optionally be coupled to a two-dimensional, reacting, nonsimilar boundary layer solver, it is usually used as a decoupled ablation solver. CMA is still in widespread use today, and has become the de facto standard against which all other ablation modeling codes are compared.

In spite of the popularity of CMA, a number of alternative one-dimensional ablation codes have been developed over the years to provide enhanced modeling capabilities. Russell and Strobel added a capability for modeling intumescing materials to CMA [13], forming the CMASWELL code [14]. The FIAT code was developed at NASA to resolve some of the stability issues with CMA [15]. The theoretical framework used in FIAT is very similar to that of CMA, except that a coupled, fully-implicit, finite-volume method is used to solve the energy and pyrolysis equations. Grid compression is also used to account for recession.

The one-dimensional ablation code produced by Amar [16, 17, 18] modeled the flow of the pyrolysis gases through the porous char using Darcy's law, thus eliminating the quasi-steady assumption. The gas phase continuity equation is written in terms of pyrolysis gas density. Pyrolysis can be modeled using an unlimited number of components, removing the three-component restriction of CMA. The control volume finite element method is employed, along with grid compression and fully-implicit time integration. Governing equations are solved sequentially using a block Gauss-Seidel method in an iterative process each time step. This provides full coupling of the governing equations, an improvement upon the loose-coupling used in CMA. The MOPAR-1D code [19, 20] developed at the University of Michigan is closely based upon Amar's work, and provides nearly-identical capabilities. One new feature included in MOPAR-1D is the option to model the porous flow of the pyrolysis gases using Forchheimer's law.

Another one-dimensional ablation code developed recently is the ITRAC code [21]. Porous flow is still modeled using Darcy's law, but in this code the gas phase continuity equation is written in terms of pressure. Pyrolysis is modeled using an extent-of-reaction equation for each of an unlimited number of reactions, which is different from the density-based pyrolysis reactions used in most other codes. Equation solution is performed sequentially in an optionally iterative process each time step. Integration of the pyrolysis equations is performed explicitly, while the energy and gas phase continuity equations are solved implicitly. A finite-volume method is used, along with a fixed grid that does not compress or translate. Nodes at the front surface of the mesh are deactivated to account for ablation (in contrast to CMA, which drops nodes at the back face of the mesh). This approach simplifies implementation of mechanical erosion and intumescence models, several of which are supported.

Most early two-dimensional ablation codes were restricted to modeling non-charring materials (such as graphite). Examples include the code of Blackwell et al. [22, 23], the code of Katte et al. [24], COYOTE [25], and ASCC [26]. The baseline version of MOPAR-MD developed by Wiebenga [27, 28] was also limited to non-charring materials, but could model anisotropic thermal conductivity.

One of the earliest two-dimensional ablation codes capable of modeling pyrolyzing materials was TITAN [29]. In this code, the governing equations for energy transport and pyrolysis are solved using a finite-volume method, body-fitted meshes, and a coupled, implicit, time-marching scheme. Flow of the pyrolysis gases is assumed to be one-dimensional (along mesh lines) and quasi-steady (no porous flow transport equation is solved; pyrolysis gases are immediately ejected). To account for recession, the mesh is allowed to compress along mesh lines. A later improvement now allows materials with orthotropic thermal conductivity to be modeled [30].

In an effort contemporaneous to the present work, the CHAR multidimensional ablation program [31] has been developed at NASA. The governing equations are solved using a finite-element method; the energy and pyrolysis gas conservation equations are solved in a coupled, implicit manner. Jacobians are computed exactly using an interesting complex-step method. Pressure is taken to be the unknown variable describing porous flow. Pyrolysis is modeled assuming constant temperature during a time step (i.e. an explicit implementation). An explicit mesh motion scheme is also used to capture the effects of recession. Adaptive mesh refinement is used to capture strong gradients.

The Porous-material Analysis Toolbox based on OpenFOAM (PATO) [32] is a library developed recently by researchers at NASA for the primary purpose of testing new physics models that can then be incorporated into production-level ablation analysis codes. Emphasis is placed on modeling the flow of the pyrolysis gases through the porous material. Pyrolysis gas species are tracked, and finite-rate gas-phase reactions within the porous material can also be modeled. Thermodynamic and transport properties are computed using the Mutation++ library [33]. PATO inherits the three-dimensional finite-volume capabilities of the OpenFOAM flow solver upon which it is based; it is first-order accurate in time and space. Governing equations are solved sequentially, an approach taken since it easily allows modifications to each equation as well as the addition of new equations.

The material response module in KATS is a three-dimensional material response code developed quite recently at the University of Kentucky [34, 35, 36]. Pyrolysis is modeled using the same three-component model used by CMA, while a time-dependent form of Darcy's law is used to model the flow of the pyrolysis gases through the char. Materials with orthotropic permeability and thermal conductivity can be modeled. The governing equations are solved implicitly and simultaneously; a finite-volume method is used. In very recent work, a structural response capability has been added to KATS, with mesh motion used to capture the geometry deformation due to thermal expansion [37]. However, one critical limitation of the KATS code is the absence of support for a thermochemical ablation boundary condition, which makes it impossible to model problems that experience surface recession. Due to this limitation, the KATS code cannot be considered to be an ablation solver in the same sense as the other codes discussed.

In general, all the ablation solvers just discussed are equally applicable to rocket nozzle problems as they are to external TPS applications.

Very early work at NASA considered the coupling of a transient, one-dimensional ablation analysis to computation of a two-dimensional, reacting boundary layer [6]. However, by the time of Milos and Rasky's 1994 review [4], the state of the art had not yet advanced to the point where fully-conjugate flowfield / ablation analyses could be performed. One of the main conclusions presented in their review article was the need for improvements to both flow and material response solvers in order to be able to perform coupled flowfield / ablation analyses for multidimensional geometries.

One of the earliest coupled flowfield / ablation analysis efforts was performed at NASA to investigate transient, one-dimensional ablation for the Stardust sample return capsule, which utilized a pyrolyzing TPS material [38]. In this study, the surface energy balance was performed with the use of B' tables. However, the flow solver mesh used in this work was not updated to account for surface recession.

Kuntz et al. [10] at Sandia investigated conjugate analysis of transient, two-dimensional ablation for the nosetip of the IRV-2 vehicle. However, only non-charring TPS materials were considered, using a surface energy balance approach that made the transport coefficient assumption and therefore required B' tables. The flow domain was periodically remeshed in order to capture the effects of surface recession. Researchers at NASA also investigated this test case, using a similar methodology [39]. However, their work assumed one-dimensional ablation.

Coupled simulations of two-dimensional ablation of pyrolyzing materials were investigated by Chen et al. [40] at NASA using the TITAN [29] material response solver; multiple external TPS test cases were considered. Pyrolysis was modeled using quasi-steady and one-dimensional assumptions. The surface energy balance was computed using a traditional B' table approach. An unblown enthalpy conductance was passed from the flow solver to the material response solver, and was assumed to be constant between time points. The flow solver mesh was periodically updated to account for surface recession, but blowing of the boundary layer was not captured by the flow solution. Wall temperature for the flow solver does not appear to be taken from the material response solution, and it is unclear what boundary condition was used for species mass fractions.

More recent research conducted at NASA investigated ablation boundary conditions for flow solvers that directly model equilibrium surface chemistry and char mass flux based upon species diffusion at the wall; transport coefficient assumptions and B' tables were not required [11, 41]. Ablation of pyrolyzing materials in external TPS applications was investigated; one-dimensional, steady-state ablation was assumed.

Previous researchers at the University of Michigan [28, 42, 43] have performed coupled ablation analyses for external thermal protection systems (such as the IRV-2 vehicle and the Stardust reentry capsule) including the transient response of the TPS material. However, only non-charring materials have been modeled assuming two-dimensional heat transfer; conjugate simulations involving pyrolyzing materials have only been performed assuming one-dimensional heat transfer and ablation. Many of these studies used a surface energy balance approach based on B' tables, though some have explored finite-rate surface chemistry.

Recent work at the University of Rome has investigated the effects of ablation on the flowfield within rocket nozzles [44, 45, 46, 47, 48]. Several of these studies modeled finite-rate surface chemistry, though some used an equilibrium chemistry approach that apparently did not make a transport coefficient assumption or use pre-computed B' tables. However, this work assumed one-dimensional, steady-state ablation and did not consider the transient thermal response of the TPS material, nor did the simulations capture multidimensional effects, which can be important near the nozzle throat. Likewise, Thakre and Yang [49] modeled nozzle flowfields assuming steady-state, one-dimensional ablation of non-charring materials.

1.3 Scope of Present Work

The goal of the present work is to establish a methodology and demonstrate a computational framework enabling conjugate analyses of transient, two-dimensional ablation of pyrolyzing TPS materials (e.g. carbon-phenolic) in rocket nozzles. The methodologies produced could also be utilized for airbreathing propulsion or external thermal management applications. Comprehensively incorporating aero-thermo-chemical processes relevant to the ablation of pyrolyzing materials in rocket nozzle applications will make it possible to rigorously capture the strong interactions and interdependencies that exist between the reacting flowfield and the ablating material. By basing thermal protection system engineering more firmly on first principles, improved accuracy is anticipated. This would allow for the majority of TPS design efforts to become more analysis-based, reducing the reliance on costly testing. Increased analysis accuracy would also enable more efficient TPS designs. An optimized TPS design will free up volume or mass that can be reallocated to additional propellant or payload, yielding increased system performance.

In Chapter II, the LeMANS flow solver is briefly introduced, followed by a detailed discussion of several new capabilities added to this flow solver in order to be able to model solid rocket nozzle flows. These new features include two turbulence models, the equilibrium two-gas method for modeling the thermodynamics of particle-laden flows, and a subsonic stagnation inlet boundary condition.

The MOPAR-MD material response solver is described in Chapter III. An overview is given of the loosely-coupled approach used to sequentially solve the pertinent governing equations. Full details are provided for the implementation of the pyrolysis and porous flow equations; derivation and implementation of the thermochemical ablation boundary condition is also presented. A discussion of the method for modeling the radiative heat transfer within nozzles is also included.

Chapter IV presents the strategy taken for coupling the LeMANS flow solver to the MOPAR-MD material response solver. The criteria used in this coupled framework for determining when the material response solver should be called are presented first. Next, five different treatments of the surface energy balance at the ablating wall, with increasing levels of fidelity, are discussed. Some improvements to the mesh interpolation scheme are briefly given, followed by a smoothing algorithm applied to variables exchanged between solvers.

The development of a new, reduced, gas-phase finite-rate chemistry mechanism is presented in Chapter V. This mechanism includes all species that are important for the ablation of carbon-phenolic materials in solid rocket nozzle applications, and has been reduced from a detailed, baseline mechanism through sensitivity studies. Development of this new mechanism is necessitated by the absence of a suitable mechanism in the literature.

Verification and validation studies of the two solvers are presented in Chapter VI. Comparisons are made to results from other codes, to theoretical values, and / or to experimental data, depending on the test case. Successful completion of the flow solver test cases indicates that the enhanced flow solver can accurately predict the turbulent, particle-laden flowfield within rocket nozzles. Test cases for the material response solver indicate that all components necessary for modeling the ablation of pyrolyzing materials have been implemented correctly and consistently with other accepted ablation codes.

The coupled solvers are used in Chapter VII to analyze the ablation of a rocket nozzle test case. Both decoupled and conjugate analyses are performed. The decoupled simulations reveal sensitivity to the wall temperature profile used when pre-computing the convective heating conditions; this reinforces the hypothesis that conjugate analyses are necessary for accurate ablation predictions. Conjugate simulations are found to be susceptible to a shape change instability; multiple mitigation strategies are employed to suppress this instability. Results from conjugate analyses using the Integrated Equilibrium Surface Chemistry treatment are found to provide improved agreement with experimental data.

A summary of this work is presented in Chapter VIII, with a discussion of key observations and conclusions. Advancements made to the state of the art by this work are highlighted. Finally, recommendations for future work are provided.

CHAPTER II

Flow Solver

2.1 Introduction

The flow solver used in this work is LeMANS [50, 51], a multi-species, reacting, Navier-Stokes solver developed at the University of Michigan. This code was originally created for the purpose of studying thermal and chemical nonequilibrium phenomena that occur in two- or three-dimensional, laminar, hypersonic flowfields. As part of this effort, several new capabilities have been added to the LeMANS flow solver, so that it is now possible to also model the turbulent, particle-laden flow through solid rocket nozzles.

2.2 Mean Flow

The Reynolds-Averaged Navier-Stokes (RANS) equations describing the mean (time-averaged) flowfield for multi-species, reacting, turbulent flows with thermo-chemical nonequilibrium can be written in integral form as

$$\frac{d}{dt}\int_{cv} \rho_s dV = -\int_{cs} \rho_s u_j \hat{n}_j dA - \int_{cs} J_{s_j} \hat{n}_j dA + \int_{cv} \dot{m}_s''' dV \tag{2.1}$$

$$\frac{d}{dt}\int_{cv} \rho_s u_i dV = -\int_{cs} \left(\rho_s u_i u_j \hat{n}_j + P \hat{n}_i\right) dA + \int_{cs} \tau_{ij} \hat{n}_j dA \tag{2.2}$$

$$\frac{d}{dt}\int_{cv} E dV = -\int_{cs} (E+P)u_j\hat{n}_j dA + \int_{cs} \left(u_i\tau_{ij} - \sum_s J_{s_j}h_s - \dot{q}''_{tr_j} - \dot{q}''_{ve_j} \right) \hat{n}_j dA \quad (2.3)$$

$$\frac{d}{dt}\int_{cv} E_{ve} dV = -\int_{cs} E_{ve}u_j\hat{n}_j dA + \int_{cs} \left(-\sum_s J_{s_j}e_{ve_s} - \dot{q}''_{ve_j} \right) \hat{n}_j dA + \int_{cv} \dot{w}_{ve} dV \quad (2.4)$$

In these equations, the Einstein summation convention is used with respect to the indices i and j only, which represent the spatial dimensions of the problem.

Equation 2.1 represents a set of mass conservation equations for each species; ρ_s denotes the density of species s, u_j is the j^{th} component of the velocity vector, $\hat{n}_j$ represents the j^{th} component of the outward-facing unit normal vector on the control surface, J_{s_j} is the j^{th} component of the mass diffusion vector for species s, and $\dot{m}'''_s$ is the volumetric mass production rate for species s. Momentum conservation in each spatial dimension is represented by Equation 2.2; P denotes the pressure and τ_{ij} is the viscous stress tensor. Conservation of total energy is described by Equation 2.3; E represents the volumetric total energy, h_s is the specific enthalpy of species s, and $\dot{q}''_{tr_j}$ and $\dot{q}''_{ve_j}$ are the j^{th} components of the translational-rotational and vibrational-electronic heat flux vectors, respectively. Finally, the vibrational-electronic energy conservation is described by Equation 2.4; E_{ve} is the volumetric vibrational-electronic energy, e_{ve_s} denotes the vibrational-electronic specific energy for species s, and $\dot{w}_{ve}$ is the volumetric vibrational-electronic energy source term.

Mass diffusion of gas-phase species is computed using a modified Fick's Law that ensures conservation of mass:

$$J_{s_j} = -\rho_g D \frac{\partial Y_s}{\partial x_j} + Y_s \sum_r \rho_g D \frac{\partial Y_r}{\partial x_j} \quad (2.5)$$

Condensed-phase species are assumed to not diffuse (see Section 2.4). In Equation 2.5, ρ_g is the total gas-phase density, Y_s is the mass fraction of species s, and D is the binary diffusion coefficient, which is composed of laminar and turbulent contributions:

$$D = D_l + D_t \tag{2.6}$$

The laminar diffusion coefficient is computed using the Lewis number, Le $\equiv \frac{\mathrm{Pr}}{\mathrm{Sc}}$, which is assumed to be constant throughout the flowfield:

$$D_l = \frac{\mathrm{Le}\kappa_{tr}}{\rho_g C_{p_{tr}}} \tag{2.7}$$

Here κ_{tr} and $C_{p_{tr}}$ are the thermal conductivity and specific heat at constant pressure, respectively, for the translational-rotational energy mode of the mixture. The diffusion due to turbulence is computed using a turbulent Schmidt number [41], Sc_t, which is also assumed to be a constant (usually, $\mathrm{Sc}_t = 0.9$ [52]):

$$D_t = \frac{\mu_t}{\rho_g \mathrm{Sc}_t} \tag{2.8}$$

In this equation μ_t is the eddy viscosity.

The viscous stresses in the flow also include laminar and turbulent contributions:

$$\tau_{ij} = \tau_{l_{ij}} + \tau_{t_{ij}} \tag{2.9}$$

The laminar viscous stresses are modeled assuming that the fluid is Newtonian, and by making use of Stoke's hypothesis:

$$\tau_{l_{ij}} = \mu \left(\frac{\partial u_i}{\partial x_j} + \frac{\partial u_j}{\partial x_i} - \frac{2}{3} \frac{\partial u_m}{\partial x_m} \delta_{ij} \right) \tag{2.10}$$

Here summation is performed with respect to index m, δ_{ij} is the Kronecker delta, and μ represents the mixture dynamic viscosity. In this work, the mixture viscosity is computed using Wilke's mixing rule in conjunction with Blottner's curve fits for individual species; see Scalabrin [50] for details. The turbulent stresses (Reynolds stresses) are computed using the Boussinesq assumption:

$$\tau_{t_{ij}} = \mu_t \left(\frac{\partial u_i}{\partial x_j} + \frac{\partial u_j}{\partial x_i} - \frac{2}{3} \frac{\partial u_m}{\partial x_m} \delta_{ij} \right) - \frac{2}{3} \rho k \delta_{ij} \tag{2.11}$$

In this equation, ρ is the total mixture density and k represents the turbulent kinetic energy.

The heat fluxes are modeled using Fourier's law, with separate temperatures for the translational-rotation and vibrational-electronic energy modes:

$$\dot{q}''_{tr_j} = -\kappa_{tr} \frac{\partial T_{tr}}{\partial x_j} \tag{2.12}$$

$$\dot{q}''_{ve_j} = -\kappa_{ve} \frac{\partial T_{ve}}{\partial x_j} \tag{2.13}$$

Here T represents temperature, κ is the mixture thermal conductivity, and the subscripts tr and ve denote the translational-rotation and vibrational-electronic energy modes, respectively. The thermal conductivities are also composed of laminar and turbulent contributions:

$$\kappa_{tr} = \kappa_{l_{tr}} + \kappa_{t_{tr}} \tag{2.14}$$

$$\kappa_{ve} = \kappa_{l_{ve}} + \kappa_{t_{ve}} \tag{2.15}$$

The laminar components are computed using Wilke's mixing rule in conjunction with Eucken's relation; see Scalabrin [50] for details. The turbulent contribution to thermal conductivity is computed using a turbulent Prandtl number [41], Pr_t, which is assumed to be a constant (usually, $\mathrm{Pr}_t = 0.9$ [52, 53, 54]):

$$\kappa_{t_{tr}} = \frac{\kappa_{tr}}{\kappa_{tr} + \kappa_{ve}} \frac{\mu_t \left(C_{p_{tr}} + C_{p_{ve}} \right)}{\mathrm{Pr}_t} \tag{2.16}$$

$$\kappa_{t_{ve}} = \frac{\kappa_{ve}}{\kappa_{tr} + \kappa_{ve}} \frac{\mu_t \left(C_{p_{tr}} + C_{p_{ve}} \right)}{\mathrm{Pr}_t} \tag{2.17}$$

Algorithms solving Equations 2.1 through 2.4 (excluding the effects of turbulence) were derived and implemented into the LeMANS code by Scalabrin [50]. A modified Steger-Warming flux vector splitting scheme (with reduced dissipation in the boundary layer) is used to compute the inviscid fluxes (first surface integral on the right hand side of Equations 2.1 through 2.4). The viscous fluxes (second surface integral on the right hand side of Equations 2.1 through 2.4) are computed using a central-difference scheme. LeMANS is second-order accurate in space; steady-state solutions are obtained through a time-marching method. Integration is generally performed using a line-implicit scheme, though a point-implicit scheme is also available. Parallelization is achieved by using MPI and METIS libraries.

Since solid rocket motor nozzle flowfields are turbulent, in this work the LeMANS flow solver is updated to include the effects of turbulence on the mean flowfield. This is accomplished by adding the relevant turbulent terms presented in the discussion above to the viscous fluxes. The Jacobians for the viscous fluxes are also updated to include the turbulent transport properties. Turbulence does not affect the inviscid fluxes, and it is assumed that turbulence has no effect on the source terms [41]. Since the goal is not to model combustion, but rather to model relatively minor changes in composition for the post-combustion flow, this assumption is believed to be reasonable. Finally, the turbulent kinetic energy is decoupled from the total energy equation, which is valid when the turbulent kinetic energy is small compared to other energy modes.

2.3 Turbulence

In this work the Menter BSL and SST $k - \omega$ turbulence models [55, 56, 57] are utilized in order to obtain values for μ_t and k, which are required for closure of the RANS equations. These closely-related models combine the near-wall accuracy provided by $k - \omega$ models with the freestream insensitivity of $k - \varepsilon$ models. A review of the literature shows that both the BSL and SST models can accurately predict convective heating [54, 58, 59]. In order to obtain the most accurate heat transfer predictions, wall functions are not employed [60]. Rather, the turbulence equations are solved through the viscous sublayer to the wall. The Menter SST model is a widely-adopted, general purpose turbulence model used for a broad range of applications, and has been shown to work particularly well for adverse pressure gradient flows. The BSL model, however, is better suited for favorable pressure gradients (as is the case in rocket nozzles), and is therefore the turbulence model primarily used in this work.

The implementation of these turbulence models into LeMANS was guided and influenced by a number of other implementation efforts described in the literature, see Refs. [53, 54, 61, 62, 63]. There are two possible strategies for solving the turbulence model equations. In the tightly-coupled approach, the turbulence model equations are solved simultaneously with the mean flow equations. This has the benefit of providing rapid convergence, but comes at the cost of a much more complicated implementation [62, 64]. Further, Wilcox [64] suggests that the coupling between turbulence model and mean flow equations is relatively weak, and that there is little advantage in solving the equations simultaneously. The alternative is a loosely-coupled approach, where the turbulence model and mean flow equations are solved sequentially. This approach may have slower convergence, but is easy to implement, and provides more flexibility [53, 63, 64]. For instance, different schemes can be used for the turbulence models than are used for the mean flow equations, and additional turbulence models can be implemented more easily. Improved stability is also obtained by loosely-coupling the mean flow and turbulence model equations [54]. The loosely-coupled method seems to be the most common approach used in the literature, and is the strategy employed in this work.

The turbulence model equations can be written in integral form as

$$\frac{d}{dt}\int_{cv} \mathbf{Q} dV = -\int_{cs} \mathbf{F}_I dA + \int_{cs} \mathbf{F}_V dA + \int_{cv} \mathbf{S} dV \tag{2.18}$$

where

$$\mathbf{Q} = \begin{bmatrix} \rho k \\ \rho \omega \end{bmatrix} \tag{2.19}$$

represents the vector of conserved turbulence variables,

$$\mathbf{F}_I = \begin{bmatrix} \rho k u_j \hat{n}_j \\ \rho \omega u_j \hat{n}_j \end{bmatrix} = \mathbf{Q} u_j \hat{n}_j \tag{2.20}$$

are the inviscid (convective) fluxes normal to the control surface,

$$\mathbf{F}_V = \begin{bmatrix} \left(\mu + \sigma_k \mu_t\right) \frac{\partial k}{\partial x_j} \hat{n}_j \\ \left(\mu + \sigma_\omega \mu_t\right) \frac{\partial \omega}{\partial x_j} \hat{n}_j \end{bmatrix} \tag{2.21}$$

are the viscous (diffusive) fluxes normal to the control surface, and

$$\mathbf{S} = \begin{bmatrix} P_k - D_k \\ P_\omega - D_\omega + C_\omega \end{bmatrix} \tag{2.22}$$

are the source terms. In these equations, ω represents the specific dissipation, σ_k and σ_ω are model coefficients (discussed later), P_k and D_k are the production and destruction of turbulent kinetic energy, and P_ω, D_ω, and C_ω are the production, destruction, and cross-diffusion of specific dissipation.

Performing the integration in Equation 2.18 for a single control volume yields

$$V_{cl}\frac{d\mathbf{Q}_{cl}}{dt} = -\sum_{f\in cl}\left(\mathbf{F}_I A\right)_f + \sum_{f\in cl}\left(\mathbf{F}_V A\right)_f + V_{cl}\mathbf{S}_{cl} \tag{2.23}$$

The subscript *cl* refers to the mesh cell of interest (taken to be to the “left” of its enclosing faces), the subscript f denotes all the faces bounding the cell, V is the volume of the cell, and A is the area of the face. The time derivative is approximated using a backward Euler method

$$\frac{d\mathbf{Q}_{cl}}{dt} = \frac{\mathbf{Q}_{cl}^{n} - \mathbf{Q}_{cl}^{n-1}}{\Delta t} = \frac{\boldsymbol{\Delta}\mathbf{Q}_{cl}}{\Delta t} \tag{2.24}$$

which yields first-order, implicit time integration. Here the superscript n refers to the n^{th} time step. The fluxes and source terms are also treated implicitly by linearizing with respect to time:

$$\mathbf{F}_I^{n} = \mathbf{F}_I^{n-1} + \left(\frac{\partial \mathbf{F}_I}{\partial \mathbf{Q}}\right)^{n-1}\boldsymbol{\Delta}\mathbf{Q} = \mathbf{F}_I^{n-1} + \mathbf{J}_I^{n-1}\boldsymbol{\Delta}\mathbf{Q} \tag{2.25}$$

$$\mathbf{F}_V^{n} = \mathbf{F}_V^{n-1} + \left(\frac{\partial \mathbf{F}_V}{\partial \mathbf{Q}}\right)^{n-1}\boldsymbol{\Delta}\mathbf{Q} = \mathbf{F}_V^{n-1} + \mathbf{J}_V^{n-1}\boldsymbol{\Delta}\mathbf{Q} \tag{2.26}$$

$$\mathbf{S}_{cl}^{n} = \mathbf{S}_{cl}^{n-1} + \left(\frac{\partial \mathbf{S}}{\partial \mathbf{Q}}\right)^{n-1}\boldsymbol{\Delta}\mathbf{Q}_{cl} = \mathbf{S}_{cl}^{n-1} + \mathbf{J}_S^{n-1}\boldsymbol{\Delta}\mathbf{Q}_{cl} \tag{2.27}$$

In these equations, $\mathbf{J}$ represents the Jacobian (sensitivity) matrices, which describe how the fluxes and sources terms are affected by changes to the conserved variables. Equations 2.25 and 2.26 must include the contributions due to changes in the conserved variables in the cell of interest as well as changes in the conserved variables in the adjacent cell to the right of the face:

$$\mathbf{J}_I\boldsymbol{\Delta}\mathbf{Q} = \mathbf{J}_I^{+}\boldsymbol{\Delta}\mathbf{Q}_{cl} + \mathbf{J}_I^{-}\boldsymbol{\Delta}\mathbf{Q}_{cr} \tag{2.28}$$

$$\mathbf{J}_V \mathbf{\Delta Q} = \mathbf{J}_V^+ \mathbf{\Delta Q}_{cl} + \mathbf{J}_V^- \mathbf{\Delta Q}_{cr} \tag{2.29}$$

In these equations, the subscript cr refers to the cell that lies to the right of the face of interest. The superscript + denotes the sensitivity matrix describing the effects of changes to the conserved quantities in the cell to the left of the face (the cl^{th} cell), while − denotes the matrix describing the effects of changes in the cell to the right of the face (the cr^{th} cell).

After making all of these substitutions, Equation 2.23 can be written as

$$\begin{aligned}\left(\frac{V_{cl}}{\Delta t} + \sum_{f\in cl} \left(\mathbf{J}_I^+ A\right)_f - \sum_{f\in cl} \left(\mathbf{J}_V^+ A\right)_f - V_{cl}\mathbf{J}_S\right) \mathbf{\Delta Q}_{cl} \\ + \left(\sum_{f\in cl} \left(\mathbf{J}_I^- A\right)_f - \sum_{f\in cl} \left(\mathbf{J}_V^- A\right)_f\right) \mathbf{\Delta Q}_{cr} = \\ - \sum_{f\in cl} \left(\mathbf{F}_I A\right)_f + \sum_{f\in cl} \left(\mathbf{F}_V A\right)_f + V_{cl}\mathbf{S}_{cl}\end{aligned} \tag{2.30}$$

Solution of this system of equations is performed using the point-implicit or line-implicit integration algorithms described by Scalabrin [50]; it is found in this work that the line-implicit algorithm has superior performance than the point-implicit algorithm. The conserved turbulence variables are updated each iteration:

$$\mathbf{Q}_{cl}^n = \mathbf{Q}_{cl}^{n-1} + \mathbf{\Delta Q}_{cl} \tag{2.31}$$

where the magnitude of the update is limited:

$$\mathbf{\Delta Q}_{cl} = \begin{cases} \min\left(\mathbf{\Delta Q}_{cl}\,,\, -0.1\mathbf{Q}_{cl}^{n-1}\right) & \mathbf{\Delta Q}_{cl} < 0.0 \\ \max\left(\mathbf{\Delta Q}_{cl}\,,\, 0.1\mathbf{Q}_{cl}^{n-1}\right) & \mathbf{\Delta Q}_{cl} > 0.0 \end{cases} \tag{2.32}$$

This limiting is performed in order to preserve positivity [62], and to eliminate other numerical issues.

The inviscid fluxes are computed using a first-order upwind scheme, following [65]. The component of the velocity normal to the face is first computed for the left and right cells:

$$u_{n_{cl}} = u_{j_{cl}} \hat{n}_j \tag{2.33}$$

$$u_{n_{cr}} = u_{j_{cr}} \hat{n}_j \tag{2.34}$$

In these equations, the subscript n refers to the normal velocity component, and summation is performed with respect to index j. The velocity at the face is then computed as

$$u^+ = \frac{1}{2}\left(u_{n_{cl}} + |u_{n_{cl}}|\right) \tag{2.35}$$

$$u^- = \frac{1}{2}\left(u_{n_{cr}} - |u_{n_{cr}}|\right) \tag{2.36}$$

If the flow across the face is from the left to the right, u^+ will be the velocity as computed from the left cell and u^- is zero. Likewise, if the flow across the face is actually from the right to the left, u^+ is zero, while u^- is the velocity as computed from the right cell. The inviscid flux across the face can then be simply computed as

$$\mathbf{F}_I = u^+ \mathbf{Q}_{cl} + u^- \mathbf{Q}_{cr} \tag{2.37}$$

When computing the sensitivity matrices for the inviscid fluxes, the average velocity normal to the face is used:

$$u_n = \frac{1}{2}\left(u_{n_{cl}} + u_{n_{cr}}\right) \tag{2.38}$$

The sign of this average velocity then dictates the sensitivity matrices:

$$\mathbf{J}_I^+ = \begin{cases} \begin{bmatrix} u_n & 0 \\ 0 & u_n \end{bmatrix} & u_n \geq 0.0 \\ \mathbf{0} & u_n < 0.0 \end{cases} \tag{2.39}$$

$$\mathbf{J}_I^- = \begin{cases} \mathbf{0} & u_n \geq 0.0 \\ \begin{bmatrix} u_n & 0 \\ 0 & u_n \end{bmatrix} & u_n < 0.0 \end{cases} \tag{2.40}$$

The viscous fluxes are computed using the same second-order central-difference method used for the viscous fluxes in the mean flow equations. Properties at the face are taken to be the average of the values in the neighboring cells:

$$\xi = \frac{1}{2}\left(\xi_{cl} + \xi_{cr}\right) \tag{2.41}$$

where ξ represents μ, μ_t, σ_k, and σ_ω. The gradients of the turbulence variables at the face are computed using the method presented in Ref. [66]. Once these quantities are obtained, the viscous fluxes can be computed using Equation 2.21. The viscous flux sensitivities are computed using the methodology developed by Scalabrin [50] for the mean flow viscous fluxes. For example, the viscous flux for the turbulent kinetic energy can be approximated as

$$F_{V_k} = \left(\mu + \sigma_k \mu_t\right) \frac{\Delta k}{\Delta x_n} = \frac{\left(\mu + \sigma_k \mu_t\right)}{\rho \Delta x_n}\left(\left(\rho k\right)_{cr} - \left(\rho k\right)_{cl}\right) \tag{2.42}$$

where $\Delta x_n = \left\|\left(x_{j_{cr}} - x_{j_{cl}}\right)\hat{n}_j\right\|$ is the magnitude of the distance between the two cell centroids perpendicular to the face. A similar equation can be written for the viscous flux for the specific dissipation. From these approximate fluxes, the sensitivity matrices are found to be:

$$\mathbf{J}_V^+ = \begin{bmatrix} -\frac{(\mu+\sigma_k\mu_t)}{\rho\Delta x_n} & 0 \\ 0 & -\frac{(\mu+\sigma_\omega\mu_t)}{\rho\Delta x_n} \end{bmatrix} \tag{2.43}$$

$$\mathbf{J}_V^- = \begin{bmatrix} \frac{(\mu+\sigma_k\mu_t)}{\rho\Delta x_n} & 0 \\ 0 & \frac{(\mu+\sigma_\omega\mu_t)}{\rho\Delta x_n} \end{bmatrix} \tag{2.44}$$

The destruction terms in the turbulence model equations are defined as

$$D_k = \beta^\star \rho\omega k \tag{2.45}$$

$$D_\omega = \beta\rho\omega^2 \tag{2.46}$$

where β and $\beta^\star$ are model coefficients. The production of turbulent kinetic energy is limited [55]:

$$P_k = \min\left(\tilde{P}_k\,,\, 20D_k\right) \tag{2.47}$$

Two different methods exist for computing the unlimited turbulent kinetic production term:

$$\tilde{P}_k = \begin{cases} \tau_{t_{ij}}\frac{\partial u_i}{\partial x_j} & \text{Standard source term} \\ \mu_t\Omega^2 - \frac{2}{3}\rho k\delta_{ij}\frac{\partial u_i}{\partial x_j} & \text{Vorticity-based source term} \end{cases} \tag{2.48}$$

The Reynolds stress tensor required for the standard source term formulation is computed as per Equation 2.11. The vorticity-based source term is an alternative formulation proposed by Menter [57]; here Ω is the magnitude of the vorticity vector. Using the vorticity-based source term can help prevent the over-prediction of turbulent kinetic energy near stagnation points [67]. Both production term formulations have been implemented and can be selected by the user. However, unless otherwise explicitly stated, all simulations in this work use the vorticity-based production term. The production term for specific dissipation is a function of the unlimited turbulent kinetic production:

$$P_\omega = \frac{\gamma\rho}{\mu_t}\tilde{P}_k \tag{2.49}$$

The cross-diffusion term in the specific dissipation equation is defined as

$$C_\omega = 2\rho\left(1 - F_1\right)\sigma_{\omega 2}\frac{1}{\omega}\frac{\partial k}{\partial x_j}\frac{\partial \omega}{\partial x_j} \tag{2.50}$$

where $\sigma_{\omega 2}$ is another model coefficient and F_1 is a blending function defined as

$$F_1 = \tanh\left(arg_1^4\right) \tag{2.51}$$

where

$$arg_1 = \min\left(\max\left(\frac{\sqrt{k}}{0.09\omega y}\,,\,\frac{500\mu}{\rho y^2\omega}\right)\,,\,\frac{4\rho\sigma_{\omega 2}k}{CD_{k\omega}y^2}\right) \tag{2.52}$$

Here y is the distance from the cell centroid to the closest wall (the wall distance) and $CD_{k\omega}$is defined as

$$CD_{k\omega} = \max\left(2\rho\sigma_{\omega 2}\frac{1}{\omega}\frac{\partial k}{\partial x_j}\frac{\partial \omega}{\partial x_j}\,,\,10^{-20}\right) \tag{2.53}$$

To prevent divide-by-zero errors from occasionally occurring when solving these equations, a lower limit is placed on specific dissipation:

$$\omega = \max\left(\omega\,,\,10^{-6}\,{}^{1}\!/\!_{\mathrm{s}}\right) \tag{2.54}$$

To improve the stability of the numerical method, an approximate Jacobian matrix is used for the turbulence model source terms:

$$\mathbf{J}_S = \begin{bmatrix} -\frac{D_k}{\rho k} & -\frac{D_k}{\rho\omega} \\ 0 & -\frac{|C_\omega| + 2D_\omega}{\rho\omega} \end{bmatrix} \tag{2.55}$$

The main purpose of the blending function F_1 is to switch between a $k-\omega$ model in the viscous sublayer to a $k-\varepsilon$ model elsewhere in the flow. It is this blending of two models that provides the BSL and SST models with their desirable characteristics.

Table 2.1: Coefficients for the Menter BSL and SST turbulence models.

BSL		SST	
Set 1	Set 2	Set 1	Set 2
$\sigma_{k1} = 0.5$	$\sigma_{k2} = 1.0$	$\sigma_{k1} = 0.85$	$\sigma_{k2} = 1.0$
$\sigma_{\omega 1} = 0.5$	$\sigma_{\omega 2} = 0.856$	$\sigma_{\omega 1} = 0.5$	$\sigma_{\omega 2} = 0.856$
$\beta_1 = 0.0750$	$\beta_2 = 0.0828$	$\beta_1 = 0.0750$	$\beta_2 = 0.0828$
$\gamma_1 = \frac{\beta_1}{\beta^\star} - \frac{\sigma_{\omega 1}\kappa^2}{\sqrt{\beta^\star}}$	$\gamma_2 = \frac{\beta_2}{\beta^\star} - \frac{\sigma_{\omega 2}\kappa^2}{\sqrt{\beta^\star}}$	$\gamma_1 = \frac{\beta_1}{\beta^\star} - \frac{\sigma_{\omega 1}\kappa^2}{\sqrt{\beta^\star}}$	$\gamma_2 = \frac{\beta_2}{\beta^\star} - \frac{\sigma_{\omega 2}\kappa^2}{\sqrt{\beta^\star}}$
$\beta^\star = 0.09$		$\beta^\star = 0.09$	
$\kappa = 0.41$		$\kappa = 0.41$	
—		$a_1 = 0.31$	

This blending function is also used to compute several of the model coefficients within the boundary layer:

$$\xi = F_1 \xi_1 + (1 - F_1)\, \xi_2 \tag{2.56}$$

where ξ represents σ_k, σ_ω, β, and γ. The full listing of model coefficients is given in Table 2.1; many of the coefficients are the same for the BSL and SST models, but there are some differences. "Set 1" corresponds to the $k-\omega$ model used in the viscous sublayer, while "Set 2" corresponds to the $k-\varepsilon$ model used elsewhere.

The primary difference between the BSL and SST model variants is in how eddy viscosity is calculated. Computation of eddy viscosity is quite simple for the BSL model:

$$\tilde{\mu}_t = \frac{\rho k}{\omega} \tag{2.57}$$

Determining eddy viscosity is more involved for the SST model:

$$\tilde{\mu}_t = \frac{a_1 \rho k}{\max\left(a_1 \omega\, ,\, \Omega F_2\right)} \tag{2.58}$$

Here a_1 is a model coefficient (see Table 2.1) and F_2 is another blending function, defined as

$$F_2 = \tanh\left(arg_2^2\right) \tag{2.59}$$

where

$$arg_2 = \max\left(2\frac{\sqrt{k}}{0.09\omega y}\,,\,\frac{500\mu}{\rho y^2\omega}\right) \tag{2.60}$$

Eddy viscosity is limited for both models:

$$\mu_t = \max\left(\min\left(\tilde{\mu}_t\,,\,10^5\mu\right)\,,\,10^{-4}\mu\right) \tag{2.61}$$

The lower bound prevents a divide-by-zero error from occurring when computing the production term for specific dissipation (Equation 2.49). The upper bound is established in order to avoid obtaining extremely large values of eddy viscosity in some areas of the flow [54, 65].

The recommended freestream conditions for k and ω are [56]

$$\omega_\infty = 10\frac{U_\infty}{L} \tag{2.62}$$

$$\mu_{t_\infty} = 0.01\mu_\infty \tag{2.63}$$

$$k_\infty = \frac{\mu_{t_\infty}\omega_\infty}{\rho_\infty} \tag{2.64}$$

In these equations the subscript ∞ refers to freestream conditions, U_∞ is the freestream velocity of the flow, and L is a characteristic length associated with the domain.

At the wall, the boundary condition for turbulent kinetic energy is always

$$k_w = 0.0 \tag{2.65}$$

where the subscript w refers to conditions on the wall. For a smooth wall without mass injection (blowing), the specific dissipation at the wall is

$$\omega_{w_0} = \frac{60\mu_w}{\rho_w \beta_1 d^2} \tag{2.66}$$

where d is the distance from the wall to the centroid of the cell adjacent to the wall and the subscript 0 refers to the wall without blowing. When there is mass injection from the wall (as is the case in ablation), the boundary condition for specific dissipation becomes [68]

$$\omega_{w_B} = u_\tau^2 \frac{\rho_w}{\mu_w} S_B \tag{2.67}$$

where the subscript B refers to the wall with blowing and u_τ is the friction characteristic velocity, defined as

$$u_\tau = \sqrt{\frac{\tau_w}{\rho_w}} \tag{2.68}$$

where τ_w is the magnitude of the shear stress on the wall. S_B in Equation 2.67 is the empirical correlation

$$S_B = \frac{20}{u_{n_w}^+ \left(1 + 5u_{n_w}^+\right)} \tag{2.69}$$

where $u_{n_w}^+$ is the normalized velocity

$$u_{n_w}^+ = \frac{u_{n_w}}{u_\tau} \tag{2.70}$$

with u_{n_w} being the component of the velocity of the injected mass that is perpendicular to the wall. It is observed that as the blowing velocity approaches zero that S_B, and hence ω_{w_B}, becomes singular. The specific dissipation on the blowing wall is therefore limited to be

$$\omega_w = \min\left(\omega_{w_0}\,,\, \omega_{w_B}\right) \tag{2.71}$$

2.4 Gas-Particle Flow

Condensed-phase particles, predominantly composed of the alumina (Al_2O_3) formed by combustion of the aluminum fuel in the propellant, are usually present in large quantities in solid rocket nozzle flow. For example, the HIPPO motor [5] (see Section 7.2) uses a propellant containing 16 % aluminum fuel (by mass); alumina comprises 30 % (by mass) of the combustion products. While particles form a large mass fraction of the flow, they normally occupy only a negligibly small volume fraction of the flow. These particles can either be in the liquid or solid state depending on temperature, and usually start out as liquid droplets in the rocket chamber which then solidify as they cool during their passage through the nozzle. (However, in this work the particles are assumed to remain in the liquid state.)

Modeling approaches for particle-laden flows are discussed in the review article by Crowe [69] and in the text by Rudinger [70]. In this work, the particle-laden combustion gases are modeled using an equilibrium two-gas method that treats the condensed phase as an additional gas species with special properties. Underlying this approach is the assumption that the condensed-phase particles are in equilibrium with the surrounding gas (equal velocity and temperature). Generally speaking, the gas and particles will not be in equilibrium (particles lag the surrounding gas), but to capture these nonequilibrium effects requires detailed information on the size distribution for the condensed-phase particles [71]. Unfortunately, data describing the particle size distribution for rocket nozzle flows are very rare. While the equilibrium two-gas approach may not be able to fully resolve all details of the particle-laden flow in rocket nozzles, this method does capture the main thermodynamic effects of the condensed-phase particles in the flow, which is sufficient for this work.

For steady-state flow, the volume fraction, ζ, of the particles can be computed as

$$\zeta = \frac{Y_p \rho_g}{\left(1 - Y_p\right) \rho_p} \tag{2.72}$$

where Y_p is the particle mass fraction, ρ_g is the gas-phase concentration (mass of all gas-phase species divided by total volume, which is the same as the gas-phase partial density computed by LeMANS), and ρ_p is the bulk density of the particle material (mass of particle divided by volume of particle). For the HIPPO nozzle test case (which is representative of most solid rocket motors), within the motor chamber (which is the worst case scenario) the volume mass fraction is estimated to be $\zeta = 3.5 \times 10^{-4}$. Inputs for these calculations are: $P = 4.48\,\mathrm{MPa}$, $Y_p = 0.30$, $\rho_p = 3900\,{}^{\mathrm{kg}}/{}_{\mathrm{m}^3}$, and $\rho_g = 3.14\,{}^{\mathrm{kg}}/{}_{\mathrm{m}^3}$. Since this value is well below the usually assumed threshold value of 1.0×10^{-3} [69, 72], it is reasonable to neglect the volume of the particles.

Since the particles occupy a negligibly small volume, for the equilibrium two-gas method the usual compressible flow equations hold without modification, provided that the mixture thermodynamic properties are correctly computed [70, 71]. These thermodynamic properties reduce simply to mass-weighted averages, which is highly compatible with the multi-species framework used in LeMANS:

$$C_{v_M} = \sum_s Y_s C_{v_s} \tag{2.73}$$

$$C_{p_M} = \sum_s Y_s C_{p_s} \tag{2.74}$$

$$\gamma_M = \frac{C_{p_M}}{C_{v_M}} \tag{2.75}$$

$$R_M = \sum_s Y_s R_s = \sum_s Y_s \frac{R_u}{\mathscr{M}_s} \tag{2.76}$$

In these equations, the subscript M refers to mixture (gas-particle) properties, the subscript s is used to denote properties of species s, and Y represents mass fraction. C_v and C_p are the specific heats assuming constant volume and constant pressure, respectively, while γ is the ratio of specific heats. R is the gas constant, R_u =

$8.314\,{}^{\mathrm{kJ}}\!/_{\mathrm{kmol\cdot K}}$ is the universal gas constant, and $\mathscr{M}$ represents molecular weight. It is necessary to set the gas constant for condensed-phase species to zero (particles do not contribute a partial pressure), which is easily achieved by specifying a very high molecular weight for the condensed-phase species. If each particle is treated as a "macro-molecule", an effective particle molecular weight can be computed as

$$\mathscr{M}_p = \frac{1}{6}\pi D^3 \rho_p N_A \tag{2.77}$$

where D is the particle diameter and $N_A = 6.022 \times 10^{26}\,{}^{1}\!/_{\mathrm{kmol}}$ is Avogadro's constant. In this work it has been assumed that each $\mathrm{Al_2O_3^\star}$ particle is one micron in diameter, yielding $\mathscr{M}_{\mathrm{Al_2O_3^\star}} = 1.23 \times 10^{12}\,{}^{\mathrm{kg}}\!/_{\mathrm{kmol}}$.

It is further generally assumed that the condensed-phase particles do not experience collisions; the condensed phase is treated as an inviscid continuum [73, 74, 75]. This means that the particles do not contribute to transport properties, nor do they diffuse, nor can they serve as collision partners for vibrational relaxation, nor do they participate in reactions. The LeMANS code has therefore been updated to exclude condensed-phase species when performing the computation of transport properties, vibrational relaxation, and reactions. Particle-laden flows must be modeled in LeMANS using the Wilke/Blottner/Eucken transport property model; the Gupta transport model has not been updated to properly treat condensed-phase species.

2.5 Stagnation Inlet Boundary Condition

The final addition to the LeMANS flow solver is the implementation of a subsonic stagnation inlet boundary condition; this is the most natural inflow boundary condition to use for rocket nozzle problems. Implementation of this boundary condition largely follows the same approach as that used in the NASA FUN3D code as described in Ref. [76].

Ghost cell quantities are computed based on the total enthalpy of the flow and the Riemann invariant propagating outward from the interior, assuming isentropic flow across the boundary. The total enthalpy is computed based upon the values in the cell inside the flow domain adjacent to the inflow boundary:

$$h_0 = \left(\frac{E}{\rho} + RT_{tr} \right)_{cl} \tag{2.78}$$

The outward-running Riemann invariant can be computed as

$$R^- = -u_{n_{cl}} - \frac{2a_{cl}}{\gamma - 1} = -u_{n_{cr}} - \frac{2a_{cr}}{\gamma - 1} \tag{2.79}$$

The subscript *cl* refers to the cell inside the flow domain adjacent to the boundary, while *cr* refers to the ghost cell outside the boundary. The velocity normal to the face, u_n, (computed using Equation 2.33) will be a negative quantity for flow into the domain. The speed of sound, a, is computed as

$$a_{cl} = \sqrt{\left(\frac{\gamma P}{\rho} \right)_{cl}} \tag{2.80}$$

and the ratio of specific heats is assumed to be constant in the vicinity of the boundary (i.e. $\gamma_{cl} = \gamma_{cr} = \gamma$). The total enthalpy can also be written as

$$h_0 = \frac{a_{cr}^2}{\gamma - 1} + \frac{1}{2} u_{n_{cr}}^2 \tag{2.81}$$

By combining Equations 2.79 and 2.81 it is possible to obtain a quadratic equation for the speed of sound in the ghost cell:

$$\left(1 + \frac{2}{\gamma - 1} \right) a_{cr}^2 + 2R^- a_{cr} + \frac{\gamma - 1}{2} \left(\left(R^- \right)^2 - 2h_0 \right) = 0 \tag{2.82}$$

The physical solution is the larger of the two roots. A check is also made to determine if a complex (nonphysical) root is obtained. In this case the assumption $a_{cr} = a_{cl}$ is made. The velocity in the ghost cell is then computed (using Equation 2.79), as is the inflow Mach number

$$M_{cr} = \frac{-u_{n_{cr}}}{a_{cr}} \tag{2.83}$$

which will be positive for flow into the domain. For subsonic inflow, the pressure and temperature in the ghost cell are computed using the standard isentropic relations:

$$P_{cr} = P_0 \left(1 + \frac{\gamma - 1}{2} M_{cr}^2\right)^{\frac{-\gamma}{\gamma-1}} \tag{2.84}$$

$$T_{tr_{cr}} = T_{tr_0} \left(1 + \frac{\gamma - 1}{2} M_{cr}^2\right)^{-1} \tag{2.85}$$

$$T_{ve_{cr}} = T_{ve_0} \left(1 + \frac{\gamma - 1}{2} M_{cr}^2\right)^{-1} \tag{2.86}$$

The stagnation conditions P_0, T_{tr_0}, and T_{ve_0} must be specified by the user, along with the species mass fractions Y_{s_0}. If the inflow is predicted to be supersonic, the stagnation conditions are used directly. With pressure, temperature, and species mass fractions defined in the ghost cell, all remaining quantities in the ghost cell can be determined in a straightforward manner.

While FUN3D implements this boundary condition in an implicit manner, in this work the stagnation inlet boundary condition has been implemented into LeMANS using an explicit approach. This explicit implementation has worked extremely well, thus rendering an extremely complicated implicit implementation unnecessary.

CHAPTER III

Material Response Solver

3.1 Introduction

The material response solver presented here (MOPAR-MD) builds upon and greatly extends a baseline capability developed by previous researchers at the University of Michigan [27, 28]. While this baseline capability did permit two-dimensional ablation analyses, it was restricted in application to non-pyrolyzing TPS materials (e.g. carbon-carbon composite or graphite). However, one strong advantage of this material response code is that it has been coupled to a reacting flow solver [50, 51] (LeMANS), which permits tightly-coupled, fully-conjugate simulations of a flowfield and the associated ablation of TPS materials. By adding the capability to model pyrolyzing materials to this material response solver, it will be possible to perform conjugate analysis of ablation within rocket nozzles.

The two-dimensional pyrolysis and ablation capability added to the MOPAR-MD material response code is largely based upon the methods used in the one-dimensional pyrolysis and ablation code developed by Amar et al. [16, 17, 18] and subsequently used in the MOPAR-1D code [19, 20] developed at the University of Michigan. The governing equations describing the thermal response of a pyrolyzing ablator on a deforming mesh are:

Mixture energy equation:

$$\underbrace{\frac{d}{dt}\int_{cv}\rho e dV}_{\text{storage}} = \underbrace{\int_{cs}\rho h u_{m_j}\hat{n}_j dA}_{\text{grid convection}} - \underbrace{\int_{cs}\phi\rho_g h_g u_{g_j}\hat{n}_j dA}_{\text{gas flux}} - \underbrace{\int_{cs}\dot{q}''_j\hat{n}_j dA}_{\text{conduction}} \tag{3.1}$$

Solid-phase continuity equation:

$$\underbrace{\frac{d}{dt}\int_{cv}\rho_s dV}_{\text{storage}} = \underbrace{\int_{cs}\rho_s u_{m_j}\hat{n}_j dA}_{\text{grid convection}} + \underbrace{\int_{cv}\dot{m}'''_s dV}_{\text{source}} \tag{3.2}$$

Gas-phase continuity equation:

$$\underbrace{\frac{d}{dt}\int_{cv}\phi\rho_g dV}_{\text{storage}} = \underbrace{\int_{cs}\phi\rho_g u_{m_j}\hat{n}_j dA}_{\text{grid convection}} - \underbrace{\int_{cs}\phi\rho_g u_{g_j}\hat{n}_j dA}_{\text{gas flux}} + \underbrace{\int_{cv}\dot{m}'''_g dV}_{\text{source}} \tag{3.3}$$

Mass conservation equation:

$$\underbrace{\int_{cv}\dot{m}'''_g dV}_{\text{source}} + \underbrace{\int_{cv}\dot{m}'''_s dV}_{\text{source}} = 0 \tag{3.4}$$

In these equations, the subscript s refers to the solid material and the subscript g refers to the pyrolysis gases. Density is denoted by ρ, e is specific energy, h refers to specific enthalpy, ϕ is the porosity of the solid material, $\dot{m}'''$ represents the volumetric mass source term, $\dot{q}''_j$ denotes the j^{th} component of the heat flux vector, $\hat{n}_j$ is the j^{th} component of the outward-pointing unit normal vector, and u_{m_j} is the j^{th} component of the mesh velocity vector. The velocity of the pyrolysis gases, u_{g_j}, required in Equations 3.1 and 3.3, is computed using a form of Darcy's law that can accommodate anisotropic permeability [77]:

$$u_{g_j} = -\frac{K_{ji}}{\phi\mu_g}\frac{\partial P_g}{\partial x_i} \tag{3.5}$$

Here K_{ji} is the permeability tensor for the material, μ represents dynamic viscosity, and P denotes pressure. The ideal gas law is used to compute pressure as a function of temperature and pyrolysis gas density.

In this material response code, a first-order, implicit time integration scheme is employed, along with a second-order spatial discretization scheme based on the control volume finite element method [22, 27, 78, 79] and a deformable, unstructured (i.e. composed of triangular elements) grid. The mesh deformation, energy, solid phase continuity, and gas phase continuity equations are loosely-coupled and solved sequentially in an iterative process each time step, as illustrated in Figure 3.1. Within each inner iteration, the mesh deformation is solved first, if the surface is receding. Next, the energy equation is solved with an iterative Newton-Raphson scheme. Pyrolysis (thermal decomposition of the TPS material) is then computed by directly solving the solid phase continuity equation. Finally, a Newton-Raphson scheme is used to solve the gas phase continuity equation to obtain the flow of the pyrolysis gases through the porous char. This process is iterated until the maximum change in the temperature solution between inner iterations drops below a threshold value; a threshold value of $\max(\Delta T) \leq 0.1\,\mathrm{K}$ has been found to work well. At this point convergence has been achieved and the solution process advances to the next time step. Typically, only a few $(2-5)$ inner iterations are required in order to achieve convergence at each time step.

3.2 Mesh Deformation

Deformation of the unstructured mesh in response to surface recession is achieved by treating the mesh as a linear elastic solid and solving the elastic solid mechanics equations. One advantage of this approach is that the deformation of the mesh is not restricted to follow grid lines, as is the case with some other codes (e.g. TITAN [29]). This mesh deformation implementation was included in the baseline MOPAR-MD code developed by other researchers; details can be found in the literature [23, 27].

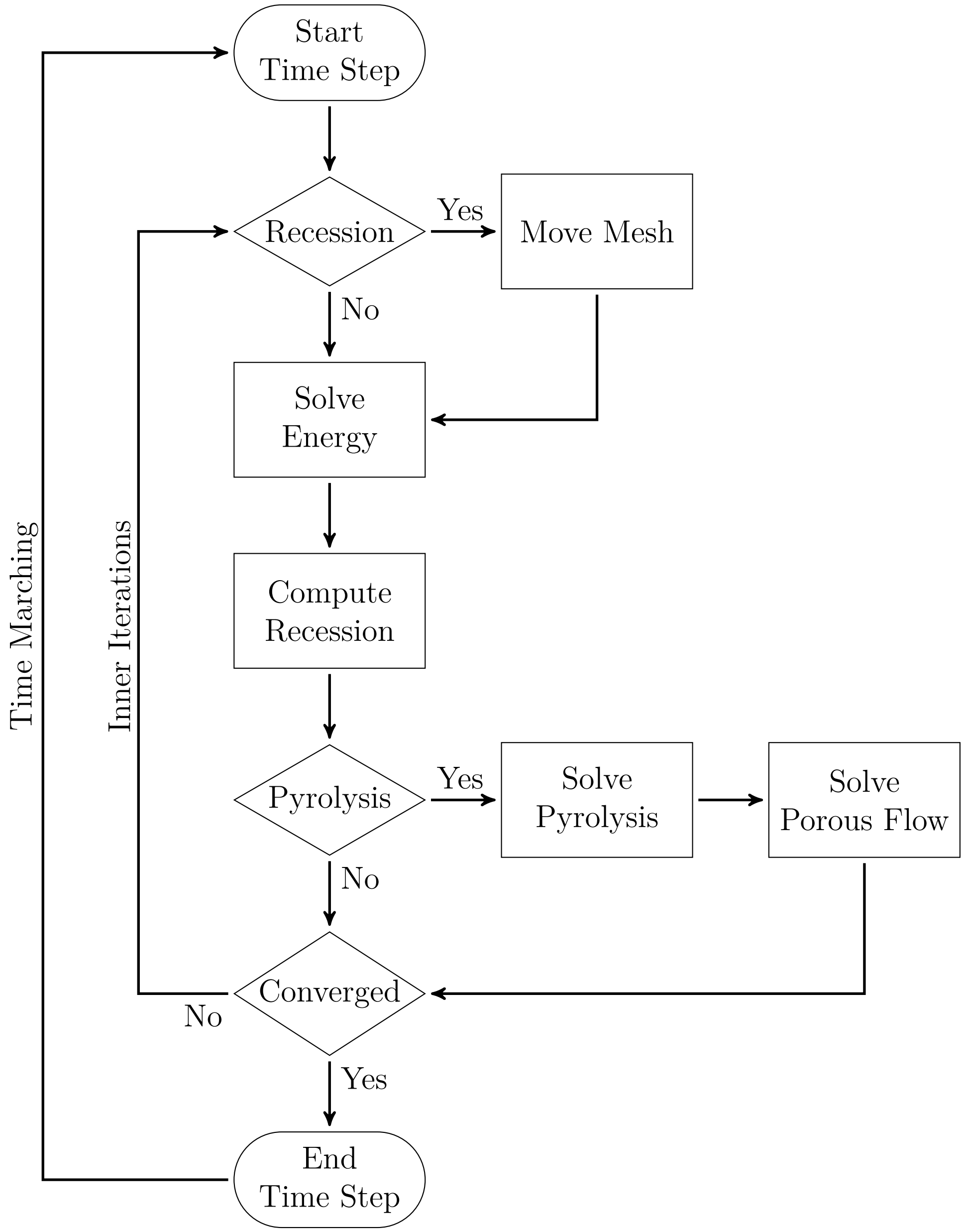

Figure 3.1: Flowchart illustrating procedure used in MOPAR-MD to solve the governing equations describing the thermal response of a pyrolyzing ablator.

3.3 Energy Equation

The mixture energy equation (Equation 3.1) can be written more compactly as

$$\frac{d}{dt}\mathbf{Q}_{stor} = \dot{\mathbf{Q}}_{grid} - \dot{\mathbf{Q}}_{flow} - \dot{\mathbf{Q}}_{cond} \tag{3.6}$$

where $\mathbf{Q}$ and $\dot{\mathbf{Q}}$ are the energy content and rate of change of energy content vectors, respectively. From left to right, the four terms in Equation 3.6 represent the change in the stored energy and the heat fluxes due to grid motion, the flow of pyrolysis gases, and conduction. Because the material properties are a function of temperature, Equation 3.6 represents a system of nonlinear equations, with one equation for each node (control volume) in the mesh. A Newton-Raphson technique is used to solve this system, which requires that each term be linearized in "iteration space". Using the conduction term as an example, this yields

$$\dot{\mathbf{Q}}_{cond}^{\nu+1} = \dot{\mathbf{Q}}_{cond}^{\nu} + \mathbf{J}_{cond}^{\nu}\mathbf{\Delta T} \tag{3.7}$$

where $\mathbf{J}$ represents the Jacobian or sensitivity matrix. All terms in Equation 3.6 are linearized in a similar fashion. The time derivative is approximated using a backward Euler method

$$\frac{d}{dt}\mathbf{Q}_{stor} = \frac{1}{\Delta t}\left[\mathbf{Q}_{stor}^{n} - \mathbf{Q}_{stor}^{n-1}\right] = \frac{1}{\Delta t}\left[\mathbf{Q}_{stor}^{\nu} + \mathbf{J}_{stor}^{\nu}\mathbf{\Delta T} - \mathbf{Q}_{stor}^{n-1}\right] \tag{3.8}$$

which yields first-order, implicit time integration.

With these approximations, the following equation is obtained:

$$\left[\frac{1}{\Delta t}\mathbf{J}_{stor}^{\nu} + \mathbf{J}_{cond}^{\nu} - \mathbf{J}_{grid}^{\nu} + \mathbf{J}_{flow}^{\nu}\right]\mathbf{\Delta T} = \dot{\mathbf{Q}}_{grid}^{\nu} - \dot{\mathbf{Q}}_{flow}^{\nu} - \dot{\mathbf{Q}}_{cond}^{\nu} - \frac{1}{\Delta t}\left[\mathbf{Q}_{stor}^{\nu} - \mathbf{Q}_{stor}^{n-1}\right] \tag{3.9}$$

This is an $N \times N$ linear system (N being the number of nodes in the mesh) that must be solved at each iteration of the Newton-Raphson method. The Generalized Minimum Residual (GMRES) method [80] is used to solve this system; restarting and the ILU(0) preconditioner [81] are used to accelerate convergence of the GMRES solver. The temperature field is updated each Newton-Raphson iteration:

$$\mathbf{T}^{\nu+1} = \mathbf{T}^{\nu} + \mathbf{\Delta T} \tag{3.10}$$

Newton-Raphson iteration is performed until the maximum temperature update falls below a user-specified threshold value. A convergence criteria of $\max(\mathbf{\Delta T}) \leq 10^{-10}\,\mathrm{K}$ has been found to work well for the energy equation.

Solution of the energy equation was previously implemented by Wiebenga for non-charring materials; details for computing most of the terms in Equation 3.9 are presented in his dissertation [27] and will not be repeated here. Minimal changes were made as part of this work in order to support pyrolyzing materials. For the energy storage, grid convection, and conduction terms (and their respective sensitivity matrices) it was only necessary to update the thermodynamic properties to include the contributions from the pyrolysis gases (see Section 3.8). However, the pyrolysis gas term and its sensitivity matrix are unique to pyrolyzing materials and had to be implemented in their entirety as part of this work.

For a single control volume (i.e. a single equation in the system represented by Equation 3.9), the pyrolysis gas convection heat flux term is

$$\dot{Q}_{flow_{cl}} = \int_{cs} \phi \rho_g h_g u_{g_j} \hat{n}_j dA \tag{3.11}$$

where the subscript cl refers to the control volume of interest. Substituting Equation

3.5 (Darcy's law) into Equation 3.11 yields

$$\dot{Q}_{flow_{cl}} = -\int_{cs} \frac{\rho_g h_g K_{ji}}{\mu_g} \frac{\partial P_g}{\partial x_i} \hat{n}_j dA \tag{3.12}$$

The pressure gradient is assumed to be constant within each element, and is thus a constant on each face forming the control surface bounding the control volume. The pyrolysis gas heat flux term can therefore be computed as

$$\dot{Q}_{flow_{cl}} = \sum_{f \in cl} \left(-\hat{n}_j \frac{\partial P_g}{\partial x_i} \int_f \frac{\rho_g h_g K_{ji}}{\mu_g} dA \right)_f \tag{3.13}$$

where the explicit summation is performed over all the faces forming the control surface that bounds the control volume of interest. Also note that there is implied summation with respect to the subscripts i and j, which represent the spatial dimensions of the problem. The integral term within Equation 3.13 represents the integration of the product of four quantities that are assumed to independently vary in a linear manner along each face. An analytical expression that represents this integral is utilized.

The sensitivity matrix describes how the heat flux term is affected by changes to the temperatures associated with each node in the mesh. Thus, one element of this matrix

$$J_{flow_{cl,k}} = \frac{\partial \dot{Q}_{flow_{cl}}}{\partial T_k} \tag{3.14}$$

gives the change in the pyrolysis gas heat flux for the cl^{th} control volume due to the change in temperature at the k^{th} node. Applying Equation 3.14 to Equation 3.12 yields

$$J_{flow_{cl,k}} = -\int_{cs} \frac{\rho_g K_{ji}}{\mu_g} \frac{\partial P_g}{\partial x_i} \hat{n}_j \frac{\partial h_g}{\partial T_k} dA \tag{3.15}$$

where it has further been assumed that ρ_g, K_{ji}, μ_g, and P_g are not sensitive to changes in temperature. (These variables do, in fact, have some temperature dependence, which is captured through the iterative, sequential solution of the energy and the gas-phase continuity equations.) The derivative of the pyrolysis gas enthalpy in Equation 3.15 can be determined by applying the chain rule:

$$\frac{\partial h_g}{\partial T_k} = \frac{\partial h_g}{\partial T}\frac{\partial T}{\partial T_k} = C_{p_g} N_k \tag{3.16}$$

where N_k is the shape function associated with node k. (The relationship between the derivative and the shape function can be observed by differentiating Equation 3.30.) Each element of the sensitivity matrix for the pyrolysis gas heat flux term can therefore be computed as

$$J_{flow_{cl,k}} = \sum_{f \in cl} \left(-\hat{n}_j \frac{\partial P_g}{\partial x_i} \int_f \frac{\rho_g C_{p_g} K_{ji} N_k}{\mu_g} dA \right)_f \tag{3.17}$$

where the integral represents integration of the product of five quantities that are assumed to independently vary in a linear manner along each face. An analytical expression that represents this integral is utilized.

Multiple boundary conditions for the energy equation were implemented into the MOPAR-MD material response solver by Wiebenga [27], including specified temperature, specified heat flux, radiation, aerodynamic heating, and thermochemical ablation. As part of this work, the thermochemical ablation boundary condition was updated to account for the presence of pyrolysis gases (see Section 3.6), and the radiation boundary condition was updated to treat “stream” radiation (radiation exchange with the combustion gases flowing through the nozzle, see Section 3.7).

3.4 Pyrolysis

Pyrolysis, or thermal decomposition, of an ablating material is described by the solid-phase continuity equation. However, the grid convection term in Equation 3.2

greatly complicates the solution of this equation for moving control volumes. An alternative approach is to consider a fixed material element in the domain, for which the solid-phase continuity equation simplifies to

$$\underbrace{\frac{d}{dt}\int_{cv}\rho_s dV}_{\text{storage}} = \underbrace{\int_{cv}\dot{m}_s''' dV}_{\text{source}} \tag{3.18}$$

Traditionally, three “species” or “components” are used to describe a pyrolyzing material (with two representing the resin and one representing the reinforcement) [9]. However, for this work a more generalized modeling approach is taken in which any number of components can be used to describe the pyrolyzing material:

$$\rho_s = \sum_i \Gamma_i \rho_i \tag{3.19}$$

Here the subscript i refers to the i^{th} pyrolyzing component and Γ represents the pyrolyzing component volume fraction. Decomposition of each component is assumed to be independent, irreversible, and described by an Arrhenius equation

$$\frac{d\rho_i}{dt} = -A_i \rho_{v_i}\left(\frac{\rho_i - \rho_{c_i}}{\rho_{v_i}}\right)^{\psi_i} \exp\left(-\frac{T_{a_i}}{T}\right) \tag{3.20}$$

where A is the Arrhenius pre-exponential factor, T_a denotes the reaction activation temperature, and ψ represents the reaction order. The subscript c refers to the fully-charred state, while v refers to the virgin state. By making use of a dimensionless relative density, defined as

$$w_i = \frac{\rho_i - \rho_{c_i}}{\rho_{v_i}} \tag{3.21}$$

Equation 3.20 can be simplified to

$$\frac{dw_i}{dt} = -A_i w_i^{\psi_i} \exp\left(-\frac{T_{a_i}}{T}\right) \tag{3.22}$$

Thus, for each fixed point in the domain, a set of ordinary differential equations describing pyrolysis is obtained. Direct integration of these ODEs is performed implicitly:

$$w_i^n = \begin{cases} \left(\left(w_i^{n-1}\right)^{1-\psi_i} - \frac{A_i \Delta t}{\Delta T}\left(1-\psi_i\right) \int \exp\left(-\frac{T_{a_i}}{T}\right) dT\right)^{\frac{1}{1-\psi_i}} & \psi_i \neq 1 \\ w_i^{n-1} \exp\left(-\frac{A_i \Delta t}{\Delta T} \int \exp\left(-\frac{T_{a_i}}{T}\right) dT\right) & \psi_i = 1 \end{cases} \tag{3.23}$$

where

$$\Delta T = T^n - T^{n-1} \tag{3.24}$$

is the change in temperature during the time step (i.e. temperature is assumed to vary linearly during the time step). The exponential integral found in Equation 3.23 is approximated using Simpson's rule:

$$\int \exp\left(-\frac{T_{a_i}}{T}\right) dT \approx \frac{\Delta T}{6}\left(\exp\left(-\frac{T_{a_i}}{T^n}\right) + 4\exp\left(-\frac{2T_{a_i}}{T^n + T^{n-1}}\right) + \exp\left(-\frac{T_{a_i}}{T^{n-1}}\right)\right) \tag{3.25}$$

Equation 3.23 is singular when there is no change in temperature over the duration of the time step. Thus, when $\frac{T^n - T^{n-1}}{T^{n-1}} < 0.001\,\%$, explicit integration is utilized:

$$w_i^n = \begin{cases} \left(\left(w_i^{n-1}\right)^{1-\psi_i} - A_i \Delta t \left(1-\psi_i\right) \exp\left(-\frac{T_{a_i}}{T^{n-1}}\right)\right)^{\frac{1}{1-\psi_i}} & \psi_i \neq 1 \\ w_i^{n-1} \exp\left(-A_i \Delta t \exp\left(-\frac{T_{a_i}}{T^{n-1}}\right)\right) & \psi_i = 1 \end{cases} \tag{3.26}$$

A minimum temperature T_{min_i} can be specified for each decomposition reaction. When the temperature at a given point remains below this threshold temperature (i.e. $\max\left(T^{n-1}, T^n\right) < T_{min_i}$), the pyrolysis calculations described in Equations 3.23 and 3.26 are bypassed and $w_i^n = w_i^{n-1}$.

The density history at any physical point in the domain only depends on the local temperature history. In order to account for the effects of mesh deformation (caused by surface recession), at each time step the solution from the previous time step is interpolated onto the new, deformed mesh. It is assumed that the change in position of a node for each time step is small enough that the new node position is located within the "old" (previous time step) boundaries of the neighboring elements. For this work, only unstructured meshes constructed from triangular elements are considered. Thus, the barycentric coordinates of the new node position relative to the old boundaries of an element can be computed as [79]

$$N_1 = \frac{x_2^{n-1} y_3^{n-1} - x_3^{n-1} y_2^{n-1} - x_p^n \left(y_3^{n-1} - y_2^{n-1}\right) + y_p^n \left(x_3^{n-1} - x_2^{n-1}\right)}{x_2^{n-1} y_3^{n-1} - x_3^{n-1} y_2^{n-1} - x_1^{n-1} \left(y_3^{n-1} - y_2^{n-1}\right) + y_1^{n-1} \left(x_3^{n-1} - x_2^{n-1}\right)} \tag{3.27}$$

$$N_2 = \frac{x_3^{n-1} y_1^{n-1} - x_1^{n-1} y_3^{n-1} - x_p^n \left(y_1^{n-1} - y_3^{n-1}\right) + y_p^n \left(x_1^{n-1} - x_3^{n-1}\right)}{x_2^{n-1} y_3^{n-1} - x_3^{n-1} y_2^{n-1} - x_1^{n-1} \left(y_3^{n-1} - y_2^{n-1}\right) + y_1^{n-1} \left(x_3^{n-1} - x_2^{n-1}\right)} \tag{3.28}$$

$$N_3 = 1 - N_1 - N_2 \tag{3.29}$$

In these equations, the numerical subscripts refer to the three vertices of the triangular element and the subscript p refers to the new nodal position of interest within the element. The triangular element for which all three barycentric coordinates are positive is the element that encompasses the new node position. One useful characteristic of barycentric coordinates is that they also serve as linear shape functions which can be used to perform interpolation within the triangular element. Thus, the old temperature and density values at the new node position can be computed as

$$\xi = \sum_{k=1}^{3} N_k \xi_k \tag{3.30}$$

where here ξ represents T^{n-1} and ρ_i^{n-1}. These quantities are then used to compute the new solid densities at the new node locations.

3.5 Porous Flow

The gas-phase continuity equation describes the flow of the pyrolysis gases through the porous char material, and is linearized and solved in a manner similar to that used for the mixture energy equation. The resulting linear system obtained is

$$\left[\frac{1}{\Delta t}\mathbf{J}^{\nu}_{stor} - \mathbf{J}^{\nu}_{grid} + \mathbf{J}^{\nu}_{flow}\right]\boldsymbol{\Delta\rho_{\mathrm{g}}} = \dot{\mathbf{M}}^{\nu}_{grid} - \dot{\mathbf{M}}^{\nu}_{flow} + \dot{\mathbf{M}}^{\nu}_{src} - \frac{1}{\Delta t}\left[\mathbf{M}^{\nu}_{stor} - \mathbf{M}^{n-1}_{stor}\right] \quad (3.31)$$

where $\mathbf{M}$ and $\dot{\mathbf{M}}$ are the pyrolysis gas mass content and rate of change of gas mass content vectors, respectively. Equation 3.31 is solved using the GMRES method [80] with restarting and the ILU(0) preconditioner [81]. The pyrolysis gas density field is updated each Newton-Raphson iteration:

$$\boldsymbol{\rho}^{\nu+1}_{\mathbf{g}} = \boldsymbol{\rho}^{\nu}_{\mathbf{g}} + \boldsymbol{\Delta\rho}_{\mathbf{g}} \quad (3.32)$$

Newton-Raphson iteration is performed until the maximum pyrolysis gas density update falls below a user-specified threshold value. A convergence criteria of $\max\left(\boldsymbol{\Delta\rho}_{\mathbf{g}}\right) \leq 10^{-5}\,{}^{\mathrm{kg}}\!/_{\mathrm{m}^3}$ has been found to work well for the gas-phase continuity equation. One advantage to this approach for solving the gas-phase continuity equation is that flow of pyrolysis gases is not constrained to follow grid lines, as is the case in some other codes (e.g. TITAN [29]).

For a single control volume, the gas mass storage term can be computed as

$$M_{stor_{cl}} = \int_{cv} \phi\rho_g dV = \sum_{f\in cl}\int_f \phi\rho_g dV \quad (3.33)$$

where the explicit summation is performed over all of the sub-volumes that constitute the control volume of interest (one sub-volume is associated with each face on the control surface). Since porosity is not a function of the pyrolysis gas density, each element of the sensitivity matrix for the storage term can be computed as

$$J_{stor_{cl,k}} = \sum_{f \in cl} \int_f \phi N_k dV \tag{3.34}$$

The integrals in Equations 3.33 and 3.34 represent the integration of the product of two quantities that are assumed to independently vary in a linear manner within each sub-volume. An analytical expression for these integrals is utilized.

The grid convection mass flux term for a control volume can be computed as

$$\dot{M}_{grid_{cl}} = \int_{cs} \phi \rho_g u_{m_j} \hat{n}_j dA = \sum_{f \in cl} \left(\hat{n}_j \int_f \phi \rho_g u_{m_j} dA \right)_f \tag{3.35}$$

where the explicit summation is performed over all the faces forming the control surface that bounds the control volume of interest, and implied summation is performed with respect to the subscript j, which represents the spatial dimensions of the problem. Since porosity, mesh velocity, and the face normal vectors are not functions of pyrolysis gas density, each element of the sensitivity matrix can be computed as

$$J_{grid_{cl,k}} = \sum_{f \in cl} \left(\hat{n}_j \int_f \phi u_{m_j} N_k dA \right)_f \tag{3.36}$$

The mass flux term due to the flow of the pyrolysis gases through the porous char can be computed for a single control volume as

$$\dot{M}_{flow_{cl}} = - \int_{cs} \frac{\rho_g K_{ji}}{\mu_g} \frac{\partial P_g}{\partial x_i} \hat{n}_j dA = \sum_{f \in cl} \left(-\hat{n}_j \frac{\partial P_g}{\partial x_i} \int_f \frac{\rho_g K_{ji}}{\mu_g} dA \right)_f \tag{3.37}$$

where Darcy's law (Equation 3.5) has been utilized, along with the fact that the pressure gradient and normal vectors are constants for each face. The elements of the sensitivity matrix for this term are computed numerically using finite differences:

$$J_{flow_{cl,k}} = \frac{\dot{M}_{flow_{cl}}\left(\left(1+\varepsilon\right)\rho_{g_k}\right) - \dot{M}_{flow_{cl}}\left(\left(1-\varepsilon\right)\rho_{g_k}\right)}{2\varepsilon\rho_{g_k}} \tag{3.38}$$

The perturbation parameter $\varepsilon = 1.0 \times 10^{-6}$ is found to work well.

The integrals in Equations 3.35 through 3.37 represent the integration of the product of three quantities that are assumed to independently vary in a linear manner along each face. An analytical expression for these integrals is utilized.

The pyrolysis gas source term for a single control volume can be computed as

$$\dot{M}_{src_{cl}} = \int_{cv} \dot{m}_g''' dV = \sum_{f \in cl} \int_f \dot{m}_g''' dV \tag{3.39}$$

where the summation is performed over all of the sub-volumes that constitute the control volume of interest. Since the volumetric gas mass source term is not a function of the pyrolysis gas density, the sensitivity matrix for this term is zero. The integral in Equation 3.39 is computed using an analytical expression.

The gas mass source term is linked to the pyrolysis of the material (solid-phase continuity equation [Equation 3.2]) via the mass conservation equation (Equation 3.4). Thus, an expression for the "instantaneous" volumetric gas mass source term can be obtained:

$$\dot{m}_g''' = \sum_i \Gamma_i A_i \rho_{v_i} \left(\frac{\rho_i - \rho_{c_i}}{\rho_{v_i}}\right)^{\psi_i} \exp\left(-\frac{T_{a_i}}{T}\right) \tag{3.40}$$

Amar assumed that this "instantaneous" value of the volumetric gas mass source term, as computed at the end of a time step, held constant for the duration of the time step [16]. However, it is observed in this work that this approach can cause a violation of the conservation of mass, since the source term can vary significantly across a time step due to the strong dependence on temperature. The mass loss error is observed to decrease in a first-order manner as the time step size is decreased, which is consistent with what would be expected from the first-order, implicit time integration scheme. To avoid this mass loss error, an alternative approach is pursued, whereby an “average” volumetric gas mass source term is computed based on the actual change in solid density over the time step:

$$\dot{m}_g''' = \frac{\rho_s^{n-1} - \rho_s^n}{\Delta t} \tag{3.41}$$

With this approach, mass conservation is preserved (all solid mass lost due to pyrolysis becomes gas mass added through the source term).

Two boundary conditions have been implemented for the porous flow equations. The first is an impermeable boundary, across which there is zero gas mass flux. Much like the adiabatic boundary condition for the energy equation, no special treatment is required (an impermeable boundary occurs by default). The second boundary condition implemented is a specified pressure boundary condition. For the nodes (i.e. control volumes) that lie on the specified pressure boundary condition, Equation 3.31 is replaced with

$$\Delta\rho_{g_{cl}} = \frac{P\mathscr{M}_g}{R_u T} - \rho_{g_{cl}}^{\nu} \tag{3.42}$$

which forces the pyrolysis gas density at the boundary to the value consistent with the desired pressure.

When performing simulations involving significant changes in temperature, numerical instabilities in the solution of the porous flow equations were encountered. These instabilities were believed to be due to the loosely-coupled treatment of the energy and gas-phase continuity equations. In the loosely-coupled solution procedure, each time step the energy equation is solved first, followed by the solid-phase and gas-phase continuity equations. The pyrolysis gas density (which has not yet been updated) is therefore in poor agreement with the temperature field (which has already been updated for the time step) when the solution of the porous flow equations is begun. This discrepancy can be so large that it is not possible to obtain a good solution. Resolution of the problem is achieved by assuming that the pressure field within the domain is only weakly affected by temperature. Therefore, an improved estimate for the pyrolysis gas density is computed based on the pressure field from the previous time step and the temperature from the current time step:

$$\rho_g = \frac{P_g^{n-1}\mathscr{M}_g^n}{R_g T^n} \tag{3.43}$$

This improved estimate is only computed for the first inner iteration of each time step; it is unnecessary for subsequent iterations. This approach does not have any impact on the final solution, but is simply a way of initializing the Newton-Raphson solver for the gas-phase continuity equation.

3.6 Thermochemical Ablation Boundary Condition

For nodes on a boundary subject to a heat flux, the energy equation (Equation 3.9) is modified to include the additional boundary heat flux, as well as the associated sensitivity matrix:

$$\begin{aligned}\left[\frac{1}{\Delta t}\mathbf{J}^{\nu}_{stor} + \mathbf{J}^{\nu}_{cond} - \mathbf{J}^{\nu}_{grid} + \mathbf{J}^{\nu}_{flow} + \mathbf{J}^{\nu}_{bnd}\right]\mathbf{\Delta T} = \\ \dot{\mathbf{Q}}^{\nu}_{grid} - \dot{\mathbf{Q}}^{\nu}_{flow} - \dot{\mathbf{Q}}^{\nu}_{cond} - \frac{1}{\Delta t}\left[\mathbf{Q}^{\nu}_{stor} - \mathbf{Q}^{n-1}_{stor}\right] - \dot{\mathbf{Q}}^{\nu}_{bnd}\end{aligned} \tag{3.44}$$

The boundary heat flux term for a single control volume can be computed as

$$Q_{bnd_{cl}} = \int_{bnd} \dot{q}''_{net}\,dA = \sum_{f\in bnd}\int_f \dot{q}''_{net}\,dA \tag{3.45}$$

where $\dot{q}''_{net}$ is the net heat flux into the solid material normal to the boundary. Summation is only performed over those faces lying on the boundary, and the integral represents the integration of a single quantity that can vary linearly along the face. An analytical expression is utilized.

For an ablating surface, the net boundary heat flux is given by

$$\dot{q}''_{net} = \dot{q}''_{conv} - \dot{q}''_{g} - \dot{q}''_{c} + \dot{q}''_{rad} \tag{3.46}$$

The radiative heat flux (denoted by the subscript rad) is not impacted by the ablation process and is easily treated separately (see Section 3.7). However, the heat fluxes associated with convection, pyrolysis gas loss, and char removal (represented by the subscripts $conv$, g, and c, respectively) are strongly linked. Considering only these three factors, the heat flux to the surface due to ablation processes is given by

$$\dot{q}''_{abl} = \dot{q}''_{conv} - \dot{q}''_{g} - \dot{q}''_{c} \tag{3.47}$$

In this work, the transport coefficient assumption and the unity Lewis number assumption (mass transfer coefficient and energy transfer coefficient are the same, $g_M = g_H$) are made, which allows the convective heat flux to be modeled as

$$\dot{q}''_{conv} = g_H \left(h_r - h_w\right) \tag{3.48}$$

where h_r is the recovery enthalpy, h_w is the enthalpy of the gas-phase species at the ablating wall, and g_H is the “enthalpy conductance”, an enthalpy-based convection coefficient. (The compound symbol “$\rho_e u_e C_H$” is often used in the literature to represent enthalpy conductance.) This enthalpy conductance includes the mitigating effects of blowing:

$$g_H = g_{H_0} \Omega_{blw} \tag{3.49}$$

where the subscript 0 refers to the enthalpy conductance in the absence of blowing. The blowing correction factor Ω_{blw} is modeled with the correlation [82]

$$\Omega_{blw} = \frac{\zeta}{e^{\zeta} - 1} \tag{3.50}$$

$$\zeta = \frac{2\lambda \left(\dot{m}_g'' + \dot{m}_c''\right)}{g_{H_0}} \tag{3.51}$$

where $\dot{m}_g''$ and $\dot{m}_c''$ are the mass fluxes of the pyrolysis gases and the char, respectively. The influence of blowing on laminar boundary layers is modeled with $\lambda = 0.5$, while $\lambda = 0.4$ is usually used for turbulent boundary layers.

The heat fluxes associated with pyrolysis gas and char lost from the material due to ablation can be computed as

$$\dot{q}_g'' = \dot{m}_g'' h_w \tag{3.52}$$

$$\dot{q}_c'' = \dot{m}_c'' h_w \tag{3.53}$$

Substituting Equations (3.48), (3.52), and (3.53) into Equation 3.47 yields

$$\dot{q}_{abl}'' = g_H \left(h_r - h_w\right) - \dot{m}_g'' h_w - \dot{m}_c'' h_w \tag{3.54}$$

Using the definitions for the nondimensional mass fluxes

$$B_g' = \frac{\dot{m}_g''}{g_M} = \frac{\dot{m}_g''}{g_H} \tag{3.55}$$

$$B_c' = \frac{\dot{m}_c''}{g_M} = \frac{\dot{m}_c''}{g_H} \tag{3.56}$$

the heat flux to the material surface due to thermochemical convection and ablation can be computed as

$$\dot{q}_{abl}'' = g_H \left[h_r - h_w \left(1 + B_c' + B_g'\right)\right] \tag{3.57}$$

The enthalpy at the wall (h_w) is the enthalpy of the ablation reaction products, and is a function not only of temperature, but also of the nondimensional mass flux of pyrolysis gases and char (B'_g and B'_c) at the boundary. Closure of Equation 3.57 is achieved by using surface energy balance tables ("B' tables") pre-computed by an equilibrium chemistry program, such as ACE [83] or Chemics [84]. The material response code uses these tables to obtain wall enthalpy and char mass flux as a function of pressure, wall temperature, and nondimensional pyrolysis gas mass flux (B'_g). However, one complicating factor is that the pyrolysis gas mass flux leaving the surface is the combination of gas lost due to flow (motion of the gases relative to the material) and the gas stored in material pores lost due to surface recession:

$$\dot{m}''_g = \phi \rho_g \left(u_{g_j} \hat{n}_j + \dot{s} \right) \tag{3.58}$$

Furthermore, surface recession rate ($\dot{s}$) is directly related to B'_c:

$$\dot{s} = \frac{\dot{m}''_c}{\rho_s} = \frac{g_M B'_c}{\rho_s} = \frac{g_H B'_c}{\rho_s} \tag{3.59}$$

As a consequence, B'_g has some dependence on B'_c. Therefore, an iterative procedure is used to determine values for h_w, B'_g, and B'_c that are consistent.

With the approach pursued in this material response code, it is not necessary to explicitly relate $\dot{q}''_{abl}$ to the in-depth temperature field when performing the surface energy balance, as is done in other codes (e.g. CMA [9], ITRAC [21]). Instead, the heat flux at the surface and the conduction into the material are brought into agreement through the iterative Newton-Raphson method used to solve the energy equation.

It is assumed that the boundary heat flux term for each control volume is only sensitive to the changes in temperature at that boundary node (i.e. the off-diagonal terms of the sensitivity matrix are zero). The diagonal terms for the boundary heat flux sensitivity matrix can therefore be computed as

$$J_{bnd_{cl}} = \sum_{f \in bnd} \int_f \frac{\partial \dot{q}''_{net}}{\partial T} dA = \sum_{f \in bnd} \int_f \left(\frac{\partial \dot{q}''_{abl}}{\partial T} + \frac{\partial \dot{q}''_{rad}}{\partial T} \right) dA \tag{3.60}$$

where summation is only performed over those faces lying on the boundary, and the integral represents the integration of a single quantity that can vary linearly along the face (an analytical expression is utilized). The temperature derivative of the ablation heat flux can be computed as

$$\frac{\partial \dot{q}''_{abl}}{\partial T} = -g_H \left(\left(1 + B'_c + B'_g\right) \frac{\partial h_w}{\partial T} + h_w \frac{\partial B'_c}{\partial T} \right) \tag{3.61}$$

where the derivatives for h_w and B'_c are obtained from the B' tables through the use of finite differences.

Two degenerate cases must be treated specially for the thermochemical ablation boundary condition. The first is when there is significant pyrolysis gas mass flux, but no convection (taken to be $g_H < 1.0 \times 10^{-6} \mathrm{kg}/\mathrm{m}^2\mathrm{s}$). Such a scenario can arise, for instance, during the cool-down period after the ablating material has been subjected to convective heating. In this case there is no char removal, and the only heat flux (other than radiation) is due to the outflow of the pyrolys gases. Thus,

$$\dot{q}''_{abl} = -\dot{m}''_g h_g \tag{3.62}$$

$$\frac{\partial \dot{q}''_{abl}}{\partial T} = -\dot{m}''_g C_{p_g} \tag{3.63}$$

where h_g and C_{p_g} are the enthalpy and specific heat at constant pressure, respectively, of the pyrolysis gases at the surface temperature. The second special case is where there is flow of gas from the external flow domain into the porous char (i.e. $\dot{m}''_g < 0$). Such a scenario primarily occurs in early transient periods before significant pyrolysis occurs. Under these conditions there is no char removal and no mitigation of convection heat flux due to blowing ($\Omega_{blw} = 1$). Thus,

$$\dot{q}''_{abl} = g_H \left(h_r - h_w\right) - \dot{m}''_g h_w \tag{3.64}$$

$$\frac{\partial \dot{q}''_{abl}}{\partial T} = -\left(g_H + \dot{m}''_g\right) \frac{\partial h_w}{\partial T} \tag{3.65}$$

where here h_w is the enthalpy of the boundary layer edge gases at the wall temperature, which comes from a separate edge gas enthalpy table (not the B' table). Finite differences are used to evaluate the temperature derivative.

3.7 Radiation Boundary Condition

The net radiative heat flux to a surface exchanging energy with a blackbody reservoir is

$$\dot{q}''_{rad} = \varepsilon\sigma \left(T_{res}^4 - T_w^4\right) \tag{3.66}$$

where $\sigma = 5.67 \times 10^{-8} \mathrm{W}/\mathrm{m^2K^4}$ is the Stefan-Boltzmann constant, and T_w and T_{res} are the wall and reservoir temperatures, respectively. For standard radiation exchange with a blackbody reservoir, the emissivity used is that of the wall, $\varepsilon = \varepsilon_w$. The sensitivity of the radiative heat flux to changes in wall temperature is given by

$$\frac{\partial \dot{q}''_{rad}}{\partial T} = \sigma \left(T_{res}^4 - T_w^4\right) \frac{\partial \varepsilon}{\partial T} - 4\varepsilon\sigma T_w^3 \tag{3.67}$$

where finite differences are used to find the temperature derivative of emissivity.

Rockets motors using aluminized propellants produce combustion products that are highly radiative (due to the presence of alumina particles). Radiation exchange therefore occurs between the wall and this “stream” of combustion products, and not with a blackbody reservoir. The combustion products are traditionally modeled as an opaque 2D slab adjacent to the nozzle surface. Radiative heat transfer between the products and the surface can computed using Equation 3.66, provided that the effective emissivity describing radiative exchange between two gray, infinite, parallel plates is utilized:

$$\varepsilon = \frac{1}{\frac{1}{\varepsilon_{stream}} + \frac{1}{\varepsilon_w} - 1} \tag{3.68}$$

Code was added to the existing radiation boundary conditions within MOPAR-MD in order to implement Equation 3.68 so that stream radiation can be modeled.

Modeling radiative heat transfer in nozzles requires that stream emissivity and stream temperature be supplied to the material response code. These stream properties are computed using the Nozzle Aerothermochemistry (NAT) code [8]. Stream temperature is taken to be that computed by a 1D isentropic expansion calculation performed by the ACE module included in NAT. The correlation

$$\varepsilon_{stream} = 1 - \exp\left(-0.808 \frac{n}{16} \rho D\right) \tag{3.69}$$

is used to compute the stream emissivity [85]. Here n is the percent of aluminum in the propellant, ρ is the local density of the combustion products (in units of $^{\mathrm{lbm}}/_{\mathrm{ft}^3}$), and D is the local diameter of the nozzle (in units of inches).

3.8 Material Properties

The thermodynamics properties used in Equation 3.1 are those for the “mixture”, and account for both the solid material and the pyrolysis gases. Mixture density is computed as

$$\rho = \phi \rho_g + \rho_s \tag{3.70}$$

while the other properties are computed as mass-weighted averages:

$$Y_g = \frac{\phi \rho_g}{\rho} \tag{3.71}$$

$$\xi = Y_g \xi_g + (1 - Y_g)\, \xi_s \tag{3.72}$$

Here ξ is used to represent any property of interest. The properties for the solid phase are in turn a function of the degree of char, or the extent of pyrolysis:

$$\beta = \frac{\rho_v - \rho_s}{\rho_v - \rho_c} \tag{3.73}$$

$$Y_v = \frac{\rho_v}{\rho_s} (1 - \beta) \tag{3.74}$$

$$\xi_s = Y_v \xi_v + (1 - Y_v)\, \xi_c \tag{3.75}$$

One exception is the permeability of the solid material, which can vary over several orders of magnitude between the virgin and char states. Experimental data suggest that the permeability varies logarithmically with respect to degree of char [86, 87, 88]. Therefore, the permeability of the pyrolyzing material is modeled as

$$\log_{10}(K) = (1 - \beta) \log_{10}(K_v) + \beta \log_{10}(K_c) \tag{3.76}$$

In MOPAR-MD, all properties are assumed to independently vary linearly within each element in the domain. This is in contrast to some other codes (e.g. CMA [9], ITRAC [21], MOPAR-1D [19, 20]), which often combine certain properties into compound pseudo-properties (e.g. “ρe”).

CHAPTER IV

Fluid-Thermal Coupling

4.1 Introduction

In this work, the LeMANS flow solver is coupled to the MOPAR-MD material response solver, enabling fully-coupled, conjugate simulations of ablation of pyrolyzing materials. The pressure trace for a rocket motor firing is divided into a number of discrete time points (see Figure 4.1). At each time point, a steady-state flowfield solution is obtained using LeMANS. The wall boundary conditions required by the flow

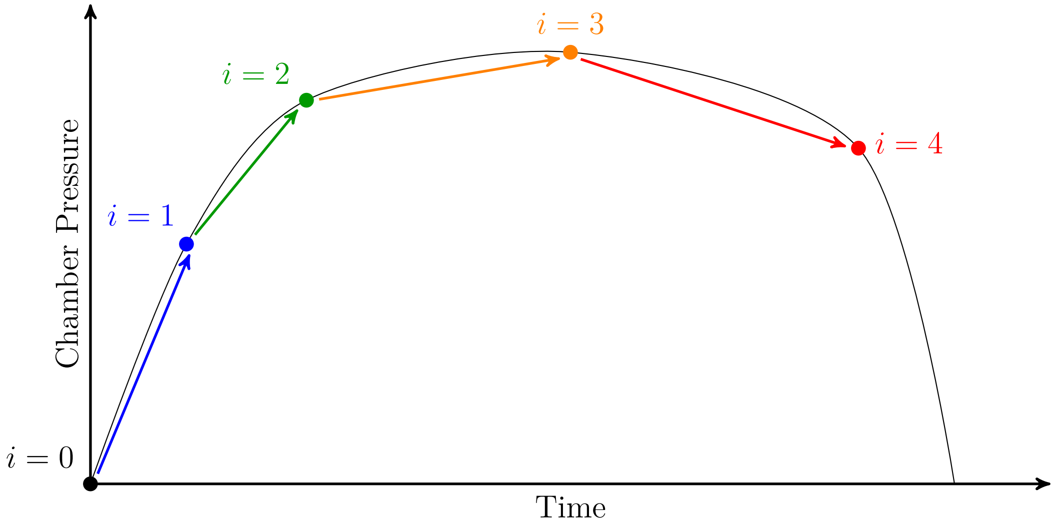

Figure 4.1: Diagram illustrating how a pressure trace is divided into a number of discrete time points (solid circles) at which steady-state flowfield solutions are obtained. Transient material response calculations (represented by arrows) are performed to obtain the flowfield boundary conditions for each time point.

Table 4.1: Variables exchanged between the flow solver and the material response solver for multiple treatments of the surface energy balance at the ablating wall.

Methodology	Flow → Solid	Solid → Flow
Noncatalytic Wall – Heat Flux	P, $\dot{q}''$, h_r	T, $\dot{m}''$, x_j
Noncatalytic Wall – Enthalpy Conductance	P, g_H, h_r	T, $\dot{m}''$, x_j
Ablating Wall – Heat Flux	P, $\dot{q}''$, h_r	T, $\dot{m}''$, x_j, Y_s
Ablating Wall – Enthalpy Conductance	P, g_H, h_r	T, $\dot{m}''$, x_j, Y_s
Integrated Equilibrium Surface Chemistry	P, $\dot{q}''$, $\dot{m}''_c$, h_w	T, $\dot{m}''_g$, x_j

solver are obtained from MOPAR-MD, which is linked into the flow solver executable as a boundary condition subroutine. At each time point, the material response solver performs a transient analysis starting from the solution obtained at the previous time point, using as boundary conditions values passed from the flow solver. These values are linearly interpolated between time points. The variables passed between solvers depend on the chosen surface energy balance approach (see Section 4.3), as given in Table 4.1. In this table, P represents pressure, T is temperature, x_j denotes the position of the wall, $\dot{q}''$ is heat flux, g_H is enthalpy conductance, Y_s represents the mass fraction of species s, h_r and h_w are the recovery and wall enthalpies, respectively, and $\dot{m}''_c$, $\dot{m}''_g$, and $\dot{m}''$ are the char, pyrolysis gas, and total mass fluxes, respectively.

An under-relaxation factor, ψ, is applied to the variables passed from the material response solver to the flow solver:

$$\xi = (1 - \psi)\,\xi_{FS} + \psi \xi_{MR} \tag{4.1}$$

Here ξ represents any variable of interest, and the subscripts FS and MR refer to the flow and material response solvers, respectively. Thus, the new values for these flowfield boundary variables are a blend of the previously-used values and the latest values predicted by the material response solver. As will be shown later (see Section 7.4.1), this under-relaxation factor helps with the convergence of the conjugate

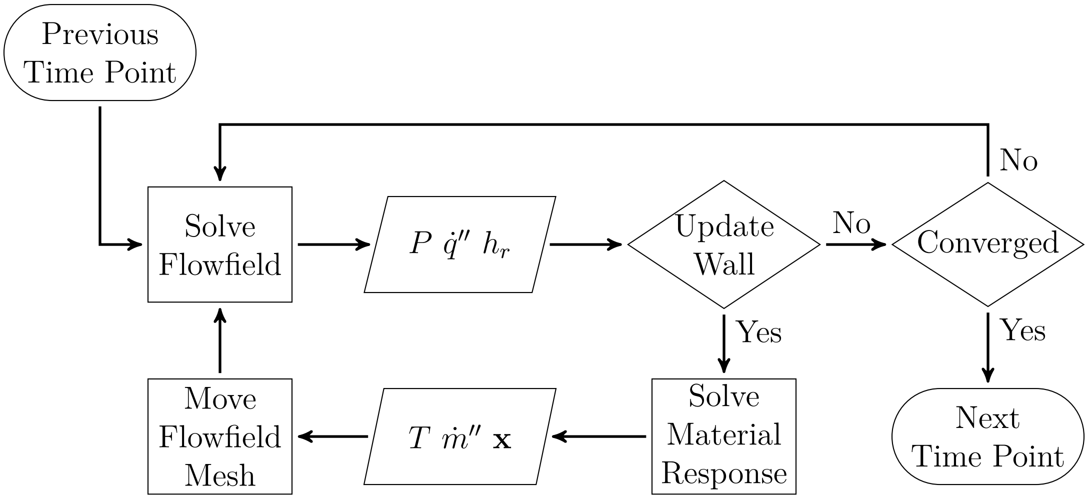

Figure 4.2: Flowchart illustrating the approach taken to obtain a converged conjugate solution for a given time point.

solution. Generally, the under-relaxation factor is applied to the temperature, mass flux, wall position, and species mass fractions. No under-relaxation factor is applied to the pyrolysis gas mass flux when using the Integrated Equilibrium Surface Chemistry method. It should also be noted that the flowfield and material response meshes do not need to have coincident nodes; interpolation is used to map values between meshes. This adds flexibility and allows each mesh to be optimized independently.

A fully converged conjugate solution is obtained for each time point before advancing to the next. This requires an iterative process, with the material response solver being called multiple times for each time point, as illustrated in Figure 4.2. Starting with the solution from the previous time point, a flow solver iteration is performed, producing updated values for the material response boundary conditions (in this example, pressure, heat flux, and recovery enthalpy). At the end of every flow iteration, a check is performed to determine whether or not the material response solver should be called to update the ablating wall boundary conditions (see Section 4.2). If it is determined that the wall values should be updated, the material response solver is called, which performs a transient thermal analysis starting from the previous time point. This yields updated values for the flow solver boundary conditions (e.g. wall temperature, injected mass flux, and wall position). The flow solver then updates the flow domain mesh to account for wall recession, and a new flow iteration is performed. If the first check determines that it is not necessary to update the wall values, a second check is performed to determine if convergence has been achieved. If convergence is not achieved, the process continues with another flowfield iteration, otherwise, the conjugate solution can advance to the next time point.

4.2 Surface Update Criteria

In this effort, the material response solver is called in order to update the flowfield wall boundary conditions once three different criteria are all satisfied. The first criterion:

$$n - n_{MR} \geq n_{min} \tag{4.2}$$

requires that some minimum number of flow iterations n_{min} be completed between calls to the material response solver. In this equation, n refers to the flow solver iteration (or time step) and n_{MR} refers to the flow solver iteration that corresponds to the previous time the material response solver was called. This criterion helps ensure that the flow has sufficient time to respond to the latest wall conditions before updating the wall again. The second criterion:

$$\max\left(100\left|\frac{\dot{q}_k''^{n} - \dot{q}_k''^{n-1}}{\dot{q}_k''^{n-1}}\right|\right) < \varepsilon_{\dot{q}''} \tag{4.3}$$

looks at the maximum change in heat flux between two subsequent flow iterations, and is a measure of the convergence of the flowfield. The subscript k refers to the k^{th} flow solver face on the ablating wall, and $\varepsilon_{\dot{q}''}$ is the convergence threshold value for the maximum change in heat flux. This criterion prevents the wall values from being updated while the flowfield is still undergoing significant changes. The third and final criterion:

$$100 \left| \frac{\dot{q}''^{n}_{RMS} - \dot{q}''^{n_{MR}}_{RMS}}{\dot{q}''^{n_{MR}}_{RMS}} \right| \geq \varepsilon_{\dot{q}''_{RMS}} \tag{4.4}$$

$$\dot{q}''_{RMS} = \sqrt{\frac{1}{N} \sum_{k}^{N} \dot{q}''^{2}_{k}} \tag{4.5}$$

looks at the change in the root mean square (RMS) heat flux since the last time the material response solver was called, and is a measure of how much the flowfield has changed since the last time the wall values were updated. The convergence threshold value for the change in RMS heat flux is denoted by $\varepsilon_{\dot{q}''_{RMS}}$. This criterion prevents the material response solver from being needlessly called if the wall heat flux has not changed significantly.

The three threshold parameters n_{min}, $\varepsilon_{\dot{q}''}$, and $\varepsilon_{\dot{q}''_{RMS}}$ must be specified by the user; trial-and-error is required to identify appropriate values for a given problem. The following values are found to be generally suitable for this effort, and are used for most simulations presented in this dissertation:

$$n_{min} = 2000$$
$$\varepsilon_{\dot{q}''} = 0.01\,\%$$
$$\varepsilon_{\dot{q}''_{RMS}} = 0.05\,\%$$

4.3 Surface Energy Balance Treatments

Five different approaches for treating the surface energy balance are identified and implemented into the conjugate ablation analysis code.

4.3.1 Noncatalytic Wall – Heat Flux

In the Noncatalytic Wall – Heat Flux (NCHF) coupling approach, a noncatalytic wall (zero species mass fraction gradient in the wall-normal direction) boundary condition is used in the flow solver, and the heat flux is passed to the material response solver. This is the same surface energy balance approach used by other researchers at the University of Michigan for some conjugate ablation studies for external thermal protection system applications [28, 43]. The surface energy balance is performed in the material response solver using pre-computed B' tables. Recall that the net heat flux to an ablating surface is given by

$$\dot{q}''_{net} = \underbrace{\dot{q}''_{conv} - \dot{q}''_{g} - \dot{q}''_{c}}_{\text{ablation}} + \dot{q}''_{rad} \tag{4.6}$$

In this treatment, the heat flux obtained from the flow solver is used directly as the convective heat flux; no approximation or modification is used:

$$\dot{q}''_{conv} = \dot{q}''_{FS} \tag{4.7}$$

However, the heat fluxes due to pyrolysis gas and char mass flux require values for the ablating wall enthalpy h_w and the nondimensional char mass flux B'_c for closure:

$$\dot{q}''_{g} = \dot{m}''_{g} h_w \tag{4.8}$$

$$\dot{q}''_{c} = \dot{m}''_{c} h_w = B'_c g_H h_w \tag{4.9}$$

These values are tabulated in the B' tables as functions of wall temperature, pressure, and nondimensional pyrolysis gas mass flux:

$$h_w = f\left(T_w, P, B'_g\right) \tag{4.10}$$

$$B'_c = f\left(T_w, P, B'_g\right) \tag{4.11}$$

Pyrolysis gas mass flux is nondimensionalized by an enthalpy conductance; note that the unity Lewis number assumption (mass transfer coefficient and energy transfer coefficient are the same, $g_M = g_H$) is made:

$$B'_g = \frac{\dot{m}''_g}{g_M} = \frac{\dot{m}''_g}{g_H} \tag{4.12}$$

Thus, to use pre-computed B' tables to provide closure for the net heat flux to the ablating boundary, it is necessary to compute an enthalpy conductance (enthalpy-based convection coefficient):

$$g_H = \frac{\dot{q}''_{FS}}{h_r - h_w} \tag{4.13}$$

In this calculation, the recovery enthalpy h_r is assumed to be equal to the gas-phase stagnation enthalpy. Since the wall enthalpy, h_w, is obtained from the B' tables and is therefore a function of g_H, an iterative procedure is used to solve Equation 4.13.

4.3.2 Noncatalytic Wall – Enthalpy Conductance

In the Noncatalytic Wall – Enthalpy Conductance (NCEC) approach, a noncatalytic wall boundary condition is still used in the flow solver, but an enthalpy conductance (heat transfer coefficient) is passed to the material response solver instead of heat flux. The enthalpy conductance is computed within the flow solver according to:

$$g_H = \frac{\dot{q}''_{FS}}{h_r - h_{FS}} \tag{4.14}$$

where h_{FS} is the enthalpy of the gas-phase species present at the noncatalytic wall. Note that the difference between the enthalpy conductance computed by Equation 4.14 for the NCEC method and the enthalpy conductance computed by Equation 4.13 for closure of the NCHF method is the choice of wall enthalpy. For the NCHF method the ablating wall enthalpy from the B' tables is used, while for the NCEC method the noncatalytic wall enthalpy from the flow solver is used, which is more appropriate for characterizing the heat flux predicted by the flow solver.

Within the material response solver, this enthalpy conductance is used to compute the convective heat flux:

$$\dot{q}''_{conv} = g_H \left(h_r - h_w \right) \tag{4.15}$$

where the wall enthalpy, h_w, comes from the B' tables. Computation of the heat fluxes due to pyrolysis gas and char mass flux is the same as for the NCHF method.

Since the wall enthalpy for a noncatalytic wall flow solution will in general be different than the ablating wall enthalpy (due to different compositions at the wall), then the heat flux used by the material response solver will not match the heat flux computed by the flow solver. However, this is consistent with the traditional decoupled ablation analysis approach, and actually represents an improvement over the decoupled approach. This improvement is because the effects of wall temperature and mass injection are being accounted for directly in the computation of the enthalpy conductance (instead of being approximated with correlations).

Additionally, using a heat transfer coefficient is a more appropriate and flexible boundary condition than using a flux. If a heat flux is specified, it is possible to obtain much larger thermal responses at the surface than would actually occur under convective heating; nothing prevents the surface temperature from exceeding the recovery temperature. These large temperature changes can destabilize the conjugate solution. In contrast, when employing an enthalpy conductance boundary condition, the actual convective heat flux to the surface decreases as the surface temperature increases. This is more physically representative of convective heating, and prevents very large temperature rises that exceed the recovery temperature. It is therefore expected that simulations using the NCEC approach will be more robust and stable than the NCHF method, and it should be possible to employ larger intervals between time points.

4.3.3 Ablating Wall – Heat Flux

The Ablating Wall – Heat Flux (AWHF) method is similar to the NCHF method in that a heat flux is passed from the flow solver to the material response solver. However, a noncatalytic wall boundary condition is not used. Instead, the species mass fractions at the wall are specified according to the equilibrium composition at the ablating wall, which is obtained as part of the procedure used to compute the B' tables. Normally this composition data is not retained, but for the AWHF method the species mass fractions are stored in an “extended” B' table as functions of wall temperature, pressure, and nondimensional pyrolysis gas mass flux:

$$Y_s = f\left(T_w, P, B'_g\right) \tag{4.16}$$

The material response solver interpolates from this “extended” B' table and passes the resultant species mass fractions at the ablating wall back to the flow solver. This surface energy balance treatment is similar to that used by Olynick et al. [38].

Species mass fractions at a given point in the flow can change by several orders of magnitude between two different time points. Such a situation can arise, for example, when the temperature at a given location at one time point is low enough so that ablation does not occur, but at the next time point has increased to a level where ablation does occur. In this situation, applying an under-relaxation factor to the species mass fractions is unable to adequately capture this significant change in composition. It is found that applying the under-relaxation factor to the logarithm of the species mass fractions provides a much better adjustment of the wall composition.

4.3.4 Ablating Wall – Enthalpy Conductance

The Ablating Wall – Enthalpy Conductance (AWEC) method is similar to the AWHF method, except that an enthalpy conductance is passed from the flow solver to the material response solver, instead of heat flux. In this regard it is similar to the NCEC method. Once a converged coupled solution is obtained, the wall enthalpy computed by the flow solver should be the same as the ablating wall enthalpy from the B' tables (other than for small differences in the thermodynamic data used in the two solvers). Therefore, the heat flux computed by the flow solver will closely match the heat flux used in the material response solver. However, this will not necessarily be the case as the solution is developing (mainly due to the under-relaxation factor applied to the wall mass fractions). This treatment is very similar to that used by Kuntz et al. [10].

4.3.5 Integrated Equilibrium Surface Chemistry

The preceding four methods all use B' tables within the material response solver to perform the surface energy balance. In the Integrated Equilibrium Surface Chemistry (IESC) approach, B' tables are completely abandoned. Instead, the equilibrium chemistry calculations at the surface are integrated into the LeMANS flow solver. Equilibrium chemistry ablation is computed based on the diffusive fluxes at the wall and the injection of the pyrolysis gases without resorting to a transport coefficient assumption, or assuming a unity Lewis number. This approach is similar to that presented by Johnston et al. [11, 89].

Consider a thin control volume located just above an ablating surface, as illustrated in Figure 4.3. Assuming no mechanical removal of char, element conservation and mass conservation dictate that [90, 91]

$$\tilde{J}_{k_w} + \left(\dot{m}_g'' + \dot{m}_c''\right) \tilde{Y}_{k_w} = \dot{m}_g'' \tilde{Y}_{k_g} + \dot{m}_c'' \tilde{Y}_{k_c} \tag{4.17}$$

Here $\tilde{J}_{k_w}$ is the diffusion of element k away from the wall into the flow, $\tilde{Y}_k$ represents the mass fraction of element k, and the subscripts c, g, and w refer to the char,

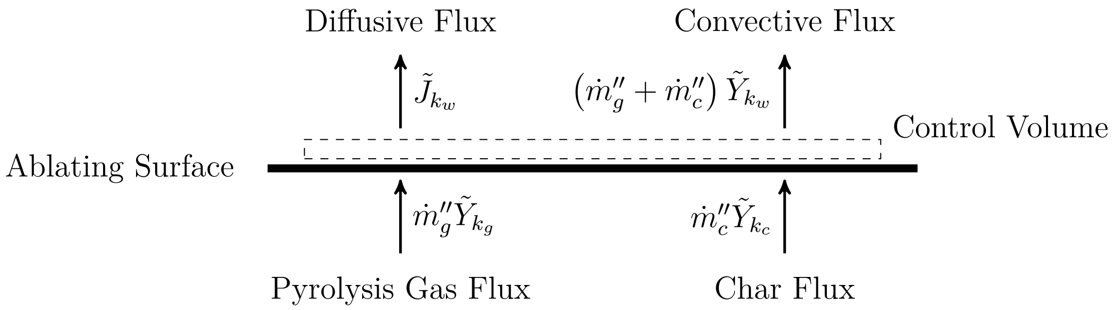

Figure 4.3: Diagram illustrating elemental mass balance at an ablating surface.

pyrolysis gases, and wall, respectively. Normally the diffusion term in Equation 4.17 is approximated using a transport coefficient, leading to the formulation of the B' tables. In the IESC approach, however, this diffusive flux is computed using the modified Fick's Law employed by the LeMANS flow solver. Assuming that the diffusive flux is dominated by the wall-normal gradient, this results in

$$\tilde{J}_{k_w} = \frac{\rho D}{d}\left(\tilde{Y}_{k_w} - \tilde{Y}_{k_{cl}}\right) - \tilde{Y}_{k_w}\tilde{J}_{error} \tag{4.18}$$

$$\tilde{J}_{error} = \sum_k \frac{\rho D}{d}\left(\tilde{Y}_{k_w} - \tilde{Y}_{k_{cl}}\right) \tag{4.19}$$

In these equations, ρ is the density, D is the binary diffusion coefficient, d is the distance from the wall to the centroid of the cell in the flow domain adjacent to the wall, and the subscript cl refers to the cell in the flow domain adjacent to the wall. $\tilde{J}_{error}$ is a correction term to ensure that the net mass diffusion is zero. Substituting Equation 4.18 into Equation 4.17 and solving for the elemental mass fraction at the wall (assuming that $\tilde{J}_{error}$ is insensitive to $\tilde{Y}_{k_w}$) yields

$$\tilde{Y}_{k_w} = \frac{\dot{m}_g''\tilde{Y}_{k_g} + \dot{m}_c''\tilde{Y}_{k_c} + \frac{\rho D}{d}\tilde{Y}_{k_{cl}}}{\dot{m}_g'' + \dot{m}_c'' + \frac{\rho D}{d} - \tilde{J}_{error}} \tag{4.20}$$

which is the desired expression giving the elemental composition at the ablating wall. However, the char mass flux $\dot{m}_c''$ remains an unknown.

Equilibrium chemistry ablation occurs when $\dot{m}_c''$ is sufficiently large to saturate the equilibrium composition adjacent to the wall with the char species (generally assumed to be carbon), i.e. $Y_c = 0$. Larger values of $\dot{m}''_c$ will super-saturate the mixture, resulting in $Y_c > 0$, but leaving the gas-phase composition unchanged. Thus, the gas-phase composition at the ablating wall can be determined by setting $\dot{m}''_c$ to a large value that will ensure super-saturation of the equilibrium solution. In this work, the char mass flux used in Equation 4.20 is computed as

$$\dot{m}''_c = \max\left(100\dot{m}''_g\,,\, 200\,{}^{\mathrm{kg}}/_{\mathrm{m^2s}}\right) \tag{4.21}$$

where the constants have been arbitrarily selected and could potentially be reduced.

Once the elemental mass fractions at the super-saturated wall have been determined, the Mutation++ library [33] is used to obtain the corresponding equilibrium solution. The saturated equilibrium composition is then obtained by setting $Y_c = 0$ and re-normalizing the gas-phase mass fractions. Solving Equation 4.20 for the char mass flux gives

$$\dot{m}''_c = \frac{\dot{m}''_g\left(\tilde{Y}_{k_g} - \tilde{Y}_{k_w}\right) - \frac{\rho D}{d}\left(\tilde{Y}_{k_w} - \tilde{Y}_{k_{cl}}\right) + \tilde{J}_{error}\tilde{Y}_{k_w}}{\tilde{Y}_{k_w} - \tilde{Y}_{k_c}} \tag{4.22}$$

where it is only necessary to use the mass fraction of a single element at the saturated wall. This method of determining $\dot{m}''_c$ is different from that used by Johnston et al. [11, 89], who instead relied on a curve fit for an equilibrium relation between gas-phase and condensed-phase carbon.

The elemental mass fractions required in these calculation can be obtained from the species mass fractions according to

$$\tilde{Y}_k = \mathscr{M}_k \sum_s \nu_{ks} \frac{Y_s}{\mathscr{M}_s} \tag{4.23}$$

where ν_{ks} is the stoichiometric coefficient giving the number of atoms of element k

present in one molecule of species s, and $\mathscr{M}$ represents molecular weight.

When calling the material response solver, the convective heat flux, char mass flux, and wall enthalpy are passed from the flow solver to the material response solver, and are assumed to vary linearly between time points. Excluding radiation (which is easily handled separately), the net heat flux to the ablating surface is computed in the material response solver as

$$\dot{q}''_{abl} = \dot{q}''_{FS} - \dot{m}''_g h_w - \dot{m}''_c h_w \tag{4.24}$$

This approach allows the pyrolysis gas mass flux (and associated heat flux) to vary in a nonlinear way between time points (while the other terms remain linear).

4.3.6 Methodology Comparison

As is shown in Section 7.4.4, the NCHF method significantly over-predicts the ablation response of the HIPPO nozzle. This is mainly because the noncatalytic wall boundary condition used in the flow solver over-predicts the heat flux to the wall of the nozzle. This is illustrated in Figure 4.4, where the convection heat flux components as computed with the NCHF and AWHF methods are compared for $t = 0.2\,\mathrm{s}$. The heat flux due to the translation-rotational and vibrational temperature gradients are similar for the two methods. However, for the AWHF method the heat flux component associated with species diffusion is negative near the throat (where ablation is occurring) and positive near the nozzle exit (where ablation is not occurring). Since (by definition) the NCHF method does not include this negative contribution from the diffusive heat flux, the total heat flux is over-predicted.

The noncatalytic wall boundary condition causes the species composition at the wall to be significantly different from the actual ablating wall composition. As a consequence, for the HIPPO nozzle the ablating wall enthalpy is greater than the

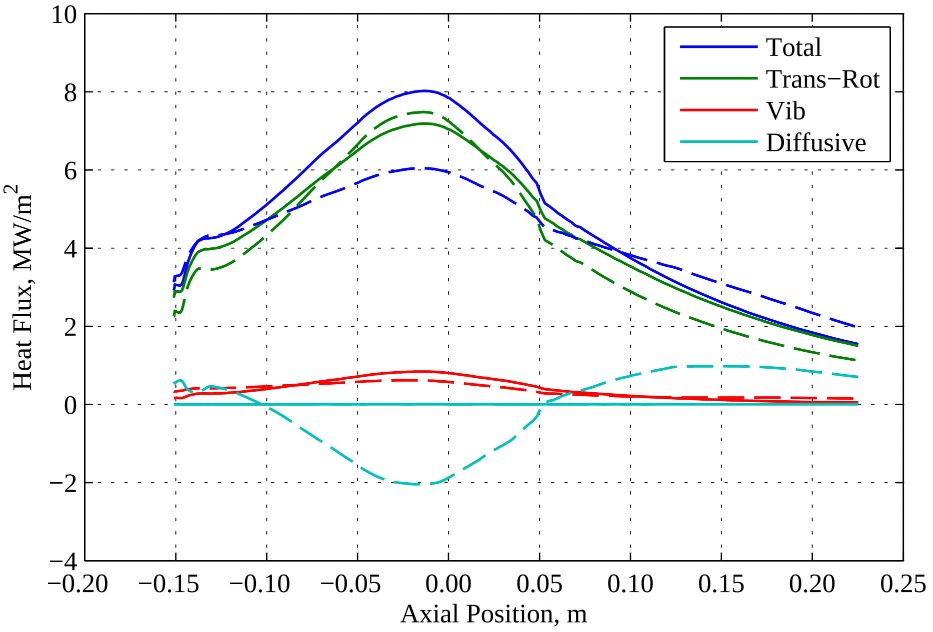

Figure 4.4: Convection heat flux components as a function of axial position for the HIPPO nozzle at $t = 0.2\,\mathrm{s}$, as computed with the NCHF method (solid lines) and the AWHF method (dashed lines).

noncatalytic wall enthalpy (see Figure 4.5). Recall Equation 3.48 suggests that heat flux should decrease as wall enthalpy increases. It is therefore reasonable to expect that the heat flux to the ablating wall should actually be less than that predicted by the noncatalytic wall. For ablation in air, the noncatalytic wall boundary condition is considered to provide the lower bound on heat flux [43], but for ablation in rocket nozzles the noncatalytic wall boundary condition appears to provide the upper bound on heat flux.

A further contributing factor to the over-prediction of the ablation response by the NCHF approach is the method used to compute the enthalpy conductance, which is required in order to use the B' tables for closure of the surface energy balance. Recall that, for the NCHF method, enthalpy conductance is computed based upon the ablating wall enthalpy (Equation 4.13). Therefore, a much larger value for enthalpy conductance is obtained than if the noncatalytic wall enthalpy was used. This is illustrated in Figure 4.6, where enthalpy conductance is computed based on the

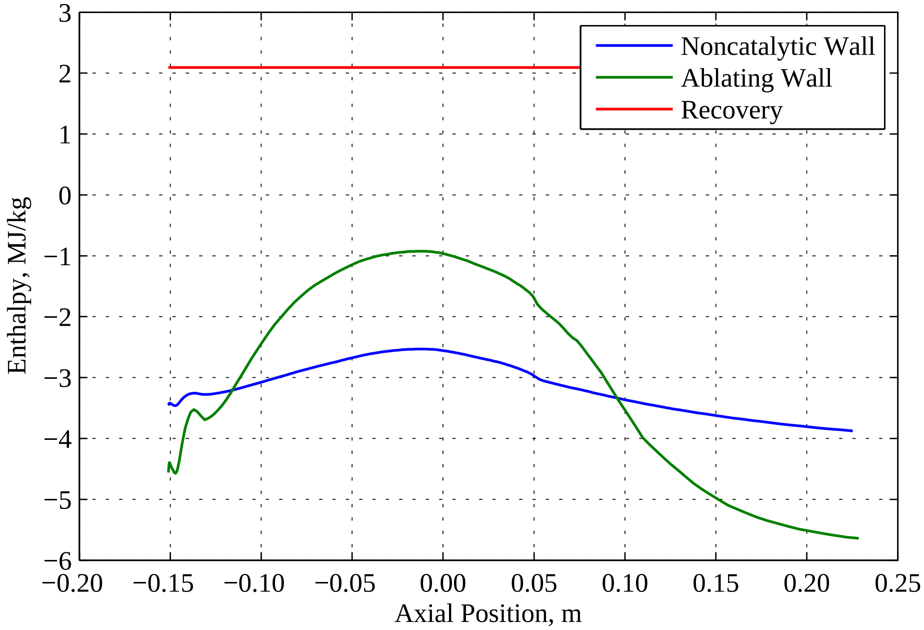

Figure 4.5: Comparison of noncatalytic wall enthalpy (from the flow solver), ablating wall enthalpy (from the B' tables), and recovery enthalpy as a function of axial position for the HIPPO nozzle at $t = 0.2\,\mathrm{s}$, as computed with the NCHF method.

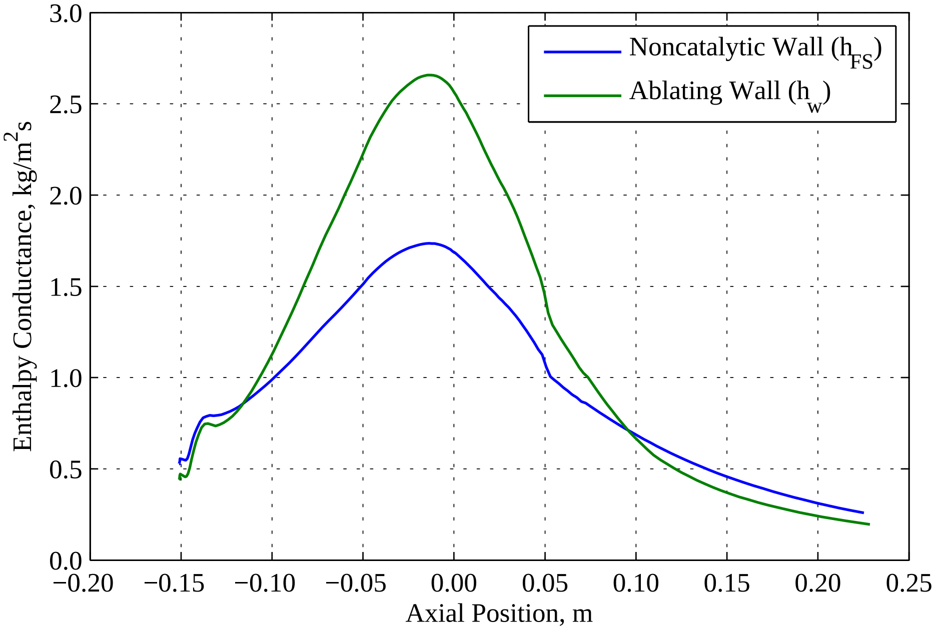

Figure 4.6: Comparison of enthalpy conductance computed based on the noncatalytic wall and ablating wall enthalpies and the total heat flux (from the NCHF method) for the HIPPO nozzle at $t = 0.2\,\mathrm{s}$.

total heat flux for the NCHF method (shown in Figure 4.4) and the two different wall enthalpies shown in Figure 4.5. Since char mass flux (and therefore recession rate) is proportional to enthalpy conductance, greater surface recession will be predicted when the noncatalytic heat flux is converted to an enthalpy conductance using the ablating wall enthalpy. Since the purpose of enthalpy conductance is to characterize a convective heating environment, enthalpy conductance should therefore always be computed using the same wall enthalpy as was used in the computation of the convection heat flux (as is the case for the other methods considered). Because of these shortcomings, the NCHF method is found to be unsuitable for modeling ablation in rocket nozzles, and its use in other applications is also questionable. The NCEC method should be preferred over the NCHF treatment.

The NCEC method is most similar to the decoupled analysis technique in that a noncatalytic wall boundary condition is used in the flow solver to obtain an enthalpy conductance, which is applied as a boundary condition in the material response solver. The NCEC method improves upon the decoupled analysis method by inherently capturing the effects of recession (changing geometry), wall temperature, and mass injection (blowing) on the convective heating. (The decoupled analysis approach largely relies on correction factors to account for these effects.) Similar to the decoupled approach, this method uses a transport coefficient assumption to adjust the convection heat flux computed by the flow solver to account for the enthalpy at the ablating wall. The NCEC method therefore does not significantly over-predict the ablation response, as is the case for the NCHF method. However, this method cannot directly capture the effects of the injection of ablation product species into the flowfield.

The AWHF and AWEC methods provide an increased level of modeling fidelity, in that the effects of ablation product species are being partially accounted for (in addition to capturing the effects of recession, wall temperature, and blowing). These two methods can inherently handle the effect that ablation product species diffusion has on the convective heating applied to the ablating wall. However, when performing the surface energy balance (specifically, when computing the heat flux due to pyrolysis gas and char mass fluxes) these approaches still make transport coefficient and unity Lewis number assumptions. This means that these methods will not be able to capture the full effect that species diffusion has on char mass flux (and hence recession rate). The only difference between these two methods is that the AWHF method passes heat flux from the flow solver to the material response solver, while the AWEC method passes enthalpy conductance. As will be shown in Section 7.4.4, these two methods produce very similar results. However, the AWEC permits larger spacing between time points, and hence more affordable conjugate simulations.

The highest level of fidelity is provided by the IESC method. With this method, the transport coefficient and unity Lewis number assumptions are not made, and precomputed B' tables are not used. Instead, the actual species diffusion at the ablating wall is used to compute the char mass flux (recession rate). Because the IESC method is directly computing mass diffusion at the ablating wall, it inherently captures the effects of a non-unity Lewis number and of chemical buffering in the boundary layer. This method can therefore fully capture the effect of ablation product species injection into the nozzle flowfield, in addition to the effects of recession, wall temperature, and blowing.

4.4 Interpolation

As mentioned previously, it is not required that the flowfield and material response meshes have coincident nodes. A scheme for interpolating values between the two meshes was implemented by Wiebenga [27]. As originally implemented, interpolation factors were computed each time that values had to be mapped between meshes (i.e. each time the material response solver was called). This technique works well so long as no gap forms between the two meshes. However, applying an under-relaxation factor to the deforming geometry, as is done in this work, causes a small gap to form between the two meshes (this gap is reduced as convergence of the conjugate solution is obtained). When this gap exists between the meshes, it is observed that the baseline interpolation scheme does not work satisfactorily; unrealistic non-smooth profiles can be produced which tend to destabilize the conjugate solution.

The solution to this issue is to compute the interpolation factors once at the beginning of the simulation based on the original, undeformed geometry. These factors are then stored and used unchanged throughout the duration of the simulation. With this approach, the interpolation scheme always yields smooth, realistic profiles, even when gaps form between the two meshes.

4.5 Smoothing

As is discussed in Section 7.4.3, when initially performing conjugate ablation simulations for the HIPPO nozzle, stability issues were encountered. In order to help resolve the instability issue encountered in this work, a smoothing algorithm employing a five-node stencil was implemented into the coupled code, following the example of Gnoffo and Johnston [89]. Nodes on the ablating boundary are ordered according to axial position. Smoothed values for a given node are obtained by averaging with the values at the two neighboring nodes on each side:

$$\xi_k = \frac{1}{5}\left(\tilde{\xi}_{k-2} + \tilde{\xi}_{k-1} + \tilde{\xi}_k + \tilde{\xi}_{k+1} + \tilde{\xi}_{k+2}\right) \tag{4.25}$$

Here ξ represents any smoothed quantity of interest, $\tilde{\xi}$ denotes the corresponding unsmoothed quantity, and the subscript k refers to the k^{th} ordered node on the ablating surface. Truncated stencils are used for the nodes near the leading and trailing edges of the ablating wall. This smoothing is applied to all variables exchanged between the solvers, except for the species mass fractions. Smoothing is also applied within the material response solver to the surface recession rate, right before the mesh deformation calculations are performed. This helps smooth geometry perturbations at the source.

This smoothing strategy has helped significantly in suppressing, but not eliminating, the instabilities. With smoothing, the instability problem has been shifted to later time points. Using a larger smoothing stencil (i.e. a seven-node stencil) could potentially delay the instabilities further, but this has not been investigated.

CHAPTER V

Reduced Reaction Mechanism

5.1 Introduction

Performing conjugate analyses of ablation in rocket nozzles requires a gas-phase reaction mechanism that includes both nozzle core flow species as well as ablation product species. The reaction mechanism proposed by Troyes et al. [92] was developed to model rocket plumes, but has been found to adequately model the nozzle flow for solid rocket motors using typical aluminized composite propellants (propellants with powdered ammonium perchlorate oxidizer and aluminum metal fuel suspended in a polymer binder). However, this mechanism does not include several species (e.g. CH_4, C_2H_2) that are important products present at the ablating surfaces of carbon-phenolic materials. Martin et al. [93] reviewed three existing mechanisms, and introduced a fourth, for modeling ablation of carbon-phenolic materials in air. Unfortunately, all of these mechanisms exclude chlorine-containing species that are important for solid rocket motor flows. Likewise, the mechanism proposed by Gökçen [94] does not contain important chlorine-containing species. Therefore, a new reduced mechanism is proposed to fill the need presented by conjugate ablation analyses.

This chapter begins with a series of studies that identify the species most relevant to the ablation of carbon-phenolic materials within solid rocket motors using aluminized composite propellants. The literature is then reviewed to identify a baseline, detailed chemical kinetics mechanism involving all relevant species. Sensitivity analyses are performed on the baseline mechanism, over a range of relevant conditions, in order to identify the key reactions and species that are important for nozzle ablation problems. The accuracy of this reduced mechanism is assessed by comparing results produced by the detailed and reduced mechanisms. The reduced mechanism identified in this effort contains 20 species and 33 reactions, and produces results in good agreement with the much larger baseline mechanism. Finally, this reduced mechanism is used to model the flow through the HIPPO nozzle; results compare favorably with those obtained using the Troyes mechanism and an equilibrium chemistry reference solution.

5.2 Species Selection

Development of the reduced reaction mechanism begins with a series of studies to determine the species most important to the ablation of carbon-phenolic materials; a study is also performed to identify important combustion products of composite solid rocket propellants.

5.2.1 Carbon-Phenolic Ablation

To identify the species relevant to ablation in rocket nozzles, a decoupled ablation analysis is performed for the HIPPO [5] nozzle, using an intermediate model similar to the improved geometric model described in Section 7.2.2. This decoupled ablation analysis is very similar to the baseline decoupled analysis discussed in detail in Section 7.3.3. Six surface probe points are spaced along the nozzle (see Figure 5.1); temperature, T, pressure, P, and non-dimensional pyrolysis gas mass flux, B'_g, are recorded as a function of time for the duration of the motor operation. From these data it is possible to determine the region of the "parameter space" in $\left(T, P, B'_g\right)$ that would be encountered by the nozzle.

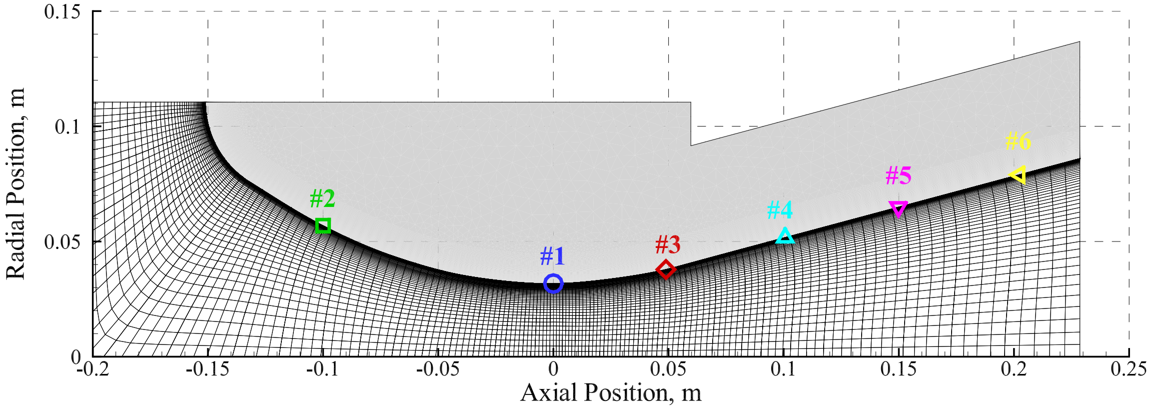

Figure 5.1: Position of the six probe points on the HIPPO nozzle.

Plots of the parameter space are given in Figure 5.2 through Figure 5.4. From Figure 5.2 it can be seen that the temperature that is experienced is fairly insensitive to the pressure, though higher pressures are generally associated with higher temperatures. From Figure 5.3 it seems that the value of B'_g that can be achieved is also fairly insensitive to pressure. However, in Figure 5.4 it can be seen that B'_g does have some dependence on temperature, e.g. for $B'_g > 0$ the temperature must be about 1000 K or greater. Also, relatively large values for B'_g are obtained for the last few time steps of the simulation (these are the more widely spaced points at lower pressures in Figure 5.3 and at higher temperatures in Figure 5.4). Note that there are a few points with $B'_g > 1$ (off the limits of these plots). At the end of the motor firing, the chamber pressure drops quickly, which also causes the enthalpy conductance (enthalpy-based heat transfer coefficient) to drop quickly. However, pyrolysis gas mass flux is driven by pyrolysis at depth, which reacts relatively slowly. Since B'_g is pyrolysis gas mass flux normalized by enthalpy conductance (see Equation 3.55), this combination of unchanged pyrolysis gas flux and dropping enthalpy conductance leads to the significantly increased B'_g values. Since these periods of large B'_g values only occur for a short period of time at the end of the simulation, they can be neglected.

Based on these plots, it is possible to establish the range of parameters for two dif-

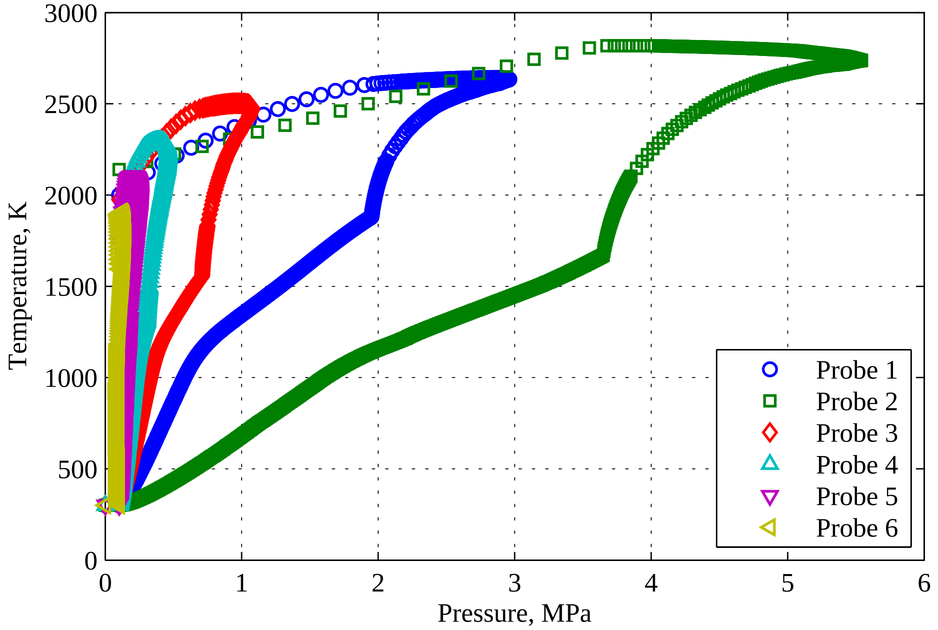

Figure 5.2: The temperature – pressure parameter space encountered by the HIPPO nozzle.

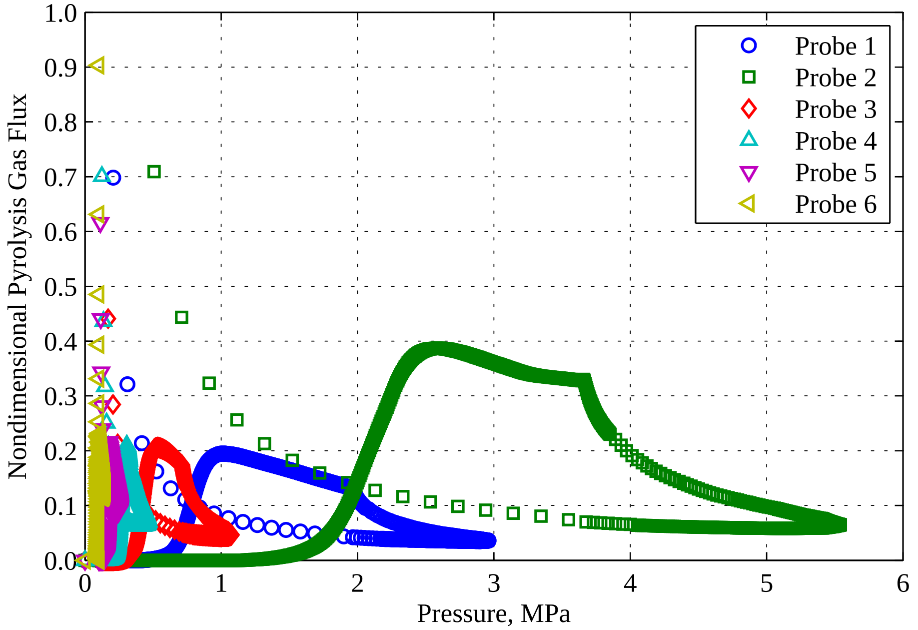

Figure 5.3: The nondimensional pyrolysis gas flux – pressure parameter space encountered by the HIPPO nozzle.

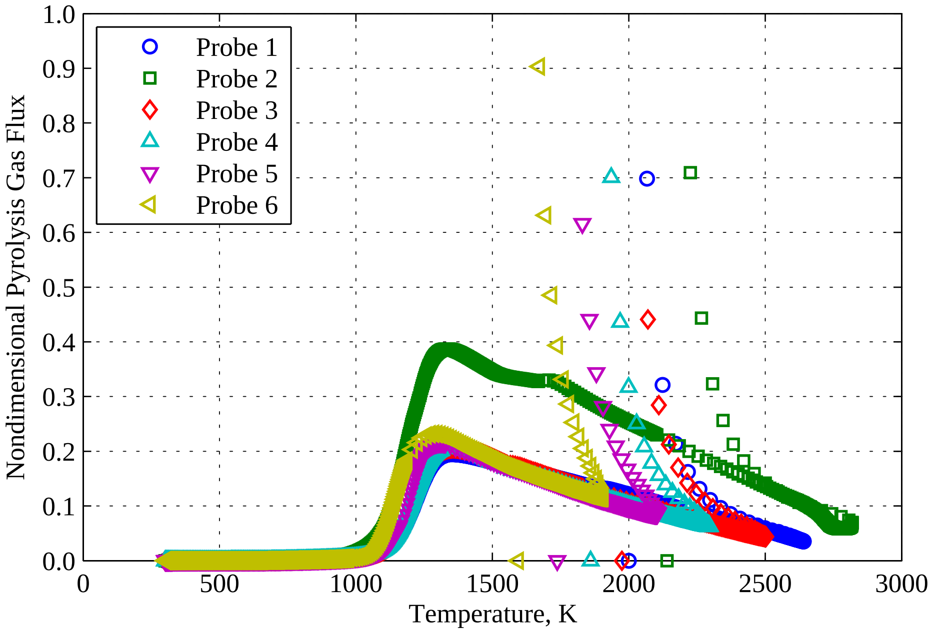

Figure 5.4: The nondimensional pyrolysis gas flux – temperature parameter space encountered by the HIPPO nozzle.

ferent studies identifying important ablation product species. Together, these studies cover virtually all of the ablating parameter space encountered by the HIPPO nozzle. The parameters for the first study, which considers the wall in the absence of pyrolysis gases, are

$$B'_g = 0$$

$$T = [300 : 100 : 3000]\ \mathrm{K}$$

$$P = [0.1, 0.2, 0.5, 1.0, 2.0, 5.0, 6.0]\ \mathrm{MPa}$$

(where the convention [initial value : increment value : final value] is used), for a total of 196 points in the parameter space. For the second study, which considers the ablating wall with and without the presence of pyrolysis gases, the parameters are

$$B'_g = [0.0, 0.001, 0.01, 0.1, 0.2, 0.3, 0.4]$$

$$T = [500 : 250 : 3000]\ \mathrm{K}$$

$$P = [0.1, 0.2, 0.5, 1.0, 2.0, 5.0, 6.0]\ \mathrm{MPa}$$

(539 points total). The Chemics [84] chemical equilibrium code (using the CEA [95] thermodynamics database) is used to compute the resultant species mass fractions for each set of conditions in these two studies. Additional inputs required by the Chemics code are the elemental composition of the boundary layer edge gases (nozzle core flow), the pyrolysis gases, and the char, obtained from Arnold et al. [5] and presented in Table B.4 in Appendix B.

5.2.2 Nozzle Core Flow

A third study is performed, to determine the relevant species within the nozzle core flow separate from ablation. The parameters for this study are

$$T = [1000 : 100 : 3500]\ \mathrm{K}$$
$$P = [0.1, 0.2, 0.5, 1.0, 2.0, 5.0, 6.0]\ \mathrm{MPa}$$

yielding 182 points. This study extends to higher temperatures to include the chamber temperature of the motor ($T_0 = 3452\,\mathrm{K}$). The Chemics program is again used to compute the species mass fractions; the elemental composition of the propellant (Table B.4) is another added input. All aluminum is assumed to react with oxygen to form condensed-phase $Al_2O_3^\star$.

5.2.3 Selected Species

The species mass fraction data produced by Chemics for each point in each study is post-processed to identify those species with mass fractions at or above a threshold value. For this work, a threshold value of 0.001 (0.1 %) is used. The error incurred by excluding species with mass fractions less than this threshold value is expected to be acceptable (errors on the order of 2 % or less are generally considered acceptable for computational fluid dynamics solutions). The number of points at which each species is identified as being significant is computed. A list is constructed for each

Table 5.1: List of important species identified for the ablating HIPPO nozzle, along with the number of points in the three studies at which they are determined to be significant. Parentheses around index number signifies species that could probably be neglected, as discussed in the text.

Index	Species	Study 1	Study 2	Study 3
1	CH_4	115	330	20
(2)	CN	1	7	–
3	CO	168	490	182
4	CO_2	95	235	182
(5)	C_2H	1	10	–
6	C_2H_2	63	225	–
(7)	C_2H_4	–	13	–
(8)	C_4H_2	7	49	–
(9)	C_6H_6	–	1	–
10	Cl	51	153	84
11	H	15	55	36
12	H_2	170	302	182
13	H_2O	99	163	182
14	HCN	97	539	–
15	HNC	49	488	–
16	HCl	196	244	182
17	N_2	196	539	182
18	NO	–	–	15
19	O	–	–	18
20	O_2	–	–	10
21	OH	–	–	56
22	$Al_2O_3^\star$	–	–	182

study, tabulating those species which are identified as being significant, along with the number of points in the study where they are deemed to be significant.

The results from these three studies are summarized in Table 5.1. A total of 22 species are identified as being potentially significant; note that $Al_2O_3^\star$ is an inert condensed-phase species. With additional consideration, several of these can be eliminated. C_6H_6 occurs at only one point (at low pressure, and with a mass fraction equal to the threshold value of 0.001), so can easily be eliminated. C_4H_2 occurs at a few points for the two ablation studies, but only at the highest temperature (3000 K), and with a relatively small mass fraction of 0.0022 or less. Since this temperature is never quite reached in the HIPPO analysis, this species can also be eliminated. Similarly, C_2H only occurs at a few points, again only at 3000 K, and with mass fractions of 0.0017 or less; it can also be neglected. CN also only occurs at only a few points, at the lowest pressure and the highest temperature, with a small mass fraction of 0.0011; it can be neglected as well. Finally, C_2H_4 occurs only at a few points, at the highest value considered for B'_g (0.4), but for a range of pressures and temperatures. Predicted mass fraction is relatively small, at 0.0022 or less. Removal of this species is not so easy to justify as for some of the others, but the small mass fraction suggests that it could be removed with the introduction of minimal error.

5.3 Reduced Model

With the important species identified, it is possible to simplify a detailed chemical kinetics mechanism into a reduced model. Mechanism reduction is guided by sensitivity analyses to eliminate those reactions that have minimal impact on the parameters of interest.

5.3.1 Baseline Mechanism

A literature survey is performed in order to identify an existing mechanism that could potentially be used to model the species identified as being important. One mechanism that has been used in the literature[96, 97, 98] to model the combustion of composite solid rocket propellants is the "reduced Jeppson" mechanism [99] as presented by Gross[100] and by Felt [101]. Results presented by Jeppson [99] indicate that simulations utilizing this mechanism can predict flame temperature profiles and propellant burning rates with good agreement to experimental data. This baseline mechanism features the 127 reactions listed in Table D.1 in Appendix D involving 37 gas-phase species:

$$\begin{multlined}\mathrm{C_2H_2, C_2H_3, C_2H_4, C_4H_6, CH_2O, CH_2, CH_3, CH_4, CO, CO_2, Cl, Cl_2,} \\ \mathrm{ClO, ClO_2, ClO_3, ClOH, H, H_2, H_2O, HCN, HCO, HCl, HClO_4, HNO,} \\ \mathrm{HO_2, N, N_2, N_2H_2, N_2O, NH, NH_2, NH_3, NO, NO_2, O, O_2, OH}\end{multlined}$$

This baseline mechanism includes all gas-phase species identified in this work as being important for ablation of rocket nozzles (except for HNC).

While this baseline mechanism is small enough that it could conceivably be used directly in flow computations supporting ablation analyses (at significant computational cost), it contains a number of large species that are unimportant for post-combustion nozzle flow. By removing these unnecessary species and associated reactions, a smaller and more efficient mechanism can be produced that allows the flow computations to be completed much more quickly.

5.3.2 Mechanism Reduction

The baseline mechanism is simplified based upon the results of sensitivity analyses performed using SENKIN [102], a tool distributed with the CHEMKIN program [103], following the same general methodology utilized by Gökçen [94] and Martin et al. [93]. SENKIN is used to compute the temperature and mass fraction histories for a homogeneous reacting mixture under adiabatic, constant pressure conditions. The first-order sensitivity coefficients (as computed from a linear sensitivity analysis) of the temperature and select species mass fractions with respect to the reaction rates are also output as functions of time. The normalized coefficient representing the sensitivity of parameter ξ with respect to reaction r is given by

$$S_{\xi,r} = \frac{k_r \frac{\partial \xi}{\partial k_r}}{\xi_{max}} \tag{5.1}$$

where the normalization factor ξ_{max} is the maximum value achieved for the parameter of interest over the course of the simulation. Temperature and the mass fractions for CO, CO_2, H_2O, HCl, CH_4, and C_2H_2 are assumed to be the relevant parameters for the nozzle ablation problem. The numerator of Equation (5.1) is a quantity obtained directly from SENKIN. The normalized sensitivity coefficient indicates the relative importance of a given reaction to changes to the parameter of interest (e.g. the mass fraction of a given species). Species mass fraction predictions are strongly affected by those reactions with large sensitivity coefficients; it is important to retain these reactions in the reduced mechanism. Reactions with relatively low sensitivity coefficients are candidates for removal from the mechanism, since the impact of these reactions on the parameters of interest will be small.

The sensitivity analysis is performed for the relevant portion of the nozzle parameter space in two studies. The first study considers flow through the nozzle in the absence of ablation; the parameter space for this study is

$$T = [1000 : 500 : 3500]\ \text{K}$$

$$P = [0.1, 0.2, 0.5, 1.0, 2.0, 5.0, 6.0]\ \text{MPa}$$

Table 5.2: Species mass fractions for mixtures representing the nozzle boundary layer edge gases (propellant gas-phase combustion products), the pyrolysis gases, and the char for the HIPPO nozzle, for use in computing initial compositions for sensitivity studies.

Species	Edge Gas	Pyrolysis Gas	Char
HCl	0.31138	0.0	0.0
CO_2	0.29469	0.38968	0.0
N_2	0.12603	0.0	0.0
H_2O	0.15891	0.0	0.0
CH_4	0.10900	0.34412	-0.44506
C_2H_2	0.0	0.26620	1.44506

for a total of 42 points. The second study considers the ablating wall; the parameter space for this study is

$$B'_g = [0.0, 0.1, 0.2, 0.3, 0.4]$$
$$T = [1000 : 500 : 3000]\ \mathrm{K}$$
$$P = [0.1, 0.2, 0.5, 1.0, 2.0, 5.0, 6.0]\ \mathrm{MPa}$$

for 175 points total. Initial species mass fractions are computed by appropriately mixing species sets representing the nozzle boundary layer edge gases, the pyrolysis gases, and the char material (see Table 5.2). The nozzle boundary layer edge gas species representation is the equilibrium composition at $T = 300\,\mathrm{K}$ and $P = 0.1\,\mathrm{MPa}$, as computed by Chemics assuming that the only participating species are HCl, CO_2, N_2, H_2O, and CH_4. Similarly, the pyrolysis gas representation is the equilibrium composition at the same conditions, assuming that the only participating species are C_2H_2, CH_4, and CO_2. Char is assumed to be purely carbon, which is modeled as an injection of C_2H_2 combined with a subtraction of an appropriate amount of CH_4 to ensure no net hydrogen addition.

Initial species mass fractions for each point in these studies are computed as a function of B'_g, B'_c, and these three species sets according to [90, 91]

$$Y_s = \frac{Y_{s_e} + B'_g Y_{s_g} + B'_c Y_{s_c}}{1 + B'_g + B'_c} \tag{5.2}$$

In this equation, Y_s represents the mass fraction of of species s; the subscripts e, g, and c refer to the boundary layer edge, the pyrolysis gases, and the char, respectively. B'_c for each point in the study is determined as a function of T, P, and B'_g from pre-computed B' tables.

The species mass fraction history data from each simulation in these studies are post-processed to identify all species that achieve a mass fraction greater than a threshold value (0.001 is used in this effort) at any time. In this way, it is possible to identify important species as predicted by the baseline mechanism. Representative mass fraction histories for a selection of the most important species are presented in Figure 5.5. The normalized sensitivity coefficients from these studies are used to identify and select the most important reactions. Reactions that have a sensitivity coefficient greater than 1% of the maximum sensitivity predicted are selected as being important (this is the same criterion used by Martin et al. [93]). A representative sensitivity coefficient history is presented in Figure 5.6; only reactions identified as being significant are included. Finally, any additional species required as participants in these important reactions are identified.

By collating the important species and reactions across all points in the parameter space explored in these sensitivity studies, a minimal essential set of species and reactions that can accurately model the post-combustion nozzle core flow and ablation products over the conditions of interest can be assembled. The sensitivity analysis identifies reactions involving several “large” hydrocarbon species (i.e. C_2H_3, C_2H_4, and C_4H_6). However, these species and associated reactions are eliminated since the equilibrium chemistry analysis preceding the sensitivity study suggests that these species are unimportant. Comparisons of the reduced mechanism with and without

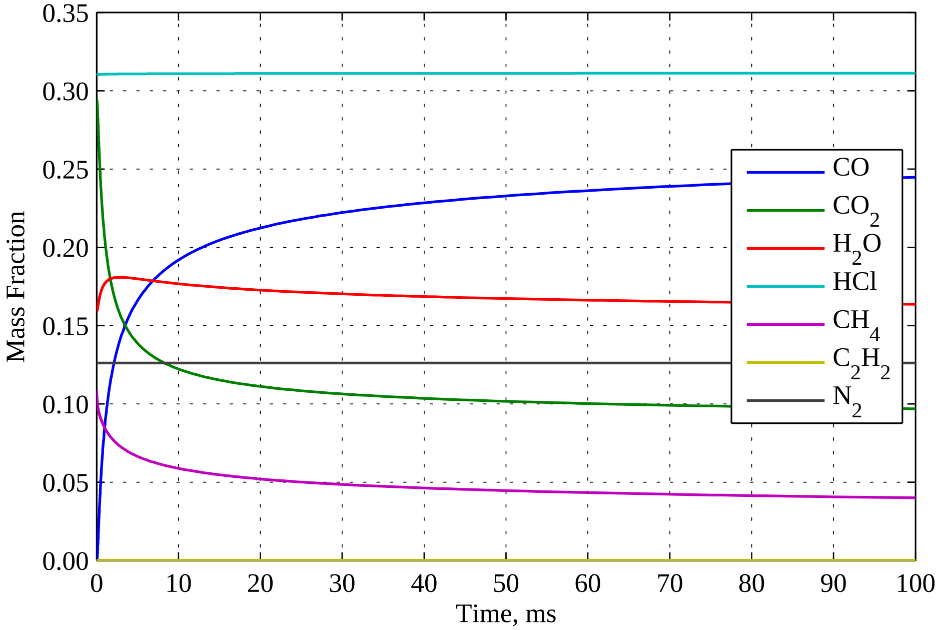

Figure 5.5: Mass fractions for select species as a function of time, as computed in the SENKIN analysis for a non-ablating case with $T = 2500\,\mathrm{K}$ and $P = 0.5\,\mathrm{MPa}$.

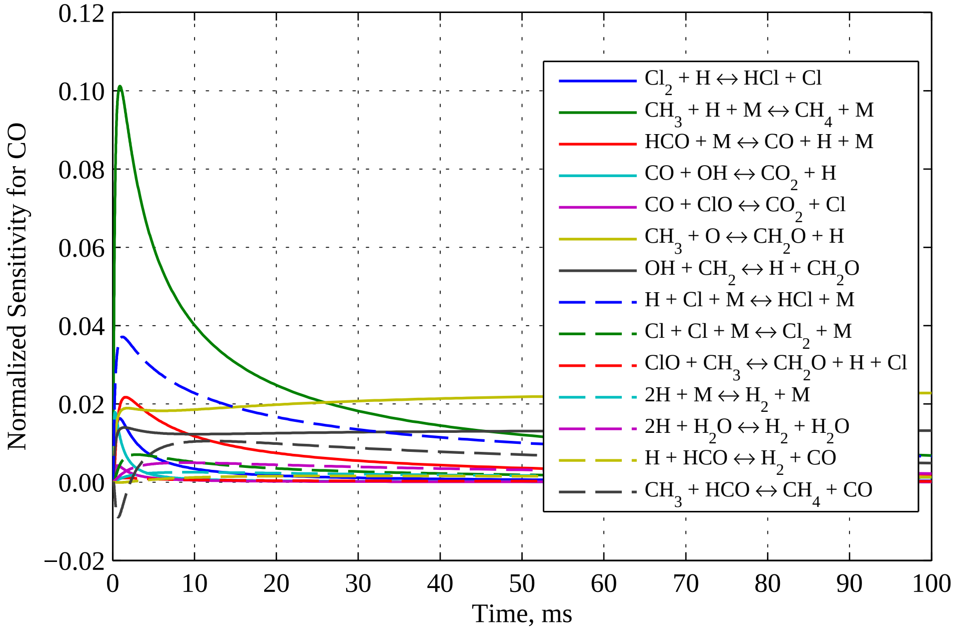

Figure 5.6: Normalized sensitivity coefficient for CO for a non-ablating case with $T = 2500\,\mathrm{K}$ and $P = 0.5\,\mathrm{MPa}$. Only reactions with a sensitivity coefficient greater than $1\,\%$ of the maximum sensitivity are plotted.

these reactions indicates that removing these reactions and species has negligible impact on the results. The preliminary reduced mechanism identified here is presented in Table 5.3, and features 33 reactions involving 18 gas-phase species. (Note that N_2 is an inert gas-phase species and only participates in reactions as a collision partner. $Al_2O_3^\star$ can be included as an inert condensed-phase species, but does not participate in the reactions in any way). Reaction rates are computed using a modified Arrhenius equation:

$$k = AT^b \exp\left(-T_a/T\right) \tag{5.3}$$

The statements such as "CH_4 enhanced by 2.0" indicate that the reaction rate is increased by the given factor (e.g. 2.0) when the given species (e.g. CH_4) acts as a collision partner.

Table 5.3: Forward reaction rates for the reduced mechanism identified in this work.

Index	Reaction	A, mol − cm − s	b	T_a, K
1	$Cl_2 + H \rightleftharpoons HCl + Cl$	8.40×10^{13}	0	578.70
2	$H_2 + OH \rightleftharpoons H_2O + H$	2.16×10^{8}	1.51	1726.04
3	$C_2H_2 + OH \rightleftharpoons CH_3 + CO$	4.84×10^{-4}	4	-106.44
4	$CH_4 + Cl \rightleftharpoons CH_3 + HCl$	2.50×10^{13}	0	1927.33
5	$CH_4 + H \rightleftharpoons CH_3 + H_2$	6.60×10^{8}	1.62	5454.90
6	$CH_4 + OH \rightleftharpoons CH_3 + H_2O$	1.00×10^{8}	1.6	1570.05
7	$CH_3 + H + M \rightleftharpoons CH_4 + M$	1.27×10^{16}	-0.63	192.73
		CH_4 enhanced by 2.0		
		CO enhanced by 1.5		
		CO_2 enhanced by 2.0		
		H_2 enhanced by 2.0		
		H_2O enhanced by 6.0		

Index	Reaction	A, mol − cm − s	b	T_a, K
8	$HCO + M \rightleftharpoons CO + H + M$	1.87×10^{17}	-1	8554.73
		CH_4 enhanced by 2.0		
		CO enhanced by 1.5		
		CO_2 enhanced by 2.0		
		H_2 enhanced by 2.0		
		H_2O enhanced by 0.0		
9	$CO + OH \rightleftharpoons CO_2 + H$	4.76×10^{7}	1.23	35.23
10	$CO + ClO \rightleftharpoons CO_2 + Cl$	3.00×10^{12}	0	503.22
11	$C_2H_2 + O \rightleftharpoons CH_2 + CO$	1.02×10^{7}	2	956.12
12	$CH_2 + H_2 \rightleftharpoons CH_3 + H$	5.00×10^{5}	2	3638.28
13	$CH_2 + H + M \rightleftharpoons CH_3 + M$	2.50×10^{16}	-0.8	0
		CH_4 enhanced by 2.0		
		CO enhanced by 1.5		
		CO_2 enhanced by 2.0		
		H_2 enhanced by 2.0		
		H_2O enhanced by 6.0		
14	$CH_4 + O \rightleftharpoons CH_3 + OH$	1.02×10^{9}	1.5	301.93
15	$CH_3 + O \rightleftharpoons CH_2O + H$	8.43×10^{13}	0	0
16	$CH_2 + O \rightleftharpoons H + HCO$	8.00×10^{13}	0	0
17	$OH + CH_3 \rightleftharpoons CH_2 + H_2O$	5.60×10^{7}	1.6	2727.45
18	$OH + CH_2 \rightleftharpoons H + CH_2O$	2.00×10^{13}	0	0

Index	Reaction	A, mol − cm − s	b	T_a, K
19	$\mathrm{H + Cl + M \rightleftharpoons HCl + M}$	5.30×10^{21}	-2	-1006.44
		CH_4 enhanced by 2.0		
		CO enhanced by 1.5		
		CO_2 enhanced by 2.0		
		H_2 enhanced by 2.0		
20	$\mathrm{Cl + Cl + M \rightleftharpoons Cl_2 + M}$	3.34×10^{14}	0	-905.80
		CH_4 enhanced by 2.0		
		CO enhanced by 1.5		
		CO_2 enhanced by 2.0		
		H_2 enhanced by 2.0		
21	$\mathrm{Cl + CH_2O \rightleftharpoons HCO + HCl}$	5.00×10^{13}	0	251.61
22	$\mathrm{ClO{+}CH_3 \rightleftharpoons CH_2O{+}H{+}Cl}$	3.33×10^{11}	0.46	15.10
23	$\mathrm{ClO + CH_3 \rightleftharpoons CH_2O + HCl}$	3.47×10^{18}	-1.8	1041.66
24	$\mathrm{H + HCl \rightleftharpoons Cl + H_2}$	7.94×10^{12}	0	1710.95
25	$\mathrm{HCl + O \rightleftharpoons Cl + OH}$	2.30×10^{11}	0.64	452.90
26	$\mathrm{2H + M \rightleftharpoons H_2 + M}$	1.00×10^{18}	-1	0
27	$\mathrm{2H + H_2 \rightleftharpoons 2H_2}$	9.00×10^{16}	-0.6	0
28	$\mathrm{2H + H_2O \rightleftharpoons H_2 + H_2O}$	6.00×10^{19}	-1.25	0
29	$\mathrm{H + HCO \rightleftharpoons H_2 + CO}$	7.34×10^{13}	0	0
30	$\mathrm{OH + OH \rightleftharpoons H_2O + O}$	6.00×10^{8}	1.3	0
31	$\mathrm{CH_2 + CH_4 \rightleftharpoons 2CH_3}$	2.46×10^{6}	2	4161.63
32	$\mathrm{CH_3 + HCO \rightleftharpoons CH_4 + CO}$	2.65×10^{13}	0	0
33	$\mathrm{CH_3{+}CH_2O \rightleftharpoons HCO{+}CH_4}$	3.32×10^{3}	2.81	2948.87

5.3.3 Evaluation of Reduced Mechanism

Accuracy of the reduced mechanism is assessed by repeating the SENKIN simulations, only using the reduced mechanism instead of the full mechanism. The temperature and mass fraction histories (for the species CO, CO_2, H_2O, HCl, CH_4, and C_2H_2) as predicted by the baseline and reduced mechanisms are compared and root mean square (RMS) differences are computed.

For the non-ablating nozzle flow study at elevated temperatures ($T > 1000\,\mathrm{K}$), excellent agreement is achieved between the reduced and the baseline mechanism. RMS differences do not generally exceed 1 %, and for most species and points in the study the RMS difference does not exceed 0.1 %. However, at the lowest temperature considered ($T = 1000\,\mathrm{K}$) very large RMS differences (exceeding 40 %) are encountered for CO and C_2H_2 (see Figure 5.7). To understand this further, the CO mass fraction as computed by the two mechanisms is presented in Figure 5.8 as a function of time for $P = 0.5\,\mathrm{MPa}$. While these differences seem dramatic, there are several indications suggesting that they are not that significant. First, the mass fraction for CO at this condition is always very small (less than 4.5×10^{-6}). Also, the time scale for this simulation is very long (on the order of hours) while the time scale for flow through the nozzle is very small (on the order of a few milliseconds). Additionally, the agreement between the two mechanisms is very good at the shorter timescales. Similar conclusions can be drawn for C_2H_2, but for this species the mass fractions are even smaller (1.0×10^{-14}). Therefore, it can be concluded that the reduced mechanism can model nozzle core flow conditions with negligible differences from the baseline mechanism.

For the study including ablation products, very good agreement is also obtained between the baseline and reduced mechanism at higher temperatures ($T > 1500\,\mathrm{K}$). RMS differences are generally less than 2 % for most species (often significantly less), though RMS differences as high as 6 % are encountered for C_2H_2. At lower temper-

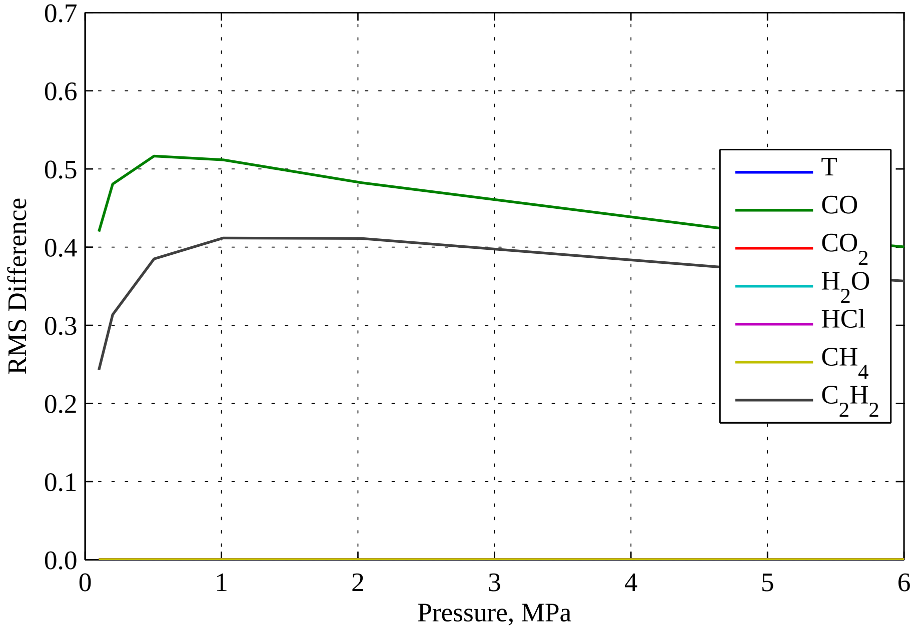

Figure 5.7: RMS difference between the results predicted by the baseline and reduced mechanisms as a function of pressure for a non-ablating case with $T = 1000\,\mathrm{K}$.

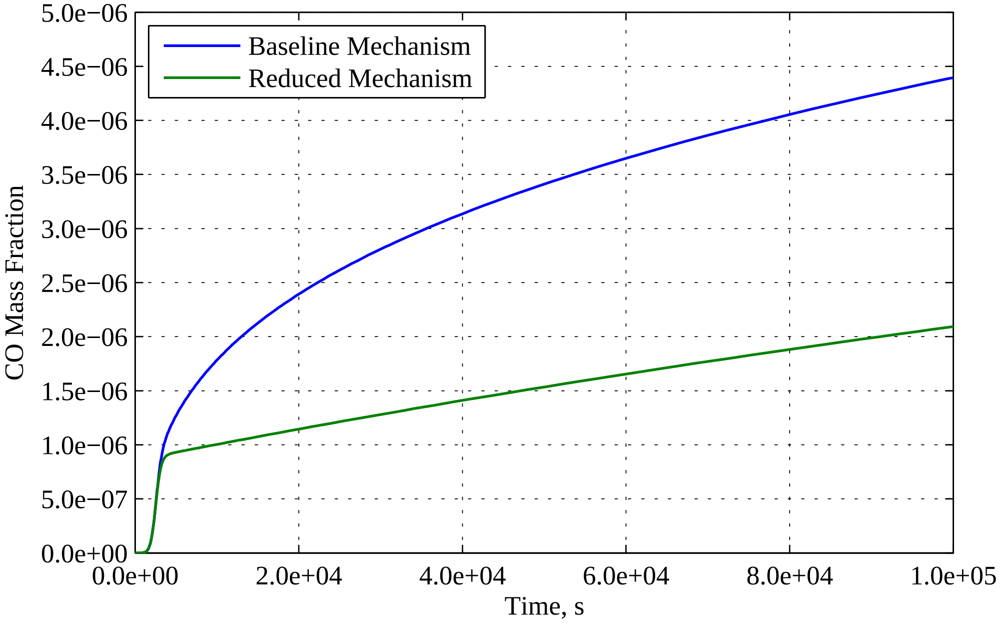

Figure 5.8: CO mass fraction history as predicted by the baseline and reduced mechanisms for a non-ablating case with $T = 1000\,\mathrm{K}$ and $P = 0.5\,\mathrm{MPa}$.

atures ($T = 1500\,\mathrm{K}$), larger differences are obtained for CO (up to 8 %) and C_2H_2 (up to 16 %), as illustrated in Figure 5.9. The CO mass fraction as computed by the two mechanisms is presented in Figure 5.10 as a function of time for $P = 0.1\,\mathrm{MPa}$ and $B'_g = 0.0$. Here the CO mass fraction is quite significant, so these differences cannot be dismissed quite so easily. However, the general trends and final values are the same for both mechanisms; only a small shift in time is observed, but this occurs at time scales much longer than would be experienced in a nozzle application. The same conclusions can be drawn for C_2H_2.

This reduced mechanism is further evaluated by investigating the ability of this reduced species set to produce accurate B' (surface energy balance) tables. B' tables are computed using the Chemics code two different ways: without restriction on the species (i.e. using all the species in the underlying thermodynamic database), and with only the 18 gas-phase species in the initial reduced mechanism. These two B' tables are compared in Figure 5.11, where it can be seen that there are significant differences for $T > 2000\,\mathrm{K}$. Clearly, using only these 18 gas-phase species is not sufficient for modeling ablation. This discrepancy is largely due to the absence of HCN, which was identified in 5.2.3 as being a potentially important species, from the reduced mechanism. When HCN is added to the reduced mechanism as an inert species, much better agreement is obtained for the B' tables (see Figure 5.11). The accuracy thus achieved is believed to be acceptable; further improvement can only be made by the addition of multiple species, which comes at significant computational cost.

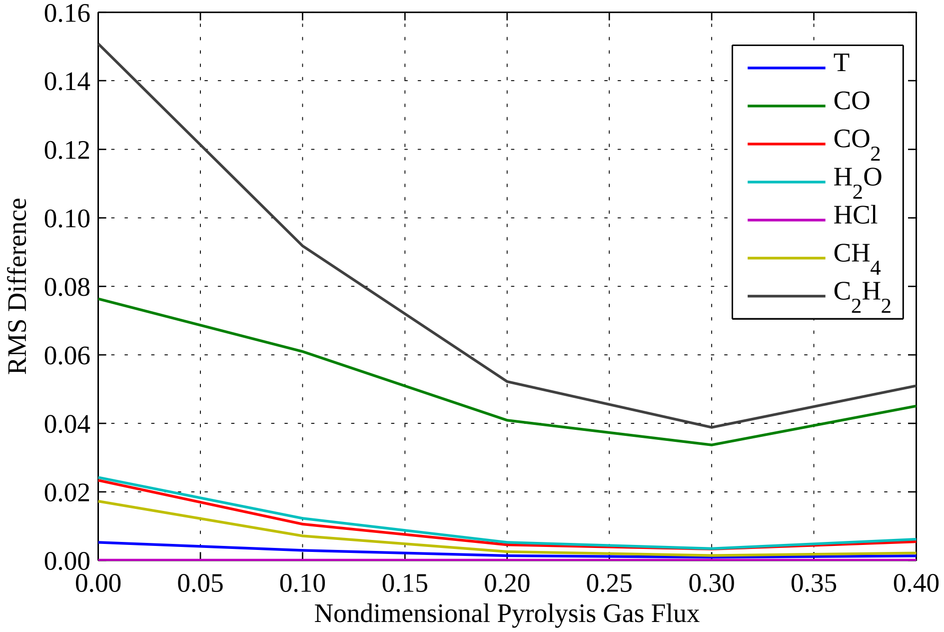

Figure 5.9: RMS difference between the results predicted by the baseline and reduced mechanisms as a function of nondimensional pyrolysis gas flux for an ablating case with $T = 1500\,\mathrm{K}$ and $P = 0.1\,\mathrm{MPa}$.

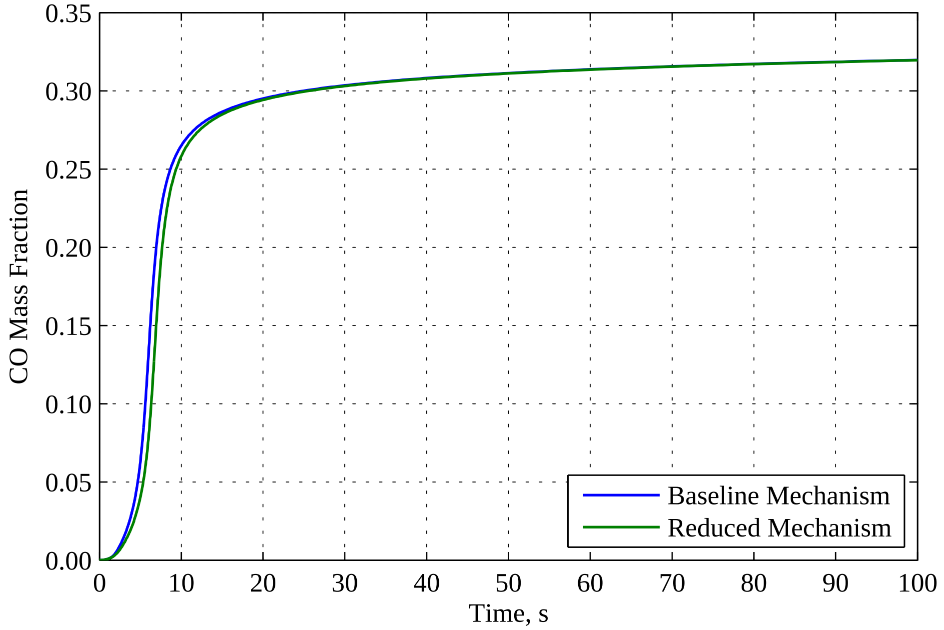

Figure 5.10: CO mass fraction history as predicted by the baseline and reduced mechanisms for an ablating case with $T = 1500\,\mathrm{K}$, $P = 0.1\,\mathrm{MPa}$, and $B'_g = 0.0$.

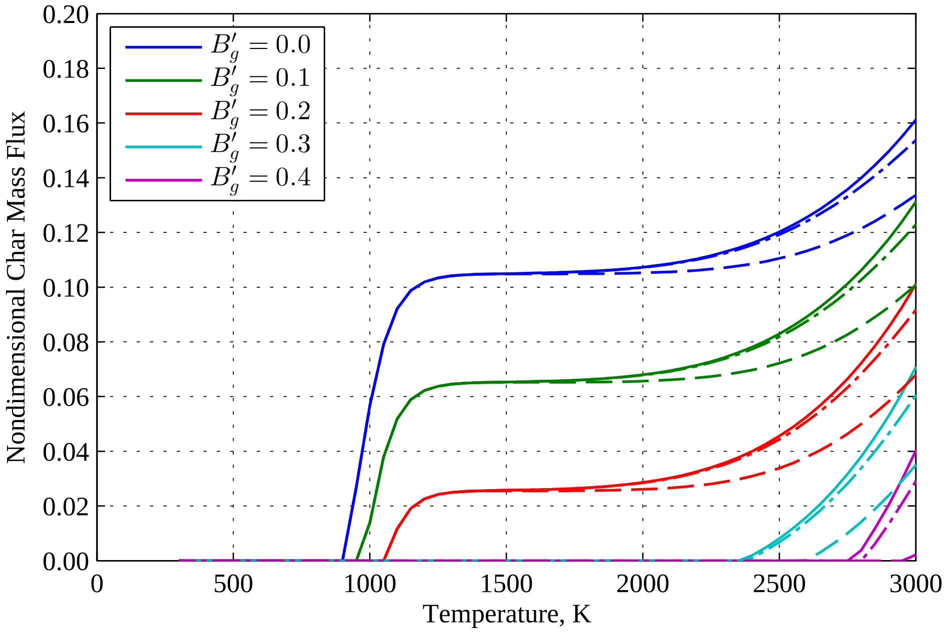

Figure 5.11: Comparison of B' tables computed using three different species sets, for $P = 0.1\,\mathrm{MPa}$. Solid lines represent results computed using all relevant species from the CEA thermodynamics database; dashed lines represent results computed using only the 18 gas-phase species initially identified as part of the mechanism reduction effort; dash-dotted lines represent results computed using these 18 species plus HCN.

5.3.4 Final Reduced Mechanism

The final reduced mechanism comprises the 33 reactions listed in Table 5.3 and 20 species:

$$\mathrm{C_2H_2, CH_2O, CH_2, CH_3, CH_4, CO, CO_2, Cl, Cl_2, ClO,}$$
$$\mathrm{H, H_2, H_2O, HCN, HCO, HCl, N_2, O, OH, Al_2O_3^{\star}}$$

Note that N_2 and HCN are inert gas-phase species (participating in reactions only as collision partners), while $Al_2O_3^{\star}$ is an inert condensed-phase species (and does not participate even as a collision partner). The evaluation presented in 5.3.3 suggests that the reduced mechanism identified here adequately reproduces predictions obtained with the baseline mechanism, and is sufficient for use in conjugate flowfield /

ablation simulations of carbon-phenolic nozzles for solid rocket motors using typical aluminized composite propellants. At higher temperatures there is negligible difference in the results between the two mechanisms. While the differences are larger at lower temperatures, these are judged to be acceptable, especially considering that low temperatures are only encountered in small regions of the flowfield (near the wall) for very short periods of time at the start of motor operation. Since the reduced mechanism includes approximately half the species and one quarter the number of reactions present in the baseline mechanism, flowfield calculations utilizing the reduced mechanism will require significantly less computational resources and time for completion.

CHAPTER VI

Code Verification & Validation Studies

6.1 Introduction

Before relying on the results produced by any analysis code, it is necessary to confirm that the algorithms utilized by the code have been implemented correctly and that they accurately reflect the physics being modeled. This involves two closely related tasks: verification and validation. Verification is the process of ensuring that the algorithms have been implemented correctly, while the process of validation ensures that these algorithms produce results consistent with reality.

In this work, a number of test cases are simulated in order to verify and validate the new features that have been added to the LeMANS flow solver and the MOPAR-MD material response solver. Verification is achieved through the favorable comparison of results to those obtained with other analysis codes or to analytical solutions, while validation is achieved through the favorable comparison to experimental data, when available. The verification and validation discussed in this chapter builds upon the rigorous verification study performed by Wiebenga [27] using the method of manufactured solutions.

6.2 Flow Solver

To ensure that the new capabilities added to the LeMANS flow solver have been correctly implemented, a series of simulations is performed for a wide range of test cases. Comparisons are made to results from other codes, to theoretical values, and/or to experimental data, depending on the test case. These test cases are discussed in the following sections. The good agreement achieved with these test cases indicates that the LeMANS flow solver can be used to accurately predict the turbulent, particle-laden flowfield within rocket nozzles.

6.2.1 Flat Plate at High Mach Number

The simplest test case considered for verifying the turbulence model implementation is the zero pressure gradient flat plate at high Mach numbers. Meshes, conditions, and comparison data are obtained from the NASA Turbulence Modeling Resource website [104]. The flat plate is two meters long; the flow domain is one meter high and includes a run-in region 0.33 meters in length upstream of the plate leading edge. Five different meshes are considered; for the $M = 2.0$ case comparisons are presented for the finest mesh (545 points in the axial direction by 385 points in the wall-normal direction), while for the $M = 5.0$ cases comparisons are presented for the second-finest mesh (273×193 points). Biasing is used to cluster the mesh near the wall and near the plate leading edge. The flow has a unit Reynolds number of $1.5 \times 10^7\,{}^1\!/\mathrm{m}$, a free stream temperature of $T_\infty = 300.33\,\mathrm{K}$, and is modeled using a non-reacting mixture of N_2 and O_2.

For the $M = 2.0$ test case, the ratio of the wall temperature to the free stream temperature is $\frac{T_w}{T_\infty} = 1.712$, meaning that the wall is approximately adiabatic. Simulations are performed for both the BSL and SST turbulence models, using both the standard and vorticity-based production terms. Simulations for this test case using the vorticity-based production term are labeled with the “-V” suffix in the plots. Skin friction coefficient is plotted as a function of momentum thickness Reynolds number, Re_θ, in Figure 6.1; comparisons are made to results obtained with CFL3D (using the SST model) and to the van Driest correlation [105]. The skin friction predictions follow the expected trends, but are higher than the reference data. For the range of Re_θ shown in these plots, the root mean square (RMS) error relative to the van Driest correlation is 11.6 % for the BSL model and 9.0 % for the SST model. The cause for this discrepancy is unknown. The BSL model predicts slightly higher friction than the SST model, but there is no observable difference between the two production term variants. The velocity profiles at the axial station corresponding to $\mathrm{Re}_\theta = 1.0 \times 10^4$ are plotted in Figure 6.2; the results obtained with LeMANS are in excellent agreement with law-of-the-wall theory and the CFL3D results. For $y^+ < 500$, the RMS error relative to the theoretical profile is 2.9 % for the BSL model and 4.1 % for the SST model. When the wake region is neglected (i.e. for $y^+ < 100$), these errors drop to 0.9 % and 1.3 %, respectively. Relative to the CFL3D results, for $y^+ < 500$, the errors are 0.5 % and 0.7 %, respectively.

For the $M = 5.0$ test case, three different wall temperatures are considered: $\frac{T_w}{T_\infty} = 1.090$, 2.725, and 5.450 (approximately adiabatic). Simulations are performed for both the BSL and SST turbulence models, using only the vorticity-based production term. Skin friction coefficient is plotted in Figure 6.3; again it is observed that there is good agreement with the reference data, and that the BSL model predicts slightly greater friction than the SST model. For the range of Re_θ shown in these plots, the RMS error relative to the van Driest correlation is less than 6.7 % for the BSL model and below 3.3 % for the SST model. The velocity profiles corresponding to $\mathrm{Re}_\theta = 1.0 \times 10^4$ are plotted in Figure 6.4; good agreement is obtained between the LeMANS results and the reference solutions. For $y^+ < 500$, the RMS error relative to the theoretical profile is below 7.2 % for the BSL model and 7.9 % for the SST model. Relative to the CLF3D results, these errors drop to 2.2 % and 1.9 %, respectively.

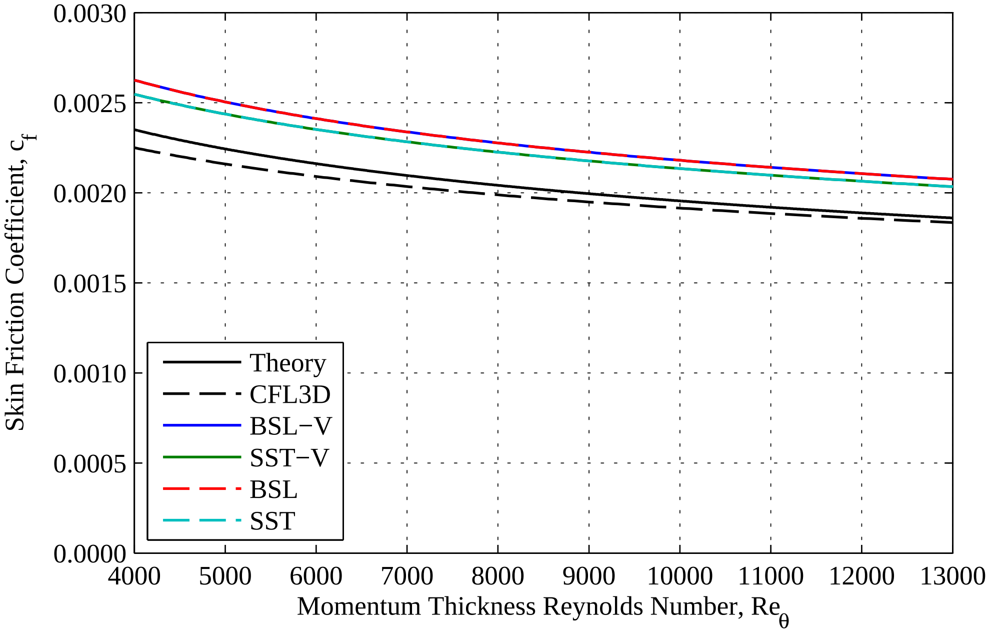

Figure 6.1: Comparison of skin friction coefficient for the $M = 2.0$ flat plate test case.

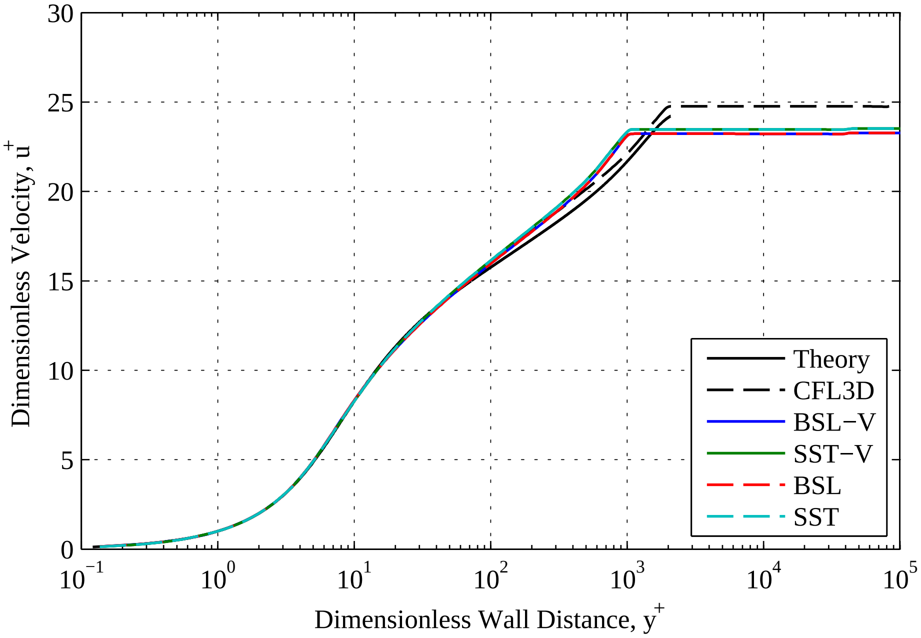

Figure 6.2: Comparison of law-of-the-wall velocity profile for the $M = 2.0$ flat plate test case.

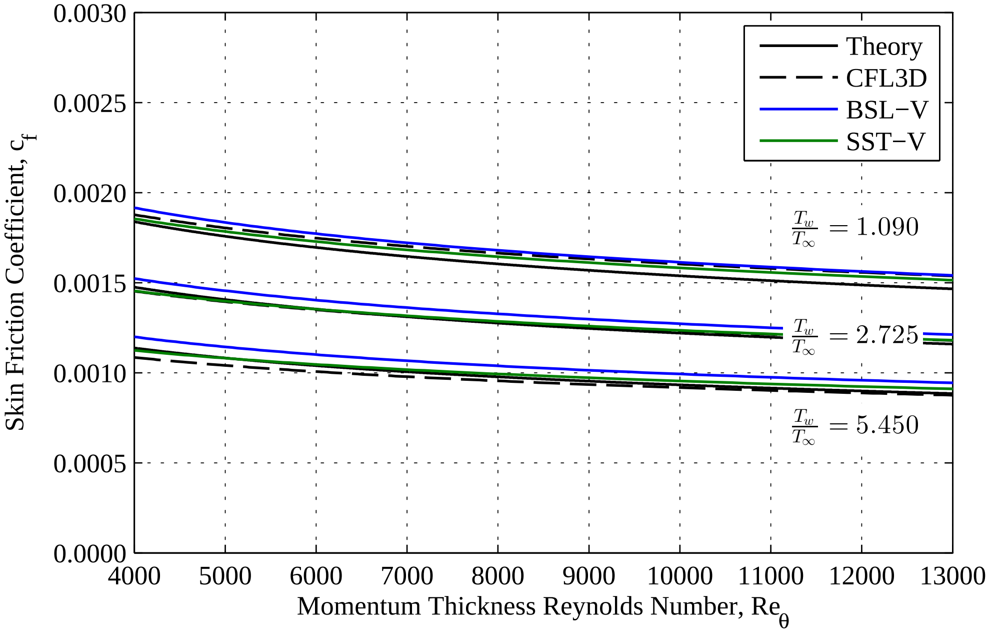

Figure 6.3: Comparison of skin friction coefficient for the $M = 5.0$ flat plate test case.

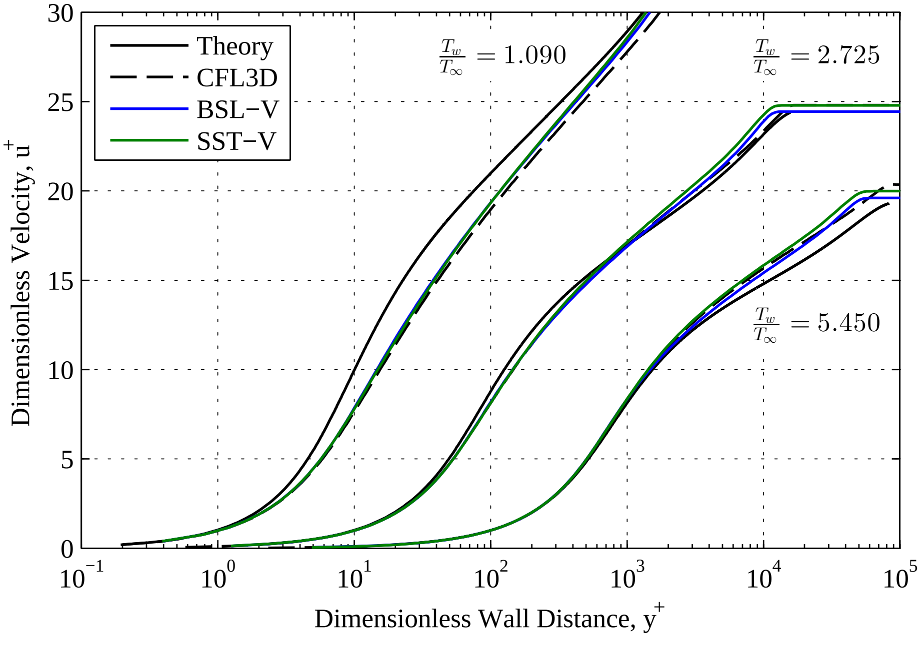

Figure 6.4: Comparison of law-of-the-wall velocity profile for the $M = 5.0$ flat plate test case. Note that profiles for larger values of $\frac{T_w}{T_\infty}$ have been shifted right by orders of magnitude for clarity.

6.2.2 Flat Plate with Mass Injection

In order to verify that the blowing wall boundary condition is correctly implemented for the specific dissipation equation, simulations using the BSL turbulence model are performed for two different flat plate test cases with mass injection. These test cases also provide validation of the turbulence model implementation for planar geometries.

The first test case considered is that presented by Moffat and Kays [106]. In this case, low-speed ($U_\infty = 13.6\,{}^{\mathrm{m}}\!/\!_{\mathrm{s}}$, $M = 0.04$) air flows over a heated porous plate that is 8 feet (2.44 m) long. Air is injected uniformly through this porous plate into the boundary layer. Experimental data available consist of Stanton number, St, (a dimensionless heat transfer coefficient) as a function of stream length Reynolds number, Re_x, for different blowing fraction values. Blowing fraction, F, is a measure of the amount of mass injected into the boundary layer, defined as

$$F = \frac{\rho_w U_w}{\rho_\infty U_\infty} \tag{6.1}$$

where ρ is density, U is velocity magnitude, and the subscripts ∞ and w represent freestream and wall conditions, respectively.

The flow domain is one foot (0.30 m) high and includes a run-in region 6 inches (0.15 m) in length upstream of the plate leading edge. The first layer of cells adjacent to the wall has a thickness of 0.002 inches (5.1×10^{-5} m); a growth rate of 1.01 is used in the wall-normal direction. This mesh yields wall y^+ values that remain below one for most of the plate. The mesh has 548 cells in the wall-tangent direction, and 68 cells in the wall-normal direction (37,264 cells total). Biasing is also used to cluster cells near the leading edge of the plate.

Simulations are performed for four blowing fraction values: $F = 0.0$ (no blowing), 0.001, 0.0019, and 0.0038. Results from these simulations are presented in Figure

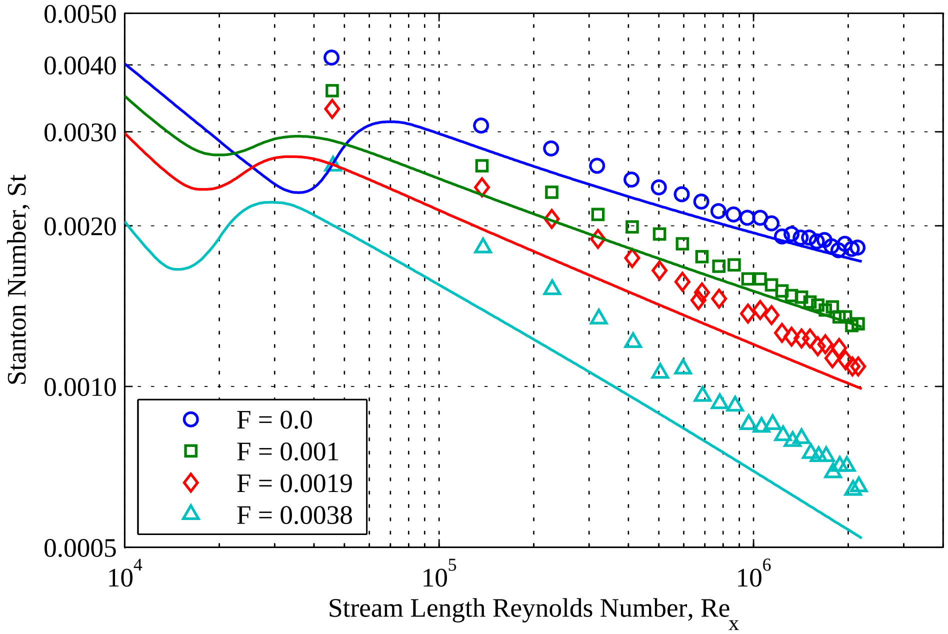

Figure 6.5: Stanton number as a function of stream length Reynolds number for multiple blowing fraction values for the Moffat test case. LeMANS simulation results are lines; symbol denote experimental data.

6.5 and compared to the experimental data. The simulation results show the same trends as observed in the experiment: Stanton number decreases as blowing is increased. However, the simulation results are somewhat lower than those measured in the experiment. For $\text{Re}_x > 1.0 \times 10^5$, the RMS error varies from 6.0 % for $F = 0.0$ to 20.8 % for $F = 0.0038$. However, these error percentages are affected by the decreasing magnitude of the Stanton number as the blowing fraction increases. The "absolute" RMS error (not a percentage) only varies from 1.30×10^{-4} for $F = 0.001$ to 2.08×10^{-4} for $F = 0.0038$, and displays no trend with respect to blowing fraction. The cause for the discrepancy between the experiment and the simulations is not clear; possibilities include differences in transport properties, or the need for further mesh refinement in the wall-normal direction. One contributing factor is that the simulation results appear to show "transitional" behavior. For example, the Stanton number increases substantially in the region $\text{Re}_x \approx 2.0 \times 10^4$ to $\text{Re}_x \approx 4.0 \times 10^4$. In the experiment, there was an impermeable plate upstream of the porous plate, but the boundary layer was tripped so that the virtual origin of the boundary layer corresponded to the start of the porous plate. Agreement of the simulation results with the experimental data is believed to be sufficient to demonstrate accurate implementation of the blowing boundary conditions, so the source of the discrepancies has not been investigated further.

The second flat plate with mass injection test case was a different experiment performed by Andersen et al. [107] in the same facility as the Moffat test case just described. The porous wall is not heated for this test case, and the freestream velocity is slightly different ($U_\infty = 9.6\,{}^{\mathrm{m}}/_{\mathrm{s}}$, $M = 0.03$). Experimental data available include skin friction coefficient as a function of axial position and boundary layer profiles at numerous axial stations. Data are available for multiple blowing fractions and pressure gradients, but simulations are performed only for zero pressure gradient and four blowing fraction values: $F = 0.0$ (no blowing), 0.001, 0.002, and 0.00375. The same mesh is used for this test case as was used for the Moffat case.

The simulated and experimental values for the skin friction coefficient are compared in Figure 6.6. Excluding a small region near the leading edge of the plate (where "transitional" behavior is once again observed), very good agreement is obtained. For axial positions greater than 0.5 m, the RMS error varies from 1.8 % for $F = 0.0$ to 8.0 % for $F = 0.0038$. However, these error percentages are affected by the decreasing magnitude of the skin friction coefficient as the blowing fraction increases. The absolute RMS error only varies from 4.65×10^{-5} for $F = 0.002$ to 7.84×10^{-5} for $F = 0.001$, and displays no trend with respect to blowing fraction. Velocity profiles at the axial station 90 inches (2.3 m) downstream of the plate leading edge are compared in Figure 6.7. Again, there is very good agreement between the simulation results and the experimental results, across all blowing fraction values considered. For $y^+ < 500$, the RMS error ranges from 3.7 % for $F = 0.0038$ to 10.9 % for $F = 0.002$ and does not display a trend with respect to blowing fraction. Wilcox [68] also considered this

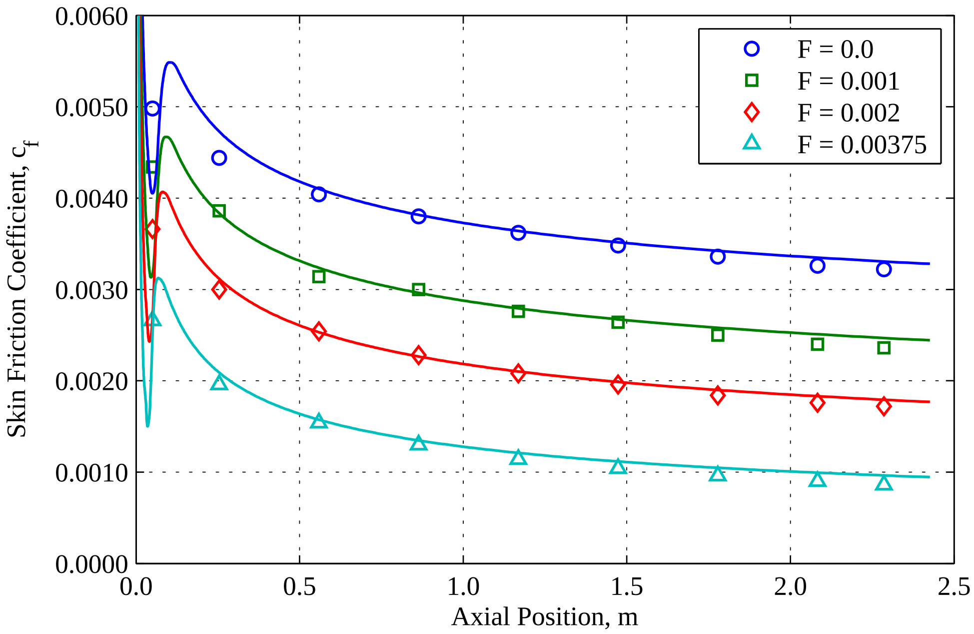

Figure 6.6: Skin friction coefficient as a function of axial position for multiple blowing fraction values for the Andersen test case. LeMANS simulation results are lines; symbol denote experimental data.

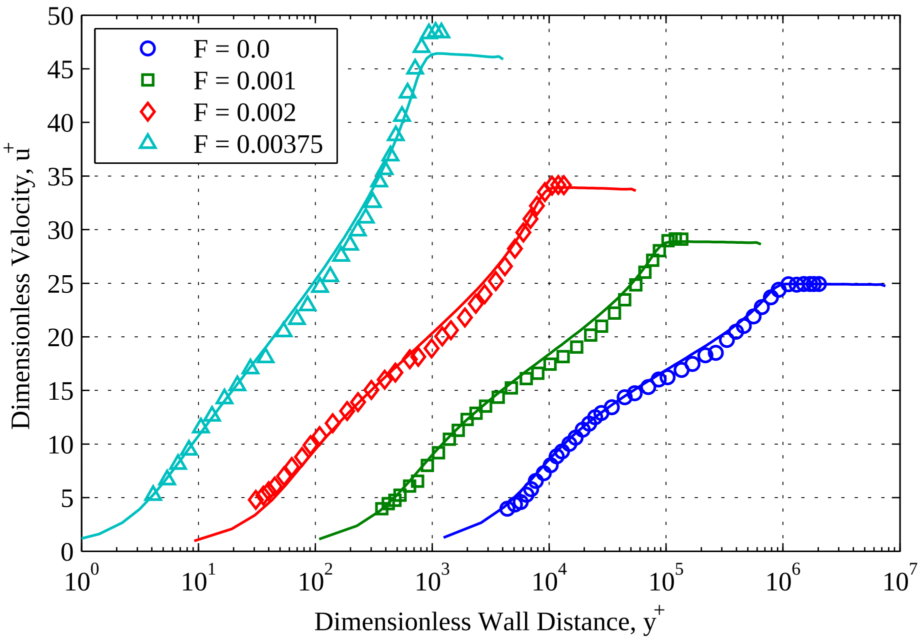

Figure 6.7: Velocity profiles at the axial station 90 inches (2.3 m) downstream of the plate leading edge for multiple blowing fraction values for the Andersen test case. LeMANS simulation results are lines; symbol denote experimental data. Note that profiles for smaller values of F have been shifted right by orders of magnitude for clarity.

test case, and graphically presented velocity profile comparisons. No quantitative assessment was made. A visual comparison suggests that the results obtained in this work are consistent with those produced by Wilcox.

The successful completion of these two test cases indicates that the blowing wall boundary condition for the specific dissipation equation in the BSL and SST turbulence models has been implemented correctly.

6.2.3 Axisymmetric Transonic Bump

In order to validate the turbulence model implementation for axisymmetric geometries, simulations are performed for an axisymmetric transonic bump test case using both the BSL and SST models. This test case features a cylinder with a circular arc "bump" that induces separation of the transonic ($M = 0.875$) flow. Meshes, conditions, and comparison data for this test case are obtained from the NASA Turbulence Modeling Resource website [104]. While five grids with increasing levels of refinement are available, simulations are only performed using the coarsest mesh (181 points in the wall-tangent direction by 81 points in the wall-normal direction).

Comparisons for the pressure coefficient can be found in Figure 6.8. The SST model implementation in LeMANS gives very good agreement with the experimental data, and in some regards it provides better agreement to the experiment than the results obtained with the CFL3D code. The LeMANS implementation of the BSL model does not agree quite as well with the experimental data, but this is also true for the results from the CFL3D code and for early benchmark results produced by Menter and Rumsey [108]. In both cases, the results obtained with LeMANS agree quite well with the CFL3D computations. The RMS absolute (not percent) error relative to the experimental data is 0.135 for the BSL model and 0.025 for the SST model. (The RMS error for the CFL3D results relative to the experimental measurements is 0.106 and 0.030, respectively.) Relative to the CFL3D results, the RMS error for the results

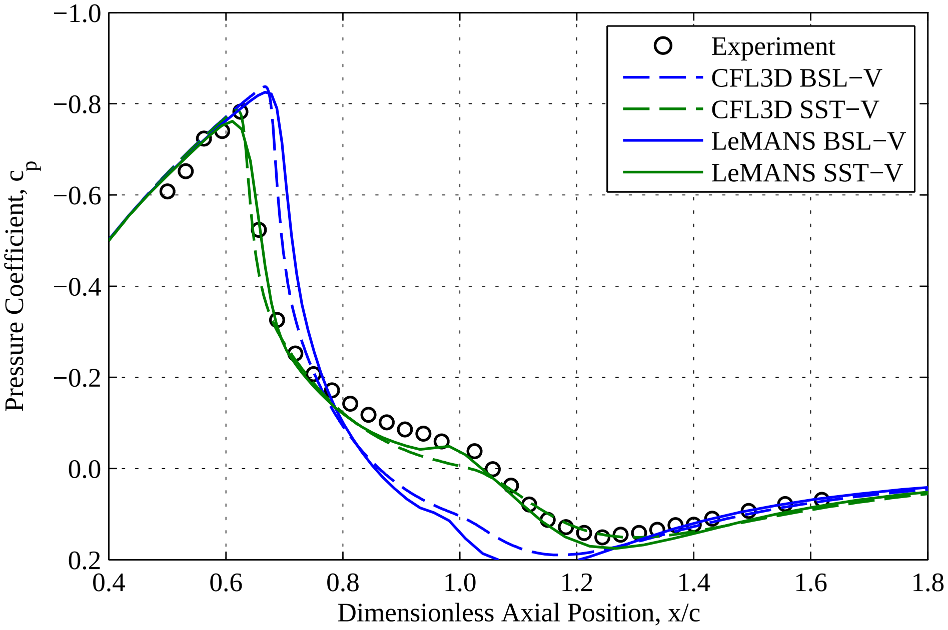

Figure 6.8: Pressure coefficient as a function of axial position for the axisymmetric transonic bump test case.

produced by LeMANS are 0.044 and 0.023, respectively.

Velocity profile comparisons are made in Figure 6.9. These plots indicate that, in general, the SST model as implemented in LeMANS does a good job of reproducing the experimental profiles. Agreement with the CFL3D results is also good, and it appears the LeMANS implementation agrees slightly better with the experimental data than does the CFL3D code. The BSL model also agrees well with the experiment, and the results from both LeMANS and CFL3D for this turbulence model are quite similar. It is difficult to make a determination as to which model provides better agreement with the data. The BSL model provides better agreement as some stations, while at others the SST model is superior. Best agreement with experimental data is consistently achieved at the $\frac{x}{c} = -0.250$ axial station (which is upstream of the separation point), while the worst agreement occurs at the $\frac{x}{c} = 0.688$ axial station (which is in the immediate vicinity of the shock and flow separation). The RMS absolute error relative to the experimental measurements varies from 0.019 to 0.262

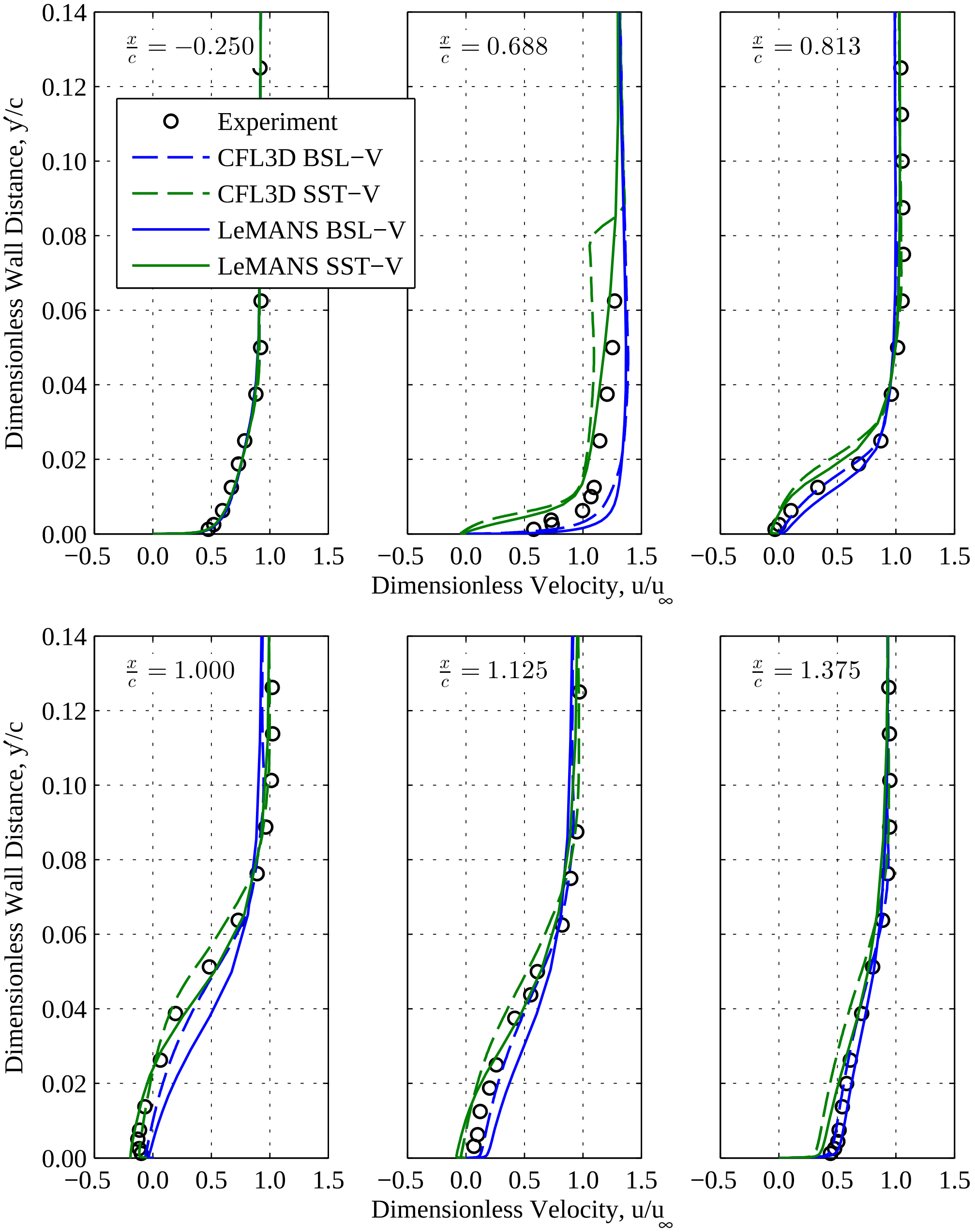

Figure 6.9: Comparison of velocity profiles for the axisymmetric transonic bump test case.

for the BSL model, and from 0.016 to 0.277 for the SST model. (The RMS error for the CFL3D results varies from 0.018 to 0.183 for the BSL model, and from 0.016 to 0.370 for the SST model.) Relative to the CFL3D results, the RMS error for the results produced by LeMANS varies from 0.004 to 0.129 for the BSL model, and from 0.005 to 0.075 for the SST model.

This test case indicates that the axisymmetric implementation of the turbulence models in LeMANS is working correctly. Most differences between the LeMANS and CFL3D results can be attributed to mesh differences (the LeMANS results are obtained using a coarse grid, while the CFL3D results were obtained using a much finer grid).

6.2.4 Kolozsi Nozzle

Since it is vitally important to accurately predict heat transfer within nozzles, one particularly useful validation case is a nozzle experimentally investigated by Kolozsi [109]. The Kolozsi nozzle was an instrumented converging-diverging nozzle (with a nominal 7.5° half-angle) through which high-pressure, high-temperature air passed. Wall temperature and heat transfer coefficient data are available for two different test runs: "Run A" was performed at a stagnation temperature of $T_0 = 675\,\mathrm{K}$ and a stagnation pressure of $P_0 = 2.55\,\mathrm{MPa}$, and "Run B" was performed at the conditions $T_0 = 622.2\,\mathrm{K}$, $P_0 = 1.56\,\mathrm{MPa}$. The mesh for this nozzle uses a structured topology and has 168 cells in the wall-tangent direction and 74 cells in the wall-normal direction. Near-wall cell thickness is $1.27{\times}10^{-6}\,\mathrm{m}$ away from the throat dropping to $1.27{\times}10^{-7}\,\mathrm{m}$ near the throat. Maximum wall-tangent cell dimension is $2.54 \times 10^{-3}\,\mathrm{m}$, reducing to $6.34 \times 10^{-4}\,\mathrm{m}$ near the throat. Biasing is used to produce smooth growth in cell size. This mesh yields wall y^+ values that remain below one for the length of the nozzle.

The heat transfer coefficient profiles as predicted by LeMANS with the two turbulence models are compared to the experimental measurements of Kolozsi in Figure

6.10 for Run A, and in Figure 6.11 for Run B. The dashed lines in these plots represent curve fits made by Kolozsi. The RMS difference between the experimental measurements and these curve fits is 10.6 % for Run A and 12.5 % for Run B. Since no estimate of experimental error or uncertainty is presented by Kolozsi, these values can be taken as a measure of error in the experiment. The shaded regions bounded by dotted lines in these plots represent this uncertainty. It can be observed that, for the most part, the experimental predictions fall within the assumed error band of the experiment. For Run A, the RMS error relative to the curve fit, for axial positions downstream of 0.025 m (eliminating nozzle entrance effect), is 17.8 % for the BSL model and 13.4 % for the SST model. For Run B, these errors are 46.5 % and 36.1 %, respectively. These large values for the error percentages are mainly driven by the differences near the exit of the nozzle, where the convection coefficient magnitudes are relatively low.

Due to the large range of convection coefficient magnitudes, absolute RMS error measurements may be preferable in place of percentages for this test case. The absolute RMS difference between the experimental measurements and the curve fit is $210\,\mathrm{W/m^2K}$ for Run A and $151\,\mathrm{W/m^2K}$ for Run B. For Run A, the absolute RMS error relative to the curve fit is $321\,\mathrm{W/m^2K}$ for the BSL model and $219\,\mathrm{W/m^2K}$ for the SST model. For Run B, these errors are $330\,\mathrm{W/m^2K}$ and $186\,\mathrm{W/m^2K}$, respectively.

From these comparisons, it is observed that the turbulence model implementation in the LeMANS flow solver can predict heat transfer within nozzles with acceptable accuracy. The BSL model produces values that are somewhat higher than those obtained with the SST model, which is consistent with the literature [54, 58].

6.2.5 HIPPO Nozzle – Particle-Laden Flow

Verification of the particle-laden flow capability added to LeMANS is achieved by simulating the flow through the HIPPO nozzle (using the initial model described

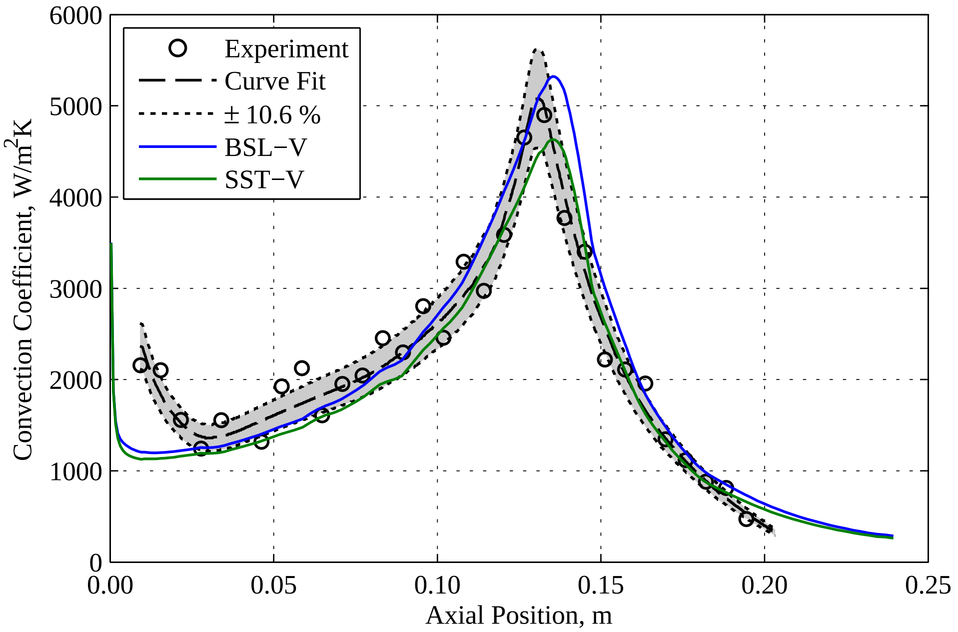

Figure 6.10: Convection coefficient as a function of axial position for the Kolozsi nozzle test case Run A.

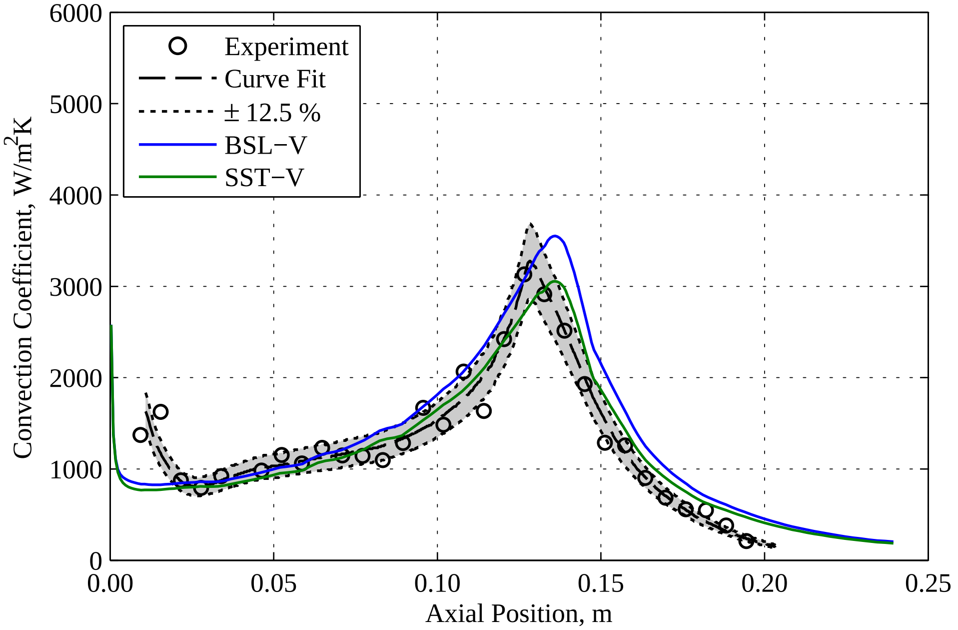

Figure 6.11: Convection coefficient as a function of axial position for the Kolozsi nozzle test case Run B.

Table 6.1: Forward reaction rates for the mechanism proposed by Troyes et al.

Index	Reaction	A, mol − cm − s	b	T_a, K
1	$H + O_2 \rightleftharpoons OH + O$	1.99×10^{14}	0	8460.75
2	$O + H_2 \rightleftharpoons H + OH$	5.12×10^{4}	2.67	3164.85
3	$OH + H_2 \rightleftharpoons H + H_2O$	1.02×10^{8}	1.6	1660.73
4	$OH + OH \rightleftharpoons O + H_2O$	1.51×10^{9}	1.14	49.85
5	$H + H + M \rightleftharpoons H_2 + M$	8.99×10^{17}	-1	0
6	$H + OH + M \rightleftharpoons H_2O + M$	2.21×10^{22}	-2	0
7	$H + O + M \rightleftharpoons OH + M$	4.71×10^{18}	-1	0
8	$O + O + M \rightleftharpoons O_2 + M$	1.45×10^{17}	-1	0
9	$CO + OH \rightleftharpoons CO_2 + H$	6.32×10^{6}	-1.5	-250.27
10	$CO + O_2 \rightleftharpoons CO_2 + O$	2.50×10^{12}	0	24070.50
11	$CO + O + M \rightleftharpoons CO_2 + M$	5.00×10^{12}	0	-1167.24
12	$H + HCl \rightleftharpoons H_2 + Cl$	1.69×10^{13}	0	2084.72
13	$H + Cl_2 \rightleftharpoons HCl + Cl$	8.55×10^{13}	0	589.16
14	$HCl + OH \rightleftharpoons H_2O + Cl$	2.71×10^{7}	1.65	-110.78
15	$HCl + O \rightleftharpoons OH + Cl$	3.37×10^{3}	2.87	1767.48
16	$Cl + Cl + M \rightleftharpoons Cl_2 + M$	4.68×10^{14}	0	-906.40
17	$H + Cl + M \rightleftharpoons HCl + M$	7.18×10^{21}	-2	0

in Section 7.2.1) and comparing the results for the nozzle centerline to the output from a 1D isentropic expansion reference solution computed using the NASA CEA chemical equilibrium code [95]. For a prescribed chamber pressure of $P_0 = 4.48\,\mathrm{MPa}$, the corresponding chamber temperature is computed using CEA to be $T_0 = 3452\,\mathrm{K}$, based on the propellant composition given by Arnold et al. [5]. Three simulations are performed with LeMANS. The first assumes finite-rate chemistry based on the mechanism proposed by Troyes et al. [92], which includes the 17 reactions listed in Table 6.1 and 13 species:

$$CO, CO_2, Cl, Cl_2, H, HCl, H_2, H_2O, N_2, O, OH, O_2, Al_2O_3^{\star}$$

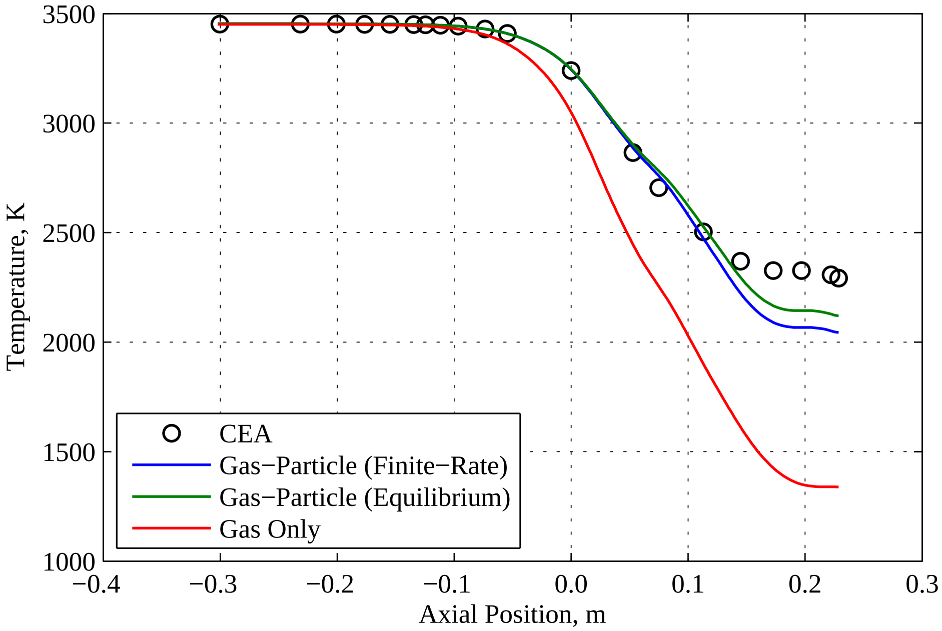

Figure 6.12: Nozzle centerline temperature as computed with LeMANS compared to the CEA reference solution.

N_2 is an inert gas-phase species (participating only as a collision partner in reactions), while $Al_2O_3^\star$ is an inert condensed-phase species and does not participate in reactions in any way. Reaction rates are computed using a modified Arrhenius equation (see Equation 5.3). The second simulation assumes equilibrium chemistry, modeled in LeMANS by increasing the forward and backward reaction rates by a factor of 1000. To show the impact that the condensed phase has on the thermodynamics of the nozzle flow, the third simulation excludes the alumina condensed phase, and only considers the 12 gaseous species.

The temperature on the nozzle centerline is plotted as a function of axial position in Figure 6.12. It can be observed that there is generally very good agreement between the CEA reference solution and the two LeMANS solutions that include the condensed phase. However, when the condensed phase is excluded, the temperatures are substantially under-predicted, clearly demonstrating the impact the condensed phase has on the nozzle flow thermodynamics. The temperature profiles for the finite-

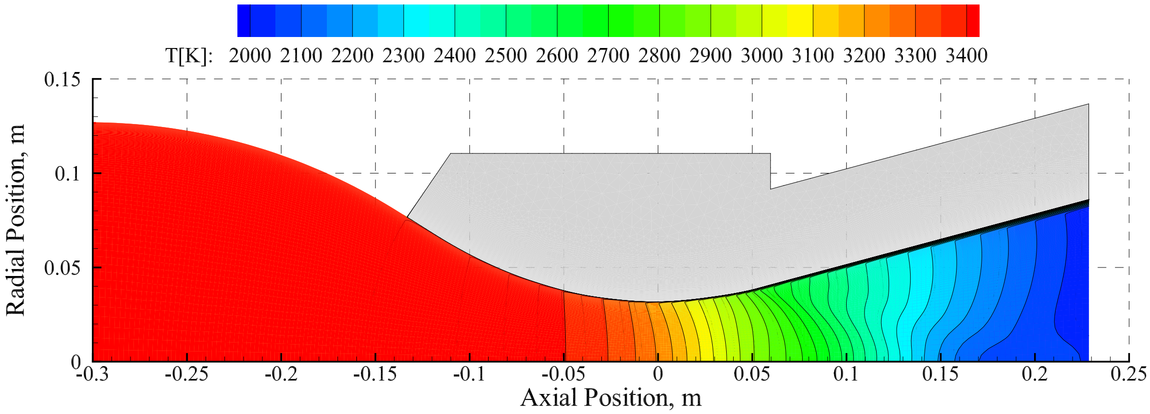

Figure 6.13: Temperature solution for the HIPPO nozzle as computed with LeMANS assuming finite-rate chemistry. Material response domain is indicated by gray region.

rate chemistry simulation and the equilibrium chemistry simulation begin to diverge in the downstream portion of the nozzle, indicating that the equilibrium chemistry assumption is not strictly valid for the full nozzle. Some discrepancies exist between the CEA reference solution and the LeMANS results near the exit of the nozzle (axial position greater than 0.13 m). The CEA temperatures “plateau” in this region, which is due to the solidification of the alumina particles. However, at this time LeMANS cannot capture the effects of particle phase change, which is why the LeMANS simulations under-predict temperatures by about 300 K in this area. The LeMANS temperatures do appear to “plateau” in this same general area, but this is due to the presence of an expansion fan. This expansion fan and other multidimensional flow features can be seen in the temperature contour plot in Figure 6.13, which clearly shows the departure of real nozzle flow from the usual 1D assumption.

These simulations serve to verify that the particle-laden flow capability and the reaction mechanism are working correctly. Additionally, these simulations reveal the importance of capturing the thermodynamics of the condensed phase, and the need for using finite-rate chemistry and a multidimensional flow solver to accurately predict nozzle flow.

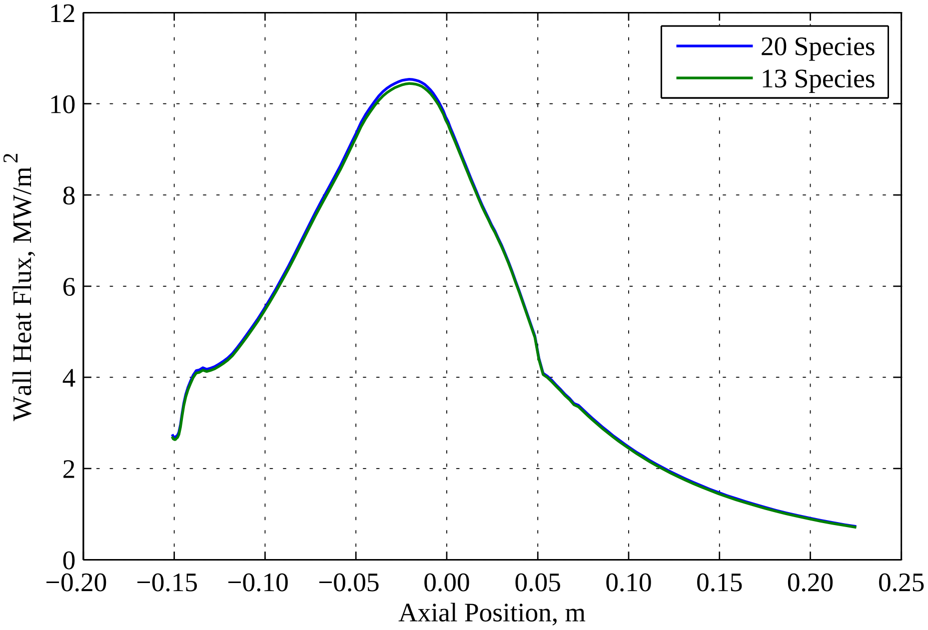

Figure 6.14: Heat flux on the wall of the HIPPO nozzle, plotted as a function of axial position. Blue line represents results from a LeMANS simulation using the 20 species reduced mechanism identified in this effort; the green line represents results from a simulation using the 13 species mechanism proposed by Troyes.

6.2.6 HIPPO Nozzle – Reduced Mechanism

Additional simulations of the HIPPO nozzle test case are performed to evaluate the new, reduced reaction mechanism produced in this work. Results obtained with the 20 species mechanism (see Section 5.3.4) are compared to those obtained with the 13 species mechanism proposed by Troyes et al. (Table 6.1), and to a reference solution obtained with the Chemics chemical equilibrium solver. The geometry and mesh used is very similar to the improved geometric model described in Section 7.2.2. The nozzle chamber conditions are $P_0 = 4.48\,\text{MPa}$ and $T_0 = 3452\,\text{K}$; the wall is assumed to be noncatalytic (species mass fraction gradients are zero in the wall-normal direction) with a temperature of 2500 K.

Wall heat flux as computed with the two mechanisms is compared in Figure 6.14. Agreement between the two mechanisms is quite good, with an RMS difference of 1.2 %. Flowfield parameters along the nozzle centerline are also compared. Pressure, temperature, and velocity are in excellent agreement, with RMS differences less than 0.4 %. Mass fractions for the twelve species in common between the two mechanisms are compared in Fig. 6.15. The agreement for most species is quite good, with the largest discrepancies occurring in the downstream portion of the nozzle. The most significant discrepancy occurs for CO_2.

The mass fraction for CO_2 is presented in Figure 6.16, and is compared to the equilibrium solution computed using Chemics and to results from two additional LeMANS simulations. These simulations modeled chemical equilibrium by increasing the forward and backward reaction rates by a factor of 1000. It can be seen that the mass fraction for CO_2 as predicted using finite-rate chemistry and the 13 species mechanism is essentially “frozen” and nearly constant throughout the nozzle. In contrast to this, the finite-rate chemistry simulation using the 20 species mechanism shows significant changes to the mass fraction for CO_2, largely following the reference chemical equilibrium solution. The equilibrium chemistry simulation using the 20 species mechanism is in excellent agreement with the reference equilibrium solution, but the equilibrium simulation using the 13 species mechanism is in poor agreement. Similar observations can be made for other species (CO in particular), though to a lesser extent.

While it is expected that chemical non-equilibrium may become noticeable in the downstream portion of the nozzle (where temperature and pressures are dropping significantly), it is expected that chemical equilibrium would prevail in the upstream (subsonic) portion of the nozzle. However, the 13 species mechanism predicts significant chemical nonequilibrium for CO_2 and CO beginning upstream of the throat. In contrast, the 20 species mechanism predicts that significant chemical nonequilibrium begins far downstream of the throat, for all species. The 20 species mechanism is therefore in better agreement with the expectation of predominately equilibrium flow with only a small region of chemical non-equilibrium near the exit. Additionally, the

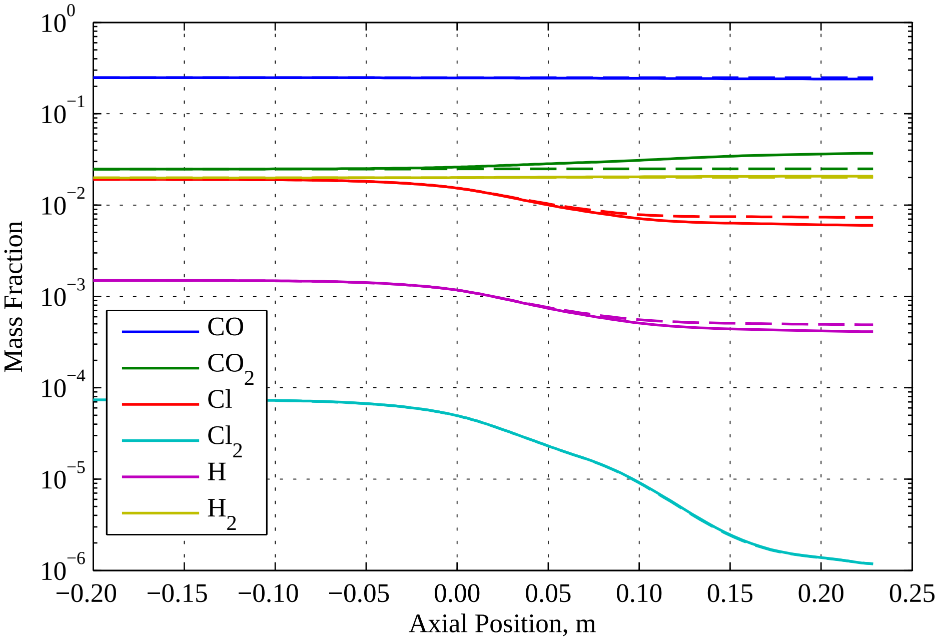

(a) First six species.

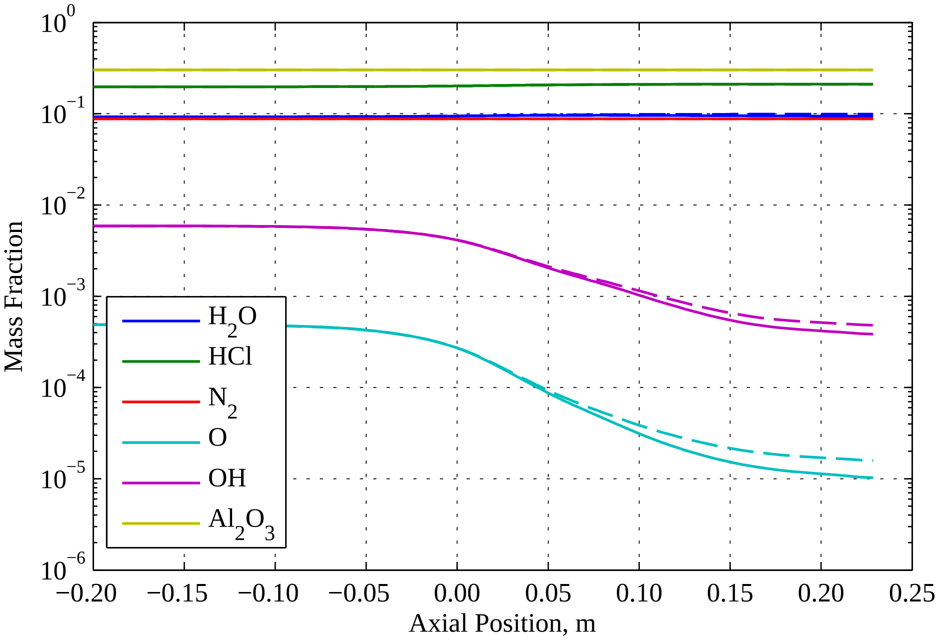

(b) Last six species.

Figure 6.15: Species mass fractions on the centerline of the HIPPO nozzle, plotted as a function of axial position. Solid lines mark LeMANS results using the 20 species reduced mechanism identified in this effort; dashed lines indicate LeMANS results using the 13 species mechanism proposed by Troyes.

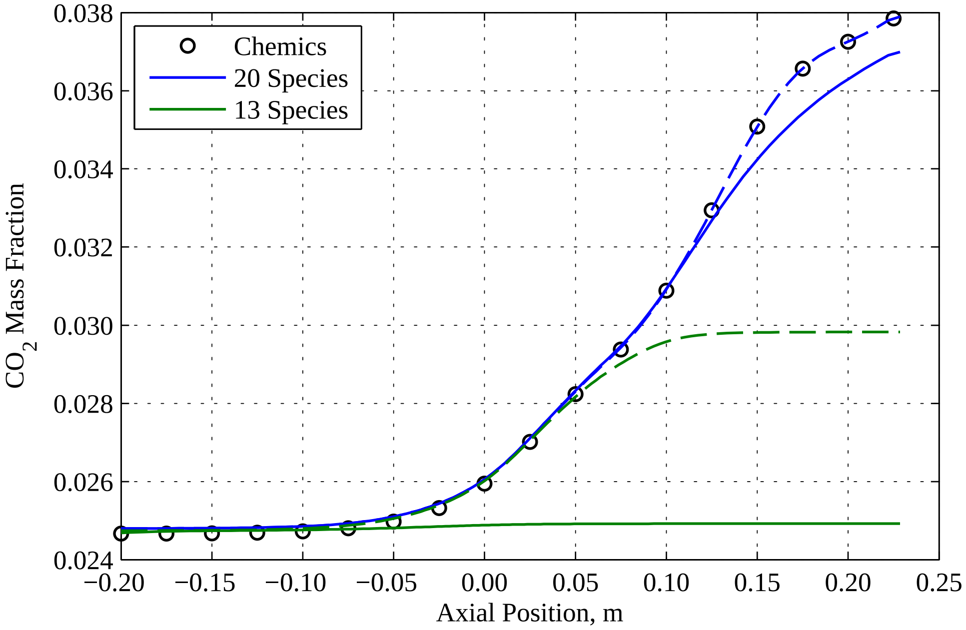

Figure 6.16: Mass fraction for CO_2 on the centerline of the HIPPO nozzle, plotted as a function of axial position. Symbols represent the Chemics reference solution, solid lines mark LeMANS results assuming finite-rate chemistry, and dashed lines indicate LeMANS results assuming equilibrium chemistry.

20 species mechanism can be used to obtain the correct equilibrium solution, whereas the 13 species mechanism cannot. The proposed mechanism therefore improves upon the Troyes mechanism, though at the cost of increased computational expense. Simulations performed with the LeMANS flow solver using the 20 species mechanism require 2.3 times as long to complete each iteration than simulations using the 13 species mechanism.

These simulations show that the reduced mechanism identified in this work is adequate for modeling the flow through the nozzles of solid rocket motors using typical aluminized composite propellants. It is further believed that this mechanism is suitable for use in coupled flowfield / ablation analyses of carbon-phenolic nozzles, subject to restrictions: $B'_g \leq 0.4$, $T \leq 3000\,\mathrm{K}$, and $P \leq 6.0\,\mathrm{MPa}$. Should it be necessary to model regions outside of this parameter space, it may be necessary to expand the mechanism with additional species and / or reactions.

6.3 Material Response Solver

The pyrolysis, porous flow, and ablation capabilities added to the MOPAR-MD material response solver are verified by performing simulations for a number of test cases that exercise different aspects of the code. By comparing results from MOPAR-MD to results produced by other, accepted ablation codes (ITRAC [21] and MOPAR-1D [19, 20]), it is possible to verify that the relevant equations have been correctly implemented into the code. Good agreement is achieved for all test cases considered, indicating that the models describing pyrolysis and ablation have been correctly implemented into MOPAR-MD.

6.3.1 Pyrolysis

The pyrolysis capability is verified by simulating a test case proposed by Ewing at al. [21], in which a slab of virgin TACOT (Theoretical Ablative Composite for Open Testing) material [110] (a hypothetical material model developed as part of the Ablation Workshop activities and somewhat representative of a low-density phenolic material, such as PICA) is held at a constant temperature of 1000 K. Simulation duration is 100 s; a time step of 0.1 s is used. Due to the uniform temperature field, the spatial extents and discretization of the domain have no impact on the pyrolysis solution. Since this is an isothermal case, an analytical solution for the density can easily be obtained:

$$w_i\left(t\right) = \left(w_{i_0}^{1-\psi_i} - A_i\left(1-\psi_i\right)\exp\left(-\frac{T_{a_i}}{T}\right)t\right)^{\frac{1}{1-\psi_i}} \tag{6.2}$$

The subscript 0 refers to the initial density. The results from this simulation are compared to the analytical solution in Figure 6.17. Very good agreement is achieved, with a negligible RMS error of 3×10^{-9}.

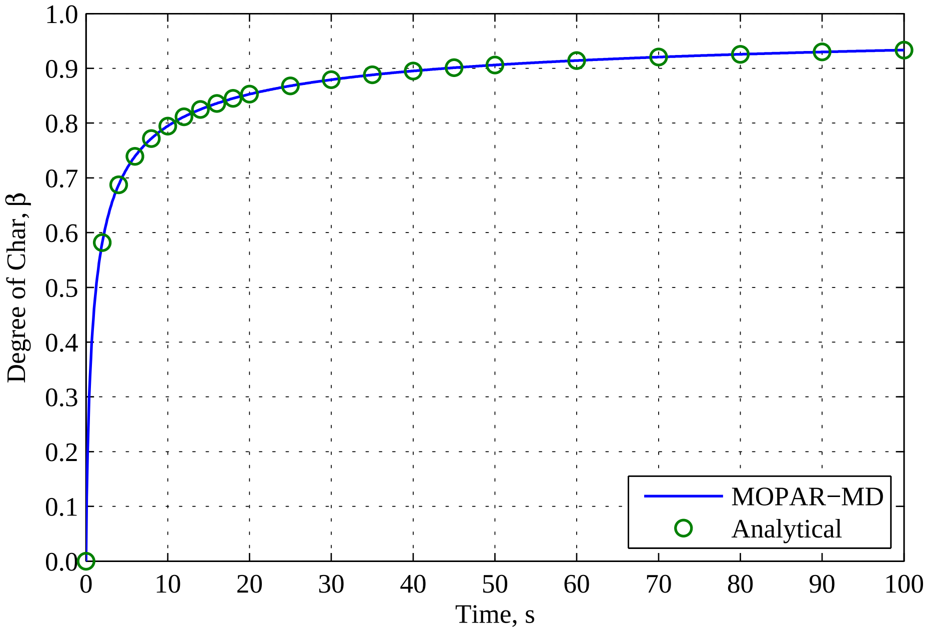

Figure 6.17: Degree of char as a function of time, for the pyrolysis verification test case.

6.3.2 Porous Flow

The porous flow capability is verified by simulating another test case described by Ewing et al. [21], in which the transient flow of air (viscosity $1.855 \times 10^{-5}\ ^{\mathrm{kg}}/_{\mathrm{m \cdot s}}$) through a 10 cm slab of porous media is modeled; element size is approximately 1 mm. The problem is isothermal (300 K); the porous solid has a porosity of 0.1 and an isotropic permeability of $1 \times 10^{-13}\,\mathrm{m}^2$. Initial pressure in the domain is 100 kPa, the same as that applied to the right boundary. The left boundary has a pressure of 200 kPa applied. A time step of 0.001 s is used; a study revealed that smaller values had negligible impact on the results. A reference solution is computed using the 1D ITRAC code using an element size of 0.1 mm and a time step of 0.0001 s. The results for this test case computed with the MOPAR-MD material response code are compared to the reference solution in Figure 6.18. Excellent agreement is observed with an RMS difference of less than 0.05 %.

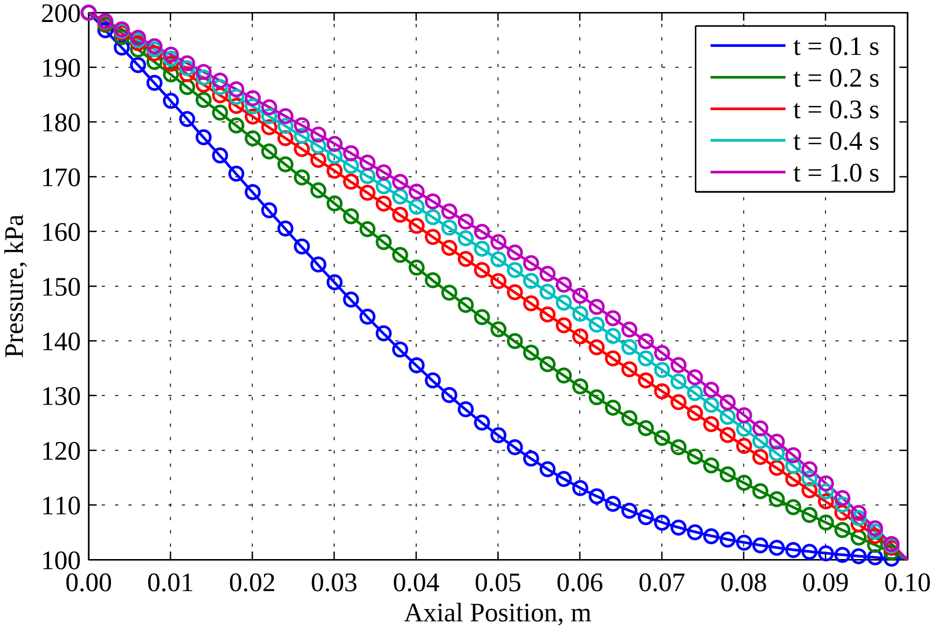

Figure 6.18: Comparison of pressure distribution predicted by MOPAR-MD (lines) and ITRAC (symbols) for the porous flow verification test case at select instances in time.

6.3.3 Ablation Workshop Test Case #1

This test case is the first in a series of test cases defined as part of the Ablation Workshop activities [111]. A specified-temperature boundary condition, which ramps up from 298 K to 1644 K over 0.1 seconds, is applied to the top surface of a 5 cm thick planar slab of TACOT material. Initial temperature is 298 K; simulation duration is 60 s. This test case does not involve an ablating boundary condition or mesh motion, but is useful for verifying that the energy, pyrolysis, and porous flow equations have been implemented correctly, without these extra complicating factors.

The quasi-1D domain modeled in MOPAR-MD is 5 mm wide (wall-tangent direction). Meshes for MOPAR-MD utilize a topology with stacked anisotropic triangular elements well suited for capturing strong gradients in the wall-normal direction. Three different levels of mesh refinement are considered for this case: 100, 200, and 300 nodes in the wall-normal (thickness) direction, (“coarse”, “medium”, and “fine”, respectively). In order to better capture the strong gradients that form near the

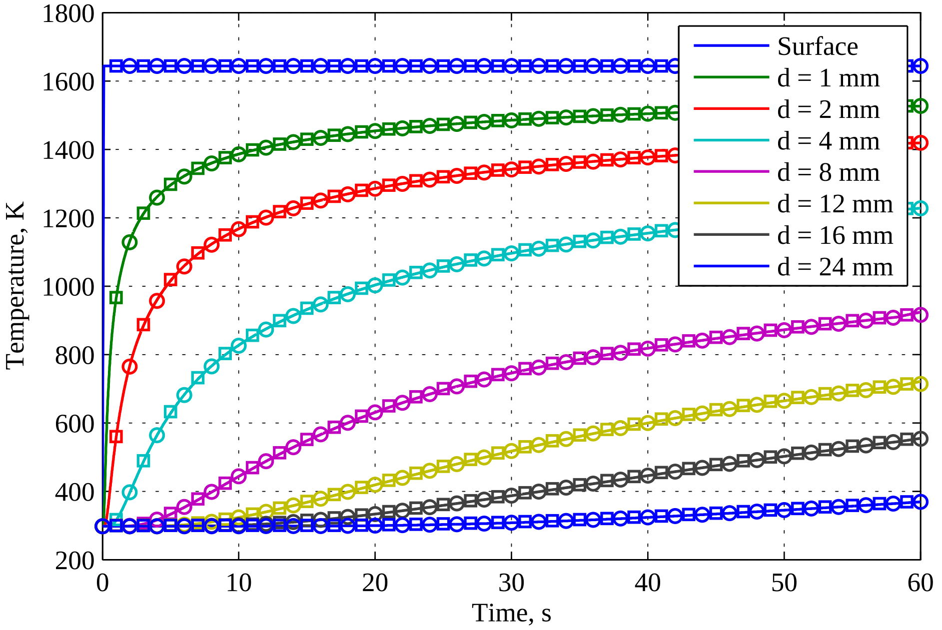

Figure 6.19: Comparison of surface and in-depth thermal response for Ablation Workshop Test Case #1 as predicted by MOPAR-MD (lines), MOPAR-1D (circles), and ITRAC (squares).

heated surface, a stretch ratio of 1.01 is used between subsequent layers of the mesh. All meshes have six nodes in the wall-tangent (width) direction. The MOPAR-1D and ITRAC codes use equivalent 1D meshes. Since there are negligible differences between the results produced with the medium and fine meshes, grid-convergence has been achieved; comparisons are made for results using the fine mesh. A constant time step of 0.01 s is used for most MOPAR-MD and ITRAC simulations; reducing the time step to 0.001 s produced negligible change in results. MOPAR-1D simulations use an automatically-computed variable time step.

The results obtained for the thermal response of the surface and seven in-depth thermocouple locations are compared in Figure 6.19. Excellent agreement is seen between the results produced by MOPAR-MD and the two 1D material response codes. RMS difference relative to MOPAR-1D is less than 0.25 %; relative to ITRAC the RMS difference is less than 0.75 %. This verifies that the equations describing heat transfer, pyrolysis, and porous flow are correctly implemented and consistent with accepted codes for the case of a pyrolyzing, but non-ablating, material.

6.3.4 Ablation Workshop Test Case #2-1

This test case comes from the second set of Ablation Workshop test cases [112]. Building upon Ablation Workshop Test Case #1, the specified-temperature boundary condition is replaced with a moderate aeroheating boundary condition. Enthalpy conductance is held constant at $0.3\,\mathrm{kg/m^2s}$; recovery enthalpy ramps from $0.0\,\mathrm{J/kg}$ to $1.5 \times 10^6\,\mathrm{J/kg}$ over 0.1 seconds. Initial temperature is $298\,\mathrm{K}$; simulation duration is $60\,\mathrm{s}$. Surface recession is prevented by artificially setting $B'_c = 0$ in the B' tables. This test case is useful for verifying correct implementation of the ablation boundary condition, without the added complication of a moving mesh.

Mesh and time step settings are re-used from Ablation Workshop Test Case #1. However, for this test case an addition level of mesh refinement ("extra-fine") is considered, with 600 nodes in the wall-normal direction. Comparisons indicate that the thermal response is essentially unchanged by using the extra-fine mesh; the fine mesh with 300 nodes in the wall-normal direction is adequate. However, it appears that MOPAR-MD requires the extra-fine mesh to achieve a mesh-independent solution for B'_g (especially for the early, highly transient portion of the simulation). The 1D codes appear to only require the fine mesh to reach grid-convergence for B'_g. For this test case, comparisons are made for results using the extra-fine mesh.

The results obtained for the thermal response of the surface and seven in-depth thermocouple locations are compared in Figure 6.20. Again, excellent agreement is observed between results from MOPAR-MD, MOPAR-1D, and ITRAC. RMS difference for the MOPAR-MD thermal response results relative to MOPAR-1D is less than $0.6\,\%$; relative to ITRAC the RMS difference is less than $0.4\,\%$. Nondimensional pyrolysis gas mass flux (B'_g) is presented as a function of time in Figure 6.21. Only the first five seconds are plotted, in order to more clearly present the differences

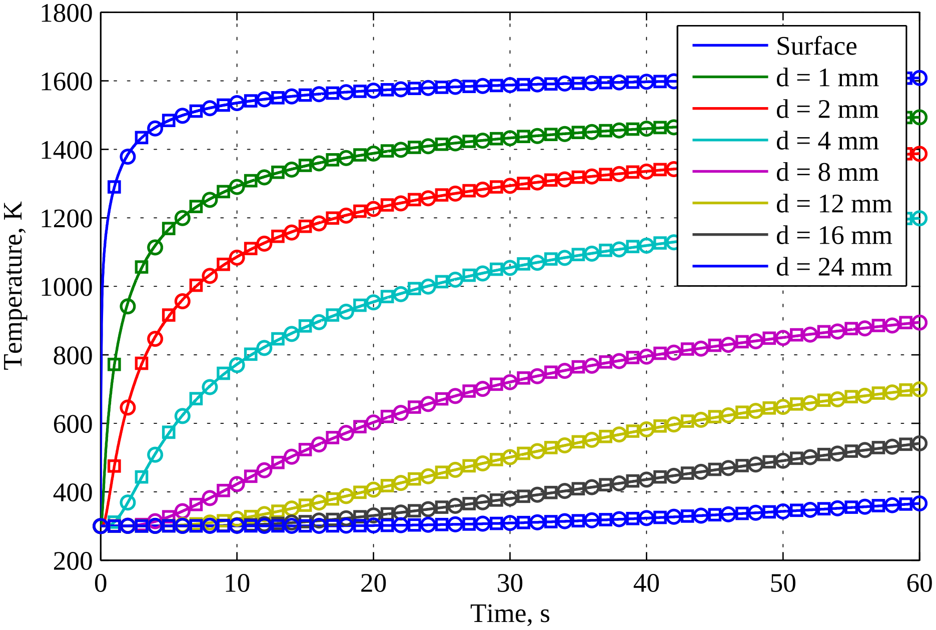

Figure 6.20: Comparison of surface and in-depth thermal response for Ablation Workshop Test Case #2-1 as predicted by MOPAR-MD (lines), MOPAR-1D (circles), and ITRAC (squares).

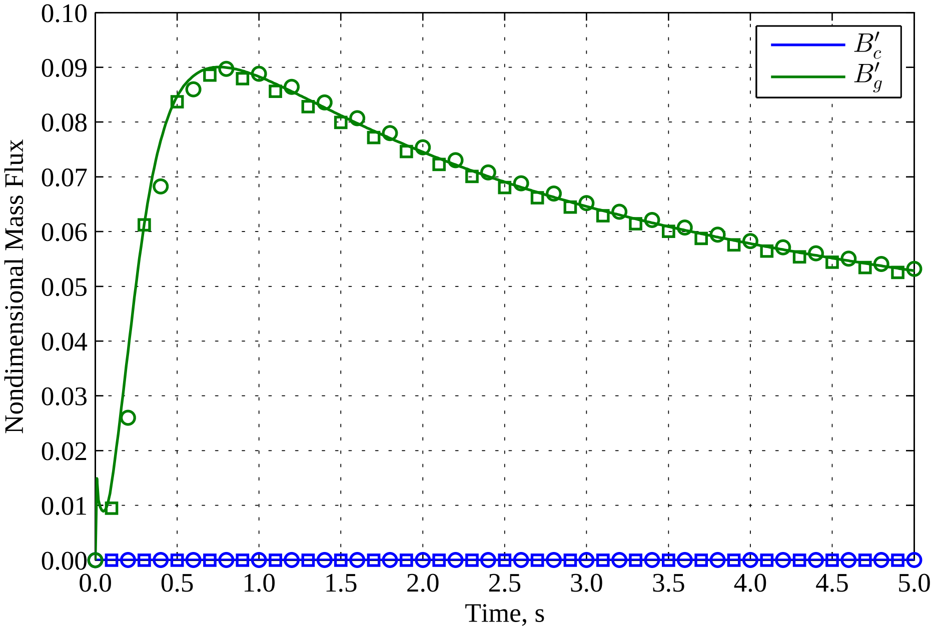

Figure 6.21: Comparison of nondimensional char mass flux (B'_c) and pyrolysis gas mass flux (B'_g) for Ablation Workshop Test Case #2-1 as predicted by MOPAR-MD (lines), MOPAR-1D (circles), and ITRAC (squares).

between the results sets. Visually, there is good agreement between the three codes considered, with all codes giving the same trends and very similar magnitudes. Quantitatively, the RMS difference for the MOPAR-MD B'_g values relative to MOPAR-1D is 2.7 %; relative to ITRAC the RMS difference is 2.4 %. This provides partial verification that the ablating boundary condition has been implemented correctly and consistently with other accepted ablation codes.

6.3.5 Ablation Workshop Test Case #2-2

This final test case extends Ablation Workshop Test Case #2-1; boundary conditions, mesh, and time step settings are the same. However, by not artificially restricting B'_c to zero, surface recession and mesh motion are now considered. With this test case it is possible to verify a complete quasi-1D ablation problem.

Comparisons are made for the “extra fine” mesh, though results from the “fine” mesh are very similar. It should be noted that in order to solve this test case correctly in ITRAC it is necessary to generate new B' tables with many more values of B'_g than was used in the tables distributed with the TACOT material description. Both MOPAR-MD and MOPAR-1D run satisfactorily with the default B' tables, demonstrating reduced sensitivity to the quality of the B' tables.

The results obtained for the thermal response of the surface and seven in-depth thermocouple locations are compared in Figure 6.22. Very good agreement is obtained between the three codes. RMS difference for the MOPAR-MD thermal response is less than 2.1 % relative to MOPAR-1D and less than 1.7 % relative to ITRAC. Nondimensional char mass flux (B'_c) and pyrolysis gas mass flux (B'_g) are presented as functions of time in Figure 6.23. Only data from the initial, transient portion of the simulations are plotted, to accentuate differences between the codes. Excellent agreement is observed here as well, with an RMS difference for B'_c of 1.1 % relative to MOPAR-1D and 0.3 % relative to ITRAC; for B'_g the RMS differences are 2.6 % and 1.8 %, re-

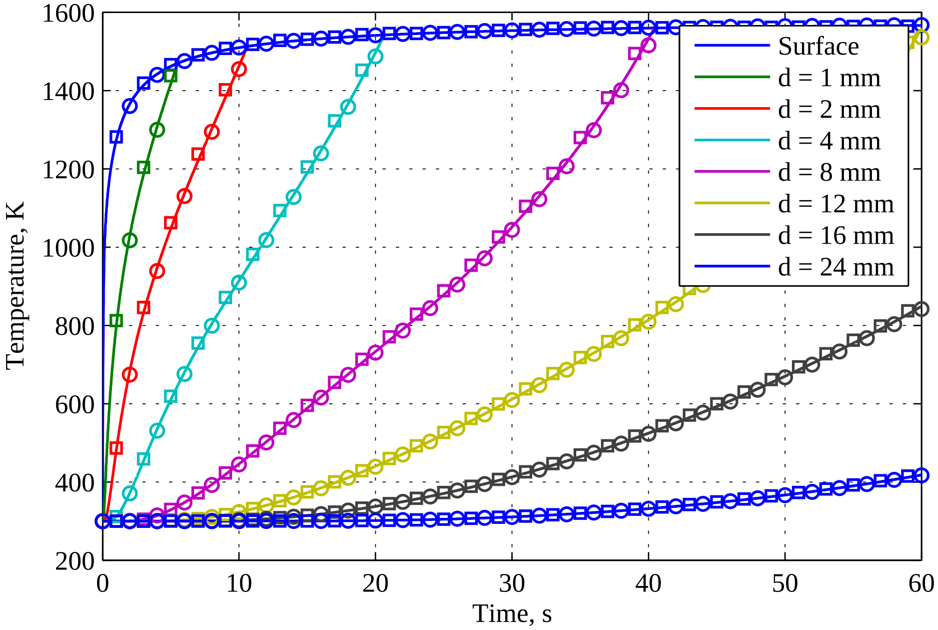

Figure 6.22: Comparison of surface and in-depth thermal response for Ablation Workshop Test Case #2-2 as predicted by MOPAR-MD (lines), MOPAR-1D (circles), and ITRAC (squares).

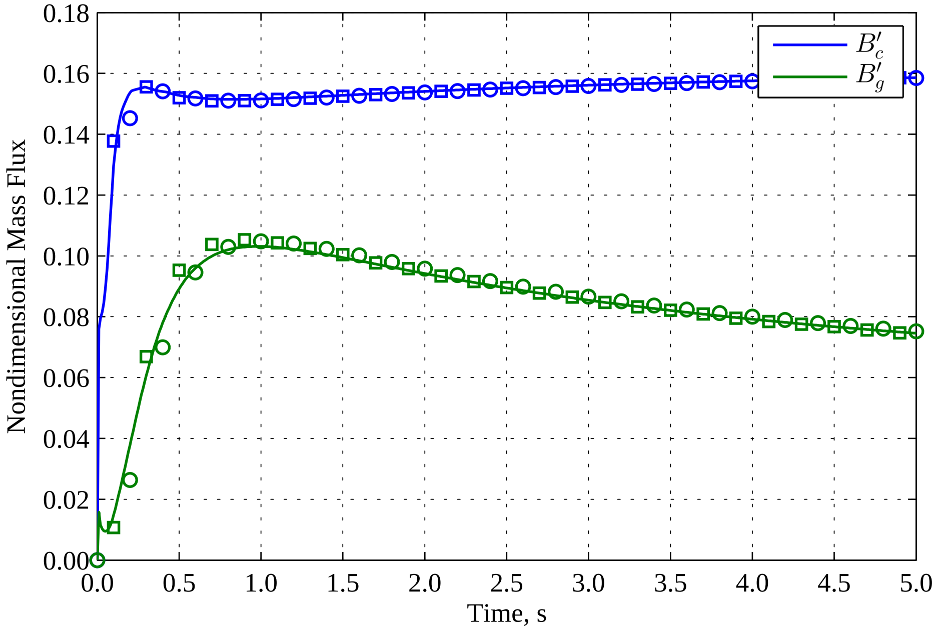

Figure 6.23: Comparison of nondimensional char mass flux (B_c') and pyrolysis gas mass flux (B_g') for Ablation Workshop Test Case #2-2 as predicted by MOPAR-MD (lines), MOPAR-1D (circles), and ITRAC (squares).

spectively. Surface recession is predicted by MOPAR-MD to be 1.2 cm; final surface recession values agree within 1.0 %. Successful simulation of this test case indicates that all components necessary for modeling the ablation of pyrolyzing materials have been implemented correctly and consistently with other accepted ablation codes.

CHAPTER VII

HIPPO Nozzle Analyses

7.1 Introduction

The updated LeMANS flow solver and MOPAR-MD material response solver are used to analyze the ablation of a rocket nozzle test case. Decoupled analyses reveal that the enthalpy conductance, and therefore the ablation response, is strongly affected by the choice of wall temperature profile used when pre-computing the convective heating conditions. This supports the hypothesis that conjugate analyses are necessary for accurate ablation predictions. Enthalpy conductance computed using the LeMANS flow solver shows more sensitivity to wall temperature profile than when enthalpy conductance is computed using a more traditional approach involving a one-dimensional isentropic expansion calculation combined with integral boundary layer computations. Radiative heat transfer is also found to be insignificant at or downstream of the nozzle throat, but can be important at upstream locations.

Conjugate analyses are performed using the five different surface energy balance treatments. Simulation parameters providing rapid convergence of the conjugate solutions are identified. An instability associated with capturing the changing nozzle geometry is encountered, and multiple mitigation strategies are employed to suppress this instability. The Noncatalytic Wall – Heat Flux method is found to be unsuitable for rocket nozzle applications, as it grossly over-predicts the thermal and ablation response of the nozzle. Best agreement with experimental data is provided by the Integrated Equilibrium Surface Chemistry method, which has the highest fidelity of all methods considered.

7.2 HIPPO Nozzle Model

The HIPPO nozzle [5] is selected as a test case for demonstrating two-dimensional modeling of pyrolysis and ablation. The HIPPO motor is a sub-scale (6.35 cm diameter throat) space shuttle solid rocket test motor. Four different motors were fired, with each nozzle manufactured from a different carbon-phenolic material. Nozzle #1 is chosen for consideration in this study. Experimental data for this test case are quite comprehensive, with surface recession and char depth being provided as a function of axial position for eight circumferential stations.

Two different models for this test case are presented in this work. The initial model (Section 7.2.1) is used for most decoupled analyses and for some very early conjugate analyses, but is found to not be well-suited for conjugate simulations. The improved model (Section 7.2.2) adds a "nose" to the nozzle geometry and corrects a few other minor problems with the geometry. Most conjugate simulations presented in this work use this improved model. A number of intermediate models leading to the improved model were also investigated, but are not presented here.

7.2.1 Initial Model

A geometrical description of the HIPPO nozzle was provided by Arnold et al. [5] only for the throat and downstream portions of the nozzle, as shown in Figure 7.1. No information was provided describing the nozzle contour more than about 0.13 m upstream of the throat. Therefore, the flow domain in this upstream region must be assumed, as shown in Figure 7.1, and is most likely different from the actual nozzle geometry. The nozzle contour geometry is constructed with splines based on points

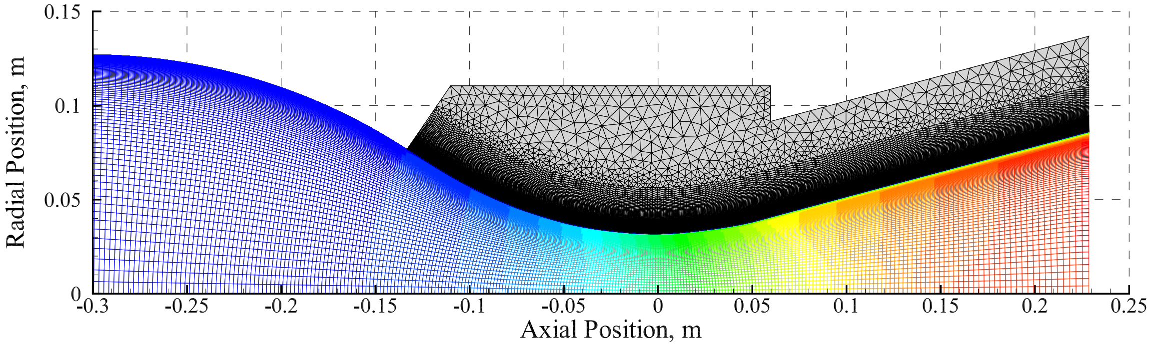

Figure 7.1: Initial model for the HIPPO nozzle. Shaded region with black mesh lines is the material response solver domain. Mesh in the flow solver domain is also illustrated and colored based on flow velocity.

digitized from Ref. [5]. In the experiment, a steel shell surrounded the carbon-phenolic material, but this is excluded in the thermal model and is replaced with an adiabatic boundary condition. This will have no impact on the results, as there is no change in temperature observed on this boundary.

The mesh for the flow domain has 150 cells in the wall-normal direction and 267 cells in the wall-tangent direction, for a total of 40,050 cells. Near-wall cell thickness is 2.54×10^{-6} m, decreasing to 6.35×10^{-7} m at the throat. The wall-tangent dimension of the cells is approximately 2.54×10^{-3} m, decreasing to 1.27×10^{-3} m near the throat. Biasing is used in order to obtain smooth meshes. Wall y^+ values remain below one for the length of the nozzle with this mesh.

For the solid domain, a 2.54 cm thick layer of stacked, anisotropic, triangular elements is generated adjacent to the ablating boundary. 80 layers of elements are used in this region, with a near-wall thickness of 2.54×10^{-5} m and a growth rate of 1.05. Wall-tangent dimension of the mesh elements is about 3.2×10^{-3} m. The diagonal faces are not aligned in this mesh. The remainder of the domain is filled with approximately isotropic triangular elements. The final mesh contains 20,235 elements and 10,292 nodes. Comparisons of results computed with this mesh to results produced by a much more refined, quasi-1D mesh for the throat region suggests that

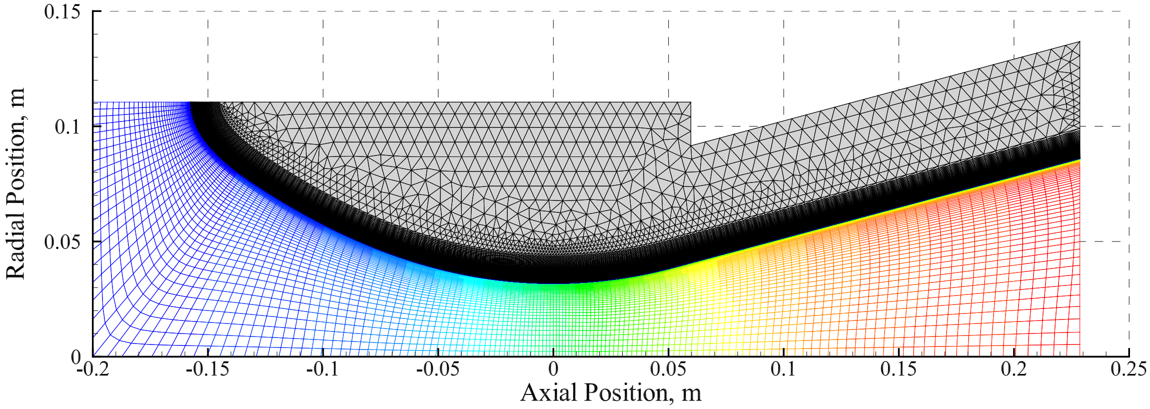

Figure 7.2: Improved geometric model for the HIPPO nozzle. Shaded region with black mesh lines is the material response solver domain. Mesh in the flow solver domain is also illustrated and colored based on flow velocity.

further mesh refinement would have minimal impact on the thermal response and surface recession of the nozzle.

The HIPPO nozzle was manufactured from MX4926 carbon-phenolic material; material properties are listed in Appendix B. The material is in the 90° orientation; the plies are oriented perpendicular to the nozzle axis. This means that the thermal conductivity and permeability are larger normal to the axis than along the axis. Simulations using this initial model for the HIPPO nozzle utilize the 13 species mechanism proposed by Troyes et al. [92] (see Table 6.1) and B' tables computed using ACE [83]. Species properties can be found in Appendix A.

7.2.2 Improved Geometric Model

The geometry for the improved model of the HIPPO nozzle is illustrated in Figure 7.2. Based on additional review of similar nozzles in the literature [113], it seems likely that the HIPPO nozzle was submerged, with a nose similar to that assumed and illustrated in Figure 7.2. Additionally, for this model, the curved nozzle contour geometry is represented by two parabolic curve segments. This provides a much smoother nozzle contour, and eliminates unrealistic oscillations in the slope of the surface that were produced by the use of splines in the initial model. The slope variations in the initial model are found to have a negative impact on the stability of the conjugate analyses.

The mesh for the flowfield is constructed of quadrilateral elements, and has 77 cells in the wall-normal direction and 150 cells in the wall-tangent direction, for a total of 11,550 cells. Near-wall cell thickness ranges from approximately 6.2×10^{-8} m at the throat increasing to 2.0×10^{-7} m at the exit; a stretch ratio of 20 % is used in the wall-normal direction. Wall y^{+} values remain below 0.1 for the length of the nozzle with this mesh. The wall-tangent dimension of the cells ranges from approximately 1.27×10^{-3} m near the throat and nose increasing to 6.8×10^{-3} m at the exit. Biasing is used in order to obtain a smooth mesh. Mesh parameters are determined from an extensive mesh refinement study (see Appendix C), which suggests that this mesh can yield heat flux values with an error of less than 0.5 %. The flowfield mesh is illustrated in Figure 7.2.

The mesh for the solid domain features a 1.27 cm thick layer of stacked, anisotropic, triangular elements adjacent to the ablating boundary. 67 layers of elements are used in this region, with a near-wall thickness of 2.54×10^{-5} m and a growth rate of 1.05. This mesh topology is obtained by first generating a structured mesh with quadrilateral cells, then triangulating each cell. It is found that it is important for the diagonal faces dividing the quadrilateral elements to be aligned in the same direction. The wall-tangent dimensions of the elements are the same as for the flowfield mesh. Coincident nodes are maintained on the ablating boundary between the flowfield mesh and the material response mesh (though this is not a requirement of the coupled code). Approximately isotropic triangular elements are used to fill the remainder of the domain. Mesh parameters are determined from a mesh refinement study (see Appendix C). The final mesh contains 21,926 elements and 11,144 nodes.

The improved geometric model employs the same MX4926 carbon-phenolic properties used with the initial model (see Appendix B). Simulations performed with the improved model use B' tables computed using the Chemics [84] chemical equilibrium program and the CEA [95] thermodynamic database. Gas-phase finite-rate chemistry is modeled using a 20 species, 33 reaction reduced mechanism developed as part of this work (see Section 5.3.4); species properties are given in Appendix A. Diffusion of gas-phase species is modeled using a constant Lewis number $\mathrm{Le} = 0.66$ ($\mathrm{Le} \equiv \frac{\mathrm{Pr}}{\mathrm{Sc}}$). An estimate of the actual variation of Lewis number is obtained from an isentropic expansion calculation performed with the Chemics code. For a chamber pressure of $P_0 = 4.48\,\mathrm{MPa}$, Lewis number ranges from $\mathrm{Le} = 0.65$ in the chamber to $\mathrm{Le} = 0.71$ at the exit, with $\mathrm{Le} = 0.66$ occurring at the throat.

7.3 Decoupled Analyses

Ablation analyses following a traditional decoupled approach are performed. There are three objectives for these decoupled analyses. First, a study is conducted to determine the relative importance of radiative heat transfer on the thermal response of the nozzle. Second, a study is performed to investigate the sensitivity of the enthalpy conductance to the wall temperature used in the flow solver. These two studies use the initial model for the HIPPO nozzle. A final decoupled analysis is performed to serve as a good baseline for comparison to the conjugate ablation analyses. This baseline decoupled simulation uses the improved geometric model for the HIPPO nozzle.

The measured pressure trace for the HIPPO nozzle is closely approximated for the decoupled analyses using seven discrete pressures, as illustrated in Figure 7.3. Boundary condition computations are performed for each discrete pressure, and linear interpolation is used to obtain boundary condition values at intermediate pressures. The convection boundary conditions (recovery enthalpy and enthalpy conductance) are computed using the LeMANS flow solver (described in Chapter II). First, simulations are performed using an adiabatic wall boundary condition; the resultant wall

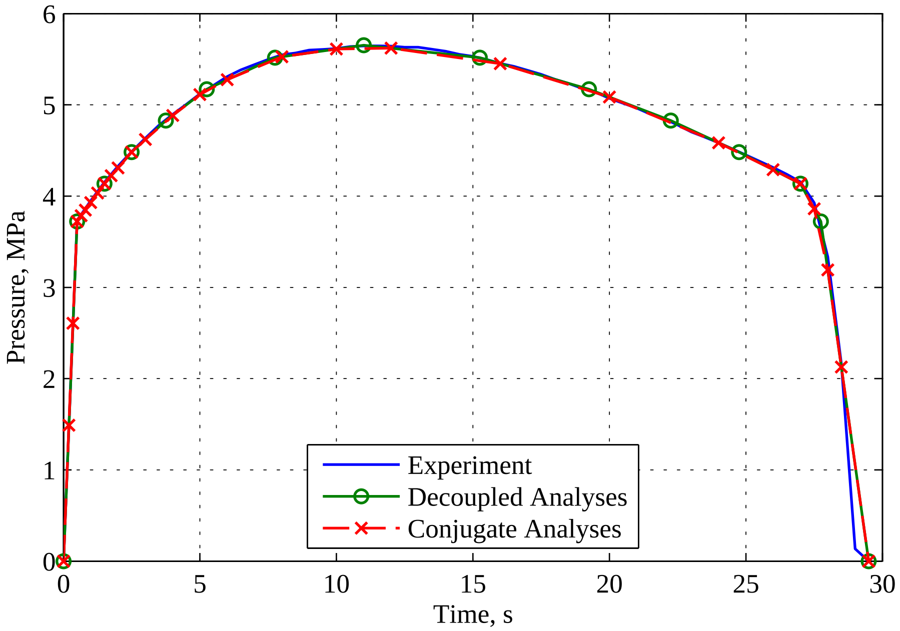

Figure 7.3: Pressure trace for the HIPPO motor, comparing the experimentally measured pressure trace to the discrete pressure traces used for the decoupled and conjugate analyses.

enthalpy is taken to be the recovery enthalpy, h_r, which is a function of axial position. Simulations with prescribed wall temperature are then performed, producing heat flux, $\dot{q}''_{FS}$, values along the length of the nozzle, as well as "cold wall" enthalpies, h_{FS}. Heat flux is then converted to enthalpy conductance, g_H, according to

$$g_H = \frac{\dot{q}''_{FS}}{h_r - h_{FS}} \tag{7.1}$$

These enthalpy conductance values are then used as boundary conditions in the decoupled material response simulations.

The enthalpy conductance values obtained with LeMANS are compared to values computed in a more traditional manner using the NAT code [8] in Figure 7.4. NAT performs a 1D isentropic expansion calculation to obtain the boundary layer edge conditions and recovery enthalpy, followed by an integral solution of the boundary layer to obtain the enthalpy conductance. In order to perform these convection

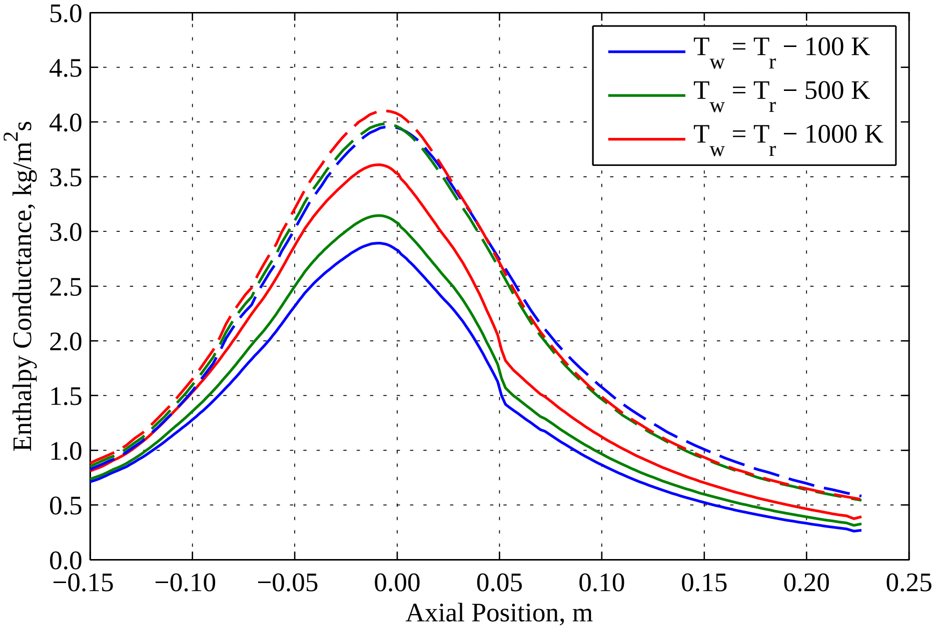

Figure 7.4: Enthalpy conductance as a function of axial position, for a range of recovery temperature offset values, as computed by LeMANS (solid lines) and NAT (dashed lines). Chamber pressure is 4.48 MPa.

boundary condition calculations, it is necessary to estimate the temperature of the nozzle wall adjacent to the flow. To explore the sensitivity of the enthalpy conductance to the assumed wall temperature, three different wall temperature profiles are considered. The profiles correspond to a wall temperature offset of 100 K, 500 K, and 1000 K below the local recovery temperature; chamber pressure is 4.48 MPa.

Several observations can be readily made from the results presented in Figure 7.4. The first is that the values for enthalpy conductance as predicted by NAT are higher than those predicted by LeMANS. The exact cause for this discrepancy is unclear, but is almost certainly due to the widely different methods employed. It is expected that the results from LeMANS are more accurate, since the underlying flow physics are being modeled with more rigor. NAT simulations of the Kolozsi nozzle (see Section 6.2.4) also over-predict the convection coefficient; LeMANS provides better agreement. Another observation that can be made is that the assumed wall temperature has a significant impact on the magnitude of the predicted enthalpy

Table 7.1: Time step schedule used for decoupled simulations.

Time, s	Δt, s
0.0	1.0×10^{-6}
1.0×10^{-5}	1.0×10^{-5}
1.0×10^{-4}	1.0×10^{-4}
0.001	0.001
0.5	0.01
1.0	0.1

conductance; lower wall temperatures yield higher enthalpy conductance values. It is also observed that the enthalpy conductance as computed with LeMANS is more sensitive to wall temperature than the NAT results. Again, the exact cause for this discrepancy is not clear, but is most likely due to LeMANS capturing more details of the nozzle flowfield.

The main conclusions that can be made from this comparison are that wall temperature has a strong impact on enthalpy conductance, and that accurate wall temperature values are required in order to obtain accurate enthalpy conductance values. This underscores the importance of being able to perform fully-coupled, conjugate analyses of the nozzle flowfield and ablation response. All ablation analyses presented in this work use convective heating conditions computed with the LeMANS flow solver.

Ablation response simulations use a variable time step according to the schedule presented in Table 7.1, which makes it possible to capture early transient effects while not using an unnecessarily small time step later in the simulation.

7.3.1 Radiation Study

This analysis is conducted to determine the impact of stream radiation on the thermal response of the nozzle. One simulation includes radiative heat transfer, using the correlation for the stream emissivity as discussed in Section 3.7; in the second simulation, radiation is neglected. For this study, when computing the convective heating conditions with LeMANS, the wall temperature is assumed to be 1000 K below the local recovery temperature (i.e. $T_w = T_r - 1000\,\mathrm{K}$). The thermal response at the surface of the throat is plotted in Figure 7.5, where it can be seen that including stream radiation increases the throat surface temperature by about 73 K, or about 2.9 %. The surface temperature distribution is compared at select instances in time in Figure 7.6. Generally, including radiation results in higher surface temperatures, especially upstream of the throat, where the differential can be several hundred degrees. However, during the ramp-down at the end of the simulation, including radiation causes the surface temperature to drop more rapidly than if radiation is neglected.

Surface recession at the throat is compared in Figure 7.7. Including stream radiation increases surface recession at the throat by only about 4 %. The surface recession distribution is compared at select instances in time in Figure 7.8. The presence or absence of radiation has almost no impact on recession downstream of the throat, but does make a noticeable difference in the converging portion of the nozzle.

What these comparisons suggest is that, assuming that the correlation for the stream emissivity is accurate, stream radiation has minimal impact on the thermal response and ablation of the throat or downstream regions of the nozzle. However, it does appear that stream radiation can have a significant effect in the motor chamber and upstream portions of the nozzle, for solid rocket motors with aluminized propellants.

7.3.2 Wall Temperature Study

This analysis is performed to determine the impact that the assumed wall temperature (when computing the convective boundary conditions) has on the thermal response of the nozzle. Three different temperature profiles are considered. The first profile assumes a wall temperature that is 1000 K below the local recovery temperature, while the second profile assumes an offset of only 500 K. The third profile is that

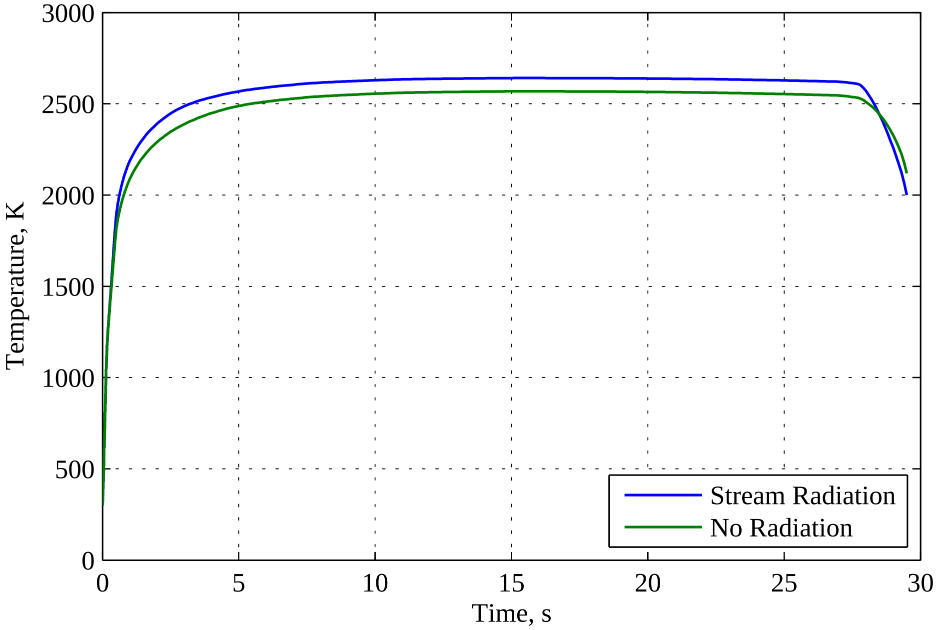

Figure 7.5: Surface temperature at the throat of the HIPPO nozzle as a function of time, for simulations including radiation (blue) and excluding radiation (green).

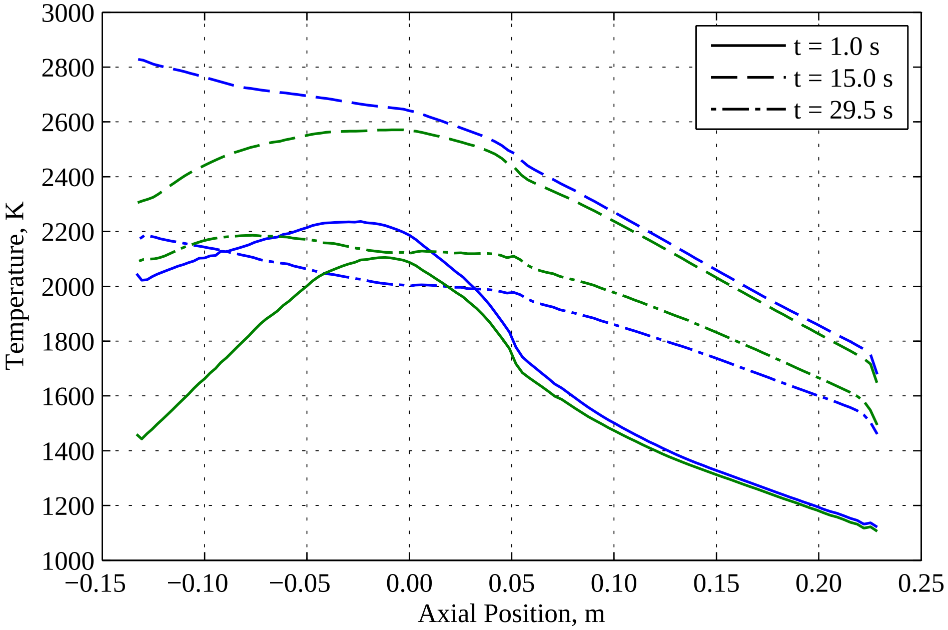

Figure 7.6: Comparison of surface temperature distribution at select instances in time for the HIPPO nozzle simulation with (blue) and without (green) radiation.

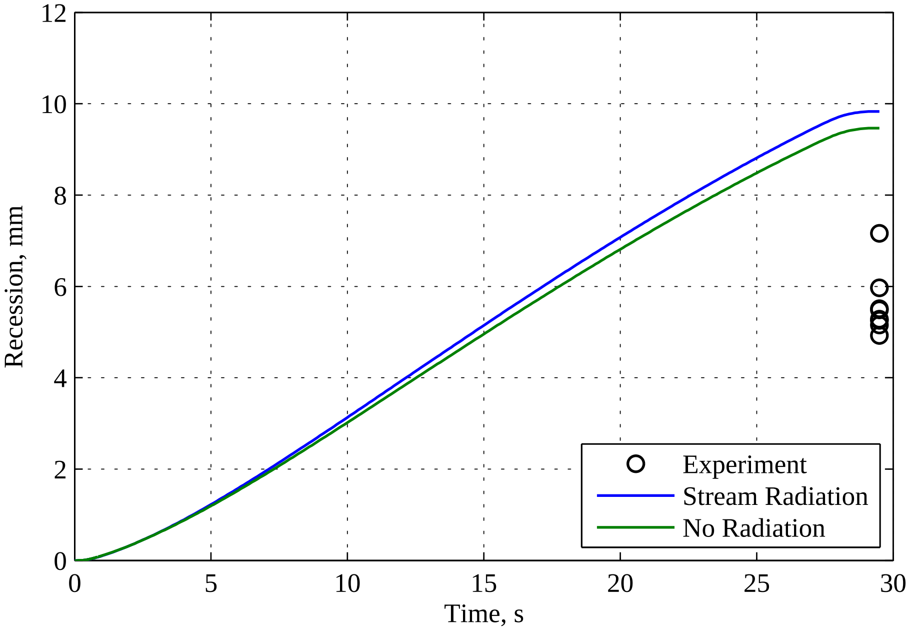

Figure 7.7: Surface recession at the throat of the HIPPO nozzle as a function of time, for simulation with (blue) and without (green) radiation. Symbols represent the final surface recession measured at the conclusion of the experiment.

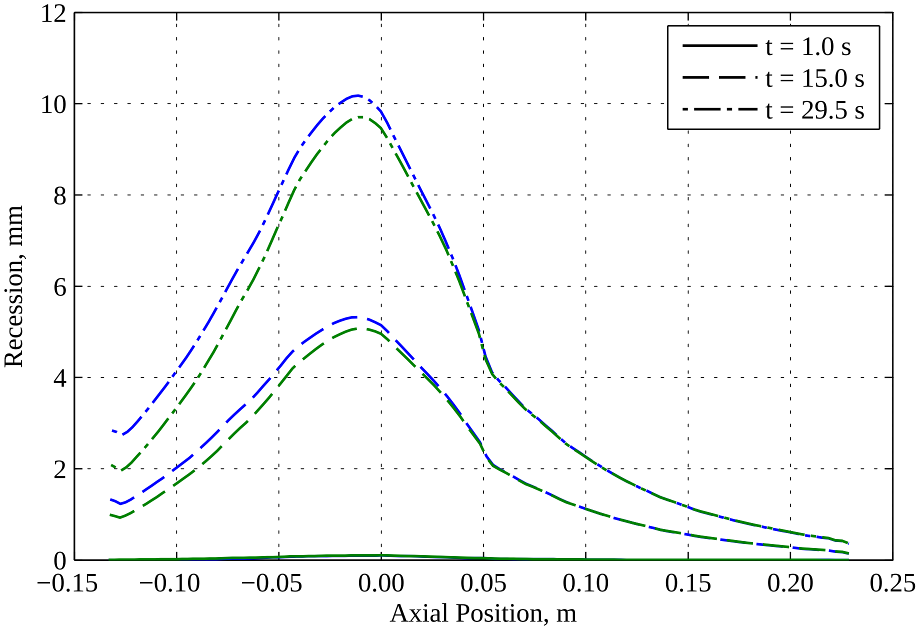

Figure 7.8: Comparison of surface recession distribution at select instances in time for the HIPPO nozzle simulation with (blue) and without (green) radiation.

obtained from a MOPAR-MD simulation of the HIPPO nozzle (at $t = 15\,\text{seconds}$). This third simulation therefore represents a very loosely-coupled approach for determining the interdependence of wall temperature and convective boundary conditions. The three wall temperature profiles are compared in Figure 7.9; representative enthalpy conductance profiles are compared in Figure 7.10. Stream radiation is computed using the methodology described in Section 3.7.

The surface temperature profiles from these three simulations are compared for select instances in time in Figure 7.11. It is observed that the assumed wall temperature profile used to compute the convective boundary conditions has minimal impact on the surface thermal response at the throat and upstream portions of the nozzle. Downstream of the throat, however, there are some differences. It can also be observed that the first two profiles considered yield quite similar results; the choice of offset value from the local recovery temperature does not greatly affect the thermal response of the nozzle. However, the third wall temperature profile produces a significantly different thermal response in the downstream portion of the nozzle, predicting surface temperatures that are up to about 200 K greater than predicted based on the first two profiles.

Surface recession profiles are compared at select instances in time in Figure 7.12. This plot suggests that the choice of wall temperature profile used when computing the convective boundary conditions has a significant impact on the predicted nozzle ablation (surface recession). The surface recession profiles predicted with the first two temperature profiles have very similar shape, but the magnitude of the recession is greater (by about 15 % at the throat) for the simulation that used an offset of 1000 K versus the simulation that assumed an offset of 500 K. The third simulation predicted the highest surface recession overall, but especially in the downstream portion of the nozzle.

These comparisons indicate that the thermal response of a nozzle is somewhat

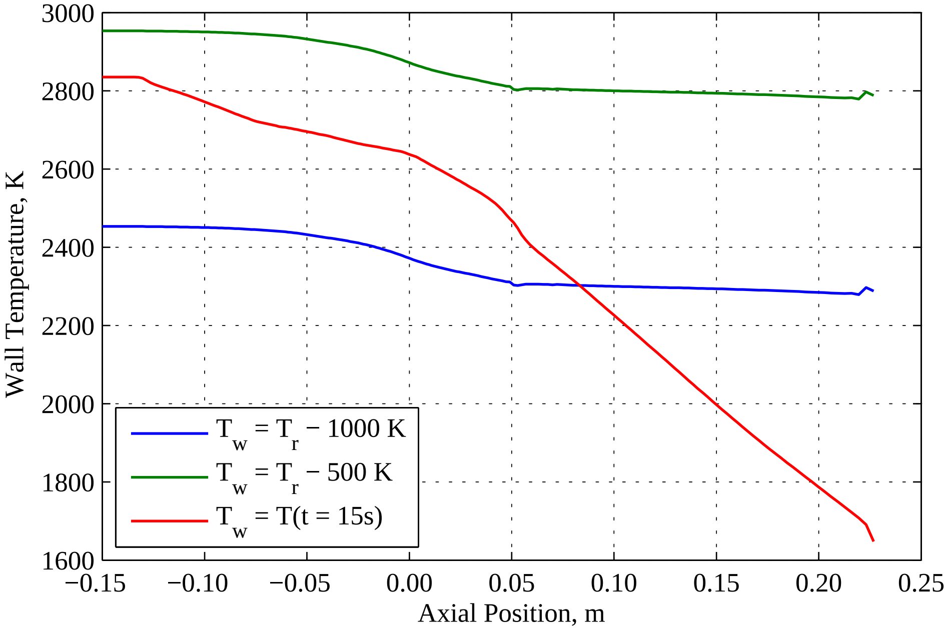

Figure 7.9: Comparison of the wall temperature profiles used for the wall temperature comparison study.

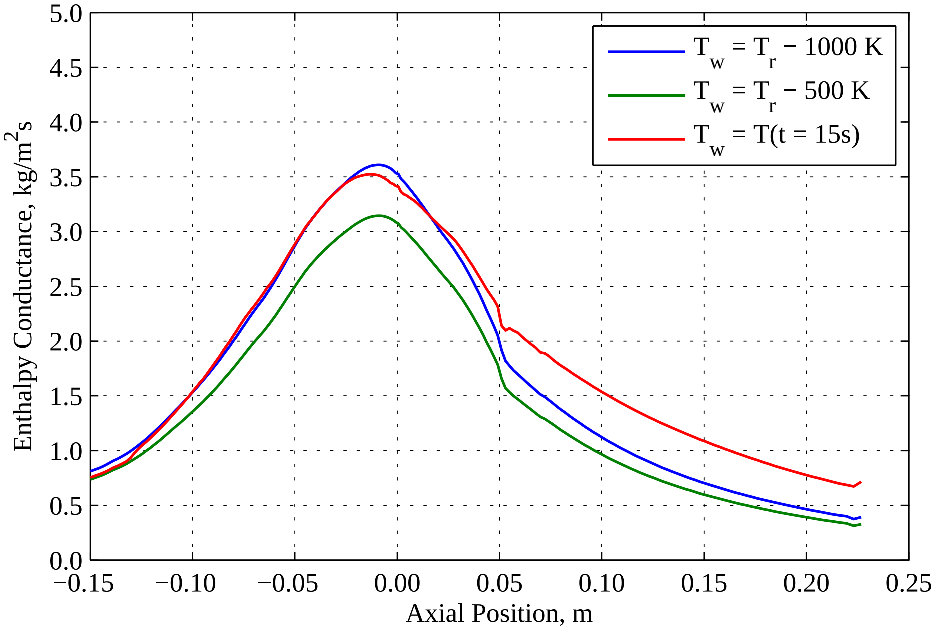

Figure 7.10: Comparison of enthalpy conductance as computed with LeMANS for the three different wall temperature profiles. Chamber pressure is 4.48 MPa.

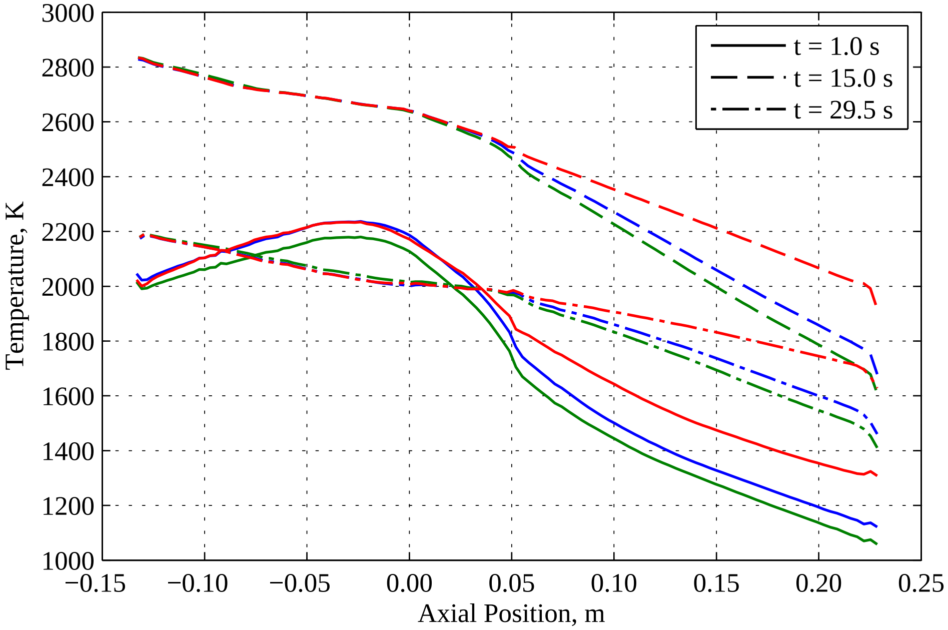

Figure 7.11: Comparison of surface temperature distribution at select instances in time for the HIPPO nozzle simulation using enthalpy conductance computed with $T_w = T_r - 1000\,\mathrm{K}$ (blue), $T_w = T_r - 500\,\mathrm{K}$ (green), and $T_w = T\,(t = 15\,\mathrm{s})$ (red).

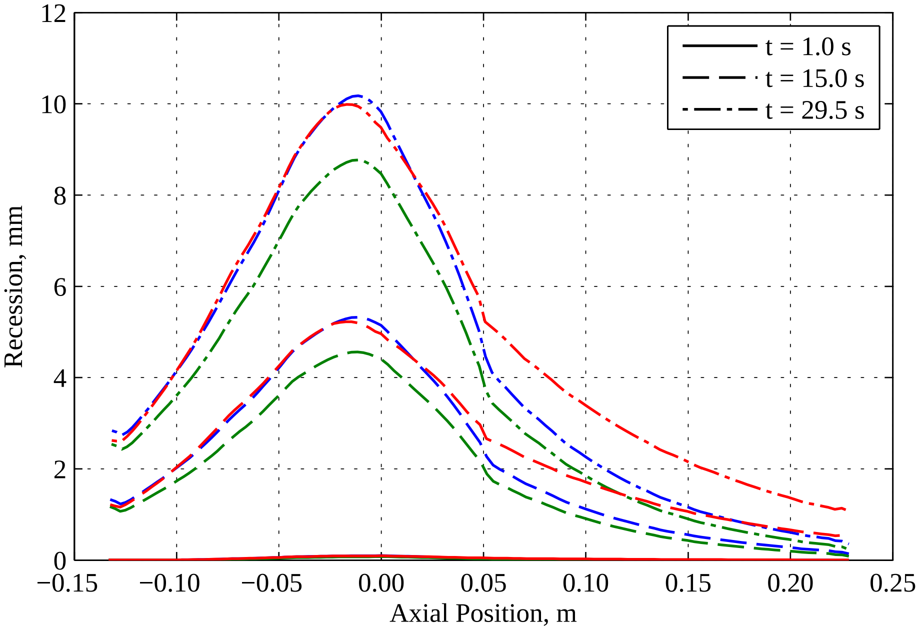

Figure 7.12: Comparison of surface recession distribution at select instances in time for the HIPPO nozzle simulation using enthalpy conductance computed with $T_w = T_r - 1000\,\mathrm{K}$ (blue), $T_w = T_r - 500\,\mathrm{K}$ (green), and $T_w = T\,(t = 15\,\mathrm{s})$ (red).

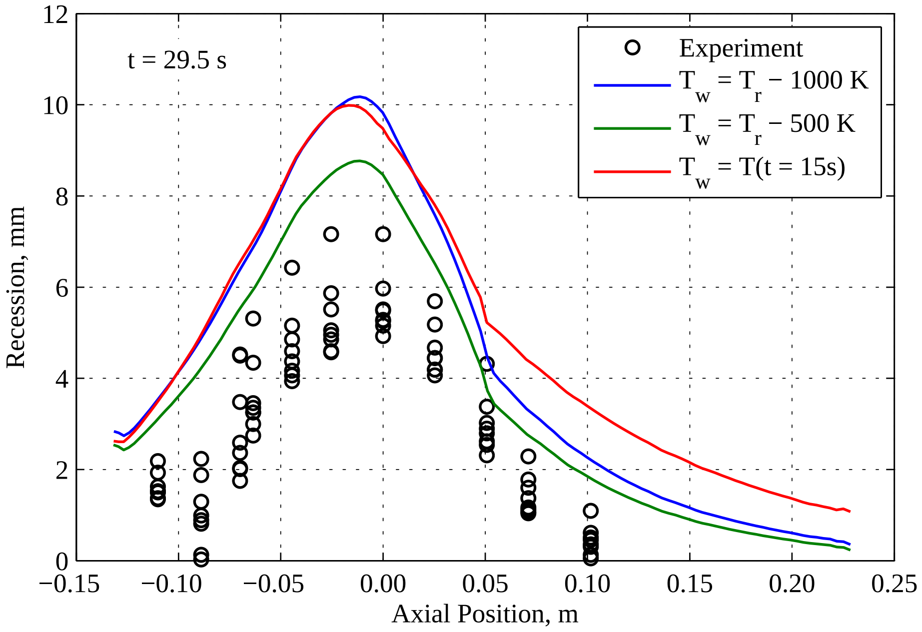

Figure 7.13: Comparison of predicted and measured surface recession the end of the HIPPO motor firing, for the wall temperature study.

dependent upon the assumed wall temperature profile used to compute convective boundary conditions, and that the surface recession response of the nozzle is quite sensitive to the assumed profile. These observations support the hypothesis that it is necessary to perform fully-conjugate, coupled flowfield / ablation simulations in order to accurately capture the thermal response and ablation of rocket nozzles.

Surface recession at the end of the motor firing as predicted by these decoupled analyses is compared to experimental measurements in Figure 7.13. It is observed that the decoupled analyses significantly over-predict surface recession for the entire length of the nozzle. This large discrepancy between the experimentally-measured surface recession and the predicted value could be the result of a number of potential causes. It is possible that the material model used in the analysis does not accurately represent the actual material used in the experiment. Part of the discrepancy could be caused by swelling of the material, for which there is some experimental evidence [5], but is not included in the model. This analysis assumed a unity Lewis number when computing the surface energy balance and recession rate. However, in reality, the Lewis number for a rocket motor is less than one, which means that the mass transport coefficient will actually be less than the heat transport coefficient. This would reduce the extent of the surface recession. The convective boundary conditions used in this analysis are all computed based on the original geometry. However, surface recession obviously modifies the nozzle geometry, which could lead to reduced enthalpy conductance values. Additionally, the wall temperature profiles used by the flow solver when computing the enthalpy conductance are different from the actual thermal response of the nozzle; this can lead to over-prediction of the convective heating conditions. Finally, in this analysis, equilibrium surface chemistry is assumed; if finite-rate chemistry were to occur at the surface this would lead to reduced surface recession. Many of these factors are addressed with the conjugate analyses presented in Section 7.4.

7.3.3 Baseline Analysis

A new decoupled analysis is performed to provide a more reasonable baseline for comparing to the results from conjugate simulations. This decoupled simulation uses the improved geometric model for the HIPPO nozzle (Section 7.2.2), and uses the same time step schedule employed for the conjugate simulations (see Table 7.2).

The general approach taken for this decoupled analysis is to use the same methodology that might be used as the first step in a traditional, decoupled analysis. Wall temperature is set to be a uniform 3000 K (which is about 500 K less than the chamber temperature) when computing the convective heating conditions. This is consistent with the first iteration of a traditional analysis, and provides a well-defined baseline for comparisons. However, enthalpy conductance (and the resultant thermal response) was shown in Section 7.3.2 to be sensitive to the choice of wall temperature when computing boundary conditions. As a result, this baseline decoupled analysis likely under-predicts the thermal response downstream of the throat, where wall temperatures are expected to be significantly less than the assumed constant value.

Recovery enthalpy is assumed to be uniform along the length of the nozzle, and is taken to be the stagnation enthalpy corresponding to each pressure. This is a small departure from the typical approach, where separate simulations using an adiabatic wall boundary condition are performed to obtain a local recovery enthalpy value. The main justification for using the stagnation enthalpy instead of a local recovery enthalpy is to be consistent with the conjugate analyses, where only a stagnation enthalpy value is available. Stagnation enthalpy is greater than the local recovery enthalpy, so this assumption will mitigate to some extent the under-prediction caused by using a constant wall temperature.

Radiation is neglected from this baseline decoupled analysis (and from all conjugate analyses presented in this dissertation). The main reason for this assumption is to prevent radiation from masking differences between the decoupled and the conjugate simulations, and between the different surface energy balance methods investigated with the conjugate analyses. Additionally, it was shown in Section 7.3.1 that radiation has only a small impact on the thermal response at or downstream of the throat (though radiation does make a significant impact upstream of the throat).

Surface recession at the end of the motor firing as predicted by this decoupled analysis is compared to experimental measurements in Figure 7.14. It is observed that the decoupled analysis over-predicts recession in the region upstream of the nozzle throat. Possible causes for this over-prediction include the unity Lewis number assumption made as part of the surface energy balance, and the inability to capture the effects of recession (modified geometry) on the enthalpy conductance. Downstream of the throat better agreement is achieved. However, this is likely fortuitous, and is believed to be caused by the expected under-prediction of enthalpy conductance in this region.

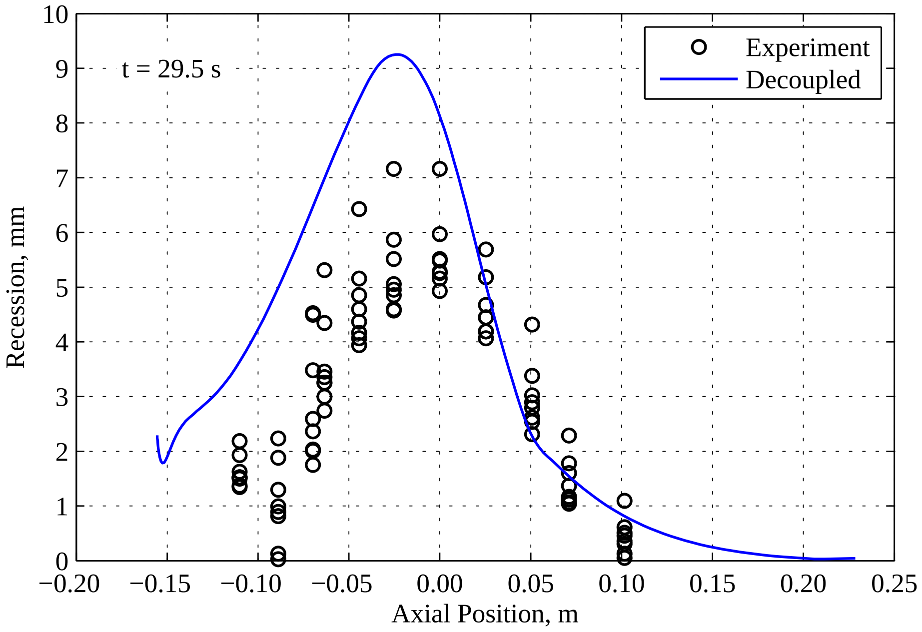

Figure 7.14: Comparison of predicted and measured surface recession at the end of the HIPPO motor firing, for the baseline decoupled analysis.

To help the reader better visualize the ablation response of the HIPPO nozzle, contour plots of temperature, pyrolysis gas pressure, and degree of char at $t = 15.0\,\text{s}$ are presented in Figure 7.15. The gray, shaded region indicates material removed due to recession. The thermal response of the nozzle is limited to a thin region adjacent to the nozzle surface; most of the nozzle material does not experience a temperature rise. The carbon-phenolic material protects the substructure very well. In the middle image, a band of relatively lower pressures can be observed adjacent to the wall, while larger pressures occur deeper in the material. This is due to the increased permeability of the char relative to the virgin material. The pressure gradient is predominately in the wall-normal direction, but there is a noticeable axial component visible near the throat. The region of very high pressures near the nozzle nose is due to constraints placed on the pyrolysis gas by the impermeable upper wall and by the vertical ply orientation. The bottom image illustrates how pyrolysis occurs in a very narrow region, which results in very high solid density gradients.

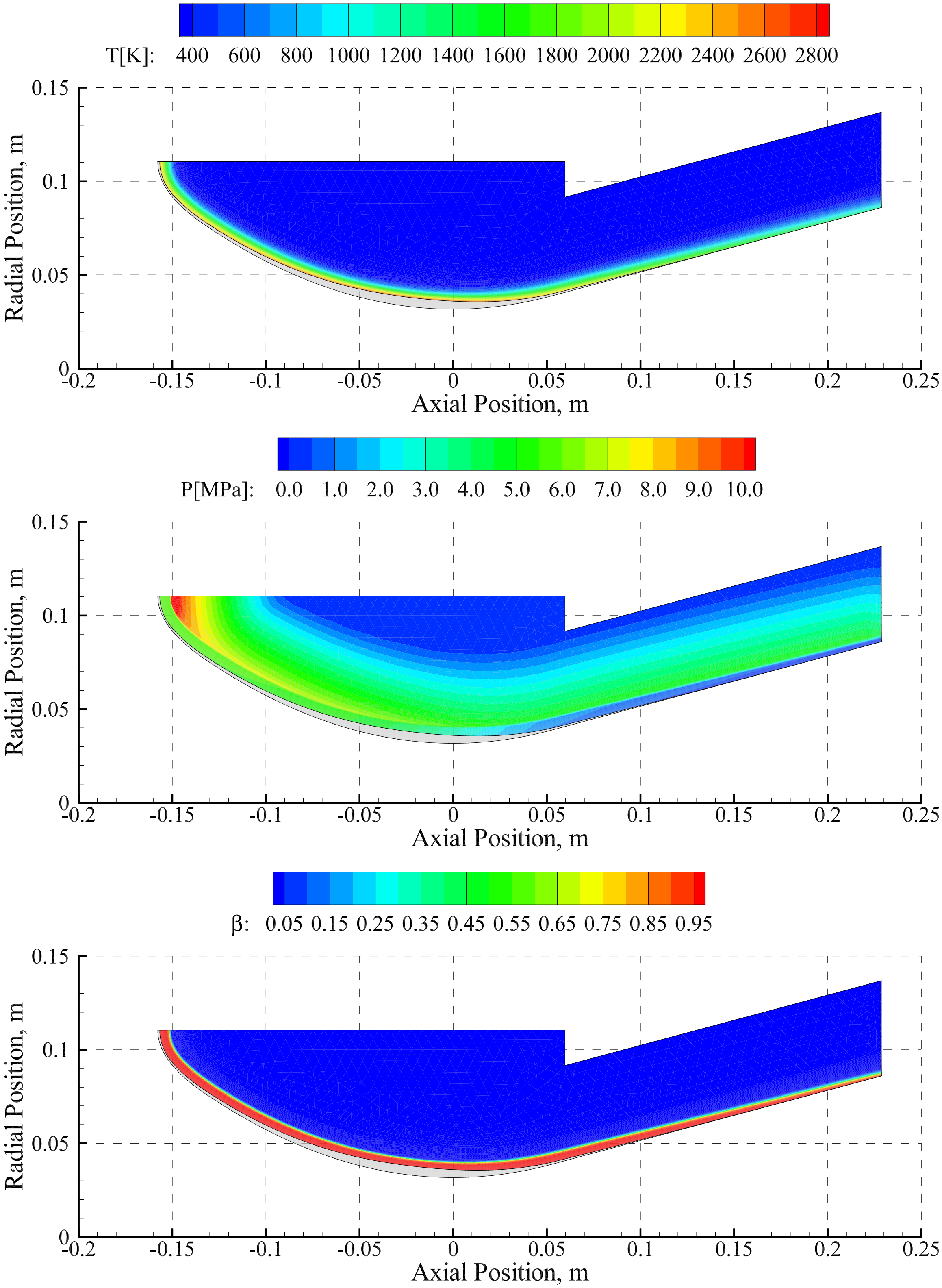

Figure 7.15: Contour plots of temperature (top), pressure (middle), and degree of char (bottom) at $t = 15.0\,\mathrm{s}$, for the baseline decoupled analysis.

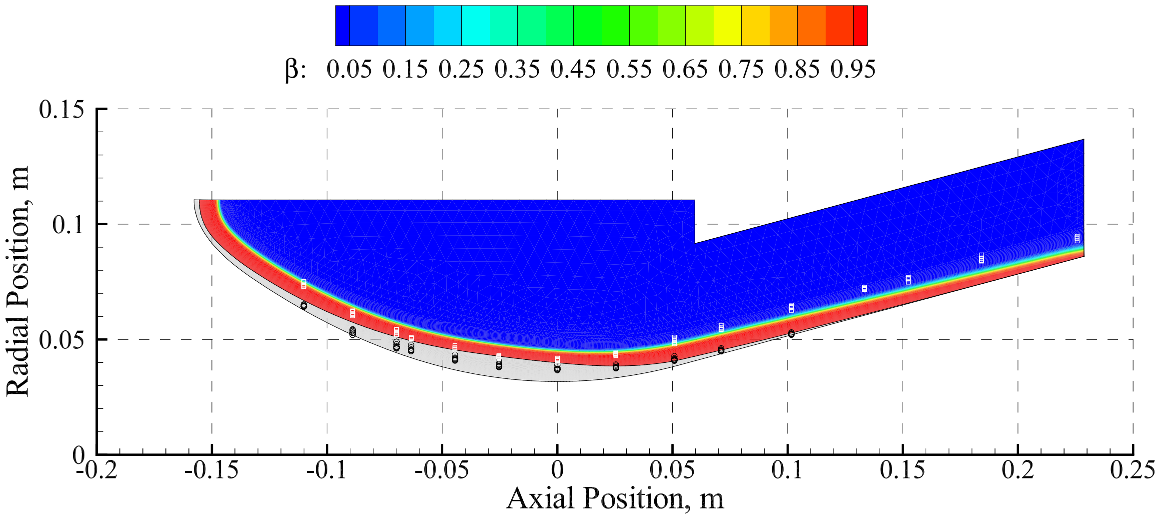

Figure 7.16: Comparison of surface recession and char depth, for the baseline decoupled analysis.

The final ($t = 29.5\,\mathrm{s}$) nozzle shape and degree of char predictions from the baseline decoupled analysis are compared to the experimentally measured surface recession (black circles) and char depths (white squares) in Figure 7.16. As has already been discussed, the baseline analysis over-predicts surface recession along most of the nozzle. Additionally, from this plot it can be seen that the predicted final shape of the nozzle is different from the experimental results. For example, the predicted location of the nozzle throat appears to shift to an axial position of about 0.025 m in the baseline simulation, while the throat position appears to be essentially unchanged in the experiment. This difference is likely caused by not accounting for the effects that the change in shape will have on the heating conditions. Conjugate simulations will be able to capture the effects of this shape change. The char depth in the exit cone also appears to be under-predicted relative to the experimental results. This is most likely due to the expected under-prediction of the convective heating conditions in the exit cone for this decoupled analysis.

Table 7.2: Time step schedule used for conjugate simulations.

Time, s	Δt, s
0.0	1.0×10^{-6}
1.0×10^{-5}	1.0×10^{-5}
1.0×10^{-4}	1.0×10^{-4}
0.001	0.001
0.01	0.01
1.0	0.05

7.4 Conjugate Analyses

Multiple conjugate ablation analysis studies are performed. The first study investigates factors impacting convergence of the conjugate solution. An additional study is performed to determine the effect that time point spacing has on the conjugate simulation results. A shape change instability preventing completion of the conjugate simulations, and various approaches towards its resolution, are then discussed. A final study compares the different surface energy balance treatments, and includes simulations employing instability-suppressing techniques.

Material response simulations for these conjugate analyses use a variable time step according to the schedule presented in Table 7.2. This time step schedule is very similar to that used by the decoupled analyses, the single change being made only so that time points for the conjugate analyses can be more precisely located.

7.4.1 Convergence Study

A study is performed to investigate the impact that the under-relaxation factor has on the convergence of the conjugate solution, and to identify the optimum value to use. Conjugate simulations are performed for the first time point ($t = 0.2\,\mathrm{s}$) for the initial model of the HIPPO nozzle (Section 7.2.1) using the Noncatalytic Wall – Heat Flux (NCHF) surface energy balance method (see Section 4.3.1). Four different under-relaxation values are considered ($\psi = 1.0, 0.75, 0.5, 0.2$) and are applied to the wall temperature and mass flux. Under-relaxation is not applied to the wall position for this study. Convergence of the conjugate solution at this time point is presented in Figure 7.17 and Figure 7.18. The RMS average heat flux on the ablating wall is plotted in Figure 7.17 as a function of the call to the material response solver. Figure 7.18 gives the percent RMS difference between the wall temperature predicted by the material response solver and the wall temperature actually used by the flow solver, which is an excellent measure of the convergence of the conjugate solution.

It can be seen from these plots that using an under-relaxation factor $\psi = 1.0$ (i.e. directly applying new wall values from the material response solver) causes oscillations in the average heat flux, and delays convergence. However, using too low of an under-relaxation factor also delays convergence of the conjugate solution, which can be most clearly seen by looking at the curve for $\psi = 0.2$ in these plots. The optimum under-relaxation factor for this case appears to be $\psi = 0.75$, which provides very rapid convergence, as can be clearly seen in Figure 7.18.

A second study is conducted to determine the effect that flowfield development has on convergence of the conjugate solution. This is investigated by varying the CFL number ramp and the minimum number of flowfield iterations between calls to the material response solver. Results from this study are presented in Figure 7.19. It is discovered that obtaining adequate development of the flowfield between calls to the material response solver is important for obtaining rapid convergence of the conjugate solution. For the simulations using the "10×" CFL ramp (in which the CFL number is ramped from 0.1 to 500 over 5000 iterations), it is found that requiring 2000 flow iterations between material response calls provides better convergence than requiring only 1000 iterations between calls. However, there is negligible added benefit from requiring 4000 flow iterations between calls. Increasing the CFL ramp by an additional factor of ten ("100×"; CFL number is ramped from 1.0 to 500 over 500 iterations) causes the flowfield to develop much more rapidly. As a result, 1000

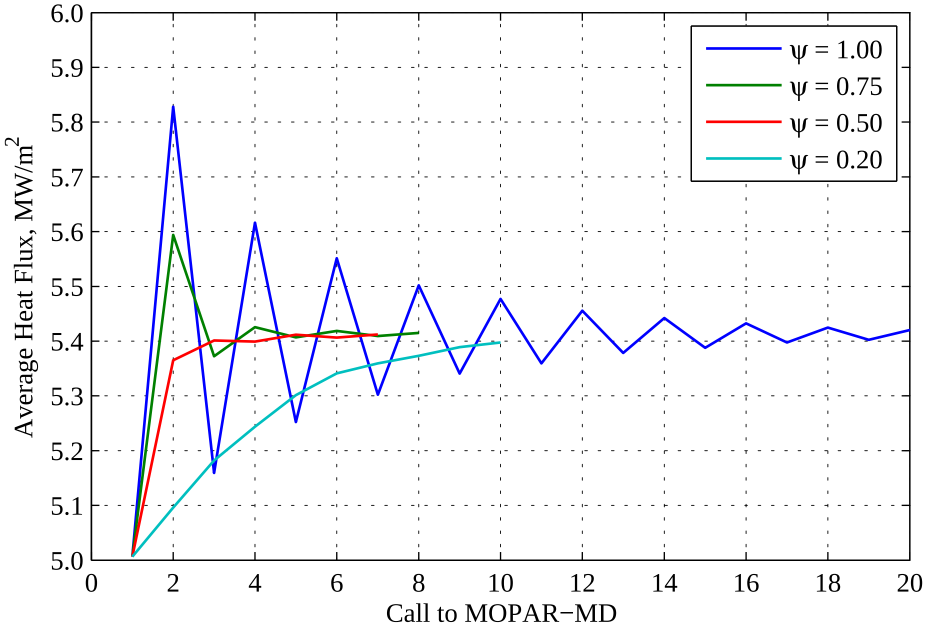

Figure 7.17: Average heat flux on the ablating boundary, as a function of the call to the material response solver and the under-relaxation factor ψ.

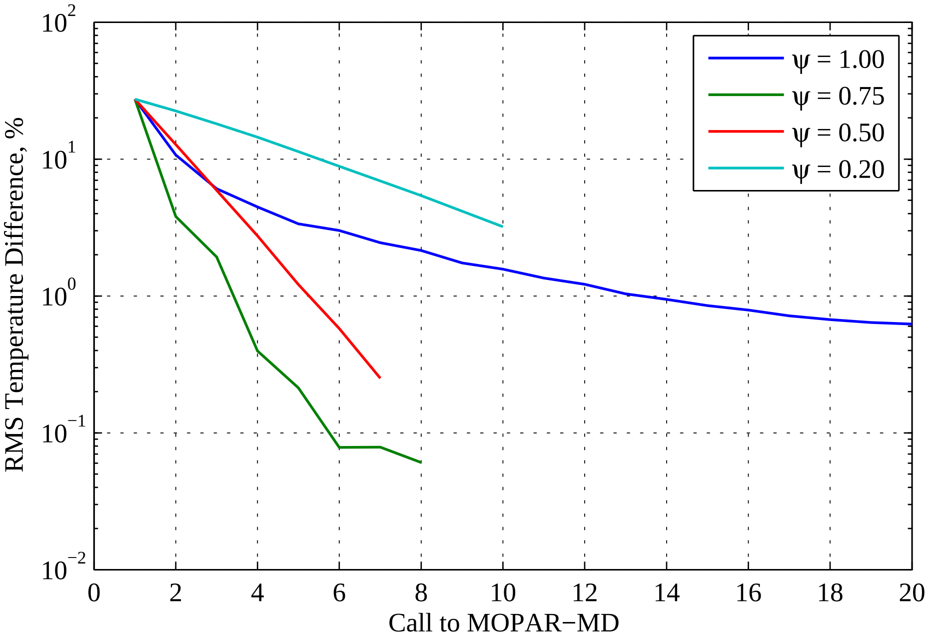

Figure 7.18: Percent root mean square difference between the wall temperature predicted by the material response solver and the wall temperature used on the flowfield boundary, as a function of the call to the material response solver and the under-relaxation factor ψ.

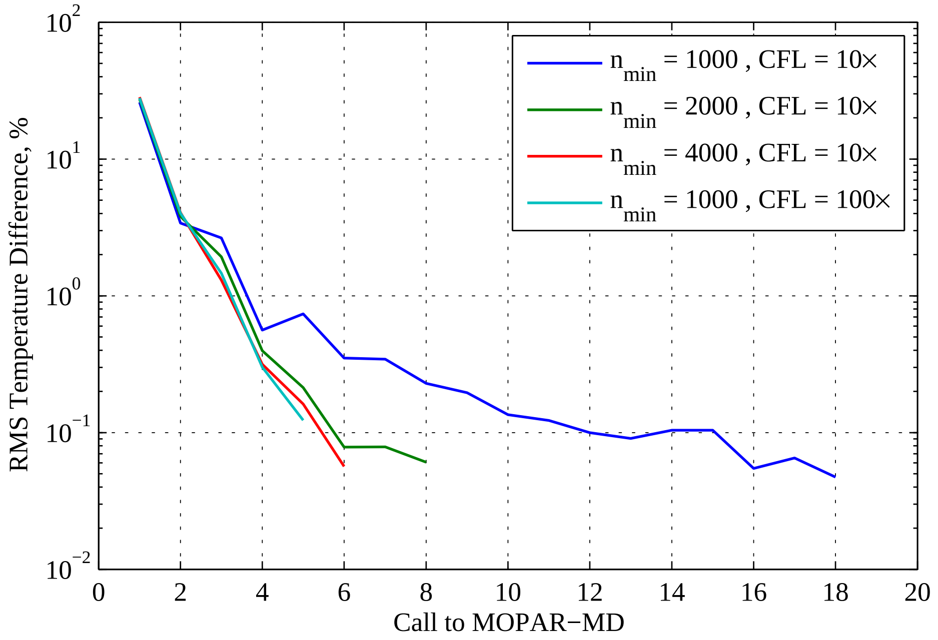

Figure 7.19: Percent root mean square difference between the wall temperature predicted by the material response solver and the wall temperature used on the flowfield boundary, as a function of the call to the material response solver and the minimum number of flowfield iterations between calls.

flow iterations between calls to the material response solver is sufficient for good convergence.

The heat flux convergence metrics (corresponding to Eqs. 4.3 and 4.4) are presented in Figure 7.20 as a function of flow solver iteration, for the simulation using $\psi = 0.75$, the “10×” CFL ramp, and requiring a minimum of 2000 flow iterations between material response calls. (This simulation appears in both convergence studies just presented.) The spikes in these convergence metrics correspond to the instances when MOPAR-MD is called to update the ablating wall conditions. The final call to the material response solver (occurring at about 17,000 iterations) is made just over 3000 iterations after the preceding call, an interval in excess of the minimum requirement of 2000 iterations. This final call to MOPAR-MD is made because the value of $\Delta\dot{q}''_{RMS}$ (the change in the RMS heat flux since the preceding call to MOPAR-MD) exceeded the threshold value of $\varepsilon_{\dot{q}''_{RMS}} = 0.1\,\%$ used in this simulation. After this

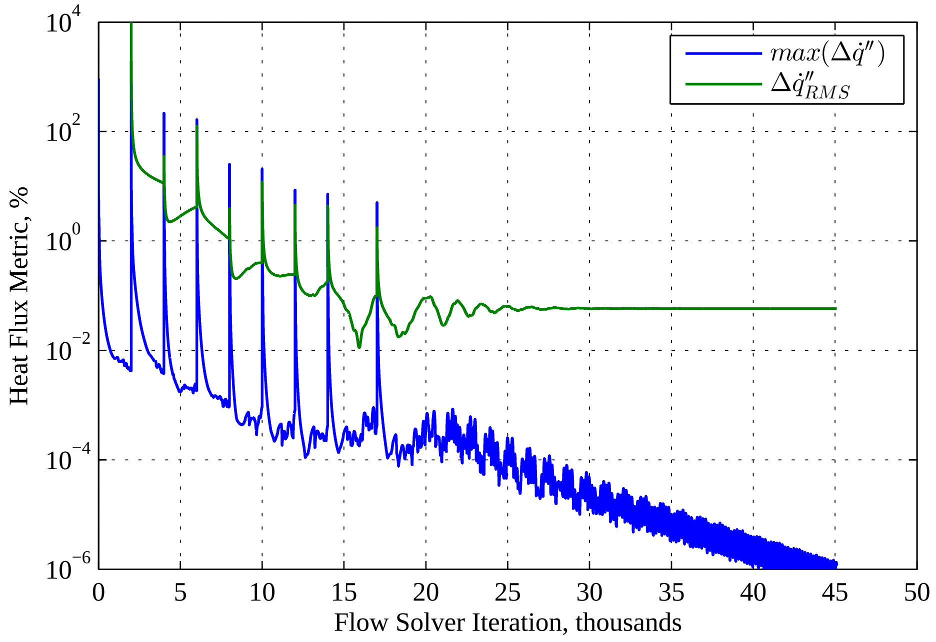

Figure 7.20: Heat flux convergence metrics as a function of flow solver iteration.

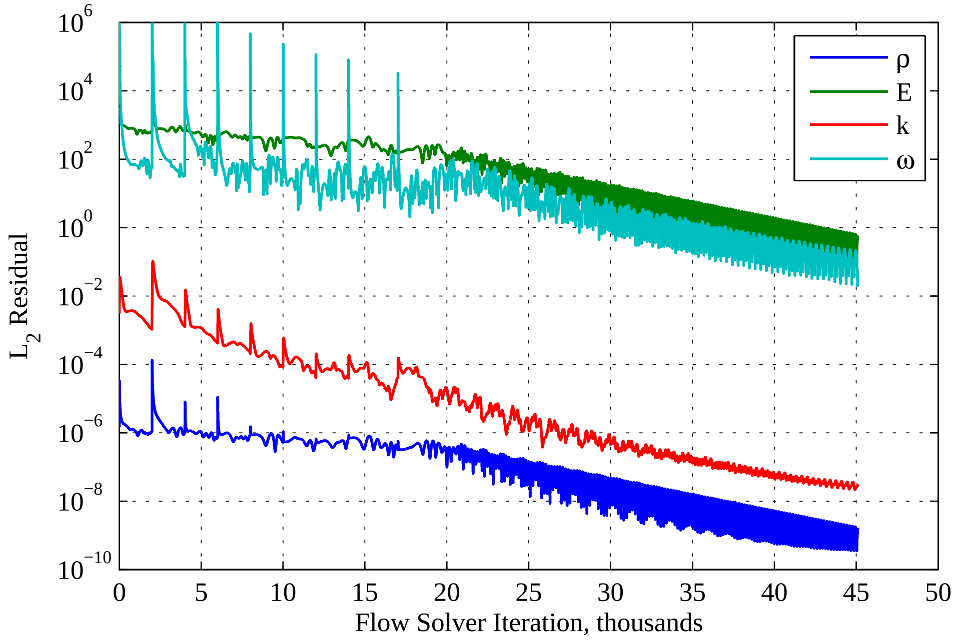

Figure 7.21: Select flow solver residuals as a function of flow solver iteration.

point, the RMS heat flux computed by the flow solver is always within 0.1 % of the value used for the final call to the material response solver, and additional calls to MOPAR-MD are not required.

Select L_2 norm flow solver residuals (for the density, total energy, turbulent kinetic energy, and turbulent specific dissipation) are presented as a function of flow solver iteration for this simulation in Figure 7.21. Again, spikes in these residuals correspond to the instances when the material response solver is called. Minimal drop in residual values is observed for the first half of the simulation. This is partly due to the lower CFL values used during the ramp period that occurs after each call to the material response solver. After the final call to MOPAR-MD, a steady drop in residual values is experienced once the maximum CFL number is reached. It should also be noted that the initial condition for this simulation is a well-converged solution for a given wall temperature profile. Large changes in residuals at the beginning of this simulation, as might be encountered for a simulation with a cruder initialization, are therefore not expected. While the residuals continue to drop several orders of magnitude after the final call to the material response solver, this results in negligible change in the heat flux on the ablating boundary, as shown in Figure 7.20.

For the computational framework used in this dissertation, it is necessary to manually terminate a simulation at a given time point and launch the subsequent time point simulation. By monitoring the flow solver residuals (e.g. Figure 7.21), the heat flux convergence metrics (e.g. Figure 7.20), and the percent RMS difference between the wall temperature predicted by the material response solver and the wall temperature actually used by the flow solver (e.g. Figures 7.18 and 7.19), it is possible to determine when convergence of the conjugate solution has been achieved (i.e. when the final call to the material response solver has been made, or when additional calls to the material response solver will result in only negligible changes to the ablating wall conditions). Once this point has been reached, the simulation can be manually terminated (if not manually terminated, the flow solver will continue to run until some specified maximum number of iterations have been completed). The simulation for the subsequent time point can then be started.

7.4.2 Time Point Spacing Study

Due to the high computational cost associated with these conjugate simulations (it could take over 24 hours of run time, on 36 Intel Xeon X5650 processors with a clock speed of 2.66 GHz, to obtain a converged solution for a given time point), it is desirable to minimize the number of time points required for a given pressure trace. A study is performed to determine the impact that time point spacing has on the predicted ablation response of the nozzle. Two conjugate simulations are performed using the NCEC surface energy balance treatment. One simulation uses a variable time point schedule with relatively small intervals between time points, as plotted as the red curve in Figure 7.3. Time points are closely spaced at the beginning of the conjugate simulations in order to capture the early transients, while the spacing is increased with time, in order to minimize the number of time points analyzed. The interval between time points is selected so that the changes in pressure, heat flux, and temperature at the nozzle throat (as obtained from the decoupled analysis described in Section 7.3.3) between time points are approximately equal. The other simulation uses a time point schedule with large intervals; this corresponds to time point schedule used for the decoupled analyses and represented by the green curve in Figure 7.3.

Surface temperature at the nozzle throat as a function of time as computed by these two conjugate simulations is compared in Figure 7.22; surface recession is compared in Figure 7.23. Other than during the very early transient portion of the simulation ($t < 0.5\,\mathrm{s}$), there is very good agreement between the two simulations. The simulation with smaller intervals between time points appears to be better able

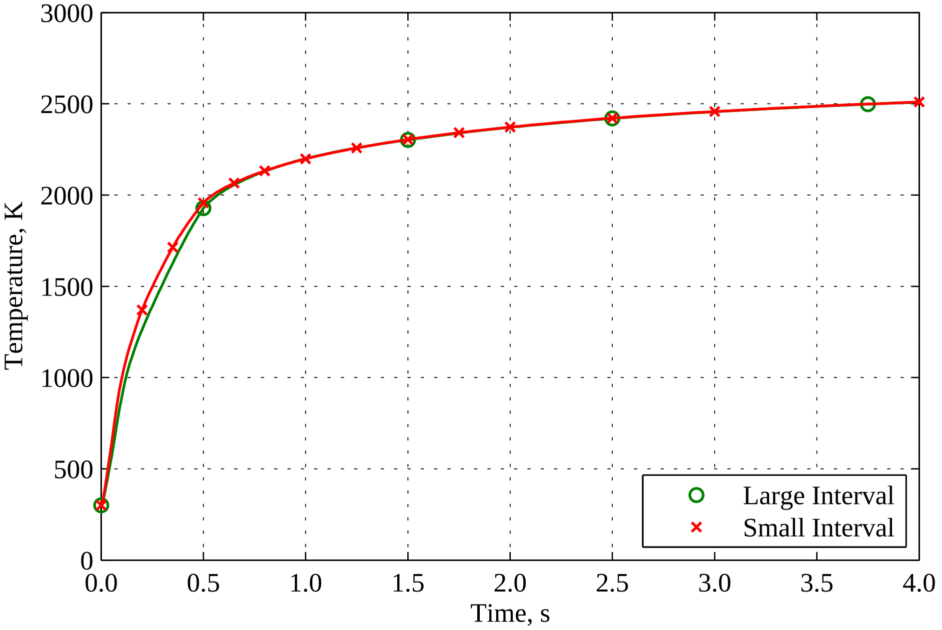

Figure 7.22: Surface temperature at the throat of the HIPPO nozzle as a function of time, as computed by the conjugate simulations using different time point intervals.

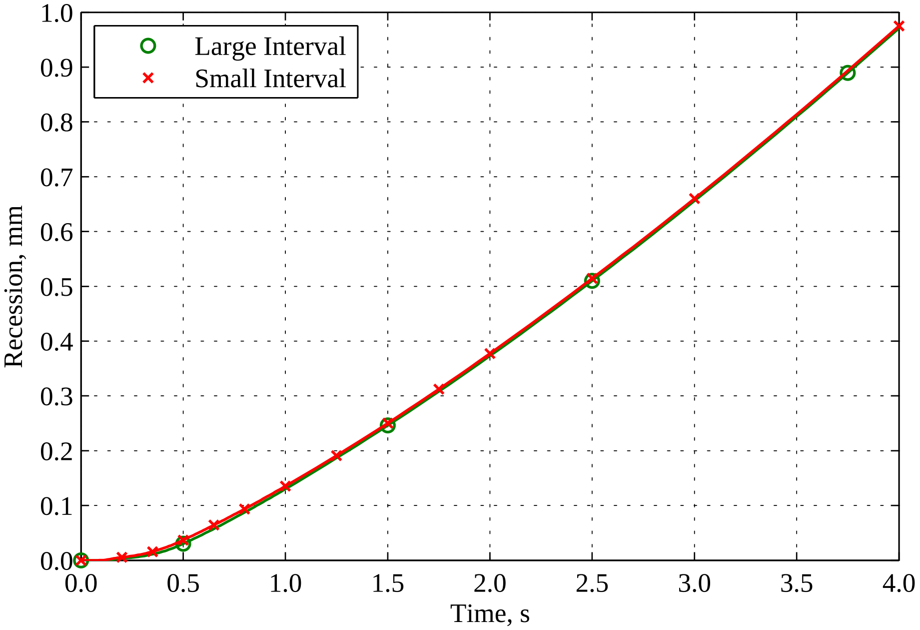

Figure 7.23: Surface recession at the throat of the HIPPO nozzle as a function of time, as computed by the conjugate simulations using different time point intervals.

to resolve the thermal response during the initial transient portion of the motor operations, which is as would be expected. However, this early transient period is not of primary importance in this present work. More important is the surface recession prediction at the end of the simulation, which does not appear to be noticeably affected by how well the initial transient is captured. The time point schedule with larger intervals therefore appears to be suitable for use in this work.

The time required to obtain a converged solution at each time point is increased significantly (up to two or three days) for the schedule with larger intervals. This is due to the increased duration of the transient ablation analysis associated with each time point. However, the number of time points required for a complete simulation is greatly reduced, which more than offsets this increased cost for each time point. The time point schedule with larger intervals is observed to work very well for simulations using the SEB treatments that pass enthalpy conductance to the material response solver (i.e. NCEC and AWEC). However, simulations using SEB treatments that pass a heat flux (i.e. AWHF and IESC) cannot successfully be completed with these large intervals between time points. With these methods, it is necessary to use a time point schedule with smaller spacings (in fact, it has not been possible to increase the time point spacing above 0.5 s for these methods).

7.4.3 Shape Change Instability

When initially performing conjugate ablation simulations of the HIPPO nozzle, stability issues were encountered. At later time points in the coupled simulations, instabilities were encountered that produced large, nonphysical spikes in the heat flux and other parameters, as illustrated in Figure 7.24. This instability is related to the coupling of the solvers; both the flow solver and material response solver remain stable. The instability appears to be related to capturing the change in geometry due to ablation. It is discussed in some detail in the literature [10, 89], and appears to be a characteristic of virtually all conjugate ablation simulations that update the flow domain to capture changes in geometry due to ablation. Results presented by other researchers [27, 28, 114] also appear to illustrate the onset of this instability, but these simulations were not advanced far enough in time for the instabilities to become a problem.

The root cause of this instability appears to be small perturbations in the geometry that arise due to the nonlinear nature of ablation. These perturbations in the surface geometry produce corresponding changes to the local heat flux, which in turn affect the local ablation response, and tend to amplify the perturbation until a non-physical solution is obtained. Kuntz et al. [10] were able to suppress this instability by linearly interpolating conditions between time points (instead of assuming constant conditions between points) and by using under-relaxation. However, the results presented suggest that the instability was not completely eliminated, and might have become problematic again if simulation was extended further in time. Gnoffo and Johnston [89] used a five-node stencil to smooth the geometry; this suppressed, but did not eliminate, the instability.

Multiple actions are taken in this dissertation in an attempt to eliminate the shape change instabillity. Both techniques used by Kuntz et al. to suppress the instability are implemented in this work (as described in Chapter IV). Additionally, fixes and improvements to the mesh-to-mesh interpolation scheme are made (discussed in Section 4.4), and a smoothing algorithm utilizing a five-node stencil is implemented (as discussed in Section 4.5). The improved HIPPO geometric model (Section 7.2.2) is also created to rectify some defects in the initial model. These efforts are able to significantly suppress the shape-change instability (onset now occurs at $t = 11\,\mathrm{s}$ as illustrated in Figure 7.25, vs. full instability at $t = 2.5\,\mathrm{s}$ as shown in Figure 7.24), but are found to be insufficient to completely resolve this issue.

The porous flow of the pyrolysis gases through the char appears to influence the

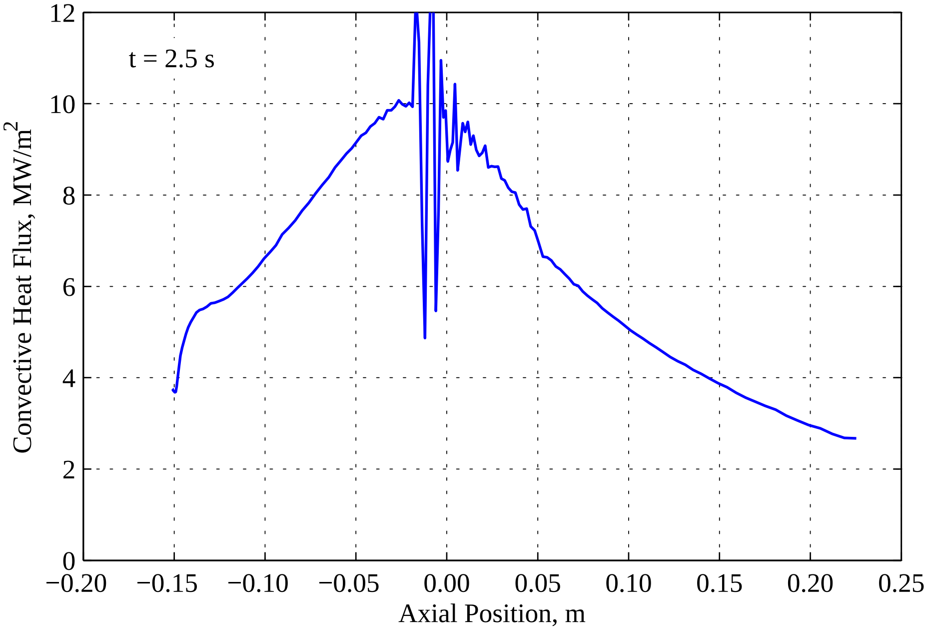

Figure 7.24: Heat flux profile illustrating effects of the shape change instability, from an early simulation.

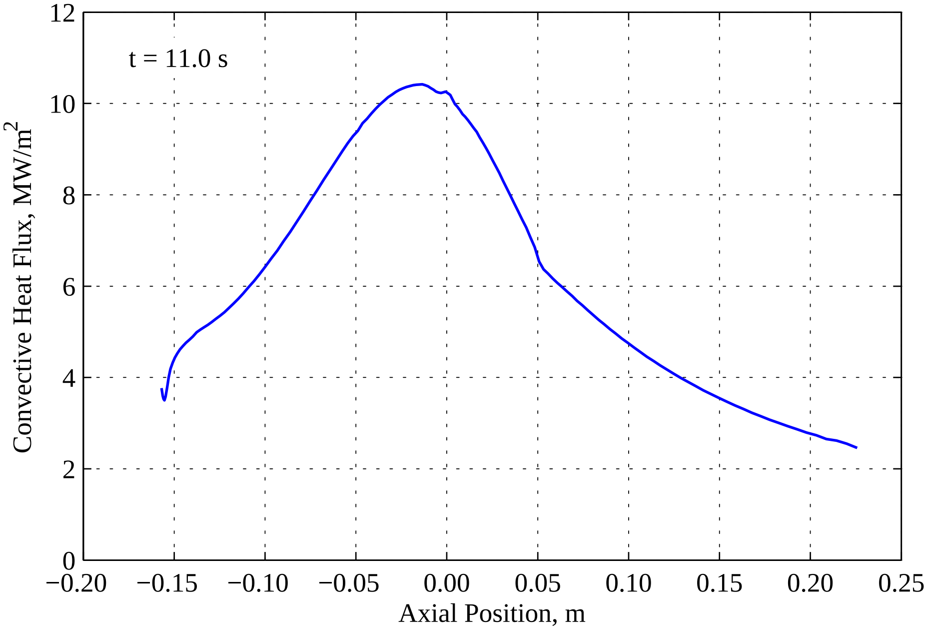

Figure 7.25: Heat flux profile illustrating onset of shape change instability at $t = 11.0\,\mathrm{s}$, after implementation of instability suppression techniques.

shape change instability. Figure 7.26 illustrates the pyrolysis gas mass flux profile in the vicinity of the nozzle throat, while convective heat flux for the same region is shown in Figure 7.27. For the conjugate simulation with unconstrained flow of the pyrolysis gases (blue curve), the large, non-physical oscillations in the pyrolysis gas mass flux correlate to the oscillations observed in the heat flux profile. Char mass flux and recession rate are strongly affected by the pyrolysis gas mass flux. All else being equal, an increase in pyrolysis gas mass flux will result in a decrease in char mass flux. Distortions in the pyrolysis gas mass flux profile can therefore be expected to, in turn, cause defects in the recession profile. Distortions in the recession profile will, in turn, affect the local heat flux, amplifying the instability.

There is a small “plateau” feature observed near the throat in the pyrolysis gas mass flux profile obtained from the baseline decoupled simulation, presented as a black dashed line in Figure 7.26. This is a physical feature that is produced by the strong axial pressure gradient at the throat, the converging-diverging nozzle geometry, and the orientation of the plies of the material. In the conjugate simulations, this small plateau feature is being amplified into the aforementioned large, non-physical oscillations. The mechanism for this amplification is unknown, but it is believed to be at least partially related to the stacked, anisotropic, triangular mesh topology that must be employed to capture the strong wall-normal gradients in the solid material. Since MOPAR-MD is a serial code, it is currently unaffordable to perform conjugate simulations that use meshes constructed from isotropic triangles. Quadrilateral mesh elements would be preferable, but these are not currently supported by the material response solver (and implementation of this capability would be non-trivial).

To try to suppress the growth of this instability, simulations are performed in which the pyrolysis gases are forced to flow in the wall-normal direction. This is accomplished by computing a separate material orientation angle (for permeability) at each node in the mesh. This angle is computed such that the material plies at

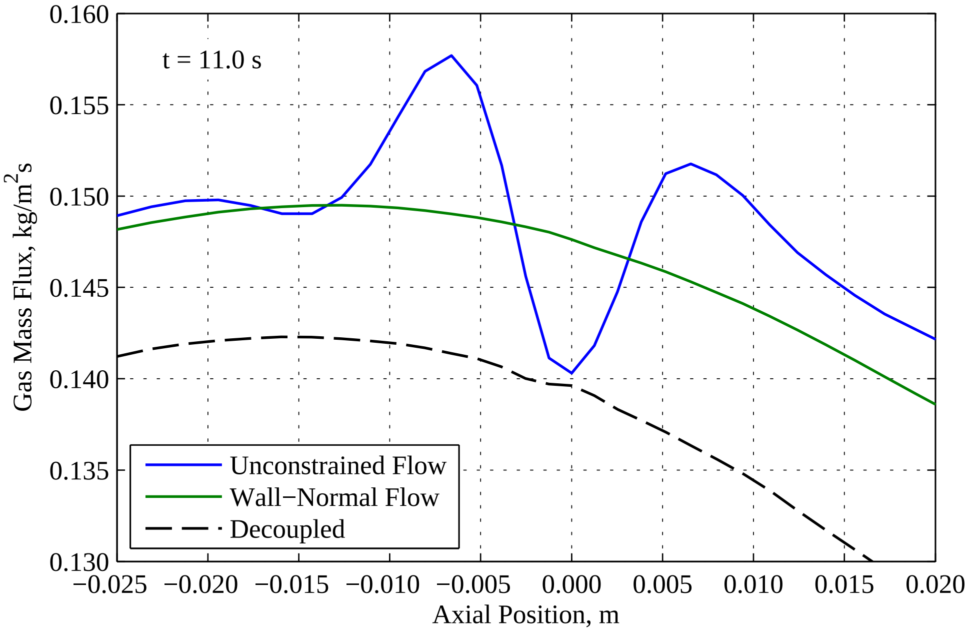

Figure 7.26: Pyrolysis gas mass flux distribution near throat at $t = 11.0\,\mathrm{s}$, as computed by the decoupled analysis and by conjugate simulations with and without constraints on porous flow.

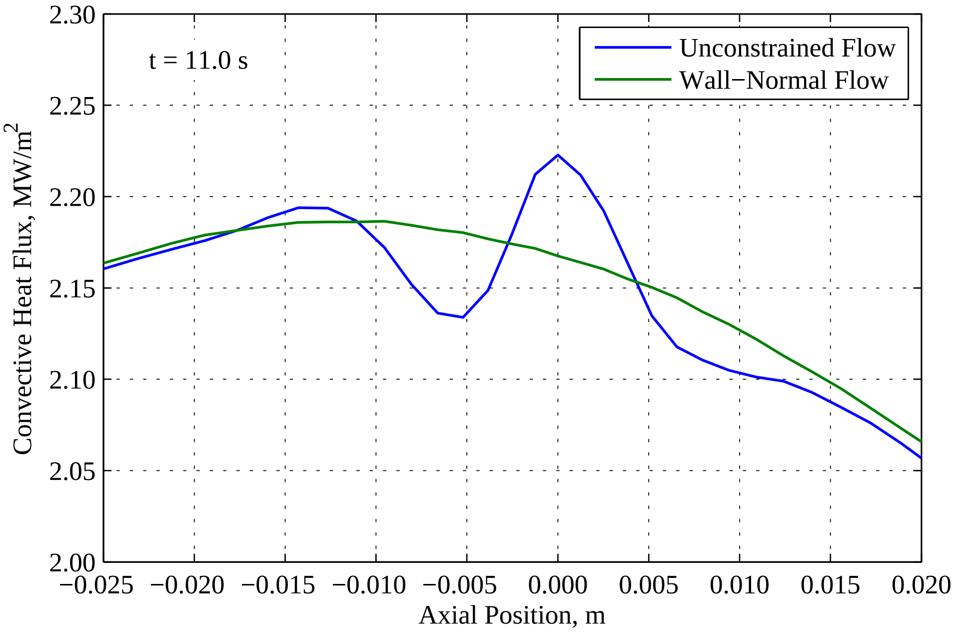

Figure 7.27: Convective heat flux distribution near throat at $t = 11.0\,\mathrm{s}$, as computed by conjugate simulations with and without constraints on porous flow.

each node point to the closest node on the ablating wall (the approximate wall-normal direction). The cross-ply permeability is also reduced to a very low value ($K_\perp = 1.0 \times 10^{-40}\,\mathrm{m}^2$) to prevent pyrolysis gases from crossing plies. Note that the anisotropic thermal conductivity is not adjusted.

A decoupled simulation is first performed to determine the impact that forcing the pyrolysis gases to flow in the wall-normal direction has on the ablation response of the nozzle. Surface temperature distribution from this simulation is compared to the results from the baseline simulation (which had unconstrained flow of the pyrolysis gases) in Figure 7.28; pyrolysis gas mass flux is compared in Figure 7.29. It is observed that constraining the pyrolysis gas flow to the wall-normal direction has negligible impact on the surface temperature, and relatively small impact on the pyrolysis gas mass flux predictions. It therefore appears that the pyrolysis gases can be forced to flow in the wall-normal direction without strongly affecting the ablation response of the HIPPO nozzle test case. (However, this may not hold for all test cases, and forcing wall-normal pyrolysis gas flow is not a preferred long-term solution.) Conjugate simulations using this technique (see Section 7.4.4) show significantly increased suppression of the shape change instability, as can be observed from the green curve plotted in Figure 7.26 and Figure 7.27.

7.4.4 Surface Energy Balance Treatment Study

Conjugate flowfield / ablation analyses are performed for the HIPPO nozzle using the five surface energy balance approaches described in Section 4.3. The improved HIPPO geometric model (Section 7.2.2) is used for these simulations. When possible, the time point schedule with large intervals is used, but for methods based on heat flux (NCHF, AWHF, and IESC) it is necessary to use the schedule with smaller spacing between time points. Initial simulations model the flow of the pyrolysis gases as being unconstrained (i.e. the gases are not forced to flow in the wall-normal

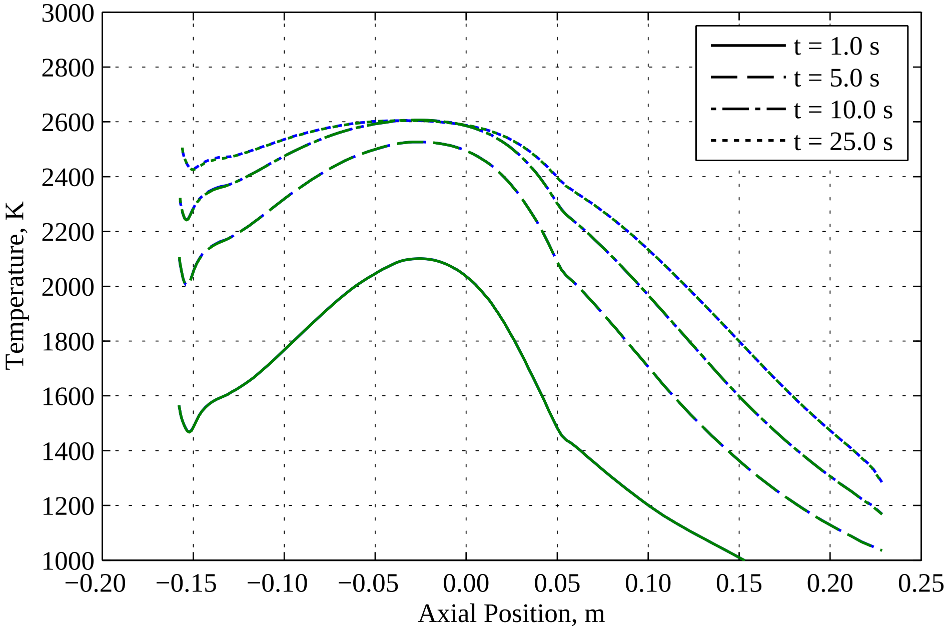

Figure 7.28: Comparison of surface temperature distribution at select instances in time for the decoupled HIPPO nozzle simulation with unconstrained (blue) and wall-normal (green) porous flow.

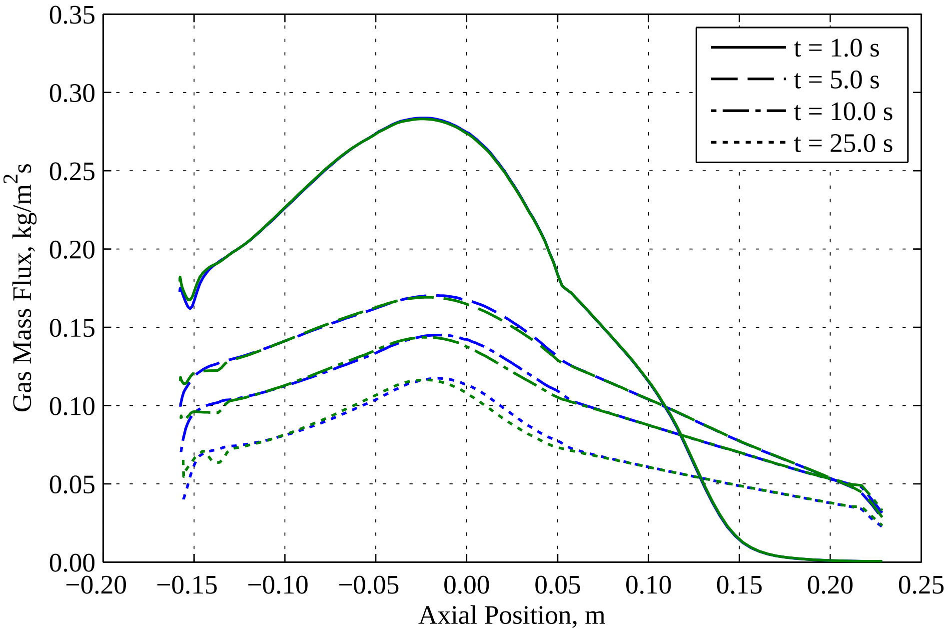

Figure 7.29: Comparison of pyrolysis gas mass flux distribution at select instances in time for the decoupled HIPPO nozzle simulation with unconstrained (blue) and wall-normal (green) porous flow.

direction). These simulations cannot be completed for the full duration of the motor operation due to issues with a shape change instability (discussed in Section 7.4.3).

Most simulations use an under-relaxation factor of $\psi = 0.5$; higher values can be successfully used for the methods using a noncatalytic wall (NCHF and NCEC), but can be unstable for the other methods. For early time points it is sometimes necessary to drop the under-relaxation factor on the species mass fractions to $\psi = 0.25$. It is necessary to use the converged solution obtained with the AWHF method as the starting point for the IESC simulation for the first time point. A converged conjugate solution can be obtained after approximately 10 calls to the material response solver for the NCHF and NCEC methods, while the other methods require approximately 20 iterations.

Surface temperature at the nozzle throat as a function of time as computed by the conjugate simulations is compared in Figure 7.30 to results from the decoupled analysis. Surface temperature distribution at $t = 4.0\,\mathrm{s}$ is compared in Figure 7.31. Upstream of the throat, there is fairly good agreement between all simulations. However, at and downstream of the throat, all conjugate simulations predict a thermal response that is more severe (higher temperatures) than that predicted with the decoupled analysis. Most of this discrepancy can be attributed to the under-prediction of the enthalpy conductance for the decoupled analysis (due to the choice of wall temperature when computing the convective heating). This under-prediction would be most significant at and downstream of the nozzle throat. The NCHF method significantly over-predicts the thermal response due to the reasons discussed in Section 4.3.6. Since this method is found to be inappropriate for conjugate ablation analyses of rocket nozzles, simulations with this method are discontinued after $t = 1.0\,\mathrm{s}$. The NCHF treatment will not be considered further in this work. The AWHF, AWEC, and IESC methods are in very close agreement with each other, and produce thermal responses most similar to the decoupled analysis results. At early points in time, the

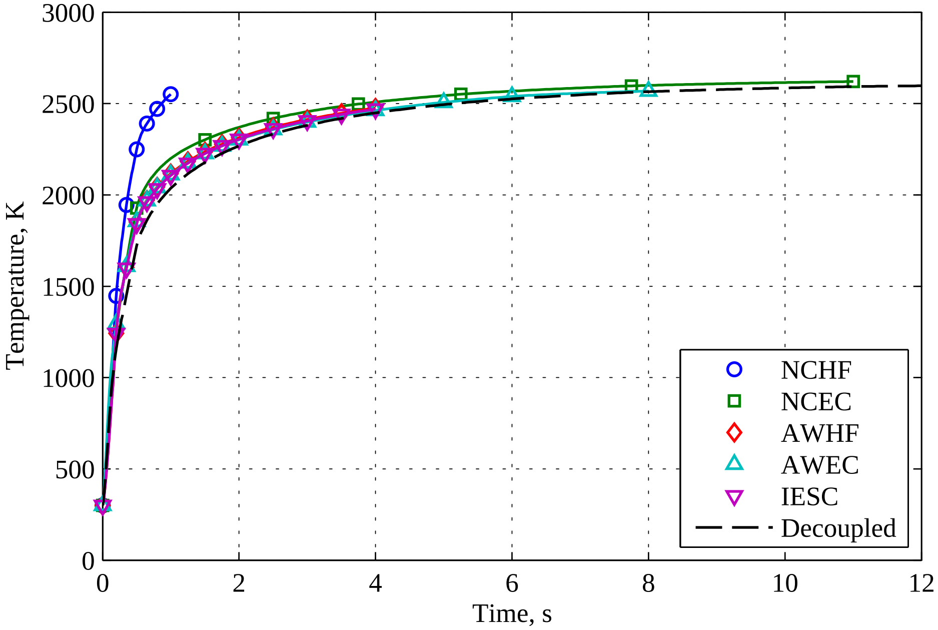

Figure 7.30: Surface temperature at the throat of the HIPPO nozzle as a function of time, as computed by the decoupled analysis and by conjugate simulations using the different surface energy balance approaches.

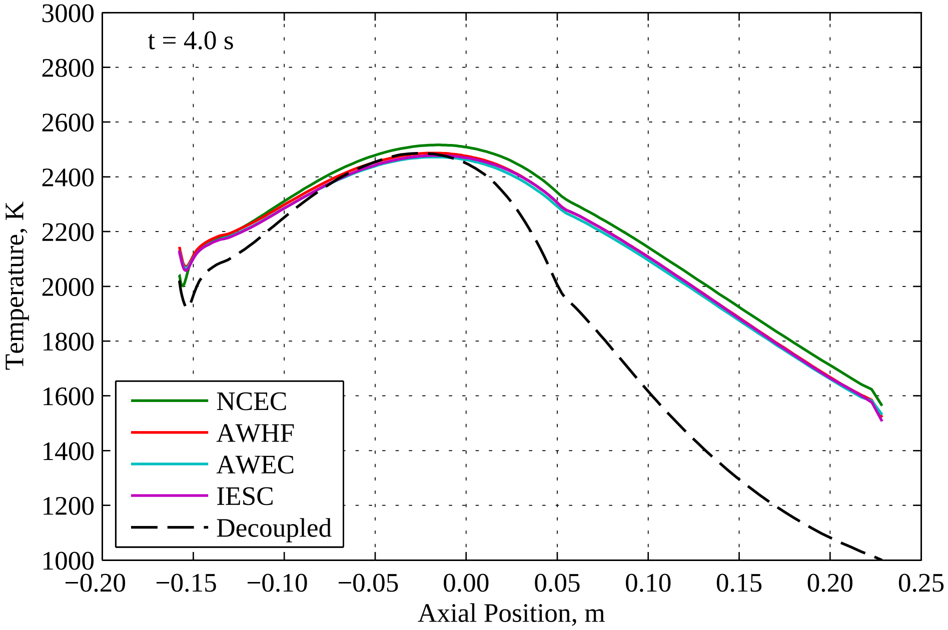

Figure 7.31: Surface temperature distribution within the HIPPO nozzle at $t = 4.0\,\mathrm{s}$, as computed by the decoupled analysis and by conjugate simulations using the different surface energy balance approaches.

NCEC method predicts a thermal response that is approximately 2 % higher than that obtained with the AWHF, AWEC, and IESC methods. This difference appears to diminish as time increases.

Surface recession at the nozzle throat is compared as a function of time in Figure 7.32. The NCHF method grossly over-predicts recession due to the over-prediction of both heat flux and enthalpy conductance, as discussed in section 4.3.6. Surface recession distribution at $t = 4.0\,\mathrm{s}$ is compared in Figure 7.33. The NCEC method provides more reasonable recession values, but still predicts recession values that are substantially greater than those obtained with the AWHF and AWEC methods. This difference is related to the fact that the NCEC method predicts enthalpy conductance values that are higher than those obtained with the AWHF and AWEC methods. Surface recession values as predicted by the AWHF and AWEC methods are nearly identical, and are in good agreement with the decoupled analysis results upstream of the throat. However, recession is still significantly over-predicted at and downstream of the throat. Of the conjugate simulation approaches, the IESC method predicts the lowest surface recession; the recession distribution is very similar to that obtained with the AWHF and AWEC methods, but shifted downwards. Upstream of the throat, the IESC method actually predicts less recession than that obtained with the decoupled analysis. At and shortly downstream of the throat, the IESC method over-predicts recession relative to the decoupled analysis, but good agreement is obtained between the two methods near the nozzle exit.

In an attempt to eliminate the shape change instability that affected these initial simulations, additional conjugate simulations are performed in which the pyrolysis gases are constrained to flow in the wall-normal direction (see Section 7.4.3). Only three surface energy balance treatments are considered: NCEC, AWEC, and IESC. The AWHF method is not considered, since it is shown above to produce results very similar to those obtained with the AWEC method, but at higher computational cost

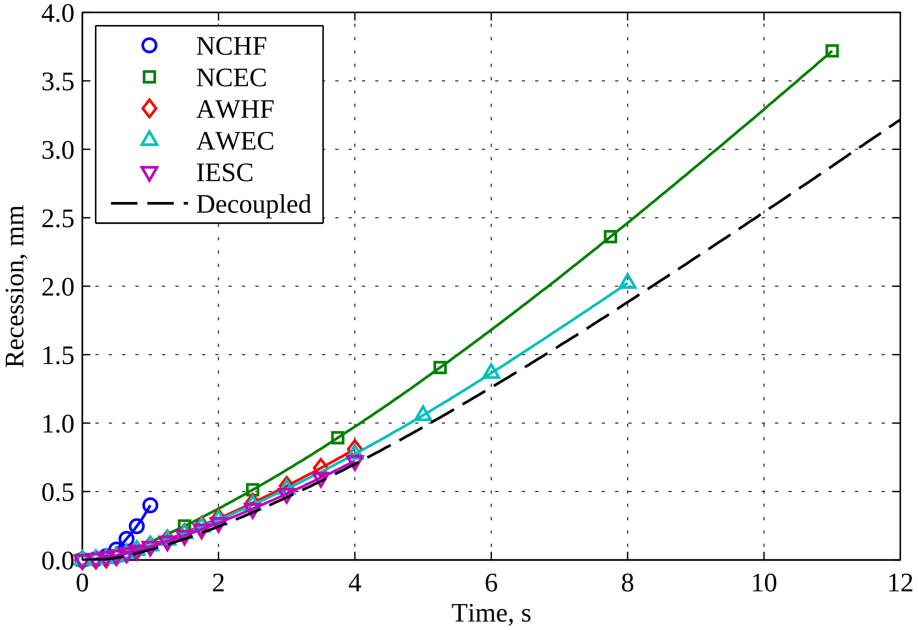

Figure 7.32: Surface recession at the throat of the HIPPO nozzle as a function of time, as computed by the decoupled analysis and by conjugate simulations using the different surface energy balance approaches.

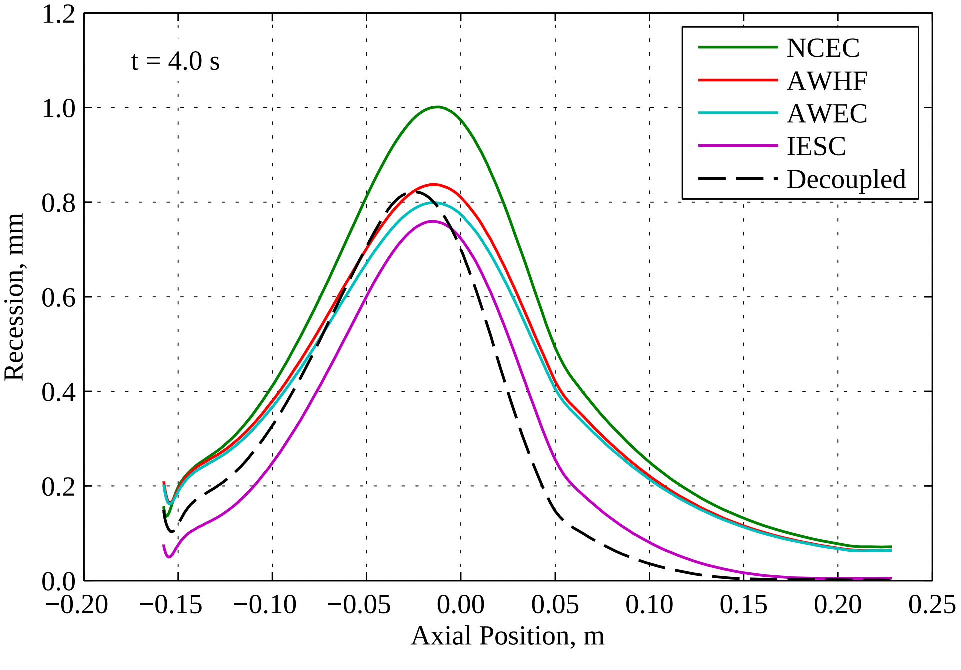

Figure 7.33: Surface recession distribution within the HIPPO nozzle at $t = 4.0\,\text{s}$, as computed by the decoupled analysis and by conjugate simulations using the different surface energy balance approaches.

(due to the smaller intervals required between time points). Simulations using the NCEC and AWEC methods use the time point schedule with relatively large intervals (green curve in Figure 7.3), while for the IESC method it is required to use much closer time point spacings (intervals cannot exceed 0.5 s).

The conjugate simulations using the NCEC and IESC methods are completed successfully for the full motor operation duration (29.5 s) without encountering the shape change instability. In this case, forcing wall-normal porous flow, in additional to all the other instability suppression techniques (e.g. under-relaxation and smoothing), is successful in eliminating the shape-change instability. However, for the simulation using the AWEC method, wall-normal porous flow is found to be insufficient to prevent the onset of this instability, which occurs at the $t = 15.25\,\mathrm{s}$ time point. One possible contributing factor is that smoothing has not been applied to the species mass fractions on the ablating wall; this is something that should be investigated in future work. In any case, the AWEC method can be expected to be more sensitive to the shape change instability than the NCEC method. Wall heat flux computations for the AWEC method are dependent upon both species mass fraction gradients and temperature gradients, while wall heat flux computations for the NCEC method are only dependent upon the temperature gradients.

Surface temperature at the nozzle throat as a function of time, as computed by these conjugate simulations, is compared in Figure 7.34 to results from the decoupled analysis. Surface temperature distribution at $t = 10.0\,\mathrm{s}$ is compared in Figure 7.35. Surface recession at the nozzle throat is compared as a function of time in Figure 7.36 and the surface recession distribution at $t = 10.0\,\mathrm{s}$ is compared in Figure 7.37. Similar observations can be made here as were made previously.

The three conjugate analyses produce temperature predictions that are in close agreement with each other, but are (downstream of the throat) substantially higher than those obtained with the decoupled analysis. Again, this is mainly due to under-

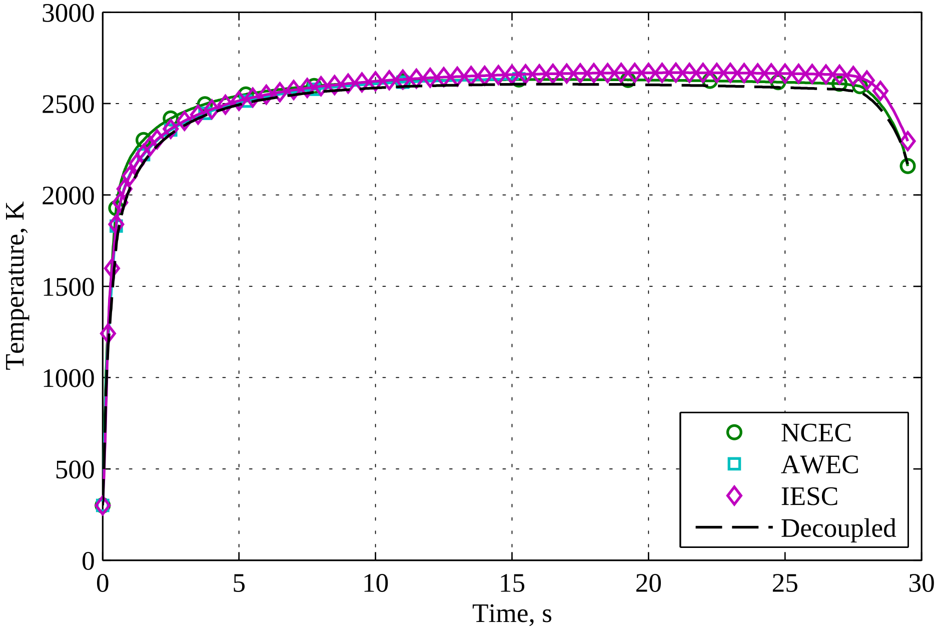

Figure 7.34: Surface temperature at the throat of the HIPPO nozzle as a function of time, as computed by the decoupled analysis and by conjugate simulations using the different surface energy balance approaches with wall-normal porous flow.

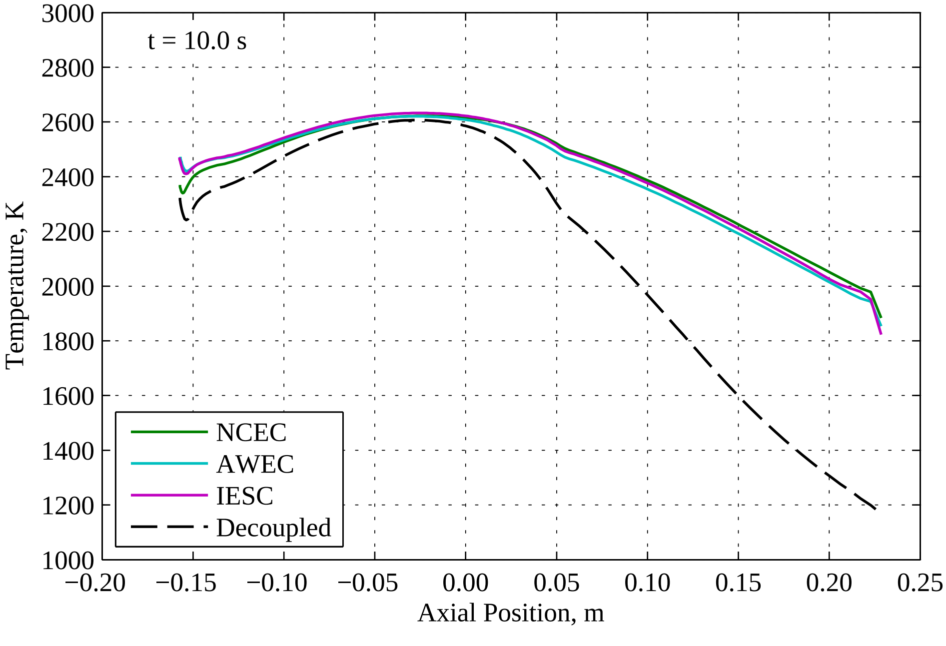

Figure 7.35: Surface temperature distribution within the HIPPO nozzle at $t = 10.0\,\text{s}$, as computed by the decoupled analysis and by conjugate simulations using the different surface energy balance approaches with wall-normal porous flow.

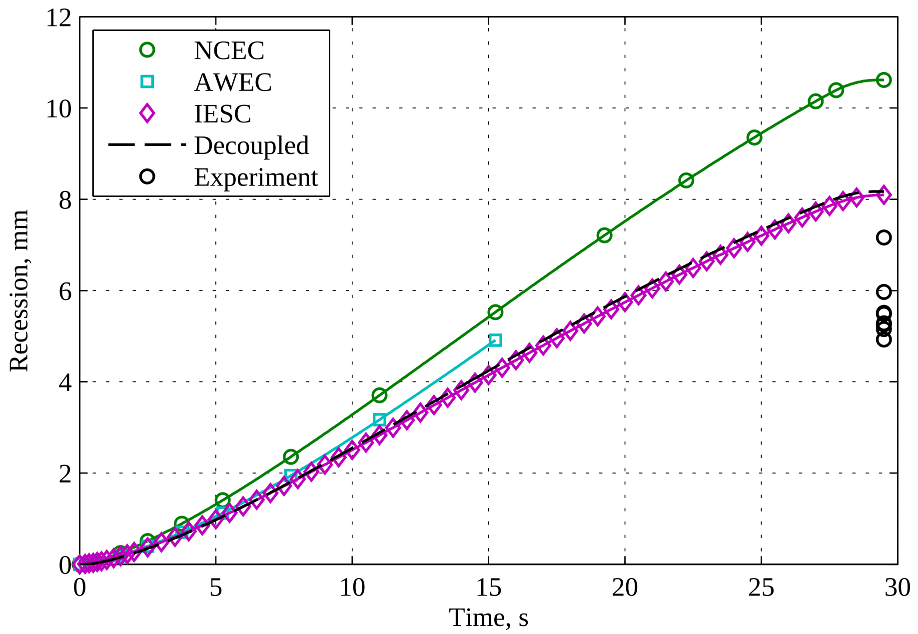

Figure 7.36: Surface recession at the throat of the HIPPO nozzle as a function of time, as computed by the decoupled analysis and by conjugate simulations using the different surface energy balance approaches with wall-normal porous flow.

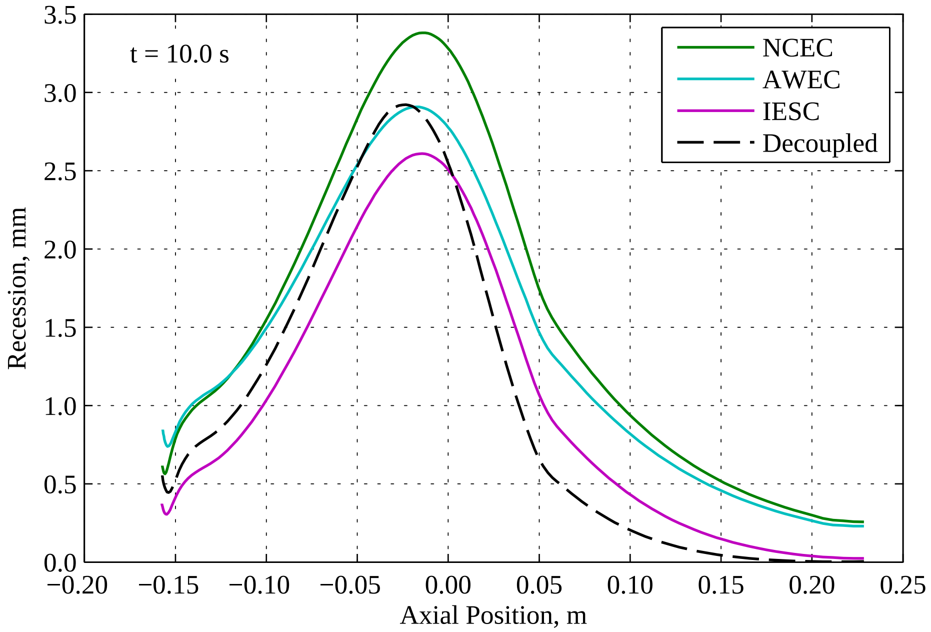

Figure 7.37: Surface recession distribution within the HIPPO nozzle at $t = 10.0\,\mathrm{s}$, as computed by the decoupled analysis and by conjugate simulations using the different surface energy balance approaches with wall-normal porous flow.

prediction of the enthalpy conductance in the exit cone for the decoupled analysis. At later times, the IESC treatment does predict slightly higher surface temperatures than those obtained with the NCEC method. At the throat, the temperature difference is less than 50 K, or less than 2 %. This can be attributed to fundamental differences in how enthalpy is computed in the LeMANS flow solver and the MOPAR-MD material response solver. For a given temperature, slightly different enthalpy values will be computed by the two codes; this discrepancy becomes greater at higher temperatures. The NCEC relies on wall enthalpies taken from the B' tables in MOPAR-MD, while the IESC method relies on the wall enthalpies computed by the flow solver. Eliminating this enthalpy mismatch should be considered in future work.

Surface recession is strongly affected by the choice of the surface energy balance treatment. The NCEC method predicts the greatest recession, which is related to the large enthalpy conductance values obtained through the use of the noncatalytic wall boundary condition in the flow solver. The AWEC method predicts somewhat less recession, especially near the throat. This is because the effect of the ablation product species on the convective heat flux (and thus, enthalpy conductance) is being inherently captured. The lowest recession predictions are obtained with the IESC method, which is expected to be the most accurate method, as it makes the fewest approximations.

The surface recession predictions from the end of the motor firing are compared to the experimentally measured values in Figure 7.38. Since the conjugate simulation using the AWEC treatment is not completed for the full duration of the motor firing, extrapolation has been used for this simulation (represented by a dashed line in Figure 7.38). The AWEC recession values obtained at $t = 11.0\,\mathrm{s}$ were extrapolated in time to the end of the motor firing ($t = 29.5\,\mathrm{s}$). The NCEC method is observed to over-predict recession by about 3 to 4 mm relative to the experimental data. In contrast, the IESC treatment over-predicts recession by only about 1 to 2 mm. Peak

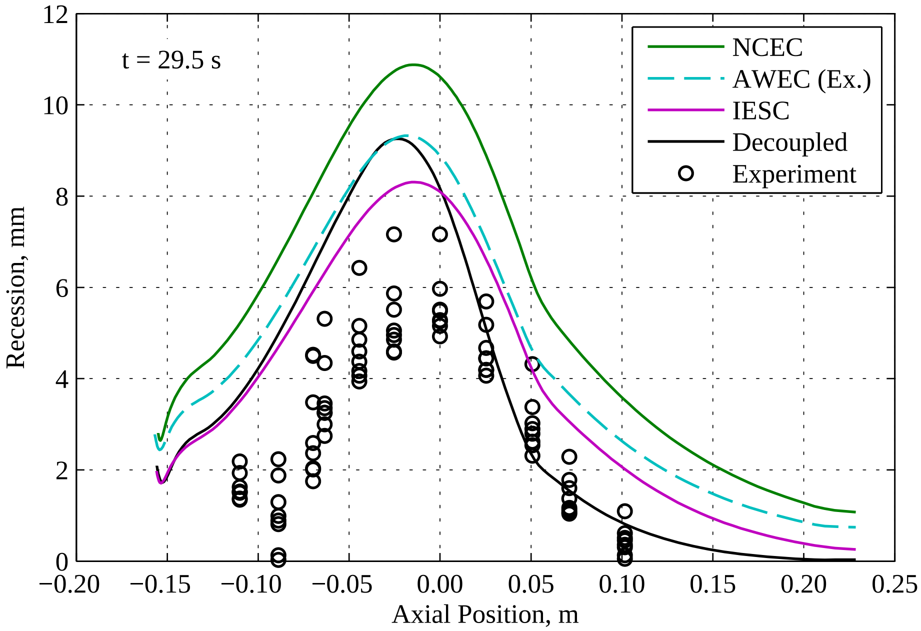

Figure 7.38: Comparison of predicted and measured final surface recession, for conjugate simulations with wall-normal porous flow.

recession as predicted by the IESC method is 1 mm less (closer to experimental values) than that predicted by the decoupled analysis. This comparison shows that the IESC method provides the best agreement with the experimental results of all the conjugate analyses, and provides a substantial improvement over the decoupled analysis. (Note that the good agreement to experimental data obtained in the exit cone by the decoupled analysis is mostly fortuitous, and is due to the under-prediction of the convective heating conditions here.)

The final ($t = 29.5\,\mathrm{s}$) nozzle shape and degree of char predictions from the conjugate analyses using the NCEC and IESC treatments are compared to the experimentally measured surface recession (black circles) and char depths (white squares) in Figure 7.39 and Figure 7.40, respectively. These images clearly show how the conjugate analyses over-predict recession along the length of the nozzle, as has already been discussed. However, much better agreement is obtained for the char depth predictions in the exit cone than was obtained from the decoupled analysis (Figure

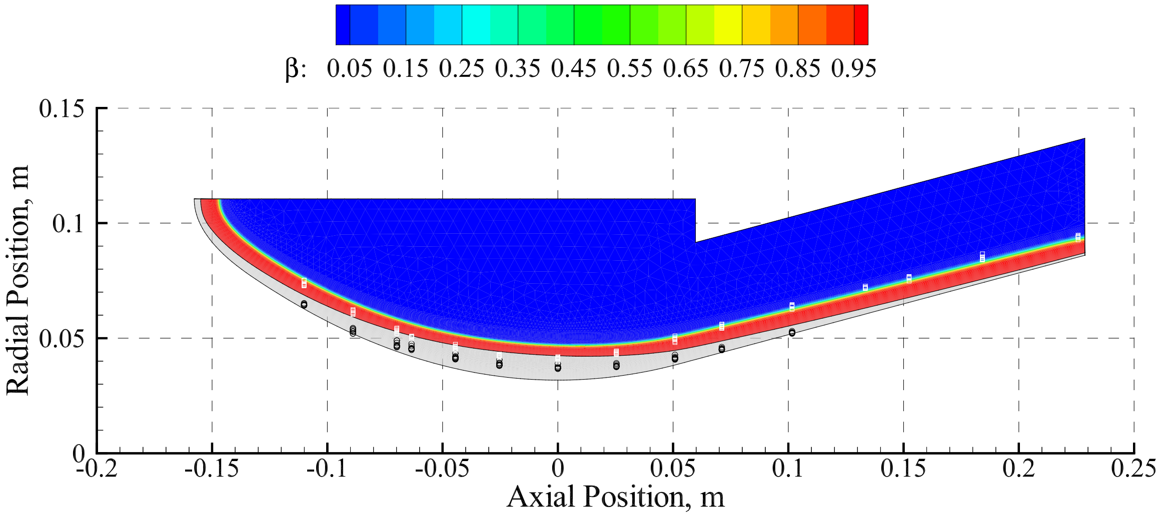

Figure 7.39: Comparison of surface recession and char depth, for the conjugate simulation using the NCEC treatment.

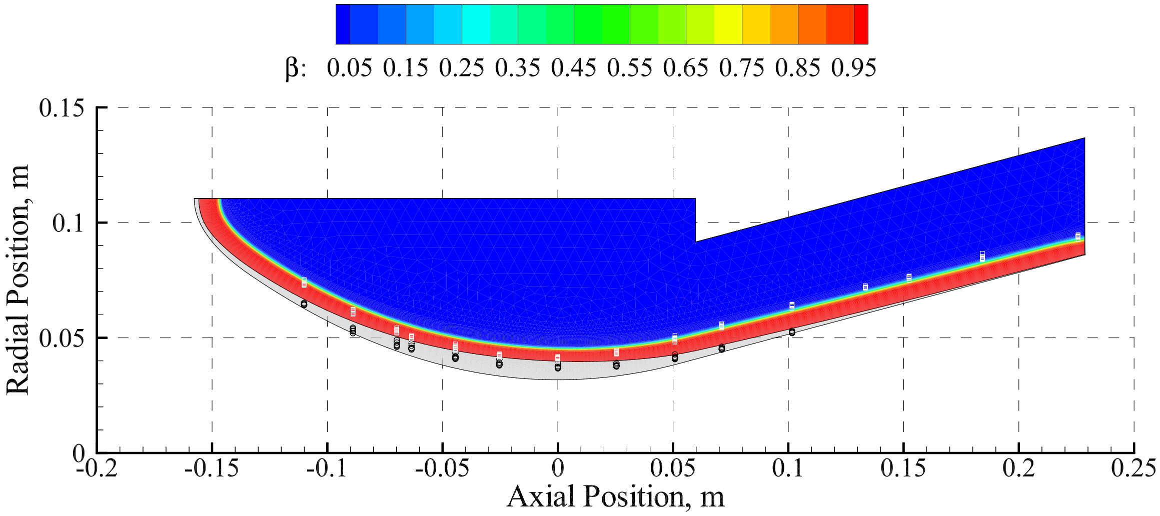

Figure 7.40: Comparison of surface recession and char depth, for the conjugate simulation using the IESC treatment.

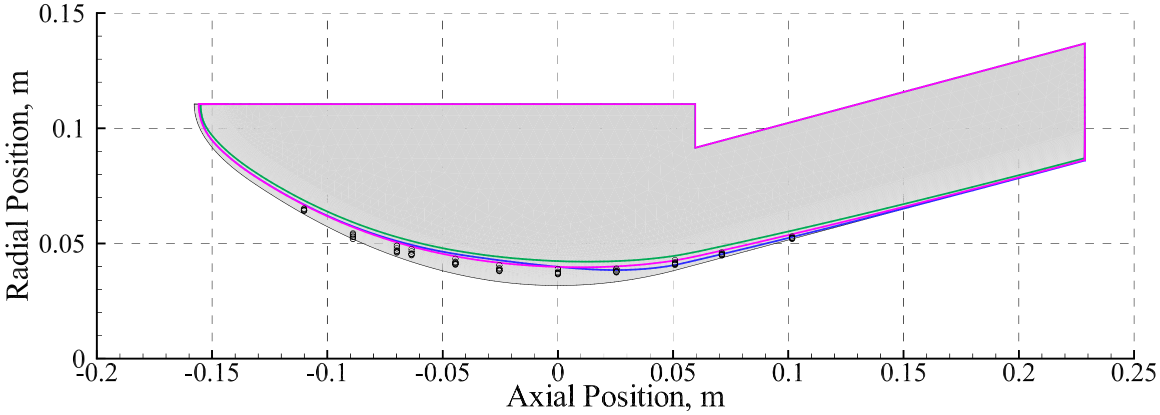

Figure 7.41: Comparison of nozzle shape at the end of the HIPPO motor firing. Symbols represent experimental measurements, blue represents results from the baseline decoupled analysis, green represents results from the conjugate simulation using the NCEC method, and magenta represents the IESC treatment.

7.16). This is most likely due to improved predictions for the convective heating in the exit cone. The final shape of the nozzle also agrees better with the experimental data than that produced by the decoupled analysis. This can be seen most clearly in Figure 7.41, where the final nozzle shapes as predicted by the baseline decoupled analysis and the NCEC and IESC conjugate analyses are compared to experimental measurements. This image also clearly illustrates the differences in the recession predictions as obtained from the decoupled analysis and the NCEC and IESC conjugate simulations.

There are several reasons why the surface recession as predicted by the IESC method is lower than that predicted with the other conjugate approaches. All the other methods model mass diffusion at the ablating wall using a transport coefficient assumption, while the IESC method directly models the diffusion of species to and from the ablating wall. Diffusion for the IESC method is based on a Lewis number of Le = 0.66, while the other methods are based on an assumption of unity Lewis number (equal heat and mass transport coefficients). All things being equal, a lower Lewis number should give less mass diffusion, and thus lower recession. Finally, since the IESC method is directly computing mass diffusion, it inherently captures the effects of the buildup of ablation product species in the boundary layer due to upstream mass injection. This chemical buffering of the boundary layer would tend to suppress ablation at downstream locations. The methods relying on a transport coefficient assumption cannot account for this chemical buffering.

However, the IESC method still appears to over-predict recession along the length of the nozzle. This over-prediction would likely be exacerbated (in the upstream nozzle region especially) once radiative heat transfer is included in the analysis. Several possible causes exist for this over-prediction. First, the material model employed in this work may not accurately represent the actual carbon-phenolic material as used in the HIPPO nozzle. Additionally, there is some evidence that intumescence of the material occurred in the experiment, which is not modeled in this work. The turbulence model used may also be over-predicting the convective heat transfer in the nozzle. Due to underlying differences in how the turbulence is being modeled, employing multiple turbulence models for a given problem will often produce results with some level of variation. Additionally, certain turbulence models work better for different classes of problems than others. Based on the limited information available in the literature, the BSL model was expected to provide the most accurate heat transfer predictions for nozzles, and was thus the model relied upon in these simulations. However, note that the SST model also provides acceptable agreement with the experimental data for the Kolozsi nozzle test case (section 6.2.4), while consistently producing lower heat transfer values than those obtained with the BSL model. Future research may determine that the SST model, or some other turbulence model not considered in this work, actually provides the most accurate predictions of heat transfer in rocket nozzles. Finally, this work assumed equilibrium surface chemistry, which should place an upper bound on the predicted surface recession. If finite-rate surface chemistry were to occur at the surface, this would lead to reduced surface recession. These factors should be investigated in future work.

CHAPTER VIII

Conclusions

8.1 Summary

Chapter I introduced and provided the motivation for the work presented in this dissertation. It was noted that rocket nozzle components are often manufactured from ablating thermal protection system materials, and that ablation must be accurately modeled in order to be able to design optimized motor systems. However, as was discussed in Chapter I, ablation modeling is complicated by the numerous participating physical processes and the strong mutual interactions between the nozzle flowfield and material response. In order to be able to accurately capture these effects, it is necessary to perform conjugate flowfield / ablation analyses instead of the decoupled analyses traditionally performed. A review and comparison of the most common ablation analysis tools available was made. Previous conjugate ablation analysis work conducted by other researchers was also reviewed. These prior efforts were found to be focused on external TPS applications, using a mixture of one- and two-dimensional ablation models and various simplifying assumptions. Ablation of pyrolyzing materials was modeled as either being fully one-dimensional or having quasi-steady, one-dimensional pyrolysis gas flow. Some previous work investigated the effect that ablation has on the flowfield in rocket nozzles, but these studies did not consider the transient ablation response of the nozzle itself. Chapter I concluded that there existed a need for a methodology that could enable conjugate simulations of transient, two-dimensional ablation of pyrolyzing TPS materials in rocket nozzles. Establishment and demonstration of this methodology became the goal of this dissertation.

Chapter II discussed the LeMANS flow solver used in this work, a laminar, multi-species, reacting Navier-Stokes solver developed by previous researchers at the University of Michigan. Emphasis was placed on the modifications and new features required for accurately modeling nozzle flowfields. New features include the Menter SST and BSL turbulence models, an equilibrium two-gas approach for modeling particle-laden flows, and a stagnation inlet boundary condition. In each case, the pertinent governing equations were presented, followed by details concerning the numerical implementation of these models into the solver.

Chapter III discussed the MOPAR-MD material response solver used in this work. The baseline version of this code was developed by a previous researcher at the University of Michigan, but numerous improvements were made in the present work, which greatly expanded and enhanced the capabilities provided by the code. Most improvements focused on bringing a capability to MOPAR-MD to model pyrolyzing materials. Pyrolysis and porous flow models were added, and the solution of the energy equation and the ablating wall boundary condition were updated to account for the presence of pyrolysis gases. The treatment of radiative heat exchange at the ablating boundary was also updated in order to be able to model radiation exchange between the nozzle surface and the combustion gases. For each new model, the governing equations were presented, as well as the details of the numerical implementation.

Chapter IV presented the conjugate analysis methodology developed in this work, along with the details of coupling the LeMANS flow solver to the MOPAR-MD material response solver. A motor pressure trace was divided into segments, and a steady-state flowfield solution was obtained at each time point. Transient material response simulations linked the time points, and provided the boundary conditions required by the flow solver. An iterative process was used to obtain a converged conjugate solution (agreement between the flow and solid domains) at each time point before advancing to the next. Details of five different approaches for treating the surface energy balance (SEB) at the ablating wall were also presented in this chapter. One of these methods, the Integrated Equilibrium Surface Chemistry (IESC) approach, eliminates the transport coefficient and unity Lewis number assumptions commonly made, and computes the surface energy balance directly from diffusive fluxes. A detailed derivation of this methodology was presented. A section was also included that discussed the fidelity of the different surface energy balance treatments. Other mechanics of the code coupling were also discussed in Chapter IV. These include criteria used to determine when to call the material response solver to update the wall conditions, as well as algorithms for performing under-relaxation, mesh-to-mesh interpolation, and smoothing.

A new, reduced, gas-phase finite-rate chemistry mechanism suitable for use in computational fluid dynamics (CFD) analyses of ablation within rocket nozzles was proposed in Chapter V. The small size of this mechanism (20 species and 33 reactions) makes it quite affordable and suitable for CFD applications, yet is comparable in accuracy over the parameter space of interest to a much larger, detailed mechanism that is commonly used to model combustion of solid rocket propellants. The proposed mechanism was produced by reducing the detailed mechanism based on linear sensitivity analyses. These sensitivity analysis identified the species and reactions that had the strongest impact on the solution for a range of ablating and non-ablating conditions. Unimportant species and reactions were then eliminated with minimal impact to accuracy.

Chapter VI presented a number of verification and validation test cases that were simulated in order to demonstrate that the new features added to the LeMANS flow solver and the MOPAR-MD material response solver had been implemented correctly. A series of high Mach number flat plate test cases demonstrated that the new turbulence models implemented into LeMANS could accurately predict the main features of a turbulent boundary layer. Other flat plate test cases validated that the turbulence models could correctly model scenarios involving mass injection, which is essential in ablation applications. An axisymmetric transonic bump test case validated the turbulence models for axisymmetric geometries. The Kolozsi nozzle test case demonstrated that the turbulence model implementation could accurately predict heat transfer within nozzles, a crucial capability. Flowfield simulations were also performed for the HIPPO nozzle test case, demonstrating correct operation of the particle-laden flow capability, the stagnation inlet boundary condition, and the reaction mechanism. Test cases for the MOPAR-MD material response solver independently verified the pyrolysis and porous flow models. Three additional test cases, in increasing order of complexity, indicated that all features of the code required for modeling the ablation of pyrolyzing materials had been implemented correctly.

Chapter VII presented the results from multiple decoupled and conjugate ablation analysis studies for the HIPPO nozzle test case. This chapter began with a discussion of the two different models used in these simulations. The initial model was used in most decoupled analyses and some of the early conjugate analyses, but was found to not be well-suited for conjugate analyses. The improved geometric model was developed to resolve the shortcomings of the initial model, and was used for most of the conjugate analyses.

Details were presented on the computation of the boundary conditions required by the material response solver. Enthalpy conductance at each pressure was computed based on the results from two different LeMANS simulations, one with an adiabatic wall, the other with a specified wall temperature. It was shown that the enthalpy conductance predictions are sensitive to the choice of wall temperature used in the flow solver. Comparisons were also made to enthalpy conductance values computed with a traditional integral boundary layer solution technique. The LeMANS flow solver produced lower values for enthalpy conductance than those obtained with the traditional technique, and demonstrated more sensitivity to wall temperature.

Two different decoupled ablation studies were presented. The first study investigated the effects of stream radiation within the nozzle. It was found that the effects of radiation could be significant in the upstream portion of the nozzle, but were minimal in the portion of the nozzle downstream of the throat. The second study investigated what effect the wall temperature profile used in the flow solver when computing the enthalpy conductance had on the ablation response of the nozzle. Three different wall temperature profiles were considered, and it was demonstrated that the choice of wall temperature profile did, in fact, make a significant impact on the ablation response of the nozzle. This impact was shown to be particularly significant in the downstream portion of the nozzle. The results from this study support the hypothesis that fully-conjugate analyses are required to accurately predict the ablation response of rocket nozzles. The section on decoupled ablation analyses concluded with a new decoupled simulation that could serve as a baseline for comparisons to the conjugate analyses.

Conjugate flowfield / ablation analyses of the HIPPO nozzle test case were then presented in a sequence of different studies. The first considered the convergence of the conjugate solution. It was found that appropriately selecting the under-relaxation factor could greatly accelerate the convergence of the conjugate solution at a time point. Obtaining adequate flowfield development between calls to the material response solver was also determined to be quite important for convergence.

The second study investigated the impact that time point spacing has on the results of the conjugate solutions. Large time point spacing is desirable, as it minimizes the computation cost to complete a simulation. It was found that relatively large intervals between time points could be used for SEB treatments based on enthalpy conductance (the Noncatalytic Wall – Enthalpy Conductance (NCEC) and Ablating Wall – Enthalpy Conductance (AWEC) treatments) without negatively affecting the results. However, it was found that only relatively small time point spacings could be successfully used for simulations using SEB treatments based on heat flux (the NCHF, Ablating Wall – Heat Flux (AWHF), and IESC treatments).

The shape change instability affecting the conjugate simulations was then investigated. It appears that this instability is related to small geometry perturbations affecting the local heat flux, which in turn affect the ablation response and amplify the perturbations. This instability was found to be a common occurrence in conjugate simulations that capture changing geometry due to recession. A number of actions taken to suppress the instability were all found to only delay the instability, and not eliminate it. However, a relationship between the instability and the porous flow solution was observed, and the particular mesh topology required by the MOPAR-MD solver was believed to be a contributing factor. Forcing the pyrolysis gases to flow in the wall-normal direction was shown to further suppress this instability, without excessive impact to the ablation response for the HIPPO test case. This technique was used for some simulations in this work, but is not believed to be a suitable long-term solution.

A study comparing the five different surface energy balance treatments was then presented. The Noncatalytic Wall – Heat Flux (NCHF) method was shown to be unsuitable for rocket nozzle applications, even though it had been used in the literature for external TPS applications. All conjugate simulations predicted a much more severe thermal response than that obtained with the baseline decoupled analysis, which is attributed to an expected under-prediction of the convective heating conditions for the decoupled simulation. Surface temperature was found to be relatively insensitive to the choice of the surface energy balance (SEB) treatment used in the conjugate analyses, while the choice of SEB treatment was found to strongly affect the predicted surface recession values. The lowest recession predictions were obtained with the Integrated Equilibrium Surface Chemistry (IESC) treatment, a welcome result consistent with the expected high level of fidelity provided by this method. However, all initial simulations in this study were terminated prior to full motor firing duration, due to issues with a shape change instability.

Chapter VII concluded with a series of conjugate simulations which forced the pyrolysis gases to flow in the wall-normal direction. The simulations using the NCEC and IESC treatments were successfully completed for the full duration of $t = 29.5\,\mathrm{s}$. However, the AWEC method still encountered the instability at the $t = 15.25\,\mathrm{s}$ time point, potentially related to not applying smoothing to the species mass fractions on the ablating wall. Comparisons of the final recession values (necessarily based on extrapolations for the AWEC simulation) indicate that the NCEC method significantly over-predicted the surface recession throughout the nozzle. Improved predictions were obtained with the AWEC method, but the lowest and therefore most accurate predictions were obtained with the IESC method. However, the IESC method still over-predicted recession relative to the experimentally measured values. Possible causes for this include deficiencies in the material model, intumescence, deficiencies in predicting heat transfer with the turbulence model, and finite-rate surface chemistry.

8.2 Contributions

This work advances the state of rocket nozzle ablation modeling in multiple ways. These contributions range from improvements to a flow solver, to the development of a new multidimensional material response solver for pyrolyzing and ablating materials, to new, high fidelity treatments of the surface energy balance at an ablating wall. Contributions have been presented in a series of conference papers [115, 116, 117] and published in one peer-reviewed journal article [118], with a second peer-reviewed journal article accepted for publication [119]. Key contributions made in this dissertation are listed below.

1. The primary contribution of this work is the establishment of a new methodology for performing conjugate analyses of transient, two-dimensional ablation of pyrolyzing materials in rocket nozzles, as realized by coupling the LeMANS flow solver and the enhanced MOPAR-MD material response solver together. By comprehensively incorporating fluid-thermal-chemical processes relevant to the ablation of pyrolyzing materials, it is now possible to rigorously capture the strong interactions and interdependencies that exist between the reacting flowfield and the ablating material. While the emphasis in this work has been on rocket nozzles, the methodology developed here is also suitable for airbreathing propulsion or external TPS applications. Improved analysis accuracy will allow future TPS design efforts to become more analysis-based, reducing development costs and yielding improved TPS designs.

2. A supporting contribution is the implementation, verification and validation of a number of physical models in the LeMANS flow solver to enable modeling of the turbulent, particle-laden flow through the nozzles of solid rocket motors. These additional models individually are not new, but the combined implementation of these models into the LeMANS code results in a new flow solver with unique capabilities. A flow solver possessing all these capabilities is a crucial component of the conjugate ablation analysis framework.

3. Another contribution made in this dissertation is the significant enhancement and verification of the MOPAR-MD material response solver. With these new capabilities, it is now possible to fully model two-dimensional ablation of pyrolyzing, anisotropic materials with a true, two-dimensional treatment of the porous flow of the pyrolysis gases. The individual models used in MOPAR-MD

are not new, and can be found in other ablation solvers. However, the combination of all these models is unique, as is the particular numerical implementation employed. While other ablation solvers developed contemporaneously with this effort may provide very similar capability, the capabilities of MOAR-MD as developed in this effort exceed those of any ablation solver commonly available prior to the initiation of this work.

4. The implementation of multiple surface energy balance treatments in the conjugate analysis framework is another key contribution of this work. This dissertation appears to be the first effort to investigate and compare multiple methods of handling the ablating boundary in coupled analyses. Five different treatments have been presented, with increasing levels of fidelity, including one method that eliminates the commonly-made transport coefficient and unity Lewis number assumptions. While these treatments are similar to other approaches considered by various researchers in the literature, the derivation, implementation, and comparisons made in this work are unique.

5. Another significant contribution is a new, reduced reaction mechanism suitable for modeling finite-rate gas-phase chemistry associated with the ablation of carbon-phenolic materials in solid rocket nozzle applications. Prior to this work, no mechanism in the literature was suitable for use in conjugate ablation analyses of carbon-phenolic materials in rocket nozzles. The reduced mechanism proposed in this dissertation provides a key component, previously missing, that enables conjugate analyses of ablation in rocket nozzles to be performed. This mechanism was created for use in coupled flowfield / ablation analyses of carbon-phenolic nozzles for nondimensional pyrolysis gas mass flux values up to 0.4, temperatures up to 3000 K, and pressures up to 6.0 MPa.

6. Finally, this dissertation contributes the results from numerous ablation anal-

yses performed for the HIPPO nozzle test case using the updated flow and material response solvers and the conjugate ablation methodology developed in this work. Decoupled analyses clearly demonstrate the sensitivity of enthalpy conductance to the wall temperature used in the flow solver when pre-computing the convective heating conditions. This sensitivity reinforces the importance of a conjugate analysis framework. Conjugate analyses showed that increasing the fidelity of the surface energy balance treatment improves agreement with experimental data. Conjugate simulations using the Integrated Equilibrium Surface Chemistry method are found to produce the best agreement with experimental recession data of all modeling approaches considered. Best practices for obtaining rapid convergence of conjugate simulations have also been identified and reported, and will enable future conjugate analyses to be completed efficiently.

8.3 Future Work

While this work has advanced the state of the art of ablation modeling significantly, numerous opportunities remain for further improvements.

Several enhancements could be made to the LeMANS flow solver. Currently, it is necessary to use the thermodynamic nonequilibrium framework to accurately capture the thermodynamics at elevated temperatures, even though the flow is in thermodynamic equilibrium. This introduces unneeded computational expense, and, for a given temperature, can yield a slightly different enthalpy for a species than that used by the material response solver. An attractive alternative would be to implement a method for using thermodynamic curve fits (as given in Ref. [120]) for each species. This should be more computationally efficient, and would provide improved agreement between the enthalpies used by the flow solver and the material response solver. More sophisticated treatments of the particle-laden flow could also be pursued, such as a true multiphase implementation. This could be particularly important if it is desired to capture the effects of particle impingement and mechanical char removal processes. Finally, the implementation of a multigrid scheme or some other acceleration technique to reduce the time required to obtain a converged flowfield solution would be a welcome improvement.

In this work, radiative heat transfer between the nozzle wall and combustion products was modeled using an empirical correlation; provenance of this correlation is questionable. Further efforts could investigate the effects of participating media radiative heat transfer using more accurate methods, such as a discrete ordinates method or a Monte-Carlo ray-tracing approach. Modeling the radiation exchange from a more fundamental basis should remove uncertainty associated with the empirical correlation currently employed, and could yield more accurate ablation predictions (particularly within rocket motor chambers and for the upstream portions of nozzles).

Future work could also investigate additional physical mechanisms that were outside the scope of this effort. A surface energy balance treatment, similar to the Integrated Equilibrium Surface Chemistry method, but based on finite-rate surface chemistry, should allow ablation at lower temperatures to be captured more accurately. The effects of mechanical ablation processes (such as melting, particle impingement, shear failure, spallation, ply lifting) could also be explored; these are known to be particularly important for some materials, like silica-phenolic. Intumescence is a defining characteristic for certain classes of ablators, and can even occur to a small extent for the carbon-phenolic material analyzed in this work; this phenomena could also be a topic for future research. Coking is another phenomena that is important for some materials that could be worthy of further consideration. This work focused on fluid-thermal coupling, but future work looking at fluid-thermal-structural coupling could capture thermal stresses within the material and be used for predicting structural failure of nozzles.

In addition to these extra physical processes, a number of numerical improvements could be made to the MOPAR-MD material response code. The greatest weakness of this material response solver is that it is a serial code, which places significant limitations on the size of problems that can be considered. It is essential that a parallelized material response solver be developed with all the current capabilities of the MOPAR-MD code. Parallelizing the existing code may be unfeasible; the simplest route may be to create a new solver that leverages the work invested in MOPAR-MD. As much as possible, existing software libraries (such as the Portable, Extensible Toolkit for Scientific Computing library [121]) should be utilized. This will enable rapid code development and should allow more of the coding to focus on ablation physics, instead of on the underlying computer science framework. The material response solver should also be updated to support quadrilateral elements, which should capture the strong wall-normal gradients better than the triangular elements currently required by MOPAR-MD. An automated adaptive mesh refinement / coarsening scheme, or some form of a sub-element scheme, would allow the strong gradients in the pyrolysis zone to be adequately resolved, while minimizing the total number of elements in the mesh. Support for modeling multiple ablating materials in one simulation should also be completed.

Analyses performed with either the existing MOPAR-MD solver, or an updated variant, could explore the sensitivity of the ablation response to the numerous parameters constituting a material model. Many of these material model parameters are not well known, and are difficult to determine. Often, educated guesses are used, and some parameters (such as the thermal conductivity of the char) are manually tuned to yield good agreement with experimental data. This investigation would identify the most important parameters in the models for ablating materials, and could guide the development of improved models for existing materials as well as the creation of models for new materials. It would likely be beneficial to perform a series of experiments to characterize common existing ablating materials, in order to generate high-fidelity material models. These new material models would be freed from the limitations imposed on existing material models by historical ablation analysis tools, and would also capture the effects of any changes to the manufacturing process or ingredients that might have occurred since the material was previously characterized.

Future conjugate analyses could also investigate multiple turbulence models, to better determine the impact that turbulence models have on the predicted ablation response. While the conjugate ablation analyses presented in this work utilized the Menter BSL model, the lower heat transfer coefficient predictions obtained for the Kolozsi test case using the Menter SST model also had acceptable agreement with the experimental measurements. It therefore seems likely that conjugate analyses of the HIPPO nozzle employing the Menter SST model would produce lower surface recession predictions, with improved agreement with experimental data. Other turbulence models, which were not considered in this work, might also be found to be suitable for nozzle simulations. One goal of this potential investigation would be to definitively identify the best turbulence model for use in nozzle ablation problems.

Turbulence model assessment has been hampered by the limited quantity of good experimental data. Most experimental investigations of nozzle heat transfer fail to report wall temperature, which, as shown in this work, strongly affects heat transfer predictions. New experiments, yielding high quality measurements of both heat transfer and wall temperature within nozzles, would be very useful. These experiments should utilize a non-ablating nozzle design with a well characterized, fully turbulent boundary layer, such as a submerged nozzle. Experiments should be performed for a range of chamber conditions and for different gas mixtures. This experimental data could be used to evaluate the ability of existing or future turbulence models to accurately predict heat transfer in nozzles.

It would be beneficial to transition the methods and techniques developed in this dissertation out of the research environment and into a production environment, for instance by utilizing the latest commercial off the shelf computational fluid dynamics and multiphysics analysis codes. These commercial solvers are more efficient than the research codes used in this work, and include sophisticated features that make it possible to obtain solutions more quickly and affordably. This would greatly reduce the time and computational expense required to complete the conjugate simulations, making it possible to exploit the improved accuracy of the conjugate analysis methodology for routine ablation analysis efforts.

Finally, well planned experiments could be performed to obtain data that can be used for additional validation of the conjugate ablation analysis methodology. A submerged nozzle design providing a well characterized, fully turbulent boundary layer should be employed. Multiple nozzles should be tested, manufactured from a variety of materials (both charring and non-charring) for which high-fidelity material models have been produced. Surface recession should be measured along the nozzle length as a function of time through the use of real-time radiography techniques; final recession values could be determined by sectioning and measuring the nozzle post-test. The thermal response of the nozzle exit cone surface could be determined using an optical pyrometer; high temperature thermocouples embedded at different locations throughout the nozzle would provide the in-depth thermal response of the nozzle. By collecting this transient thermal response and recession data throughout the nozzle, it will be possible to obtain a detailed view of the nozzle ablation response. Conjugate analyses for these test cases could then be compared to this wealth of data, providing insight into areas where the conjugate analysis methodology could be improved. By considering multiple nozzle materials, it should also be possible to determine how well different physical phenomena are being captured by the analyses.

APPENDICES

APPENDIX A

Species Properties

Thermodynamic Properties

The thermodynamic properties for the 20 species included in the reduced reaction mechanism identified in this work (see Section 5.3.4) are tabulated in Table A.1. Wherever possible, thermodynamic properties were taken from the NIST-JANAF Thermochemical Tables [122]. Other data sources are as indicated by the notes in the table. $\mathscr{M}$ represents species molecular weight. Specific heat at constant volume for the translational mode C_{v_t} is computed as

$$C_{v_t} = \frac{3}{2}\frac{R_u}{\mathscr{M}} \tag{A.1}$$

for all gas-phase species, where $R_u = 8.314\,{}^{\text{kJ}}/_{\text{kmol}\cdot\text{K}}$ is the universal gas constant. Specific heat at constant volume for the rotational mode C_{v_r} is computed for gas-phase species as

$$C_{v_r} = \frac{n}{2}\frac{R_u}{\mathscr{M}} \tag{A.2}$$

where n is the rotational degrees of freedom for the species. For atoms $n = 0$, for linear molecules (e.g. CO, CO_2) $n = 2$, and for non-linear molecules (e.g. H_2O) $n = 3$.

The characteristic temperature for each vibrational mode is given by θ_v. Dissociation energy is represented by D_0. When this value is not available from the literature it is computed as

$$D_0 = \sum_k \nu_k \Delta h^0_{f_k} - \Delta h^0_f \tag{A.3}$$

where Δh^0_f is the heat of formation of the species, $\Delta h^0_{f_k}$ is the heat of formation for atoms of the k^{th} element formed by the dissociation reaction, and ν_k is the stoichiometric coefficient giving the number of atoms of the k^{th} element in each molecule of the species.

The symbol h_f represents an "effective" heat of formation for each species. It is necessary to use an effective heat of formation, instead of a "true" heat of formation, to account for a difference in the reference temperature T_{ref} used by the LeMANS and MOPAR-MD codes. LeMANS uses a reference state of $T_{ref} = 0\,\mathrm{K}$, while MOPAR-MD uses the the more common reference state of $T_{ref} = 298.15\,\mathrm{K}$ (which is also used by most other ablation codes). When performing conjugate simulations it is necessary to use a consistent reference state. Specific enthalpy h, based on a given reference temperature, can be computed as

$$h\left(T\right) = \underbrace{\left(\tilde{h}\left(T\right) - \tilde{h}\left(T_{ref}\right)\right)}_{\text{sensible enthalpy}} + \Delta h^0_f \tag{A.4}$$

where $\tilde{h}$ is a quantity represented as

$$\tilde{h}\left(T\right) = \left(C_{v_t} + C_{v_r} + \frac{R_u}{\mathscr{M}}\right) T + e_{ve}\left(T\right) \tag{A.5}$$

Here e_{ve} represents the vibrational-electronic specific energy. LeMANS computes specific enthalpy according to [50]

$$h\left(T\right) = \tilde{h}\left(T\right) + \Delta h^0_f = \left(C_{v_t} + C_{v_r} + \frac{R_u}{\mathscr{M}}\right) T + e_{ve}\left(T\right) + \Delta h^0_f \tag{A.6}$$

which implicitly assumes $T_{ref} = 0\,\mathrm{K}$ (note that $\tilde{h}\left(0\right) = 0$). By defining the effective heat of formation as

$$h_f \equiv \Delta h_f^0 - \tilde{h}\left(T_{ref}\right) = \Delta h_f^0 - \left(C_{v_t} + C_{v_r} + \frac{R_u}{\mathscr{M}}\right) T_{ref} - e_{ve}\left(T_{ref}\right) \tag{A.7}$$

and using this in place of the heat of formation in Equation A.6, it is possible to make the specific enthalpy computed by LeMANS consistent with the specific enthalpy for a non-zero reference temperature:

$$\begin{aligned} &h\left(T\right) = \\ &\left(C_{v_t} + C_{v_r} + \frac{R_u}{\mathscr{M}}\right) T + e_{ve}\left(T\right) + \left(\Delta h_f^0 - \left(C_{v_t} + C_{v_r} + \frac{R_u}{\mathscr{M}}\right) T_{ref} - e_{ve}\left(T_{ref}\right)\right) = \\ &\quad \left(C_{v_t} + C_{v_r} + \frac{R_u}{\mathscr{M}}\right) T + e_{ve}\left(T\right) - \left(C_{v_t} + C_{v_r} + \frac{R_u}{\mathscr{M}}\right) T_{ref} - e_{ve}\left(T_{ref}\right) + \Delta h_f^0 = \\ &\qquad \left(\tilde{h}\left(T\right) - \tilde{h}\left(T_{ref}\right)\right) + \Delta h_f^0 \end{aligned} \tag{A.8}$$

In this way, it is possible to obtain specific enthalpy values from LeMANS that are consistent with those used in the material response solver.

Properties for O_2, which is a species included in the 13 species mechanism proposed by Troyes et al. [92], but not in the 20 species mechanism identified as part of this work, are taken from Scalabrin [50].

Calculation of the equilibrium constant for reactions requires coefficients for the standard NASA curve fits for specific enthalpy and specific entropy. These coefficients were taken directly from Ref. [120], and are not presented here.

Table A.1: Thermodynamic properties for the 20 species included in the mechanism identified in this work.

Species	$\mathscr{M}$	h_f	C_{v_t}	C_{v_r}	θ_v	D_0	Notes
	(kg/kmol)	(J/kg)	(J/kg·K)	(J/kg·K)	(K)	(J/kg)	
C_2H_2	26.04	8.32E+06	478.98	319.32	4854.0	6.22E+07	1
					2839.9		
					4721.9		
					879.4		
					879.4		
					1049.3		
					1049.3		
CH_2O	30.03	-4.19E+06	415.36	415.36	3980.2	5.00E+07	1
					2512.2		
					2159.0		
					4091.0		
					1794.7		
					1674.0		
CH_2	14.03	2.68E+07	889.13	889.13	4250.1	5.40E+07	1
					1519.3		
					4493.3		

Species	$\mathscr{M}$	h_f	C_{v_t}	C_{v_r}	θ_v	D_0	Notes
	$\left({}^{\mathrm{kg}}\!/\!_{\mathrm{kmol}}\right)$	$\left({}^{\mathrm{J}}\!/\!_{\mathrm{kg}}\right)$	$\left({}^{\mathrm{J}}\!/\!_{\mathrm{kg\cdot K}}\right)$	$\left({}^{\mathrm{J}}\!/\!_{\mathrm{kg\cdot K}}\right)$	(K)	$\left({}^{\mathrm{J}}\!/\!_{\mathrm{kg}}\right)$	
CH_3	15.03	9.00E+06	829.52	829.52	4319.2	8.05E+07	1
					834.5		
					4581.1		
					4581.1		
					1989.8		
					1989.8		
CH_4	16.04	-5.29E+06	777.40	777.40	4196.2	1.02E+08	1
					2207.1		
					2207.1		
					4343.2		
					4343.2		
					4343.2		
					1879.0		
					1879.0		
					1879.0		
CO	28.01	-4.26E+06	445.25	296.83	3121.5	3.82E+07	
CO_2	44.01	-9.15E+06	283.38	188.92	1992.5	3.63E+07	1
					960.1		
					960.1		
					3380.1		
Cl	35.45	3.25E+06	351.78	0	0	0	
Cl_2	70.91	-1.29E+05	175.89	117.26	805.4	3.37E+06	
ClO	51.45	1.80E+06	242.39	161.60	1228.3	5.16E+06	1
H	1.01	2.10E+08	12373.45	0	0	0	

Species	$\mathscr{M}$	h_f	C_{v_t}	C_{v_r}	θ_v	D_0	Notes
	$(\mathrm{kg}/\mathrm{kmol})$	(J/kg)	$(\mathrm{J}/\mathrm{kg{\cdot}K})$	$(\mathrm{J}/\mathrm{kg{\cdot}K})$	(K)	(J/kg)	
H_2	2.02	-4.30E+06	6186.72	4124.48	6338.2	2.14E+08	2
H_2O	18.02	-1.40E+07	692.28	692.28	5253.1	5.09E+07	
					2294.4		
					5403.9		
HCN	27.03	4.66E+06	461.48	307.65	3016.1	4.67E+07	1
					1026.6		
					1026.6		
					4764.5		
HCO	29.02	1.15E+06	429.79	429.79	3579.7	3.90E+07	1
					1558.2		
					2618.6		
HCl	36.46	-2.77E+06	342.06	228.04	4157.5	1.17E+07	1
N_2	28.01	-3.10E+05	445.20	296.80	3392.0	3.36E+07	2
O	16.00	1.52E+07	779.51	0	0	0	
OH	17.01	1.78E+06	733.31	488.87	5374.1	2.50E+07	
$Al_2O_3^\star$	1.23E+12	-1.65E+07	1597.67	0	0	0	3

Notes:

1. Values for D_0 computed as per Equation A.3.
2. Values for θ_v taken from Ref. [123].
3. Condensed-phase (liquid) species. Value for $\mathscr{M}$ computed as described in Section 2.4. Other properties taken from the CEA database [95].

Transport Properties

Dynamic viscosity, μ, for each gas-phase species is computed using Blottner's curve fit [124], which has the form

$$\mu = 0.1 \exp\left(\left(A \ln\left(T\right) + B\right) \ln\left(T\right) + C\right) \tag{A.9}$$

where A, B, and C are coefficients, which can be found tabulated in Table A.2. The source for these coefficients is as indicated by the notes in the table. Wilke's mixing rule is used to compute the mixture viscosity [50].

For the simulations of the HIPPO nozzle presented in this work, a constant Lewis number $\mathrm{Le} = 0.66$ ($\mathrm{Le} \equiv \frac{\mathrm{Pr}}{\mathrm{Sc}}$) has been used, as obtained from an isentropic expansion calculation performed with the Chemics code [84].

Table A.2: Viscosity coefficients for the 20 species included in the mechanism identified in this work.

Species	*A*	*B*	*C*	Notes
C_2H_2	-2.61E-02	1.07E+00	-1.43E+01	1
CH_2O	-7.66E-02	1.90E+00	-1.76E+01	2
CH_2	-9.16E-03	7.85E-01	-1.33E+01	2
CH_3	-9.16E-03	7.85E-01	-1.33E+01	2
CH_4	-8.14E-03	7.94E-01	-1.33E+01	1
CO	2.66E-02	2.96E-01	-1.11E+01	1
CO_2	-3.30E-02	1.19E+00	-1.44E+01	1
Cl	-9.00E-03	7.91E-01	-1.27E+01	3
Cl_2	-3.97E-02	1.29E+00	-1.49E+01	1
ClO	-1.82E-02	9.39E-01	-1.33E+01	3
H	-1.42E-02	1.06E+00	-1.55E+01	1
H_2	4.18E-02	1.16E-01	-1.13E+01	1
H_2O	-1.04E-01	2.43E+00	-1.97E+01	1
HCN	-1.03E-01	2.47E+00	-2.03E+01	1
HCO	-7.66E-02	1.90E+00	-1.76E+01	2
HCl	-4.88E-02	1.45E+00	-1.54E+01	1
N_2	2.68E-02	3.18E-01	-1.13E+01	4
O	2.03E-02	4.29E-01	-1.16E+01	4
OH	-8.06E-02	2.04E+00	-1.79E+01	1

Notes:

1. Curve fit to data taken from Ref. [125].
2. Curve fit to data computed using CHEMKIN [103].
3. Curve fit to data taken from Ref. [126].
4. Coefficients taken from Ref. [124].

APPENDIX B

Material Properties

The HIPPO nozzle was manufactured from MX4926 carbon-phenolic material in the 90° orientation; the plies are oriented perpendicular to the nozzle axis. Except as otherwise indicated, properties describing this material are taken from Ref. [5].

The decomposition kinetics parameters describing the pyrolysis of MX4926 carbon-phenolic are tabulated in Table B.1. In this table, Γ is the component volume fraction, ρ_v and ρ_c are the virgin and char densities for each component, A is the decomposition reaction Arrhenius pre-exponential factor, T_a denotes the reaction activation temperature, ψ represents the reaction order, and T_{min} is the threshold temperature below which the reaction is inactive.

Specific heat, C_p, and thermal conductivity, κ, are tabulated as a function of temperature for MX4976 carbon-phenolic in the virgin and char states in Table B.2. This material is orthotropic; $\kappa_{\parallel}$ represents the thermal conductivity along the plies, while $\kappa_{\perp}$ represents the thermal conductivity in the cross-ply direction. The cross-ply conductivity was taken from Ref. [127].

Additional thermal and porous flow properties are given in Table B.3. In this table, ε represents emissivity, Δh_f^0 is the heat of formation, ϕ denotes porosity, and $K_{\parallel}$ and $K_{\perp}$ are the in-plane and cross-ply permeability values, respectively. Porosity

Table B.1: Decomposition kinetics parameters for MX4926 carbon-phenolic.

Reaction	Γ	ρ_v ($^{\text{kg}}/_{\text{m}^3}$)	ρ_c ($^{\text{kg}}/_{\text{m}^3}$)	A ($^1/_\text{s}$)	T_a (K)	ψ	T_{min} (K)
A	0.372	973.1	519.0	4.48×10^9	2.04×10^4	3.0	300.0
B	0.372	324.4	0	1.4×10^4	8.56×10^3	3.0	300.0
C	0.628	1560.2	1560.2	0	0	3.0	555.6

Table B.2: Specific heat and thermal conductivity for MX4926 carbon-phenolic.

		Virgin			Char	
T (K)	C_p ($^\text{J}/_{\text{kg}\cdot\text{K}}$)	$\kappa_\parallel$ ($^\text{W}/_{\text{m}\cdot\text{K}}$)	$\kappa_\perp$($^\text{W}/_{\text{m}\cdot\text{K}}$)	C_p ($^\text{J}/_{\text{kg}\cdot\text{K}}$)	$\kappa_\parallel$ ($^\text{W}/_{\text{m}\cdot\text{K}}$)	$\kappa_\perp$($^\text{W}/_{\text{m}\cdot\text{K}}$)
277.8	879.2	1.47	0.87	879.2	1.94	1.14
444.4	1507.2	1.68	0.98	1431.9	1.95	1.17
555.6	1507.2	1.82	1.07	1800.3	1.96	1.18
644.4	1507.2	1.94	1.14	1856.6	1.99	1.19
833.3	1976.2	1.94	1.14	1976.2	1.99	1.21
1111.1	2026.4	1.94	1.14	2026.4	2.59	1.46
1666.7	2064.1	1.94	1.14	2064.1	5.58	3.36
2222.2	2085.0	1.94	1.14	2085.0	9.16	7.26
2777.8	2093.4	1.94	1.14	2093.4	13.24	11.71
3333.3	2093.4	1.94	1.14	2093.4	17.66	16.51

Table B.3: Additional properties for MX4926 carbon-phenolic.

Property	Virgin	Char
ε	0.85	0.85
Δh_f^0 ($^\text{J}/_\text{kg}$)	-8.44×10^5	0
ϕ	0.01	0.35
$K_\parallel$ (m^2)	2.0×10^{-18}	6.5×10^{-14}
$K_\perp$ (m^2)	6.0×10^{-20}	3.9×10^{-14}

Table B.4: Elemental mass fractions for the propellant, the nozzle boundary layer edge gases (gas-phase combustion products), the pyrolysis gases, and the char for the HIPPO nozzle.

Element	Propellant	Edge Gas	Pyrolysis Gas	Char
H	0.03752	0.05378	0.10710	0
C	0.11304	0.16203	0.60957	0
N	0.08793	0.12603	0	0
O	0.39027	0.35539	0.28333	0
Al	0.16001	0	0	0
Cl	0.21123	0.30277	0	0

data are taken from Ref. [16], while permeability data come from Ref. [88].

Elemental mass factions for the propellant, nozzle boundary layer edge gases (which are the gas-phase combustion products), the pyrolysis gases, and the char are tabulated in Table B.4. These mass fractions are used as inputs when using a chemical equilibrium solver to compute chamber conditions, B' tables, and pyrolysis gas property tables (which include enthalpy, specific heat, and viscosity).

APPENDIX C

Mesh Refinement Studies

Flow Domain

A sequence of mesh refinement studies is performed to determine appropriate settings for the HIPPO nozzle flow domain. An intermediate geometry model of the HIPPO nozzle is used for these studies. This intermediate model has a nose similar (but not identical) to the nose used in the improved model of Section 7.2.1, but the contour downstream of this nose is the same as that used for the initial model of Section 7.2.2 (i.e. this portion of the nozzle is modeled using splines, not parabolas). Three different mesh parameters are investigated in these studies: near-wall cell thickness (wall y^+), wall-tangent mesh resolution, and wall-normal stretch ratio.

For the first study, the mesh resolution in the wall-normal direction is considered. Four meshes are utilized: coarse (94 cells in wall-normal direction), medium (104 cells), fine (110), and extra-fine (118). Maximum wall y^+ values (at the throat) are approximately 0.8, 0.32, 0.16, and 0.08, respectively (see Figure C.1). All meshes use a “medium” wall-tangent mesh resolution of 150 cells, and have a stretch ratio of

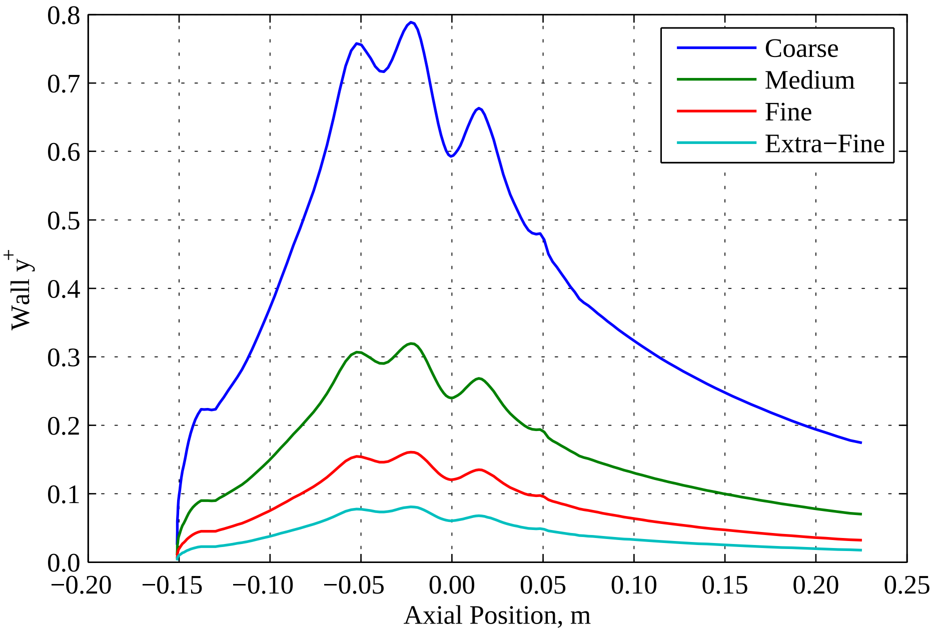

Figure C.1: Wall y^+ as a function of axial position and wall-normal mesh refinement level.

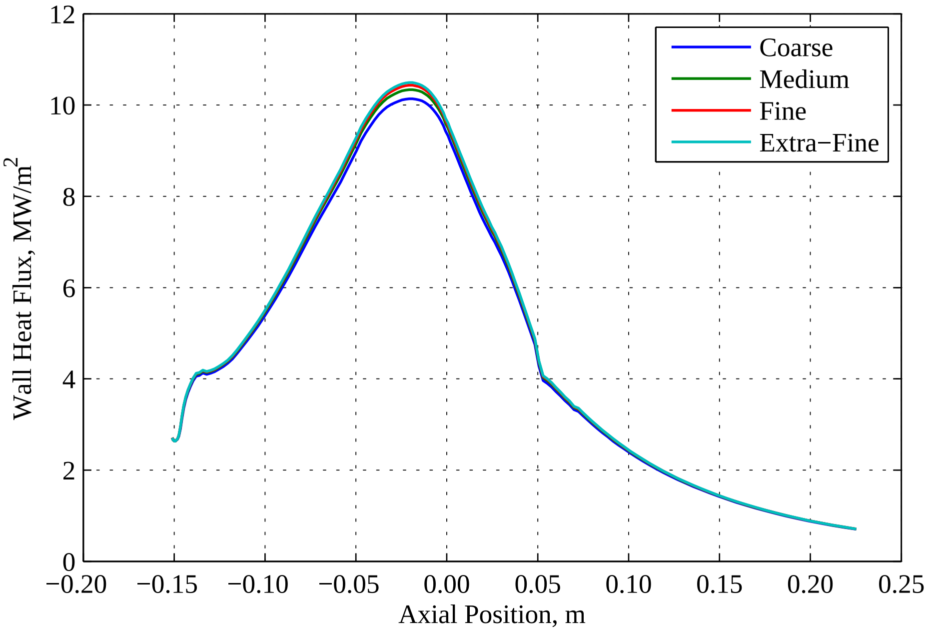

Figure C.2: Heat flux as a function of axial position and wall-normal mesh refinement level.

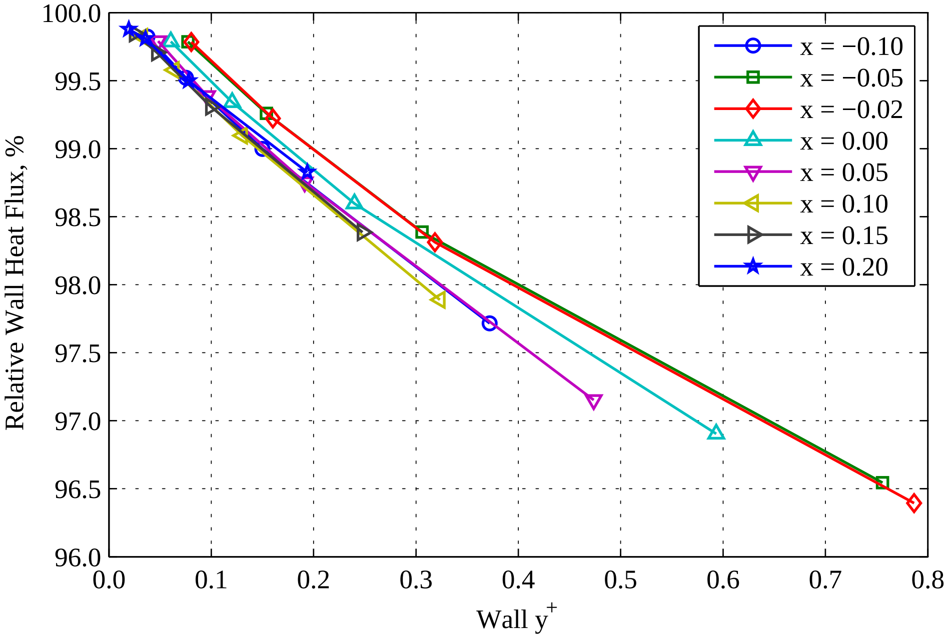

Figure C.3: Relative heat flux as a function of wall y^+ (wall-normal mesh refinement) for select axial stations.

10 % in the wall-normal direction. Heat flux is plotted in Figure C.2 as a function of axial position, where it can be seen that the heat flux is influenced by the choice of wall-normal mesh refinement.

To better quantify the effect of the mesh on the heat flux, a line is fit to the heat flux at select axial positions as a function of wall y^+. In this way, an estimate for the heat flux in the limit of wall $y^+ = 0$ is obtained. The relative heat flux as a function of wall y^+ is computed by dividing the heat flux obtained from the simulations by this estimated heat flux in the limit of wall $y^+ = 0$. This relative heat flux, which is a measure of the accuracy of the solution obtained with any given mesh, is plotted in Figure C.3 for a number of stations along the length of the nozzle. It can be seen from this plot that to obtain an error of 1 % or less it is necessary to have a wall $y^+ \leq 0.15$ (either the fine or extra-fine mesh). Errors of up to 4 % are experienced with the coarsest mesh, even though the wall y^+ is less than one. The general rule of thumb that meshes with wall $y^+ \approx 1$ are adequate therefore seems to only hold for

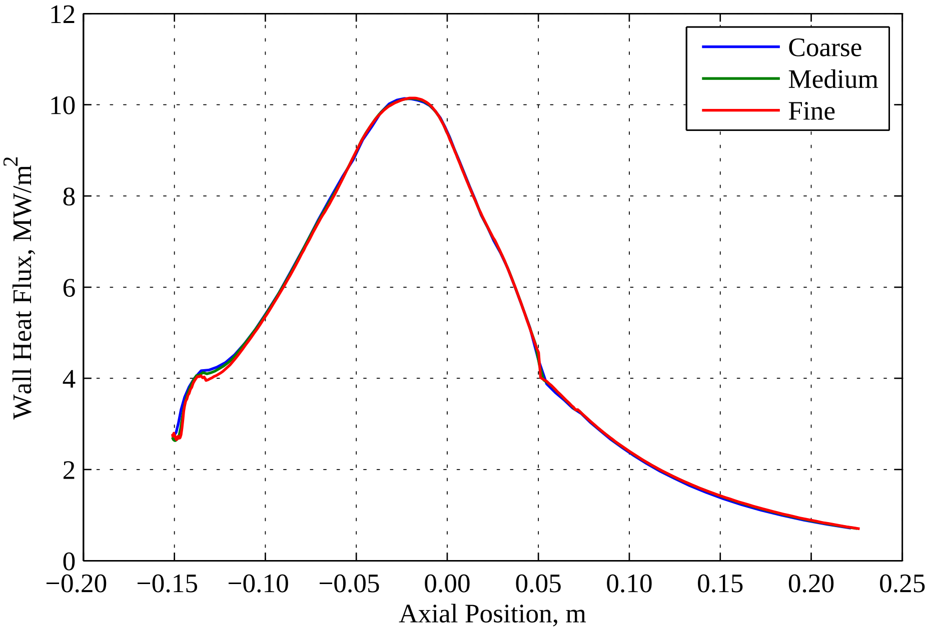

Figure C.4: Heat flux as a function of axial position and wall-tangent mesh refinement level.

force and moment predictions; accurately capturing heat flux requires a more refined mesh. There appears to be a predominantly linear relationship between heat flux and wall y^+; these trends hold across all axial positions on the nozzle.

For the second study, the mesh resolution in the wall-tangent direction is considered. Three meshes are utilized: coarse (75 cells in wall-tangent direction), medium (150 cells), and fine (300). All meshes used the coarse wall-normal mesh (94 cells in wall-normal direction) and a 10 % stretch ratio in the wall-normal direction. Heat flux is plotted in Figure C.4, where it can be seen that, aside from a few localized regions where there are changes in curvature of the geometry, the wall-tangent mesh resolution has negligible influence. Pressure, temperature, and velocity contours from the three meshes are compared in Figure C.5. All three meshes agree well in the converging portion of the nozzle, and in the near-wall region along the length of the nozzle. However, larger differences appear in the core of the nozzle downstream of the throat. This is largely due to the varying ability of the different meshes to capture the ex-

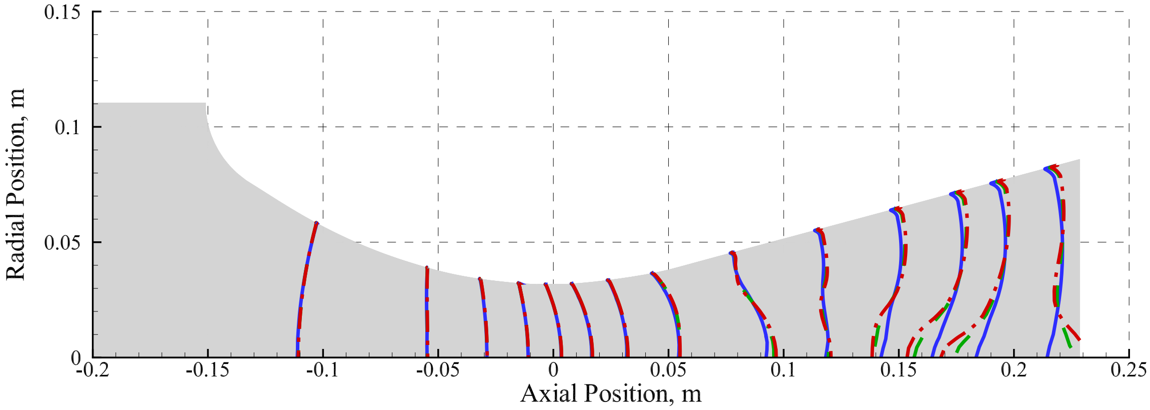

(a) Pressure.

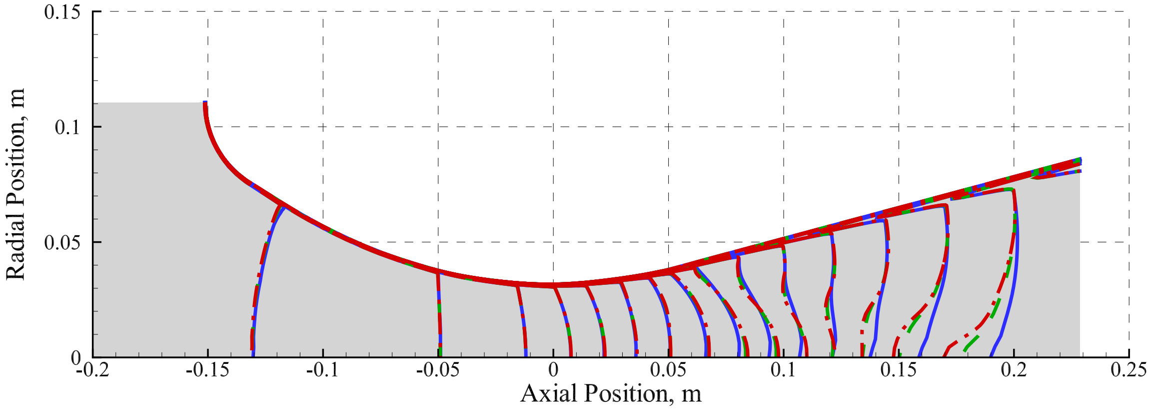

(b) Temperature.

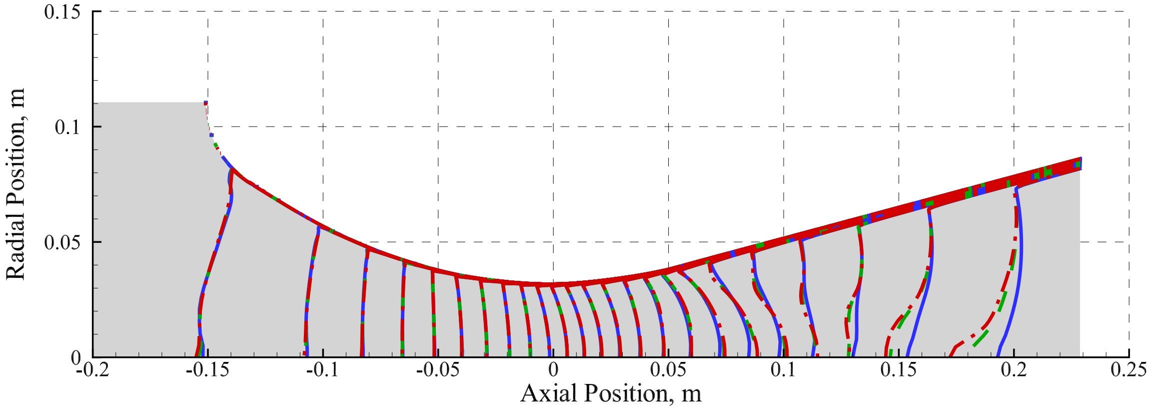

(c) Velocity.

Figure C.5: Comparison of pressure (top), temperature (middle), and velocity (bottom) contours as a function of wall-tangent mesh refinement level. Blue is coarse mesh, green is medium, red is fine.

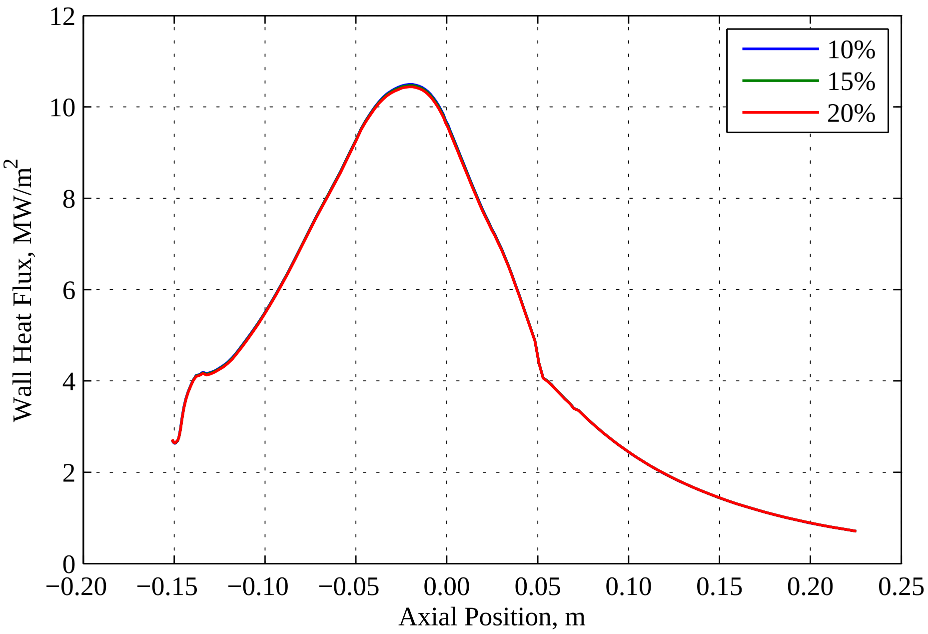

Figure C.6: Heat flux as a function of axial position and wall-normal stretch ratio.

pansion fan emanating from the throat region. The medium and fine meshes produce slightly different results, but agree reasonably well. The coarse mesh produces results that are more significantly different. Because of the small differences between the medium and fine mesh, and because the objective of this research is primarily focused on the wall region, it is decided that a mesh with the medium wall-tangent resolution is adequate.

The final study investigates the effect of stretch ratio in the wall-normal direction. Three different stretch ratios are considered: 10 %, 15 %, and 20 %. The mesh near-wall cell thickness corresponds to the extra-fine mesh that produced the smallest wall y^+ values; the wall-tangent mesh resolution corresponded to the medium mesh. Cell counts in the wall-normal direction are 118, 95, and 82, respectively. Heat flux for this study is plotted as a function of axial position in Figure C.6. At the location of peak heating (near the throat) the differences between the 10 % stretch ratio and the 20 % stretch ratio meshes are less than 0.5 %. It is therefore decided to use a mesh with a 20 % stretch ratio.

Based on the findings from these mesh refinement studies, a final mesh is constructed for the improved model for the HIPPO nozzle (see Section 7.2.2). A few minor optimizations beyond the meshes just described are included. The medium wall-tangent mesh spacing, the extra-fine near-wall thickness (smallest wall y^+), and a 20 % stretch ratio in the wall-normal direction near the wall are used. The mesh contains 150 cells in the wall-tangent direction and 77 cells in the wall-normal direction, for a total of 11,500 cells. It is expected that this mesh can yield heat flux values with an error of less than 0.5 %.

Material Response Domain

A sequence of mesh refinement studies is also performed to determine appropriate settings for the HIPPO nozzle solid domain. Three different mesh parameters are investigated in these studies: wall-tangent mesh resolution, near-wall cell thickness, and stretch ratio. The impact of the alignment of the diagonal faces in the mesh is also investigated.

To capture the strong wall-normal gradients, the mesh for the solid domain features a layer of stacked, anisotropic, triangular elements adjacent to the ablating boundary. This mesh topology is obtained by first generating a structured mesh with quadrilateral cells, then triangulating each cell. Depending on how this triangulation is performed, the direction of these diagonal faces can either be random or aligned. Meshes with random diagonal orientation produce non-physical surface profiles, as can be easily observed for the pyrolysis gas mass flux profile presented in Figure C.7. Other variables are also affected, but to a lesser extent. For example, the surface temperature profiles presented in Figure C.8 for the non-aligned diagonal mesh have small-amplitude defects that can not be observed on the scale of the plot. The defects in these surface profiles are mainly an aesthetic problem for decoupled analyses, but are found to be very destabilizing when attempting conjugate analyses. However,

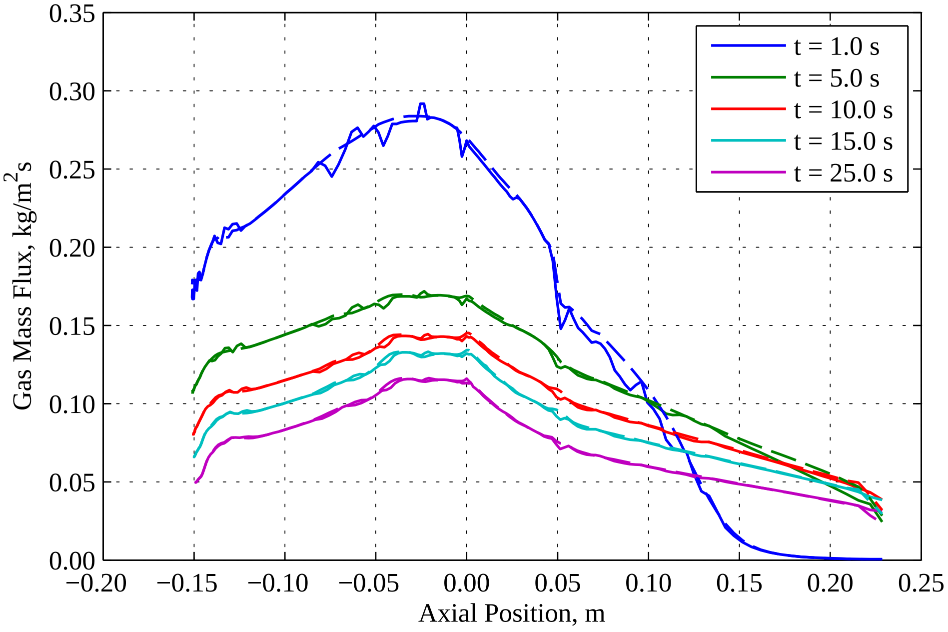

Figure C.7: Pyrolysis gas mass flux as a function of axial position and diagonal face alignment at select instances in time. Mesh with non-aligned diagonal faces is represented by solid lines, while mesh with aligned diagonal faces is represented by dashed lines.

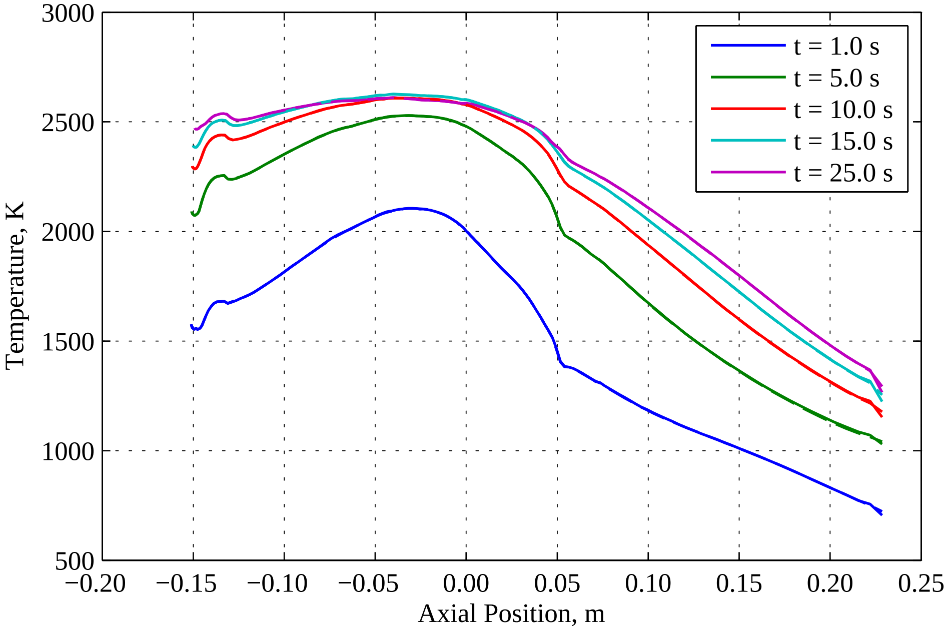

Figure C.8: Surface temperature as a function of axial position and diagonal face alignment at select instances in time. Mesh with non-aligned diagonal faces is represented by solid lines, while mesh with aligned diagonal faces is represented by dashed lines.

forcing the diagonal faces to all be aligned eliminates these defects and produces smooth profiles for all variables, as observed in Figures C.7 and C.8.

A study investigating the effects of wall-tangent mesh refinement is performed. Three meshes are utilized: coarse (75 cells in wall-tangent direction), medium (150 cells), and fine (300). All meshes used a fine wall-normal mesh (with a near-wall thickness of $2.54 \times 10^{-5}\,\mathrm{m}$) and a $5\,\%$ stretch ratio in the wall-normal direction. Pyrolysis gas mass flux profiles are compared in Figure C.9; only minor differences are observed between the results produced by the different meshes. Surface temperature profiles are compared in Figure C.10; the results produced by the different meshes are virtually indistinguishable. Based on these observations, it is determined that the medium wall-tangent mesh refinement is adequate.

The next study investigates the impact of the thickness of the first layer of cells adjacent to the ablating wall. Two values for this near-wall thickness are considered: $2.54 \times 10^{-4}\,\mathrm{m}$ (coarse mesh) and $2.54 \times 10^{-5}\,\mathrm{m}$ (fine mesh); wall-normal stretch ratio is $5\,\%$. Pyrolysis gas mass flux at the nozzle throat is plotted as a function of time in Figure C.11. Nonphysical oscillations in the pyrolysis gas flux are predicted with the coarse mesh, while these oscillations are absent from the results computed with the fine mesh. This suggests that the coarse mesh is unable to adequately capture the very sharp solid density gradient that moves through the domain as pyrolysis occurs. Similar oscillations were reported in Ref. [12] for simulations of nylon phenolic; these oscillations were attributed to the rapid thermal decomposition and could be eliminated by refining the mesh.

The final study investigates the effect of stretch ratio in the wall-normal direction. Three different stretch ratios are considered: $5\,\%$, $10\,\%$, and $20\,\%$. Near-wall thickness is $2.54 \times 10^{-5}\,\mathrm{m}$. Figure C.12 presents pyrolysis gas mass flux as a function of time. Sizable oscillations are observed for the $20\,\%$ stretch ratio; this mesh is too coarse to adequately capture the pyrolysis front. Oscillations of a much smllaer amplitude

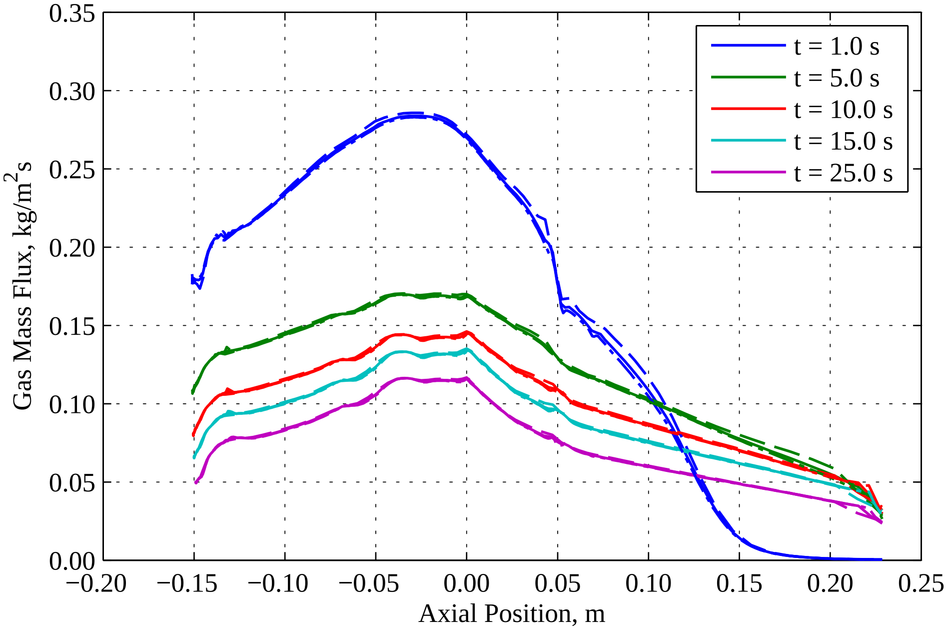

Figure C.9: Pyrolysis gas mass flux as a function of axial position and wall-tangent mesh refinement level at select instances in time. Coarse mesh is represented by dashed lines, medium mesh by solid lines, and fine mesh by dash-dotted lines.

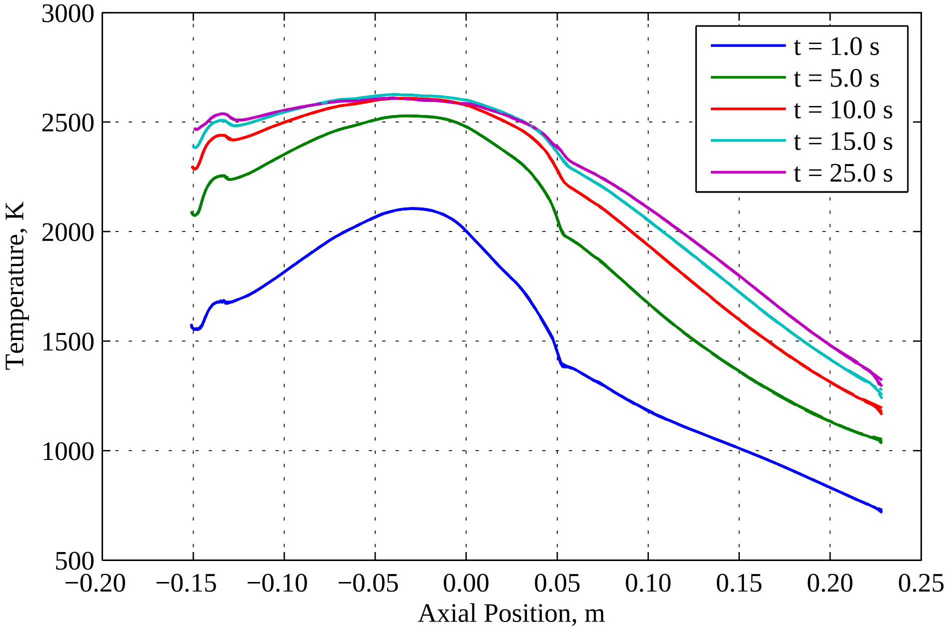

Figure C.10: Surface temperature as a function of axial position and wall-tangent mesh refinement level at select instances in time. Coarse mesh is represented by dashed lines, medium mesh by solid lines, and fine mesh by dash-dotted lines.

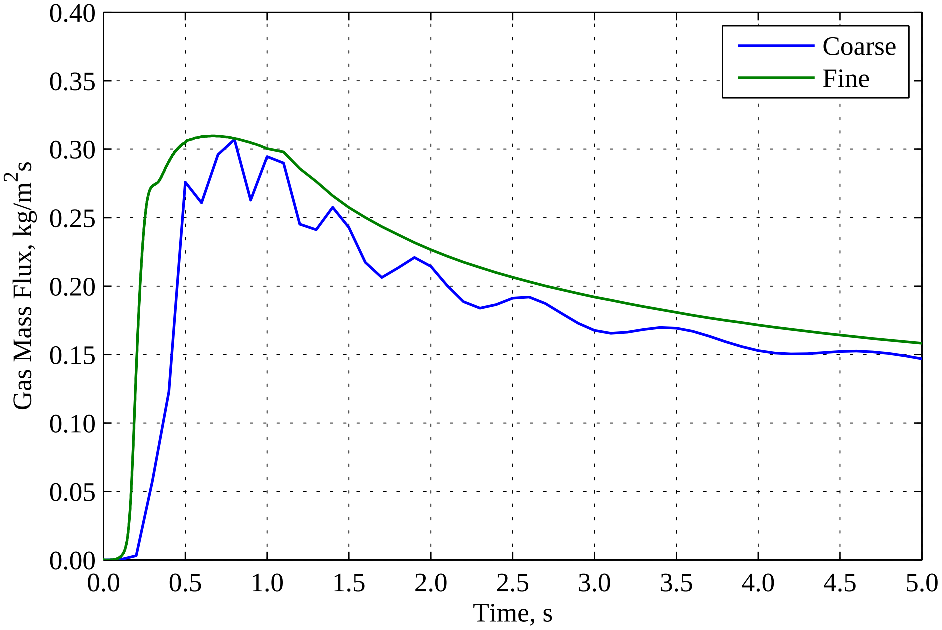

Figure C.11: Pyrolysis gas mass flux at the throat as a function of time and near-wall cell thickness.

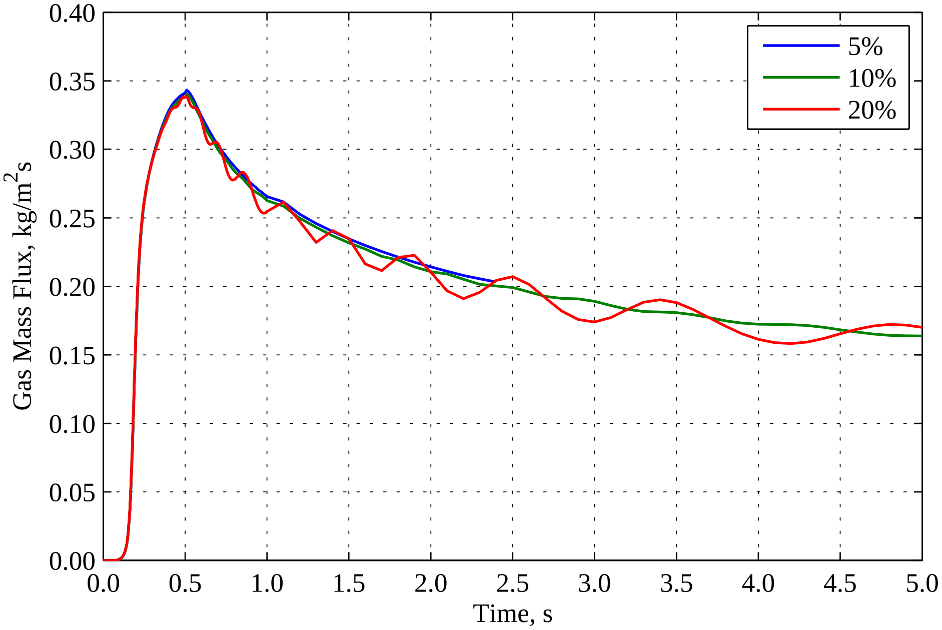

Figure C.12: Pyrolysis gas mass flux at the throat as a function of time and wall-normal stretch ratio.

are produced with the mesh with a 10 % stretch ratio, while oscillations appear to be absent from the results of the simulation using the mesh with a 5 % stretch ratio.

Based on the findings from these mesh refinement studies, a final mesh is constructed for the solid domain of the improved model for the HIPPO nozzle (see Section 7.2.2). This mesh uses the medium wall-tangent refinement, a near-wall thickness of 2.54×10^{-5} m, and a 5 % stretch ratio.

APPENDIX D

Jeppson Mechanism

The detailed mechanism used as the basis for the new, reduced mechanism developed in this work (see Chapter V) is the “reduced Jeppson” mechanism [99] as presented by Gross[100] and by Felt [101]. This baseline mechanism features the 127 reactions listed in Table D.1 involving 37 gas-phase species:

$$C_2H_2, C_2H_3, C_2H_4, C_4H_6, CH_2O, CH_2, CH_3, CH_4, CO, CO_2, Cl, Cl_2,$$
$$ClO, ClO_2, ClO_3, ClOH, H, H_2, H_2O, HCN, HCO, HCl, HClO_4, HNO,$$
$$HO_2, N, N_2, N_2H_2, N_2O, NH, NH_2, NH_3, NO, NO_2, O, O_2, OH$$

Reaction rates are computed using a modified Arrhenius equation:

$$k = AT^b \exp\left(-T_a/T\right) \tag{D.1}$$

The statements such as “CH_4 enhanced by 2.0” indicate that the reaction rate is increased by the given factor (e.g. 2.0) when the given species (e.g. CH_4) acts as a collision partner.

Table D.1: Forward reaction rates for the “reduced Jeppson” mechanism.

Index	Reaction	A, mol $-$ cm $-$ s	b	T_a, K
1	$HClO_4 \rightleftharpoons ClO_3 + OH$	1.00×10^{14}	0	19675.89
2	$HClO_4 + HNO \rightleftharpoons ClO_3 + H_2O + NO$	1.50×10^{13}	0	3019.32
3	$HClO_4 + HCO \rightleftharpoons ClO_3 + CO + H_2O$	5.00×10^{13}	0	0
4	$HClO_4 + HCO \rightleftharpoons ClO_2 + CO_2 + H_2O$	1.50×10^{12}	0	0
5	$ClO_3 \rightleftharpoons ClO + O_2$	1.70×10^{13}	0.50	0
6	$Cl_2 + O_2 + M \rightleftharpoons ClO_2 + Cl + M$	6.00×10^{8}	0	5636.06
		CH_4 enhanced by 2.0		
		CO enhanced by 1.5		
		CO_2 enhanced by 2.0		
		H_2 enhanced by 2.0		
		H_2O enhanced by 6.0		
7	$ClO + NO \rightleftharpoons Cl + NO_2$	6.78×10^{12}	0	156.50
8	$ClO + ClOH \rightleftharpoons Cl_2 + HO_2$	1.00×10^{11}	0	5032.20
9	$ClOH + OH \rightleftharpoons ClO + H_2O$	1.80×10^{13}	0	0
10	$HCl + OH \rightleftharpoons Cl + H_2O$	5.00×10^{11}	0	377.41
11	$Cl_2 + H \rightleftharpoons HCl + Cl$	8.40×10^{13}	0	578.70
12	$ClO + NH_3 \rightleftharpoons ClOH + NH_2$	6.00×10^{11}	0.50	3220.61
13	$NH_3 + Cl \rightleftharpoons NH_2 + HCl$	4.50×10^{11}	0.50	50.32
14	$NH_3 + OH \rightleftharpoons NH_2 + H_2O$	5.00×10^{7}	1.60	480.57
15	$NH_2 + O_2 \rightleftharpoons HNO + OH$	3.00×10^{9}	0	0

Index	Reaction	A, mol − cm − s	b	T_a, K
16	$NH_2 + NO \rightleftharpoons H_2O + N_2$	6.20×10^{15}	-1.25	0
17	$HNO + OH \rightleftharpoons NO + H_2O$	1.30×10^{7}	1.90	-478.06
18	$HNO + O_2 \rightleftharpoons NO_2 + OH$	1.50×10^{13}	0	5032.20
19	$HNO + H \rightleftharpoons H_2 + NO$	4.50×10^{11}	0.72	332.13
20	$NO + H + M \rightleftharpoons HNO + M$	8.90×10^{19}	-1.32	372.38
		CH_4 enhanced by 2.0		
		CO enhanced by 1.5		
		CO_2 enhanced by 2.0		
		H_2 enhanced by 2.0		
		H_2O enhanced by 6.0		
21	$HO_2 + N_2 \rightleftharpoons HNO + NO$	2.70×10^{10}	0.50	21034.58
22	$NO + HO_2 \rightleftharpoons NO_2 + OH$	2.11×10^{12}	0	241.55
23	$H + NO_2 \rightleftharpoons NO + OH$	3.47×10^{14}	0	744.77
24	$H_2 + OH \rightleftharpoons H_2O + H$	2.16×10^{8}	1.51	1726.04
25	$C_2H_3 + O_2 \rightleftharpoons CH_2O + HCO$	3.98×10^{12}	0	-120.77
26	$C_2H_2 + H + M \rightleftharpoons C_2H_3 + M$	5.60×10^{12}	0	1207.73
		CH_4 enhanced by 2.0		
		CO enhanced by 1.5		
		CO_2 enhanced by 2.0		
		H_2 enhanced by 2.0		
		H_2O enhanced by 6.0		
27	$C_2H_2 + OH \rightleftharpoons CH_3 + CO$	4.84×10^{-4}	4.00	-1006.44

Index	Reaction	A, mol − cm − s	b	T_a, K
28	$H_2 + CO + M \rightleftharpoons CH_2O + M$	4.30×10^7	1.50	40056.29
		CH_4 enhanced by 2.0		
		CO enhanced by 1.5		
		CO_2 enhanced by 2.0		
		H_2 enhanced by 2.0		
		H_2O enhanced by 6.0		
29	$CH_4 + Cl \rightleftharpoons CH_3 + HCl$	2.50×10^{13}	0	1927.33
30	$CH_4 + ClO \rightleftharpoons CH_3 + ClOH$	6.00×10^{11}	0.50	2868.35
31	$CH_4 + H \rightleftharpoons CH_3 + H_2$	6.60×10^8	1.62	5454.90
32	$CH_4 + OH \rightleftharpoons CH_3 + H_2O$	1.00×10^8	1.60	1570.05
33	$CH_3 + H + M \rightleftharpoons CH_4 + M$	1.27×10^{16}	-0.63	192.73
		CH_4 enhanced by 2.0		
		CO enhanced by 1.5		
		CO_2 enhanced by 2.0		
		H_2 enhanced by 2.0		
		H_2O enhanced by 6.0		
34	$HCO + M \rightleftharpoons CO + H + M$	1.87×10^{17}	-1.00	8554.73
		CH_4 enhanced by 2.0		
		CO enhanced by 1.5		
		CO_2 enhanced by 2.0		
		H_2 enhanced by 2.0		
		H_2O enhanced by 0.0		
35	$HCN + OH \rightleftharpoons NH_2 + CO$	1.62×10^2	2.56	4528.98
36	$CO + OH \rightleftharpoons CO_2 + H$	4.76×10^7	1.23	35.23
37	$CO + ClO \rightleftharpoons CO_2 + Cl$	3.00×10^{12}	0	503.22

Index	Reaction	A, $\mathrm{mol-cm-s}$	b	T_a, K
38	$CO + ClO_2 \rightleftharpoons CO_2 + ClO$	1.00×10^{10}	0	0
39	$C_2H_4 + OH \rightleftharpoons H_2O + C_2H_3$	3.60×10^{6}	2.00	1258.05
40	$C_4H_6 + OH \rightleftharpoons 2C_2H_2 + H_2 + OH$	5.00×10^{12}	0.68	553.54
41	$C_4H_6 + ClO \rightleftharpoons 2C_2H_2 + ClOH + H$	5.00×10^{12}	0.50	3220.61
42	$C_4H_6 + Cl \rightleftharpoons 2C_2H_2 + HCl + H$	6.75×10^{12}	0.50	50.32
43	$C_4H_6 \rightleftharpoons 2C_2H_3$	2.50×10^{18}	0	50321.97
44	$C_4H_6 + H \rightleftharpoons C_2H_3 + C_2H_2 + H_2$	2.30×10^{12}	0	10064.39
45	$H + O_2 \rightleftharpoons O + OH$	8.30×10^{13}	0	7252.91
46	$C_2H_2 + O \rightleftharpoons CH_2 + CO$	1.02×10^{7}	2.00	956.12
47	$CH_2 + H_2 \rightleftharpoons CH_3 + H$	5.00×10^{5}	2.00	3638.28
48	$CH_2 + H + M \rightleftharpoons CH_3 + M$	2.50×10^{16}	-0.80	0
		CH_4 enhanced by 2.0		
		CO enhanced by 1.5		
		CO_2 enhanced by 2.0		
		H_2 enhanced by 2.0		
		H_2O enhanced by 6.0		
49	$CH_4 + O \rightleftharpoons CH_3 + OH$	1.02×10^{9}	1.50	301.93
50	$CH_3 + O \rightleftharpoons CH_2O + H$	8.43×10^{13}	0	0
51	$CH_2 + O \rightleftharpoons H + HCO$	8.00×10^{13}	0	0
52	$CH_3 + O_2 \rightleftharpoons OH + CH_2O$	3.60×10^{10}	0	4498.78
53	$OH + CH_3 \rightleftharpoons CH_2 + H_2O$	5.60×10^{7}	1.60	2727.45

Index	Reaction	A, mol − cm − s	b	T_a, K
54	$OH + CH_2 \rightleftharpoons H + CH_2O$	2.00×10^{13}	0	0
55	$CH_2 + O_2 \rightleftharpoons OH + HCO$	1.32×10^{13}	0	754.83
56	$C_2H_4 + O_2 \rightleftharpoons 2CO + 2H_2$	1.80×10^{14}	0	17864.30
57	$NH_2 + NO_2 \rightleftharpoons 2HNO$	1.40×10^{12}	0	0
58	$NH_2 + ClO \rightleftharpoons HNO + HCl$	2.50×10^{12}	0	0
59	$O_2 + HNO \rightleftharpoons NO + HO_2$	1.00×10^{13}	0	6541.86
60	$H + Cl + M \rightleftharpoons HCl + M$	5.30×10^{21}	-2.00	-1006.44
		CH_4 enhanced by 2.0		
		CO enhanced by 1.5		
		CO_2 enhanced by 2.0		
		H_2 enhanced by 2.0		
61	$Cl + Cl + M \rightleftharpoons Cl_2 + M$	3.34×10^{14}	0	-905.80
		CH_4 enhanced by 2.0		
		CO enhanced by 1.5		
		CO_2 enhanced by 2.0		
		H_2 enhanced by 2.0		
62	$Cl + HO_2 \rightleftharpoons ClO + OH$	2.47×10^{13}	0	449.88
63	$Cl + CH_2O \rightleftharpoons HCO + HCl$	5.00×10^{13}	0	251.61
64	$ClO + O \rightleftharpoons Cl + O_2$	6.60×10^{13}	0	221.42
65	$ClO{+}CH_3 \rightleftharpoons CH_2O{+}H{+}Cl$	3.33×10^{11}	0.46	15.10
66	$ClO + CH_3 \rightleftharpoons CH_2O + HCl$	3.47×10^{18}	-1.80	1041.66
67	$H + HCl \rightleftharpoons Cl + H_2$	7.94×10^{12}	0	1710.95
68	$HCl + O \rightleftharpoons Cl + OH$	2.30×10^{11}	0.64	452.90
69	$Cl_2 + O \rightleftharpoons Cl + ClO$	2.51×10^{12}	0	1368.76

Index	Reaction	A, mol − cm − s	b	T_a, K
70	$N_2O + M \rightleftharpoons N_2 + O + M$	6.20×10^{14}	0	28230.63
		CH_4 enhanced by 2.0		
		CO enhanced by 1.5		
		CO_2 enhanced by 2.0		
		H_2 enhanced by 2.0		
		H_2O enhanced by 6.0		
71	$N_2O + OH \rightleftharpoons N_2 + HO_2$	2.00×10^{12}	0	10597.81
72	$N_2O + O \rightleftharpoons NO + NO$	2.90×10^{13}	0	11649.54
73	$N_2O + O \rightleftharpoons N_2 + O_2$	1.40×10^{12}	0	5439.80
74	$N_2O + H \rightleftharpoons N_2 + OH$	4.40×10^{14}	0	9500.79
75	$2H + M \rightleftharpoons H_2 + M$	1.00×10^{18}	-1.00	0
		CH_4 enhanced by 2.0		
76	$2H + H_2 \rightleftharpoons 2H_2$	9.00×10^{16}	-0.60	0
77	$2H + H_2O \rightleftharpoons H_2 + H_2O$	6.00×10^{19}	-1.25	0
78	$2H + CO_2 \rightleftharpoons H_2 + CO_2$	5.50×10^{20}	-2.00	0
79	$H + HCO \rightleftharpoons H_2 + CO$	7.34×10^{13}	0	0
80	$H + CH_2O \rightleftharpoons HCO + H_2$	2.30×10^{10}	1.05	1648.04
81	$H + C_2H_3 \rightleftharpoons H_2 + C_2H_2$	3.00×10^{13}	0	0
82	$H + C_2H_4 \rightleftharpoons C_2H_3 + H_2$	1.33×10^{6}	2.53	6159.41
83	$C_2H_4 + M \rightleftharpoons H_2 + C_2H_2 + M$	8.00×10^{12}	0.44	44670.81
		CH_4 enhanced by 2.0		
		CO enhanced by 1.5		
		CO_2 enhanced by 2.0		
		H_2 enhanced by 2.0		
		H_2O enhanced by 6.0		

Index	Reaction	A, mol − cm − s	b	T_a, K
84	$ClO_2 + NO \rightleftharpoons ClO + NO_2$	1.00×10^{11}	0	0
85	$Cl + ClO_2 \rightleftharpoons ClO + ClO$	5.00×10^{13}	0	3019.32
86	$ClO + ClO \rightleftharpoons Cl_2 + O_2$	1.00×10^{11}	0	0
87	$Cl + HO_2 \rightleftharpoons HCl + O_2$	1.80×10^{13}	0	0
88	$Cl + O_2 + M \rightleftharpoons ClO_2 + M$	8.00×10^{6}	0	2616.74
89	$ClOH + O \rightleftharpoons HCl + O_2$	1.20×10^{14}	0	0
90	$NO_2 + O \rightleftharpoons NO + O_2$	1.00×10^{13}	0	301.93
91	$HNO + HNO \rightleftharpoons H_2O + N_2O$	3.95×10^{12}	0	2516.10
92	$NO_2{+}NO_2 \rightleftharpoons NO{+}NO{+}O_2$	1.00×10^{14}	0	12580.49
93	$Cl + N_2O \rightleftharpoons ClO + N_2$	1.20×10^{14}	0	16857.86
94	$HClO_4 + HNO \rightleftharpoons ClO_2 + H_2O + NO_2$	2.00×10^{13}	0	3019.32
95	$OH + OH \rightleftharpoons H_2O + O$	6.00×10^{8}	1.30	0
96	$NH_2 + NO_2 \rightleftharpoons H_2O + N_2O$	4.50×10^{11}	0	0
97	$HNO + NH_2 \rightleftharpoons NH_3 + NO$	5.00×10^{11}	0.50	503.22
98	$ClOH + HCl \rightleftharpoons Cl_2 + H_2O$	4.00×10^{12}	0	5032.20
99	$HClO_4 + NH_2 \rightleftharpoons ClO_2 + H_2O + HNO$	1.00×10^{12}	0	0
100	$HClO_4 + NH_2 \rightleftharpoons ClOH + HNO + HO_2$	1.00×10^{11}	0	0
101	$HClO_4 + NO \rightleftharpoons ClO + HO_2 + NO_2$	1.00×10^{13}	0	5032.20
102	$ClO_2 + ClO_2 \rightleftharpoons ClO + ClO_3$	1.80×10^{13}	0	9057.95
103	$ClO + HNO \rightleftharpoons HCl + NO_2$	3.00×10^{12}	0	0
104	$HCl + HO_2 \rightleftharpoons ClO + H_2O$	3.00×10^{12}	0	0

Index	Reaction	A, mol − cm − s	b	T_a, K
105	$NH_2 + NO \rightleftharpoons H + N_2 + OH$	6.30×10^{19}	-2.50	956.12
106	$NH_2 + OH \rightleftharpoons H_2O + NH$	4.00×10^{6}	2.00	503.22
107	$NH_2 + NH_2 \rightleftharpoons NH + NH_3$	5.00×10^{13}	0	5032.20
108	$NH + NO \rightleftharpoons N_2 + OH$	1.00×10^{13}	0	0
109	$NH + NO \rightleftharpoons H + N_2 + O$	2.30×10^{13}	0	0
110	$Cl + NH_2 \rightleftharpoons HCl + NH$	5.00×10^{10}	0.50	0
111	$ClO_2 + NH \rightleftharpoons ClO + HNO$	1.00×10^{14}	0	0
112	$HClO_4 + NH \rightleftharpoons$ $ClO_2 + HNO + OH$	1.00×10^{14}	0	0
113	$N + NO_2 \rightleftharpoons NO + NO$	1.00×10^{14}	0	0
114	$N + N_2O \rightleftharpoons N_2 + NO$	5.00×10^{13}	0	0
115	$NH + OH \rightleftharpoons H_2O + N$	5.00×10^{11}	0.50	1006.44
116	$NH + OH \rightleftharpoons H_2 + NO$	1.60×10^{12}	0.60	754.83
117	$NH + NH_2 \rightleftharpoons N + NH_3$	1.00×10^{13}	0	1006.44
118	$NH + NH_2 \rightleftharpoons H + N_2H_2$	5.00×10^{13}	0	0
119	$NH_2 + NH_2 \rightleftharpoons H_2 + N_2H_2$	5.00×10^{11}	0	0
120	$N_2H_2 + NO \rightleftharpoons N_2O + NH_2$	3.00×10^{12}	0	0
121	$ClOH + H \rightleftharpoons ClO + H_2$	6.00×10^{12}	0	0
122	$HClO_4 + NH \rightleftharpoons$ $ClO_3 + H_2O + N$	1.00×10^{14}	0	5535.42
123	$HO_2 + CH_3 \rightleftharpoons O_2 + CH_4$	1.00×10^{12}	0	0
124	$CH_2 + CH_4 \rightleftharpoons 2CH_3$	2.46×10^{6}	2.00	4161.63
125	$CH_3 + HCO \rightleftharpoons CH_4 + CO$	2.65×10^{13}	0	0
126	$CH_3 + CH_2O \rightleftharpoons HCO + CH_4$	3.32×10^{3}	2.81	2948.87
127	$CH_3 + C_2H_4 \rightleftharpoons C_2H_3 + CH_4$	2.27×10^{5}	2.00	4629.62

BIBLIOGRAPHY

BIBLIOGRAPHY

[1] Lewis Campbell and William Garnett, *The Life of James Clerk Maxwell*, Macmillan, 1882.

[2] George P. Sutton and Oscar Biblarz, *Rocket Propulsion Elements*, John Wiley & Sons, 7th edition, 2001.

[3] L. Powers, R. Bailey, and B. Morrison, “Shuttle Solid Rocket Motor Nozzle Alternate Ablative Evaluation,” *AIAA/SAE/ASME 17th Joint Propulsion Conference*, July 1981, doi:10.2514/6.1981-1461. AIAA 1981–1461.

[4] Frank S. Milos and Daniel J. Rasky, “Review of Numerical Procedures for Computational Surface Thermochemistry,” *Journal of Thermophysics and Heat Transfer*, 8(1):24–34, January–March 1994, doi:10.2514/3.497.

[5] J. Arnold, J. Dodson, and B. Laub, “Subscale Solid Motor Nozzle Tests — Phase IV and Nozzle Materials Screening and Thermal Characterization — Phase V,” NASA CR 161254, National Aeronautics and Space Administration, June 1979.

[6] Robert M Kendall, Eugene P Bartlett, Roald A Rindall, and Carl B Moyer, “An Analysis of the Coupled Chemically Reacting Boundary Layer and Charring Ablator, Part I: Summary Report,” NASA CR–1060, National Aeronautics and Space Administration, Washington, D.C., June 1968.

[7] D. R. Bartz, “A Simple Equation for Rapid Estimation of Rocket Nozzle Convective Heat Transfer Coefficients,” *Jet Propulsion*, 37(1):49–51, January 1957.

[8] Aerotherm Corporation, Huntsville, AL, *User’s Manual, Nozzle Aero Thermochemistry (NAT) Computer Code, Version 2.0*, February 1994.

[9] Acurex Corporation, Mountain View, CA, *User’s Manual, Non-Proprietary, Aerotherm Charring Material Thermal Response and Ablation Program, CMA87S*, November 1987.

[10] David W. Kuntz, Basil Hassan, and Donald L. Potter, “Predictions of Ablating Hypersonic Vehicles Using an Iterative Coupled Fluid/Thermal Approach,” *Journal of Thermophysics and Heat Transfer*, 15(2):129–139, April–June 2001, doi:10.2514/2.6594.

[11] Christopher O. Johnston, Peter A. Gnoffo, and Alireza Mazaheri, "Study of Ablation-Flowfield Coupling Relevant to the Orion Heat Shield," *Journal of Thermophysics and Heat Transfer*, 26(2):213–221, April–June 2012, doi: 10.2514/1.T3769.

[12] Carl B. Moyer and Roald A. Rindal, "An Analysis of the Coupled Chemically Reacting Boundary Layer and Charring Ablator, Part II: Finite Difference Solution for the In-Depth Response of Charring Materials Considering Surface Chemical and Energy Balances," NASA CR–1061, National Aeronautics and Space Administration, Washington, D.C., 1968.

[13] Gerald W. Russell and Forrest Strobel, "Modeling Approach for Intumescing Charring Heatshield Materials," *Journal of Spacecraft and Rockets*, 43(4):739–749, July–August 2006, doi:10.2514/1.15153.

[14] ITT Industries, Advanced Engineering and Sciences, Huntsville, AL, *User's Manual, Charring Material Thermal Response and Ablation Program with Intumescence and Shear Removal Modeling Capabilities, CMASWELL*, January 2006.

[15] Y.-K. Chen and Frank S. Milos, "Ablation and Thermal Response Program for Spacecraft Heatshield Analysis," *Journal of Spacecraft and Rockets*, 36(3):475–483, May 1999, doi:10.2514/2.3469.

[16] Adam Joseph Amar, *Modeling of One-Dimensional Ablation with Porous Flow Using Finite Control Volume Procedure*, Master's thesis, North Carolina State University, Raleigh, NC, 2006.

[17] Adam J. Amar, Bennie F. Blackwell, and Jack R. Edwards, "One-Dimensional Ablation Using a Full Newton's Method and Finite Control Volume Procedure," *Journal of Thermophysics and Heat Transfer*, 22(1):71–82, January–March 2008, doi:10.2514/1.29610.

[18] Adam J. Amar, Bennie F. Blackwell, and J. R. Edwards, "Development and Verification of a One-Dimensional Ablation Code Including Pyrolysis Gas Flow," *Journal of Thermophysics and Heat Transfer*, 23(1):59–71, January–March 2009, doi:10.2514/1.36882.

[19] Alexandre Martin and Iain D. Boyd, "Non-Darcian Behavior of Pyrolysis Gas in a Thermal Protection System," *Journal of Thermophysics and Heat Transfer*, 24(1):60–68, January–March 2010, doi:10.2514/1.44103.

[20] Alexandre Martin and Iain Boyd, "Simulation of Pyrolysis Gas Within a Thermal Protection System," *40th Thermophysics Conference*, June 2008, doi: 10.2514/6.2008-3805. AIAA 2008–3805.

[21] Mark E. Ewing, Travis S. Laker, and David T. Walker, "Numerical Modeling of Ablation Heat Transfer," *Journal of Thermophysics and Heat Transfer*, 27(4):615–632, October–December 2013, doi:10.2514/1.T4164.

[22] B. F. Blackwell and R. E. Hogan, “Numerical Solution of Axisymmetric Heat Conduction Problems Using Finite Control Volume Technique,” *Journal of Thermophysics and Heat Transfer*, 7(3):462–471, January–March 1993, doi:10.2514/3.441.

[23] R. E. Hogan, B. F. Blackwell, and R. J. Cochran, “Application of Moving Grid Control Volume Finite Element Method to Ablation Problems,” *Journal of Thermophysics and Heat Transfer*, 10(2):312–319, April–June 1996, doi:10.2514/3.789.

[24] Subrahmanya S. Katte, S. K. Das, and S. P. Venkateshan, “Two-Dimensional Ablation in Cylindrical Geometry,” *Journal of Thermophysics and Heat Transfer*, 14(4):548–556, October–December 2000, doi:10.2514/2.6556.

[25] David K. Gartling, Roy E. Hogan, and Micheal W. Glass, “COYOTE — A Finite Element Computer Program for Nonlinear Heat Conduction Problems, Part I — Theoretical Background,” Sandia Report SAND2009-4926, Sandia National Laboratories, Albuquerque, New Mexico, May 2009.

[26] H. H. C. King, K. K. Muramoto, A. L. Murray, and S. W. Pronchick, “ABRES Shape Change Code (ASCC86) — Technical Report and User’s Manual,” Technical Report BMO TR-87-57, Acurex Corp., Aerotherm Div., December 1986.

[27] Jonathan E. Wiebenga, *High-Fidelity Material Response Modeling as Part of an Aerothermoelastic Framework for Hypersonic Flows*, Ph.D. thesis, University of Michigan, Ann Arbor, MI, 2014.

[28] Jonathan Wiebenga and Iain Boyd, “Computation of Multi-Dimensional Material Response Coupled to Hypersonic Flow,” *43rd AIAA Thermophysics Conference*, June 2012, doi:10.2514/6.2012-2873. AIAA 2012–2873.

[29] Y.-K. Chen and F. S. Milos, “Two-Dimensional Implicit Thermal Response and Ablation Program for Charring Materials,” *Journal of Spacecraft and Rockets*, 38(4):473–481, July–August 2001, doi:10.2514/2.3724.

[30] F. S. Milos and Y.-K. Chen, “Two-Dimensional Ablation, Thermal Response, and Sizing Program for Pyrolyzing Ablators,” *Journal of Spacecraft and Rockets*, 46(6):1089–1099, November–December 2009, doi:10.2514/1.36575.

[31] Adam J. Amar, A. Brandon Oliver, Benjamin S. Kirk, Giovanni Salazar, and Justin Droba, “Overview of the CHarring Ablator Response (CHAR) Code,” *46th AIAA Thermophysics Conference*, June 2016, doi:10.2514/6.2016-3385. AIAA 2016–3385.

[32] Jean Lachaud and Nagi N. Mansour, “Porous-Material Analysis Toolbox Based on OpenFOAM and Applications,” *Journal of Thermophysics and Heat Transfer*, 28(2):191–202, April–June 2014, doi:10.2514/1.T4262.

[33] James B. Scoggins and Thierry E. Magin, "Development of Mutation++: Multicomponent Thermodynamic and Transport Properties for Ionized Plasmas written in C++," *11th AIAA/ASME Joint Thermophysics and Heat Transfer Conference*, June 2014, doi:10.2514/6.2014-2966. AIAA 2014–2966.

[34] Haoyue Weng and Alexandre Martin, "Multidimensional Modeling of Pyrolysis Gas Transport Inside Charring Ablative Materials," *Journal of Thermophysics and Heat Transfer*, 28(4):583–597, October–December 2014, doi:10.2514/1.T4434.

[35] Haoyue Weng and Alexandre Martin, "Numerical Investigation of Thermal Response Using Orthotropic Charring Ablative Material," *Journal of Thermophysics and Heat Transfer*, 29(3):429–438, July–September 2015, doi:10.2514/1.T4576.

[36] Haoyue Weng, Sean C.C. Bailey, and Alexandre Martin, "Numerical study of iso-Q sample geometric effects on charring ablative materials," *International Journal of Heat and Mass Transfer*, 80:570–596, 2015, doi:10.1016/j.ijheatmasstransfer.2014.09.040.

[37] Rui Fu, Haoyue Weng, Jonathan F. Wenk, and Alexandre Martin, "Two-way strongly coupled thermo-mechanical solver for ablation problems," *55th AIAA Aerospace Sciences Meeting*, January 2017, doi:10.2514/6.2017-0439. AIAA 2017–0439.

[38] David Olynick, Y.-K. Chen, and Michael E. Tauber, "Aerothermodynamics of the Stardust Sample Return Capsule," *Journal of Spacecraft and Rockets*, 36(3):442–462, May–June 1999, doi:10.2514/2.3466.

[39] Richard Thompson and Peter Gnoffo, "Implementation of a Blowing Boundary Condition in the LAURA Code," *46th AIAA Aerospace Sciences Meeting and Exhibit*, January 2008, doi:10.2514/6.2008-1243. AIAA 2008–1243.

[40] Yih-Kanq Chen, Frank S. Milos, and Tahir Gokcen, "Loosely Coupled Simulation for Two-Dimensional Ablation and Shape Change," *Journal of Spacecraft and Rockets*, 47(5):775–785, September–October 2010, doi:10.2514/1.39667.

[41] Peter Gnoffo, Scott Berry, and John Van Norman, "Uncertainty Assessments of 2D and Axisymmetric Hypersonic Shock Wave - Turbulent Boundary Layer Interaction Simulations at Compression Corners," *42nd AIAA Thermophysics Conference*, June 2011, doi:10.2514/6.2011-3142. AIAA 2011–3142.

[42] Hicham Alkandry, Iain D. Boyd, and Alexandre Martin, "Coupled Flow Field Simulations of Charring Ablators with Nonequilibrium Surface Chemistry," *44th AIAA Thermophysics Conference*, June 2013, doi:10.2514/6.2013-2634. AIAA 2013–2634.

[43] Alexandre Martin and Iain D. Boyd, "Strongly Coupled Computation of Material Response and Nonequilibrium Flow for Hypersonic Ablation," *Journal of Spacecraft and Rockets*, 25(1):89–104, January–February 2015, doi: 10.2514/1.A32847.

[44] Daniele Bianchi, Alessandro Turchi, Francesco Nasuti, and Marcello Onofri, "Chemical Erosion of Carbon-Phenolic Rocket Nozzles with Finite-Rate Surface Chemistry," *Journal of Propulsion and Power*, 29(5):1220–1230, September–October 2013, doi:10.2514/1.B34791.

[45] Daniele Bianchi and Francesco Nasuti, "Carbon-Carbon Nozzle Erosion and Shape-Change Effects in Full-Scale Solid-Rocket Motors," *Journal of Propulsion and Power*, 28(4):820–830, July–August 2012, doi:10.2514/1.B34267.

[46] Daniele Bianchi, Francesco Nasuti, Marcello Onofri, and Emanuele Martelli, "Thermochemical Erosion Analysis for Graphite/Carbon-Carbon Rocket Nozzles," *Journal of Propulsion and Power*, 27(1):197–205, January–February 2011, doi:10.2514/1.47754.

[47] Daniele Bianchi, Francesco Nasuti, and Emanuele Martelli, "Navier-Stokes Simulations of Hypersonic Flows with Coupled Graphite Ablation," *Journal of Spacecraft and Rockets*, 47(4):554–562, July–August 2010, doi:10.2514/1.47995.

[48] Daniele Bianchi, Francesco Nasuti, and Emanuele Martelli, "Coupled Analysis of Flow and Surface Ablation in Carbon-Carbon Rocket Nozzles," *Journal of Spacecraft and Rockets*, 46(3):492–500, May 2009, doi:10.2514/1.40197.

[49] Piyush Thakre and Vigor Yang, "Chemical Erosion of Carbon-Carbon/Graphite Nozzles in Solid-Propellant Rocket Motors," *Journal of Propulsion and Power*, 24(4):822–833, July–August 2008, doi:10.2514/1.34946.

[50] Leonardo C. Scalabrin, *Numerical Simulation of Weakly Ionized Hypersonic Flow Over Reentry Capsules*, Ph.D. thesis, University of Michigan, Ann Arbor, MI, 2007.

[51] Alexandre Martin, Leonardo C Scalabrin, and Iain D Boyd, "High performance modeling of atmospheric re-entry vehicles," *Journal of Physics: Conference Series*, 341:012002, February 2012, doi:10.1088/1742-6596/341/1/012002.

[52] Peter S. Bernard and James M. Wallace, *Turbulent Flow; Analysis, Measurement, and Prediction*, John Wiley & Sons, 2002.

[53] Y. Moryossef and Y. Levy, "Unconditionally positive implicit procedure for two-equation turbulence models: Application to k-ω turbulence models," *Journal of Computational Physics*, 220(1):88–108, 2006, doi:10.1016/j.jcp.2006.05.001.

[54] Xiao-Ling Tong, Edward Luke, and Lin Tang, "Evaluation of the Shear-Stress Transport Turbulence Model for Heat Transfer Applications," *41st Aerospace*

Sciences Meeting and Exhibit, January 2003, doi:10.2514/6.2003-769. AIAA 2003–0769.

[55] F. Menter, “Zonal Two Equation k-w Turbulence Models For Aerodynamic Flows,” *24th AIAA Fluid Dynamics Conference*, July 1993, doi:10.2514/6.1993-2906. AIAA 1993–2906.

[56] F. R. Menter, “Two-Equation Eddy-Viscosity Turbulence Models for Engineering Applications,” *AIAA Journal*, 32(8):1598–1605, August 1994, doi:10.2514/3.12149.

[57] Florian R. Menter, “Improved Two-Equation k-ω Turbulence Models for Aerodynamic Flows,” NASA TM–103975, National Aeronautics and Space Administration, Moffet Field, CA, October 1992.

[58] X.-L. Tong and E. Luke, “Turbulence Models and Heat Transfer in Nozzle Flows,” *AIAA Journal*, 42(11):2391–2393, November 2004, doi:10.2514/1.8900.

[59] Yildirim Suzen and Klaus Hoffmann, “Performance Study of Turbulence Models for Heat Transfer Predictions,” *32nd AIAA Thermophysics Conference*, June 1997, doi:10.2514/6.1997-2568. AIAA 1997–2568.

[60] Qunzhen Wang, “On the Prediction of Convective Heat Transfer Coefficients Using General-Purpose CFD Codes,” *39th AIAA Aerospace Sciences Meeting & Exhibit*, January 2001, doi:10.2514/6.2001-361. AIAA 2001–0361.

[61] B. Merci, J. Steelant, J. Vierendeels, K. Riemslagh, and E. Dick, “Computational Treatment of Source Terms in Two-Equation Turbulence Models,” *AIAA Journal*, 38(11):2085–2093, November 2000, doi:10.2514/2.870.

[62] Soo Hyung Park and Jang Hyuk Kwon, “Implementation of k-ω Turbulence Models in an Implicit Multigrid Method,” *AIAA Journal*, 42(7):1348–1357, July 2004, doi:10.2514/1.2461.

[63] M. Wasserman, Y. Mor-Yossef, I. Yavneh, and J.B. Greenberg, “A robust implicit multigrid method for RANS equations with two-equation turbulence models,” *Journal of Computational Physics*, 229(16):5820–5842, August 2010, doi:10.1016/j.jcp.2010.04.023.

[64] David C. Wilcox, *Turbulence Modeling for CFD*, DCW Industries, 2nd edition, 1998.

[65] Sherrie L. Krist, Robert T. Biedron, and Christopher L. Rumsey, “CFL3D User’s Manual (Version 5.0),” NASA TM-1998-208444, National Aeronautics and Space Administration, June 1998.

[66] P. Jawahar and Hemant Kamath, “A High-Resolution Procedure for Euler and Navier-Stokes Computations on Unstructured Grids,” *Journal of Computational Physics*, 164(1):165–203, 2000, doi:10.1006/jcph.2000.6596.

[67] C. L. Rumsey and E. M. Lee-Rausch, “NASA Trapezoidal Wing Computations Including Transition and Advanced Turbulence Modeling,” *30th AIAA Applied Aerodynamics Conference*, June 2012, doi:10.2514/6.2012-2843. AIAA 2012–2843.

[68] David C. Wilcox, “Reassessment of the scale-determining equation for advanced turbulence models,” *AIAA Journal*, 26(11):1299–1310, November 1988, doi:10.2514/3.10041.

[69] C. T. Crowe, “Review — Numerical Models for Dilute Gas-Particle Flows,” *Journal of Fluids Engineering*, 104(3):297, 1982, doi:10.1115/1.3241835.

[70] G. Rudinger, *Fundamentals of Gas-Particle Flow*, Handbook of Powder Technology, Elsevier, 1980.

[71] S. M. Dash, D. E. Wolf, R. A. Beddini, and H. S. Pergament, “Analysis of two-phase flow processes in rocket exhaust plumes,” *Journal of Spacecraft and Rockets*, 22(3):367–380, May–June 1985, doi:10.2514/3.25758.

[72] W.K . Melville and K. N. C. Bray, “A model of the two-phase turbulent jet,” *International Journal of Heat and Mass Transfer*, 22(5):647–656, May 1979, doi:10.1016/0017-9310(79)90113-3.

[73] Hsiao Tzu Chang, Lih Wu Hourng, and Lai Chen Chien, “Application of Flux-Vector-Splitting Scheme to a Dilute Gas-Particle JPL Nozzle Flow,” *International Journal for Numerical Methods in Fluids*, 22(10):921–935, May 1996, doi:10.1002/(sici)1097-0363(19960530)22:10<921::aid-fld382>3.0.co;2-1.

[74] Masoud Mirzaei, Abdollah Shadaram, and Maryam Shahyar, “Numerical Simulation of Supersonic Gas-Particle Flow Using Eulerian-Eulerian Approach,” *14th AIAA/AHI Space Planes and Hypersonic Systems and Technologies Conference*, November 2006, doi:10.2514/6.2006-7944. AIAA 2009–7944.

[75] R. Padmapriya and K. P. J. Reddy, “Numerical Analysis of Dusty Hypersonic Viscous Gas Flow over a Flat Plate,” *AIAA Journal*, 39(7):1313–1319, July 2001, doi:10.2514/2.1449.

[76] Jan-Renee Carlson, “Inflow/Outflow Boundary Conditions with Application to FUN3D,” NASA TM-2011-217181, National Aeronautics and Space Administration, October 2011.

[77] Donald A. Nield and Adrian Bejan, *Convection in Porous Media*, Springer, 4th edition, 2013, doi:10.1007/978-1-4614-5541-7.

[78] Bantwal Rabindranath Baliga, *A Control-Volume Based Finite-Element Method for Convective Heat and Mass Transfer*, Ph.D. thesis, University of Minnesota, Minneapolis, MN, 1978.

[79] Vaughan R. Voller, *Basic Control Volume Finite Element Methods for Fluids and Solids.*, World Scientific Publishing Co. Pte. Ltd., 2009.

[80] Yousef Saad and Martin H. Schultz, "GMRES: A Generalized Minimal Residual Algorithm for Solving Nonsymmetric Linear Systems," *SIAM Journal on Scientific and Statistical Computing*, 7(3):856–869, 1986.

[81] Yousef Saad, *Iterative Methods for Sparse Linear Systems*, SIAM, 2nd edition, 2003.

[82] William M. Kays, Michael E. Crawford, and Bernhard Weigand, *Convective Heat and Mass Transfer*, McGraw-Hill, 4th edition, 2005.

[83] Aerotherm Corporation, Mountain View, CA, *Aerotherm Chemical Equilibrium (ACE93)*, July 1993.

[84] Mark E. Ewing and Daron A. Isaac, "Mathematical Modeling of Multiphase Chemical Equilibrium," *Journal of Thermophysics and Heat Transfer*, 29(3):551–562, July–September 2015, doi:10.2514/1.T4397.

[85] Blaine E. Pearce, "Radiative Heat Transfer within a Solid-Propellant Rocket Motor," *Journal of Spacecraft and Rockets*, 15(2):125–128, March–April 1978, doi:10.2514/3.28003.

[86] Toshiyuki Suzuki, Keisuke Sawada, Tetsuya Yamada, and Yoshifumi Inatani, "Gas Permeability of Oblique-Layered Carbon-Cloth Ablator," *Journal of Thermophysics and Heat Transfer*, 18(4):548–550, October–December 2004, doi:10.2514/1.6242.

[87] Hugh Leslie Nicholas McManus, *High-Temperature Thermomechanical Behavior of Carbon-Phenolic and Carbon-Carbon Composites*, Ph.D. thesis, Stanford University, Stanford, CA, 1990.

[88] H. L. N. McManus and G. S. Springer, "High Temperature Thermomechanical Behavior of Carbon-Phenolic and Carbon-Carbon Composites, II. Results," *Journal of Composite Materials*, 26(2):230–255, January 1992, doi:10.1177/002199839202600205.

[89] Peter A. Gnoffo and Christopher O. Johnston, "A Boundary Condition Relaxation Algorithm for Strongly Coupled, Ablating Flows including Shape Change," *42nd AIAA Thermophysics Conference*, June 2011, doi:10.2514/6.2011-3760. AIAA 2011–3760.

[90] Bennie Blackwell and Micah Howard, "An Element Potential Based Chemical Equilibrium Solver for Gas/Surface Thermochemistry," *50th AIAA Aerospace Sciences Meeting*, January 2012, doi:10.2514/6.2012-815. AIAA 2012–0815.

[91] F. S. Milos and Y.-K. Chen, "Ablation, Thermal Response, and Chemistry Program for Analysis of Thermal Protection Systems," *10th AIAA/ASME Joint Thermophysics and Heat Transfer Conference*, June 2010, doi:10.2514/6.2010-4663. AIAA 2010–4663.

[92] Julien Troyes, Isabelle Dubois, Vincent Borie, and Annie Boischot, "Multi-Phase Reactive Numerical Simulations of a Model Solid Rocket Exhaust Jet," *42nd AIAA/ASME/SAE/ASEE Joint Propulsion Conference & Exhibit*, July 2006, doi:10.2514/6.2006-4414. AIAA 2003–4414.

[93] Alexandre Martin, Ioana Cozmuta, Michael J. Wright, and Iain D. Boyd, "Kinetic Rates for Gas-Phase Chemistry of Phenolic-Based Carbon Ablator in Atmospheric Air," *Journal of Thermophysics and Heat Transfer*, 29(2):222–240, April–June 2015, doi:10.2514/1.T4184.

[94] Tahir Gökçen, "N2-CH4-Ar Chemical Kinetic Model for Simulations of Atmospheric Entry to Titan," *Journal of Thermophysics and Heat Transfer*, 21(1):9–18, January–March 2007, doi:10.2514/1.22095.

[95] Bonnie J. McBride and Sanford Gordon, "Computer Program for Calculation of Complex Chemical Equilibrium Compositions and Applications. Part 2: User's Manual and Program Description," NASA RP-1311-P2, National Aeronautics and Space Administration, June 1996.

[96] Matthew L. Gross and Merrill W. Beckstead, "Diffusion Flame Calculations for Composite Propellants Using a Vorticity-Velocity Formulation," *Journal of Propulsion and Power*, 25(1):74–82, January–February 2009, doi:10.2514/1.36360.

[97] Matthew L. Gross and Merrill W. Beckstead, "Diffusion flame calculations for composite propellants predicting particle-size effects," *Combustion and Flame*, 157(5):864–873, May 2010, doi:10.1016/j.combustflame.2009.09.004.

[98] Chen Cheng, Fu Ting Bao, Yu Zhao, and Hao Xu, "Premixed Combustion of a Fine AP/HTPB Composite Propellant Based on Detailed Chemical Kinetics," *Applied Mechanics and Materials*, 390:320–326, August 2013, doi:10.4028/www.scientific.net/amm.390.320.

[99] M. B. Jeppson, M. W. Beckstead, and Q. Jing, "A Kinetic Model for the Premixed Combustion of a Fine AP/HTPB Composite Propellant," in "35th JANNAF Combustion Meeting," volume I, pages 639–653, 1998. CPIA-PUB-680-VOL-I.

[100] Matthew L. Gross, *Two-Dimensional Modeling of AP/HTPB Utilizing a Vorticity Formulation and One-Dimensional Modeling of AP and ADN*, Ph.D. thesis, Brigham Young University, 2007.

[101] Scott A. Felt, *Two-Dimensional Modeling of AP Composite Propellant Flame Structure with Detailed Kinetics*, Ph.D. thesis, Brigham Young University, August 2004.

[102] A. E. Lutz, R. J. Kee, and J. A. Miller, “SENKIN: A Fortran Program for Predicting Homogeneous Gas Phase Chemical Kinetics with Sensitivity Analysis,” Sandia Report SAND87-8248, Sandia National Laboratories, 1988.

[103] R. J. Kee, F. M. Rupley, and J. A. Miller, “CHEMKIN-II: A Fortran Chemical Kinetics Package for the Analysis of Gas-Phase Chemical Kinetics,” Sandia Report SAND89-8009B, Sandia National Laboratories, 1991.

[104] “NASA Turbulence Modeling Resource homepage,” June 2014. https://turbmodels.larc.nasa.gov/ [cited 2 June 2014].

[105] Frank M. White, *Viscous Fluid Flow*, McGraw-Hill, 3rd edition, 2006.

[106] Robert J. Moffat and William M. Kays, “The turbulent boundary layer on a porous plate: Experimental heat transfer with uniform blowing and suction,” *International Journal of Heat and Mass Transfer*, 11(10):1547–1566, October 1968, doi:10.1016/0017-9310(68)90116-6.

[107] P. S. Andersen, W. M. Kays, and R. J. Moffat, “The Turbulent Boundary Layer on a Porous Plate: An Experimental Study of the Fluid Mechanics for Adverse Free-Stream Pressure Gradients,” NASA CR 127817, National Aeronautics and Space Administration, 1972.

[108] Florian R. Menter and Christopher L. Rumsey, “Assessment of Two-Equation Turbulence Models for Transonic Flows,” *25th AIAA Fluid Dynamics Conference*, June 1994, doi:10.2514/6.1994-2343. AIAA 1994–2343.

[109] John James Kolozsi, *An Investigation of Heat Transfer through the Turbulent Boundary Layer in an Axially Symmetric, Convergent-Divergent Nozzle*, Master’s thesis, Ohio State University, Columbus, OH, 1958.

[110] “Theoretical Ablative Composite for Open Testing (TACOT) Ver. 2.2,” http://ablation2012.engineering.uky.edu/files/2012/02/TACOT_2.2.xls [cited 23 June 2015].

[111] Jean Lachaud, Alexandre Martin, Ioana Cozmuta, and Bernie Laub, “Ablation Workshop Test Case,” *4th Ablation Workshop*, March 2011. http://ablation2012.engineering.uky.edu/files/2012/02/Test_Case_1.pdf [cited 23 June 2015].

[112] Jean Lachaud, Alexandre Martin, Tom van Eekelen, and Ioana Cozmuta, “Ablation Test-Case Series #2,” *5th Ablation Workshop*, March 2012. http://ablation2012.engineering.uky.edu/files/2012/02/Test_Case_2.pdf [cited 23 June 2015].

[113] W. J. Kearney and R. A. Ellis, “Improved Performance Solid Rocket Nozzles of Advanced and Low-Cost Carbon/Carbon Materials,” in “1979 JANNAF Propulsion Meeting,” pages 115–132, Anaheim, CA, March 1979.

[114] Alexandre Martin and Iain D. Boyd, “Strongly coupled computation of material response and nonequilibrium flow for hypersonic ablation,” *41st AIAA Thermophysics Conference*, June 2009, doi:10.2514/6.2009-3597. AIAA 2009–3597.

[115] Peter G. Cross and Iain D. Boyd, “Two-Dimensional Modeling of Ablation and Pyrolysis with Application to Rocket Nozzles,” *46th AIAA Thermophysics Conference*, June 2016, doi:10.2514/6.2016-3383. AIAA 2016–3383.

[116] Peter G. Cross and Iain D. Boyd, “Conjugate Analysis of Rocket Nozzle Ablation,” *47th AIAA Thermophysics Conference*, June 2017, doi:10.2514/6.2017-3351. AIAA 2017–3351.

[117] Peter G. Cross and Iain D. Boyd, “Reduced Reaction Mechanism for Rocket Nozzle Ablation Simulations,” *47th AIAA Thermophysics Conference*, June 2017, doi:10.2514/6.2017-3682. AIAA 2017–3682.

[118] Peter G. Cross and Iain D. Boyd, “Two-Dimensional Modeling of Ablation and Pyrolysis with Application to Rocket Nozzles,” *Journal of Spacecraft and Rockets*, 54(1):212–224, January–February 2017, doi:10.2514/1.A33656.

[119] Peter G. Cross and Iain D. Boyd, “Reduced Reaction Mechanism for Rocket Nozzle Ablation Simulations,” *Journal of Thermophysics and Heat Transfer*, doi:10.2514/1.T5291. In press.

[120] Bonnie J. McBride, Michael J. Zehe, and Sanford Gordon, “NASA Glenn Coefficients for Calculating Thermodynamic Properties of Individual Species,” TP 2002–211556, National Aeronautics and Space Administration, September 2002.

[121] Satish Balay, Kris Buschelman, Victor Eijkhout, William D. Gropp, Dinesh Kaushik, Matthew G. Knepley, Lois Curfman McInnes, Barry F. Smith, and Hong Zhang, “PETSc Users Manual,” Technical Report ANL-95/11 - Revision 2.3.0, Argonne National Laboratory, April 2004.

[122] Malcom W. Chase, Jr., “NIST-JANAF Thermochemical Tables, Fourth Edition,” Journal of Physical and Chemical Reference Data Monograph 9, National Institute of Standards and Technology, 1998.

[123] D. R. Hull and H. Prophet, “JANAF Thermochemical Tables, Second Edition,” NSRDS–NBS 37, National Bureau of Standards, June 1971. Second Edition.

[124] F. G. Blottner, Margaret Johnson, and Molly Ellis, “Chemically Reacting Viscous Flow Program for Multi-Component Gas Mixtures,” Technical Report SC–RR-70-754, Sandia National Laboratories, December 1971.

[125] Roger A. Svehla, “Transport Coefficients for the NASA Lewis Chemical Equilibrium Program,” NASA TM 4647, National Aeronautics and Space Administration, April 1995.

[126] Bonnie J. McBride, Sanford Gordon, and Martin A. Reno, “Coefficients for Calculating Thermodynamic and Transport Properties of Individual Species,” NASA TM 4513, National Aeronautics and Space Administration, October 1993.

[127] John W. Schaefer, Thomas J. Dahm, David A. Rodriguez, John J. Reese, Jr., and Mitchell R. Wool, “Studies of Ablative Material Performance for Solid Rocket Nozzle Applications,” NASA CR–72429, National Aeronautics and Space Administration, March 1968. Aerotherm Report No. 68-30.